# SCANNING TUNNELING MICROSCOPY AND SPECTROSCOPY:

## I. SEMIMETALS AND SEMICONDUCTORS

## II. ATOM-RESOLVED IMAGING OF DNA

Thesis by

Robert James Driscoll

In Partial Fulfillment of the Requirements

for the Degree of

Doctor of Philosophy

California Institute of Technology

Pasadena, California

1993

(Submitted September 8, 1992)

*Acknowledgements*

There are many people I must thank and acknowledge for helping me to earn my Ph.D. degree. First on the list is my advisor, John Baldeschwieler, who got me started in the STM field. John's constant optimism and encouragement in the face of what often seemed impossible odds kept me plugging along with experiments.

All the people in the JDB group that have come and gone during my tenure have been invaluable friends who have helped me in some way. Michael Weimer and John Kramar were my "mentors," who were patient enough to teach me how to use the UHV-STM system they constructed. Special thanks also go to Michael Youngquist, a close friend with whom I collaborated on several projects, most notably the DNA experiments. Mike, in addition to making these experiments possible with "instant" changes in software, provided good company during some very lengthy stints in the lab.

Bill Kaiser and Richard Colton helped develop my experimental skills during my first two years. Shenda Baker must also be acknowledged - - she was a constant presence in lab, especially during the early years involved in building a STM. Joseph Meier and Charles Spence of Leroy Hood's group inspired the DNA experiments and kindly provided samples.

The biggest thanks go to those very special people in my life. My fiancé Kikuye encouraged me to write-up, and gave me a motivational "boost" whenever I needed one. My roommates and friends also deserve the greatest acknowledgements. Without the friendship of Mike Kosinski, Terry Coley, and Jon Hurley, I would not have enjoyed my graduate life as much as I did. My parents supported me throughout my life at all levels of education and encouraged me to attend Caltech. I thank them from the bottom of my heart.

*Abstract*

The topographic and electronic structure of semiconductor and semimetal surfaces were investigated using scanning tunneling microscopy (STM) and scanning tunneling spectroscopy (STS), respectively. The long-range morphology and atomic-scale characteristics of cleaved materials such as highly oriented pyrolitic graphite (HOPG), boronated pyrolitic graphite (BPG), titanium disulfide, and gallium arsenide (GaAs) were revealed by STM performed under ultrahigh vacuum (UHV) conditions.

Atomic resolution constant-current and current-imaging data, as well as barrier height information obtained from tunneling gap modulation, are presented. Both point and line defects were observed on these surfaces; the origin and role of native and adsorbed surface defects are discussed. Visual evidence of coulombic screening caused by adsorption of charged species on *n*-type GaAs(110) is provided. The atomic corrugation of the GaAs surface was measured to be as little as 0.03 Å peak-to-valley, attesting to the stability of the microscope design. The BPG sample used in these studies consisted of up to 0.5% boron; boron is the only known substitutional impurity of graphite. Boron substituent atoms appeared as small protrusions approximately 3 Å in diameter, with an atom density consistent with the assumed concentration. The BPG surface exhibited frequent line defects, including large-angle grain boundaries, and monolayer-depth etch pits. Images of BPG in air using graphite tips showed similar results; the validity of the popular "sliding-planes" mechanism for graphite imaging is evaluated.

The effects of anisotropic stress on the morphology and reconstruction of a thermally annealed Si(111) wafer were explored. The height and orientation of step bunches, as well as terrace widths, on the (7x7) surface

were determined. Electromigration effects were also observed; although the overall surface slope was conserved, the step bunches were "smeared out" by reversal of the current direction during heating. Line fault defects at step kinks were observed; a theory for the origin and structure of these features based on stress relief is proposed. Current imaging tunneling spectroscopy (CITS) and localized STS revealed differences between the adatom sites of the (7x7) surface. Atom-resolved barrier height images were also obtained; comparison to constant-current images may in fact provide a means of differentiating between defects and adsorbed species on the surface. The local effective barrier height was seen to depend strongly on the "cleanliness" of the STM tip. The barrier height increased dramatically following voltage pulsing on the order of ten volts. The large height of the step bunches also provided a good test to evaluate the sharpness of the STM tip; examples of "tip changes" affecting image resolution and "multiple-tipping" are provided. Silicon samples annealed at temperatures below 1000°C revealed substantial silicon carbide (SiC) contamination which effected step pinning. No SiC islands were observed on samples annealed above 1250°C.

In addition, atom-resolved STM images of duplex DNA supported on a HOPG surface were obtained in UHV. These images revealed double-helical structure, major and minor groove alternation, base pairs, and atomic-scale substructure. Comparison of the DNA dimensions derived from the STM data were in agreement with those from x-ray crystallography for "random-sequence" A-form DNA. Cross-sectional profiles of the experimental STM data showed excellent correlation with the atomic contours of the van der Waals surface of A-DNA. Barrier height cross-sections showed general correlation with the atomic-scale topography over the phosphate-sugar

backbone but distinct anticorrelation (complementarity) over the base pair region. The problems of aggregation and deposition coverage are discussed in the context of possible future applications of STM to DNA sequencing. The use of alternate techniques of DNA deposition, including electrospray ionization, for increased experimental reproducibility are described. The limitations of HOPG as a substrate for biomolecular adsorbates in STM experiments are evaluated.

# *TABLE OF CONTENTS*

*Chapter 2 (continued)*

*Chapter 2 (continued)*

# *Chapter 1*

# *INTRODUCTION*

## *INTRODUCTION*

### *Historical Background*

The scanning tunneling microscope (STM), invented in 1982 by Binnig and Rohrer,[1] represented a revolution in surface science by providing a technique with real-space atomic resolution imaging capability. Based on the topografiner developed by Young *et al.*[2] in the early 1970's, the STM exploited vacuum tunneling between a sharp metal tip and a conducting surface as a source of sensitive feedback control. Binnig *et al.*[3] first demonstrated the ability of STM to reveal the surface atomic arrangement of semiconductors in ultrahigh vacuum (UHV) with sub-ångström vertical resolution. These studies resolved a long-standing question about the structure and adatom arrangement of the (7x7) reconstruction on the silicon(111) surface. As a consequence, the theoretical dimer-adatom-stacking fault (DAS) model developed by Takayanagi *et al.*[4] was adopted.

In the decade since its invention, STM has been used successfully in a number of applications other than topographical studies in UHV. It is possible to resolve individual surface atoms in environments ranging from air[5] to liquids.[6] The STM is capable of providing information on local electronic properties including the density of states (DOS) through application of scanning tunneling spectroscopy (STS) techniques, such as current-voltage (*I-V*) spectroscopy,[7] and current imaging tunneling spectroscopy (CITS).[8] In addition, molecular beam epitaxial growth processes,[9] adsorbates on semiconductors, e.g., oxygen on gallium arsenide,[10] and chemical reactions, e.g., hydrogen with silicon,[11] have been investigated with STM. The STM has been applied to a wide variety of materials and phenomena, including charge-density waves,[12] liquid crystal molecules,[13] and fullerenes.[14] Numerous

scanned probe variants of STM have been introduced, including most notably, the atomic force microscope (AFM).[15] The AFM has permitted investigations to be expanded to non-conducting surfaces and adsorbates. More recently, STM has been applied to structural studies of biological materials and to atomic-scale lithography. In fact, STM has successfully imaged DNA with atomic-scale resolution[16] and has been used to manipulate single atoms[17,18] on surfaces. In the near future, it may become possible to use STM to sequence DNA and to create incredibly dense storage media.

***Basic STM Theory***

The STM operates on the quantum mechanical phenomenon of electron tunneling[19] between a conducting surface and a sharp (ideally terminated with a single atom) probe tip. Tunneling is the finite probability of a particle to penetrate an energy barrier larger than the particle's energy. When the tip is brought within several ångströms of the sample and a small bias voltage (mV to V) applied, electrons tunnel between them; the direction of tunneling depends on the polarity of the bias. The tunneling current is typically on the order of 1 nanoamp, and is extremely sensitive to the tip-sample separation (analogous to the tunneling barrier width). For a one-dimensional square barrier, the tunneling current $I$ is exponentially dependent on the tip-sample separation $s$, such that $I \propto \exp(A\phi^{1/2}s)$, where $\phi$ is the height of the barrier, usually estimated by the average of the tip and sample work functions, and $A$ is a pre-factor equal to 1.025 $eV^{-1/2}Å^{-1}$. It is this exponential dependence which is responsible for the unsurpassed vertical sensitivity of STM. In fact, for a work function of 5 eV, the tunneling current varies an order of magnitude for each 1 Å change in $s$.

Excellent reviews of basic STM theory have been published;[20,21] however, the most useful theory has been presented by Tersoff and Hamann,[22] using a formalism based on the transfer Hamiltonian approach developed by Bardeen.[23] In this approach, the tunneling barrier is treated as a perturbing Hamiltonian, in which the tip and sample are considered to be independent systems with little coupling. The tunneling current is calculated from the overlap of the tails of the wavefunctions of the two electrodes in the region of the tunneling barrier. Assuming a spherically symmetric tip, it is found that the tunneling current is a convolution of the electronic states of the tip and sample. At low voltages, as used in STM, the tunneling current can be simplified to $I \propto V\rho_s\rho_t$, where $V$ is the bias voltage, $\rho_s$ is the surface density of states of the sample at the center of the tip, and $\rho_t$ is the density of states of the tip at the Fermi level. As a result, STM images reflect contours of constant local density of states (LDOS). The STM is therefore a highly localized probe, both spatially and electronically, of the states near the Fermi levels of the tip and sample. The STM "topography" is a convolution of the geometric and electronic structure of the sample and reveals the LDOS variations of the sample within an energy window defined by the bias voltage and is a function of the tip-sample separation.

Lang[24] has shown that the observed size of an atom on a surface is dependent on the bias voltage and the gap width. In addition, the bias polarity can be chosen such that the STM image reveals either filled or empty surface states of the sample, especially on certain semiconductors where the spatial distribution of the surface state densities for the conduction band and the valence band differ significantly. For this reason, it is sometimes necessary to obtain images over a range of bias voltages in order to obtain a

more complete picture of the "true" surface structure. For example, alternate-bias polarity images on GaAs(110)[25] reveal the topographical positions of the Ga and As atoms individually. Alternate-bias imaging has also been used to reveal startling differences in the occupied and unoccupied states of the Si(111)-(7x7)[26,27] reconstructed surface.

***Imaging Modes of STM***

There are two major modes of STM imaging: (1) the constant current (or height imaging) mode, and (2) the constant height (or current imaging) mode. In either case, the tip is brought within tunneling distance (~ 1 to 10 Å) of the sample (close enough for tip and sample wavefunctions to overlap) under application of a small bias voltage (≤ 1 V), such that a tunneling current, typically 1 nA, is established. In order to build up a STM image, the tip is rastered across the surface by means of piezoelectric ceramics, which are materials which expand or contract upon application of an electric field. Piezoceramics typically expand on the order of 10 Å per volt, and therefore, it is quite straightforward to position and move the tip with sub-Å precision. An image is formed by collection of a series of closely-spaced "scan lines" and is essentially a map of the tip height $z$ versus the lateral tip position $x,y$.

The constant current (or "slow-scan") mode was first historically and remains the more popular means of data collection. A feedback circuit is used to maintain the tunneling current constant while the tip is scanned across the sample by changing the height ($z$ piezoceramic extension) of the tip in response to changes in the surface topography. In the constant height (or "fast-scan") mode, the tip is scanned rapidly across the sample at nearly constant height while the current is monitored. In this method, the feedback network responds only quickly enough to keep the average current constant.

The variations in the tunneling current $I$ are then plotted directly as a function of tip position to obtain an image. The constant height mode permits much faster scanning and is consequently less prone to deleterious phenomena such as piezoceramic creep, thermal drift, and vibrational noise. In addition, observation of processes in real-time is possible and data collection time can be significantly reduced; however, atomically flat surfaces are required since the scan rate is typically faster than the feedback response. The differences between the two techniques are schematically illustrated in Figure 1.

***Spectroscopy with a STM***

There exist a number of spectroscopic techniques associated with STM which are generally referred to as scanning tunneling spectroscopy (STS). An excellent review of STS has been published.[28] As aforementioned, the tunneling current is sensitively dependent upon the bias voltage and the tip-sample separation. This allows the STM to be used as a spectroscopic tool.

The most common form of STS is current-voltage ($I$-$V$) spectroscopy, in which the response of the tunneling current is monitored as the bias voltage is ramped over a desired voltage range. In most cases, the tip is held at a particular position over the surface while the voltage is ramped without feedback control, in order to avoid simultaneous compensatory changes in the gap width. The $I$-$V$ curve shows the voltage dependence of the tunneling current, and information about both occupied and unoccupied states can be obtained. Usually the differential conductance ($\mathrm{d}I/\mathrm{d}V$) or the normalized conductance $(\mathrm{d}I/\mathrm{d}V)/(I/V)$ (or $\mathrm{d}\ln I/\mathrm{d}\ln V$) is plotted versus the voltage; derivative methods are more sensitive to weak spectral features. The normalized conductance has been shown[29] to correspond closely with the

LDOS of the sample with little z dependence. Typically many (on the order of 100) *I-V* curves are collected and averaged to reduce noise. This process requires several seconds, during which the tip has thermally drifted a few Å, such that the data is unit-cell averaged. General information on Fermi-level pinning[30] and semiconductor carrier type (*n*- or *p*-type)[31] can be obtained from this kind of spectroscopy. The *I-V* spectra may also be obtained at specific points in an image to obtain site-specific electronic information. Hamers *et al.*[8] have developed a spectroscopic technique referred to as current imaging tunneling spectroscopy (CITS), in which an *I-V* curve can be taken at each point or at selected points during a topographic scan, resulting in spatially resolved *I-V* relations. In such a way, a current image at any voltage contained within the voltage ramp range used in the *I-V* curve may be "built up" from the library of *I-V*'s. Consequently, the electronic information (at any desired voltage) can be directly compared to topographic features, and one can construct real-space images of the surface states. Peaks in the derivatives of these spectra are interpreted as corresponding to energies of high LDOS, e.g., surface states or resonances.

It is possible also to extract information on the "local effective barrier height" (commonly referred to as the work function) by exploiting the tunneling equation provided earlier. The exponential proportionality factor for the separation dependence of the tunneling current is the square root of the barrier height. The barrier height is determined typically by modulating the tip-surface separation (by applying a small voltage modulation to the z piezo) at a frequency greater than the feedback bandwidth while the logarithm of the tunneling current is detected using lock-in techniques. In this manner, the barrier height $\phi$ is equal to $(\mathrm{d} \ln I / \mathrm{d} s)$. The barrier height may also be

determined during topographical scanning to provide atomically-resolved barrier height images.[32] Barrier height imaging, being a frequency-limited technique using ac lock-in detection, is less sensitive to vibrational noise. As a result, barrier height images are often of higher quality than the corresponding topographical images. This data may provide additional information on the chemical identity of surface species.

## *CALTECH UHV-STM DESCRIPTION*

### *General Design Features*

An extensive analysis of the engineering requirements for a STM is provided by Pohl.[33] The overall description of the Caltech UHV-STM system has been provided previously.[34] However, there have since been instrumental modifications, and additional experimental details heretofore unmentioned are necessary.

The STM used in these experiments is based on the "pocket-size" design developed by Gerber *et al.*,[35] consisting of a stack of stainless steel plates separated by viton rubber spacers for vibration isolation. Additionally, the STM is placed on a two-stage spring suspension, with a primary resonance of ~ 1 Hz, for additional immunity to vibrational interference. The STM stage is damped by magnetic eddy currents using copper blocks. Coarse positioning and approach of the sample to the tip are provided by a piezoceramic walker or "louse." Scanning is afforded by a set of three orthogonal piezoceramic elements, constructed of PZT-5A material, with an expansion coefficient of ~ 10 Å/V. The expansion of these elements are calibrated periodically by scanning materials, e.g., HOPG, with known lattice constants.

The UHV system consists of two individually-pumped chambers, one which houses the STM and one which is used for heating or ion sputtering of the sample, separated by a gate valve. Both chambers are equipped with quadrupole mass spectrometers. The samples and tips are introduced to the vacuum system via a fast-entry load lock, and can then be transferred to either chamber using a long-stroke rack-and-pinion translator. The samples are placed on stubs suitable for manipulation with standard wobble sticks. The samples are usually held in place using indium solder; however, in certain cases with semiconductor wafers requiring heating, e.g., silicon(111),[36] "custom" stubs were necessary. An apparatus for resistive heating of silicon samples was recently installed in the STM chamber.[37] The modifications adopted for *in situ* tip transfer have been detailed previously.[38] The base pressure of the STM vacuum chamber is ~ $3 \times 10^{-10}$ torr, sufficiently low for most semiconductor investigations.

***Data Acquisition/Image Processing***

The Caltech UHV-STM is capable of taking either constant current or constant height images, from atomic-scale areas up to a maximum of approximately 0.5 μm on a side. The general features of the system are described in Ref. 34. The bias voltage is applied at the sample, and the tips are typically ac or dc electrochemically etched tungsten wire. The constant current images can be obtained simultaneously with barrier height images using a small dither (≤ 1 Å) on the z piezoceramic. Alternate-bias "fast-scan" imaging is also a feature of this system. The image axes can also be rotated through 360° using an Optical Electronics Inc. (Tucson, AZ) analog image rotator (Model 6125A). This capability is useful for orienting the feature of interest to a desired angle in the image. Current-voltage spectra may be taken

at any selected point within a scan and numerous spectra may be averaged. In addition, CITS may also be performed, with spectra obtained after each five topographical points typically.

The images are displayed (and presented in this thesis) in a variety of ways. The real-time graphics display is usually a line plot of $x$ versus $y+z$. Post-acquisition image processing includes top-view gray- or color-scale displays, plotting $z$ color intensity versus $x$ and $y$. In addition, three-dimensional projections are possible,[39] with the ability to "fill" between data points and to "key" with respect to height or local slope (simulated lighting). In all cases, a constant-slope least-squares-fit plane is subtracted from the image to remove image tilt. Cross-sectional linecuts, in which the $z$ value is plotted along a chosen line in the $x$-$y$ plane, provides height and shape information on specific image features. Image filtering includes a weighted iterative three-point sliding window average for smoothing of the data. In addition, both one- and two-dimensional fast Fourier transform (FFT) routines[39] are available for obtaining power spectra or for data filtering, usually in the form of low- or high-pass (rather than band-pass) filtering.

### *PURPOSE OF THIS WORK*

The purpose of this work is two-fold, consistent with the split nature of this thesis. The first section examines the ability of STM and STS to investigate the nature and structure of atomic-scale defects, both native and adsorbed, on semimetal and semiconductor surfaces. It is shown that the STM is an ideal technique for investigating the local nature of surfaces, especially point and line defects. Other techniques, like low energy electron diffraction (LEED) or electron microscopy (EM), lack either the real-space

capability or the resolution required for studying low-concentration atomic-scale surface imperfections. For example, LEED samples and averages broad areas of the surface and provides reciprocal-space data on the atomic arrangement of surfaces, insensitive to localized imperfections or other reconstructions. The goal of this section is to illustrate the ability of STM to reveal subtle physical and electronic surface phenomena not accessible to other techniques. The second section demonstrates for the first time the ability of STM to reveal atomic-scale features on biological molecules like DNA. Almost since the invention of STM, there has been interest in imaging biological molecules.[40] Even though STM was believed to be "limited" to conductive materials, many attempts, including metal coating[41] and conductive replicas,[42] were made in an effort to equal or better the resolution possible with electron microscopy. Until this time, resolution no better than ~ 10 Å was attained on the double-helix. However, reliable and reproducible imaging of DNA on the atomic scale remains elusive. The goal of this section is to demonstrate the biological capability of STM and to propose the possibility of sequencing DNA with STM in the future. In addition, some of the factors that may need to be modified, especially the substrate identity and deposition technique, are discussed.

*SUMMARY OF CHAPTERS*

This thesis is divided into five chapters. There are two major subdivisions to the thesis: (I) STM and STS of semimetals and semiconductors, and (II) atom-resolved imaging of DNA. Chapter 1 is an introduction to the technique of STM, describes the general theme of this thesis, and provides a brief description of the Caltech UHV-STM system.

Chapters 2 through 4 deal individually with the STM and/or STS investigation of a variety of semimetals and semiconductors, concentrating heavily on gallium arsenide(110) and silicon(111)-(7x7). Chapter 5 deals with the imaging of the DNA double helix.

Chapter 2 presents a series of STM investigations of cleaved semimetals, such as highly oriented pyrolitic graphite (HOPG), titanium disulfide ($TiS_2$), and boronated pyrolitic graphite (BPG). The long-range morphologies as well as atomic topologies of these surfaces are provided. The imaging of point defects, including missing atoms and individual boron substituent atoms in BPG, is demonstrated. The use of HOPG or BPG as a substrate for adsorbates, especially biologically important molecules, is discussed. The successful imaging of individual boron defects with a graphite tip makes it necessary to reconsider the validity of this approach for simulating "sliding graphite planes" and consequently we evaluate the popular "sliding-planes" mechanism for graphite imaging. This subject is addressed with respect to previous work.[43]

Chapter 3 provides a detailed STM investigation of the cleaved semiconductor, GaAs(110) surface. The preparation of a clean and flat sample is described and experimental results are provided. The study focuses on the observation and imaging of atomic-scale native and adsorbed defects, including point defects and steps. The chapter also describes the interesting visual effects of coulombic screening caused by adsorption of charged species. In addition, the Fourier transform power spectrum of the surface determined by analysis of STM data is provided and discussed.

In chapter 4, both STM and STS are used to investigate an annealed and stressed silicon(111) wafer. The chapter primarily deals with the

formation and study of the (7x7) reconstruction on heated (annealed) silicon. The visual effects of step pinning caused by silicon carbide islands on samples heated to insufficiently high temperatures are provided. The anisotropically stressed sample shows interesting step bunching, and the effects of cooling rate and current reversal during heating are discussed. Also presented is the selective atom-resolved imaging of filled and unfilled states, by both alternate-bias imaging and CITS. In addition, a rarely observed line fault defect, caused by the relief of surface stress was imaged and a model for its structure is postulated.

Chapter 5 represents the first demonstration of the ability of STM to resolve the atomic features of biological molecules. The chapter describes experiments on duplex DNA and discusses the successes and failures in our attempts at imaging DNA reproducibly. The topographical images are compared to barrier height measurements to reveal interesting relationships. The possible application of STM to the sequencing of DNA is briefly discussed.

**Figure 1**

A schematic illustrating the two major imaging modes of STM: (a) constant current (height imaging) or "slow-scan," and (b) constant height (current imaging) or "fast-scan" imaging. In the constant current mode, a feedback circuit maintains the tunneling current at a preset reference level while scanning. The z piezoceramic is adjusted via application of voltage in order for the tip to follow the contours of the surface. In the constant height mode, the scan rate is so fast that the feedback responds only to the overall sample slope. The variations in the tunneling current during scanning are measured directly to obtain the image. This "fast-scan" imaging requires an atomically flat sample. The figure is taken from Ref. 20.

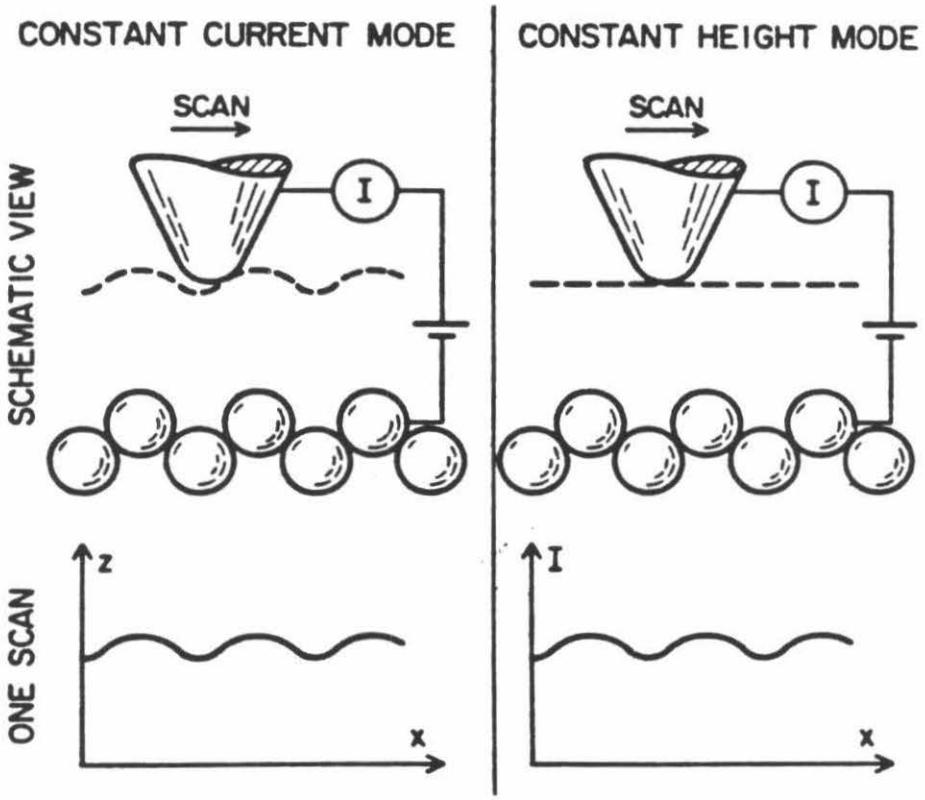
CONSTANT CURRENT MODE
CONSTANT HEIGHT MODE
SCAN
SCAN
I
I
SCHEMATIC VIEW
ONE SCAN
z
x
I
x

## *REFERENCES*


1. G. Binnig and H. Rohrer, *Helv. Phys. Acta* **55**, 726 (1982).
2. R.D. Young, J. Ward, and F. Scire, *Rev. Sci. Instrum.* **43**, 999 (1972).
3. G. Binnig, H. Rohrer, Ch. Gerber, and E. Weibel, *Phys. Rev. Lett.* **50**, 120 (1983).
4. K. Takayanagi, T. Tanishiro, M. Takahashi, and S. Takahashi, *J. Vac. Sci. Technol. A* **3**, 1502 (1985).
5. R. Sonnenfeld and P.K. Hansma, *Science* **232**, 211 (1986).
6. S.-I. Park and C.F. Quate, *Appl. Phys. Lett.* **48**, 112 (1986).
7. G. Binnig and H. Rohrer, *IBM J. Res. Develop.* **30**, 335 (1986).
8. R.J. Hamers, R.M. Tromp, and J.E. Demuth, *Phys. Rev. Lett.* **56**, 1972 (1986).
9. for example, see D.M. Chen, J.A. Golovchenko, P. Bedrossian, and K. Mortensen, *Phys. Rev. Lett.* **61**, 2867 (1988).
10. J.A. Stroscio, R.M. Feenstra, and A.P. Fein, *Phys. Rev. Lett.* **58**, 1668 (1987).
11. J.J. Boland, *Surf. Sci.* **244**, 1 (1991).
12. R.E. Thomson, U. Walter, E. Ganz, J. Clarke, A, Zettl, P. Rauch, and F.J. DiSalvo, *Phys. Rev. B* **38**, 10734 (1988).
13. D.P.E. Smith, J.K.H. Hörber, G. Binnig, and H. Nejoh, *Nature* **344**, 641 (1990).
14. Y.Z. Li, M. Chander, J.C. Patrin, J.H. Weaver, L.P.F. Chibante, and R.E. Smalley, *Science* **253**, 429 (1991).
15. G. Binnig, C.F. Quate, and Ch. Gerber, *Phys. Rev. Lett.* **56**, 930 (1986).
16. R.J. Driscoll, M.G. Youngquist, and J.D. Baldeschwieler, *Nature* **346**, 294 (1990).
17. D.M. Eigler and E.K. Schweizer, *Nature* **344**, 524 (1990).
18. I.-W. Lyo and P. Avouris, *Science* **253**, 173 (1991).
19. R.H. Fowler and L. Nordheim, *Proc. R. Soc. London A***119**, 173 (1928).
20. P.K. Hansma and J. Tersoff, *J. Appl. Phys.* **61**, R1 (1987).
21. Y. Kuk and P.J. Silverman, *Rev. Sci. Instrum.* **60**, 165 (1989).
22. J. Tersoff and D.R. Hamann, *Phys. Rev. Lett.* **50**, 1998 (1983); *Phys. Rev. B* **31**, 805 (1985).

23. J. Bardeen, *Phys. Rev. Lett.* **6**, 57 (1961).

24. N.D. Lang, *Phys. Rev. Lett.* **55**, 230 (1985); *Phys. Rev. Lett.* **56**, 1164 (1986); *Phys. Rev. Lett.* **58**, 45 (1987).

25. R.M. Feenstra, J.A. Stroscio, J. Tersoff, and A.P. Fein, *Phys. Rev. Lett.* **58**, 1192 (1987).

26. Th. Berghaus, A. Brodde, H. Neddemeyer, and St. Tosch, *J. Vac. Sci. Technol. A* **6**, 478 (1988); *J. Vac. Sci. Technol. A* **6**, 483 (1988).

27. R.M. Tromp, R.J. Hamers, and J.E. Demuth, *Phys. Rev. B* **34**, 1388 (1986); *Science* **234**, 304 (1986).

28. R.M. Tromp, *J. Phys.: Condens. Matter* **1**, 10211 (1989).

29. R.M. Feenstra, W.A. Thompson, and A.P. Fein, *Phys. Rev. Lett.* **56**, 608 (1986); J.A. Stroscio, R.M. Feenstra, and A.P. Fein, *Phys. Rev. Lett.* **57**, 2579 (1986).

30. H. Salemink and O. Albrektsen, *J. Vac. Sci. Technol. B* **9**, 779 (1991).

31. W.J. Kaiser, L.D. Bell, M.H. Hecht, and F.J. Grunthaner, *J. Vac. Sci. Technol. A* **6**, 519 (1988).

32. J.S. Villarubia and J.J. Boland, *Phys. Rev. Lett.* **63**, 306 (1989).

33. D.W. Pohl, *IBM J. Res. Develop.* **30**, 417 (1986).

34. J.A. Kramar, Ph.D. Thesis, "Tunneling Microscopy and Spectroscopy of Molybdenum Disulfide," California Institute of Technology, 1990.

35. Ch. Gerber, G. Binnig, H. Fuchs, O. Marti, and H. Rohrer, *Rev. Sci. Instrum.* **57**, 1688 (1986).

36. original silicon sample stub used in these experiments is courtesy of Shenda Baker.

37. silicon heater courtesy of Shenda Baker - - described in ref. 38.

38. S.M. Baker, Ph.D. Thesis, "Scanning Tunneling Microscopy and Spectroscopy of Silicon and Carbon Surfaces," California Institute of Technology, 1992.

39. developed by M.G. Youngquist.

40. G. Binnig and H. Rohrer, in *Trends in Physics* (eds. J. Janta and J. Pantoflicek), 38-46 (European Physical Society, The Hague, 1984).

41. M. Amrein, A. Stasiak, H. Gross, E. Stoll, and G. Travaglini, *Science* **240**, 514 (1988).

42. J.A.N. Zasadzinski, J. Schneir, J. Gurley, V.B. Elings, and P.K. Hansma, *Science* **239**, 1013 (1988).

43. R.J. Colton, S.M. Baker, W.J. Kaiser, and J.D. Baldeschwieler, *Appl. Phys. Lett.* **51**, 305 (1987).

# *Chapter 2*

# *SCANNING TUNNELING MICROSCOPY OF CLEAVED SEMIMETALS*

*INTRODUCTION*

Cleaved semimetals represent an important and popular class of materials for study by STM. In fact, highly oriented pyrolitic graphite (HOPG), a typical semimetal, is the standard calibration surface for STM and is used to test the atomic-resolution capabilities of STM instruments. Additionally, HOPG is used in a majority of STM experiments requiring a substrate for adsorbate deposition. The reason for this popularity is that HOPG, like many other cleavable layered materials, is easy to prepare for STM applications. Simple cleavage with adhesive tape reveals a fresh surface which is atomically flat over regions microns in size. In addition, many of these materials are relatively inert chemically and remain "clean" for extended periods of study. This characteristic is especially important for STM studies performed under ambient conditions. Conversely, the inertness of the basal (cleavage) plane of HOPG makes it problematic to securely "attach" deposited molecules. This drawback is discussed in the following section of this thesis.

Semimetals are a relatively small class of materials which differ from semiconductors in that there is a slight overlap of conduction and valence bands (negative bandgap). The conduction band edge is very slightly lower in energy than the valence band edge. This small overlap in energy of the conduction and valence bands leads to a small concentration of holes in the valence band and of electrons in the conduction band.[1] Arsenic, antimony, bismuth, and carbon (in the form of graphite) are examples of semimetal elements. Like semiconductors, semimetals may be doped with suitable impurities to vary the relative numbers of holes and electrons. The carrier concentrations for semimetals generally fall in the range $10^{17}$ to $10^{21}$ per $cm^3$; those for semiconductors (at room temperature) vary from $10^{13}$ to $10^{17}$ and

those of metals are around $10^{23}$. A pure semimetal at absolute zero is a conductor; there are partially filled electron and hole bands. A semiconductor at absolute zero is an insulator; conduction occurs only because carriers are either thermally excited or introduced by impurities.

The layered materials most commonly studied by STM are graphite and the family of chalcogenides, such as titanium disulfide ($TiS_2$)[2] and the charge-density-wave (CDW) compound titanium diselenide, $TiSe_2$. The examples provided here are also semimetals. There are three STM studies of cleaved, layered semimetals included here in this chapter. They are addressed individually in the order HOPG, $TiS_2$, and boronated pyrolitic graphite (BPG).

## *A. Highly Oriented Pyrolitic Graphite, HOPG*

### *Background*

#### Physical Properties of HOPG

Carbon is found in nature in one of three major allotropic forms: amorphous, graphite, and diamond. Graphite is an important and widely used material, used for pencil leads, as a lubricant, and for making crucibles and electrodes. Graphite is characterized by delocalized $sp^2$ bonding, with a bond order value of 1.67.[3] The structure of graphite is made up of hexagonal unit cells, which contain three unique atomic sites, commonly referred to as A, B, and C sites. The structure of graphite is provided in Figure 1. Site A is a surface atom with a neighboring atom directly beneath it in the next layer, site B is a surface atom without an underlying atom, and site C is a surface hollow. The interlayer spacing is 3.35 Å, the interatomic spacing is 1.42 Å, and the spacing between unit cells is 2.46 Å. Layered materials like graphite have covalent bonding within each layer but only weak van der Waals

bonding between layers. This fact gives rise to the extreme anisotropy in both reaction and conductivity between in-plane and orthogonal directions. Reaction rates at defects and step edges is indeed greatly enhanced over the basal plane, being at least $10^5$ higher.[4] Synthetic graphite is used throughout the studies reported here. The primary manufacturer of graphite is Union Carbide[5]. There are many types of pyrolitic graphites,[6] prepared by annealing carbon at temperatures between 2000°C and 2500°C. There are additionally several grades (graded by the manufacturer) of HOPG, ranging in "quality," depending on the x-ray diffraction linewidth (representative of the orientational alignment of the polycrystalline grains) and the microcrystallite size. These grades range (in order of decreasing quality/increasing angular misalignment) from ZYA to ZYB through ZYH. The ZYA grade HOPG is used for x-ray monochromator calibration and has a x-ray mosaic spread less than 0.4°, while that for ZYH is up to 3.5°.[7] The microcrystallite size is larger for higher grades (~ 1 μm for ZYA), and it is known that lower grades of graphite are rougher topographically and have a higher frequency of surface defects, especially steps, as well as greater surface and bulk disorder.[8] It is also more difficult to obtain visually good cleaves using lower grades of HOPG.[8]

STM Studies of HOPG

Graphite, like many layered materials, is ideal for STM experiments because it is easily cleaved, atomically flat, and remains relatively clean to air exposure, due to its extremely low gas adsorption efficiency. No contamination is detected by Auger analysis or STM after brief air exposure.[9] In addition, the atomic structure is well known and the electronic structure is relatively simple to calculate.[10] HOPG was, in fact, the first material to be imaged at atomic resolution by STM in air[11] and under water.[12] The

experimental observations were in general agreement with theoretical calculations by Selloni *et al.*.[13] Their calculations predicted that for electrons near the Fermi energy (zero bias) the maximum corrugation, with a height difference near 1 Å, should occur between site B and the hollow at site C. However, occasionally, unreasonably large corrugation heights have been observed.[14,15] Other anomalous characteristics include asymmetric and dynamic images,[16,17] moiré patterns,[18] low barrier heights,[19,20] and unreasonable gap distance characteristics[17] in which there is only a very weak dependence of the tunneling current on the assumed gap width (atomically resolved images are obtained with the tip progressively displaced over a range on the order of 100 Å). The observations of "giant" corrugations have been associated with the unusual electronic structure of a single graphite layer, in which the Fermi surface collapses to a single point in the surface Brillouin zone.[21] In addition, others have proposed the possibility of large-scale surface deformations induced by elastic interactions between the STM tip and the surface,[22] especially in the case of contaminated tip-surface junctions.[15,20] The observation of asymmetric or dynamic images and low barrier heights have been explained by a combination of multiple-tipping (also tip asymmetry)[23] and tip-surface contact; as a result, the notion of sliding graphite planes[17,24] as a mechanism for graphite imaging, especially at low tunneling resistances, has become quite popular. This proposed mechanism has been used to explain the apparent lack of defects on the HOPG surface. Graphite tips (pencil leads) have been used to evaluate the possibility of this contrast source by simulating the condition of two planes of graphite sliding across one another.[17,25] This mechanism is also discussed later in this chapter in section C in relation to the STM imaging of boronated pyrolitic graphite with a

graphite tip. In any case, when images of HOPG are obtained with what are believed to be tips terminated with a single atom, only one of the two surface atomic sites is apparently imaged. From theoretical considerations,[16] it is believed that the atoms that are imaged are B site atoms, those without atomic neighbors in the underlying layer. Only alternate atoms are imaged, and therefore, the symmetry is threefold, rather than sixfold.

***Experimental***

The HOPG used throughout these studies was ZYA monochromator-grade obtained from Union Carbide. The samples were cut to appropriate sizes for the sample stub (ca. 7mm x 7 mm) and were mounted using indium solder. In most cases, the samples were freshly cleaved with adhesive tape in a nitrogen flow (until a visibly "pristine" surface was obtained), immediately introduced to the load lock, and pumped to vacuum. Occasionally, the samples were cleaved in air; however, again they were placed into the vacuum system within minutes of cleavage. No observable differences were noted between these samples. The STM experiments were performed in UHV ($< 10^{-9}$ torr) using the Caltech UHV-STM unless otherwise noted.[26] In addition, an electrochemically etched tungsten tip was typically used; information on whether an ac or dc etch was used is provided with the data. On several occasions, a mechanically cut platinum or platinum-iridium tip was used.[27] The experimental conditions are provided with the data.

***Results and Discussion***

Long-Range Morphology

The HOPG surface is found to be atomically flat over regions hundreds to thousands of ångströms in size. Since the maximum scan range of our STM is approximately 0.5 microns, the HOPG images over this range are often

atomically flat and featureless, devoid of any steps or roughness. In addition, the surface is relatively free of gross microstructural defects. The most common features are steps, which are usually straight and lie along the three principal symmetry axes (120° to each other) defined by the crystal orientation of that particular region. The steps usually range from one to several atomic layers high (a single atomic step is 3.35 Å high and can be used for vertical *z* piezoceramic calibration). Occasionally, an exfoliated region of graphite is observed in which a graphite layer is "peeled away" or "folded back" on itself. In UHV studies, no visible contamination has been encountered with STM on HOPG, even along step edges. This is presumably due to the clean environment provided by the UHV conditions. However, "build-up" of contamination is frequently seen in images obtained in air,[28] especially on samples that are not freshly cleaved. In addition, repetitive "ghosting" of large surface features caused by imaging with multiple tips is frequently observed, regardless of the type of tip preparation; multiple tipping however is more frequent with mechanically cut tips. No large-scale moiré patterns,[18] tilt boundaries between grains,[18] charge density waves,[29] or superlattices,[30] as reported elsewhere, have been observed in our vacuum studies.

Atom-Resolved Imaging

Graphite is imaged at atomic resolution primarily for calibration prior to imaging other surfaces; the piezoceramic elements of the STM require periodic calibration since their expansion coefficients can change considerably following the vacuum chamber heating needed to attain UHV conditions. The atomic structure of the HOPG surface exhibits a variety of appearances when imaged with STM, regardless of the mode of imaging (constant current, constant height, or barrier height modes). Most often, only alternate atomic

sites (B type carbons) are imaged, spaced 2.46 Å apart, consistent with the unit cell spacing. However, hexagonally shaped rings are also commonly observed; an example of this, in a constant height image, is provided in Figure 2. The image is 10 by 13 Å and is shown in both a top-view grayscale and a solid-modeled 3-D projection. These anomalous images are more common and pronounced at lower tunneling resistances (a combination of relatively low bias voltages and high tunneling currents). This is expected since the gap width is presumably decreased under these conditions and there exists, consequently, a greater possibility of appreciable interaction between the tip and sample, and perhaps even physical contact. Tunneling conditions typically found in the literature for HOPG imaging are 1-10 nA current and 10-100 mV bias. It is generally found that it becomes more difficult to observe atomic features at higher gap resistances since the tip is presumably further away, and consequently, the variations in the density of states decrease with increased gap widths. It is also found that it is more difficult to obtain atomic-resolution images on HOPG in UHV than in air, presumably because in air there is intervention by contamination. Figure 3 provides a STM constant current image (top) taken simultaneously with a gap-modulated barrier height image (bottom). The tunneling current for these images was 100 pA and the sample bias was 500 mV; the corresponding gap resistance was 5 GΩ. The images are approximately 120 by 100 Å in size. Either image represents one of the largest atomically-resolved images of HOPG in combination with one of the highest gap resistances reported in the STM literature. The atomic corrugation is ~ 0.5 Å, a value we typically measure in UHV; no "giant" corrugations have been observed. Barrier height images of HOPG are not typically performed, even though it is usually easier to obtain high-quality

images using a frequency-limited lock-in technique such as is used in barrier height imaging. In fact, no barrier height images of HOPG have been published. Figure 3 provides a typical barrier height image at the bottom. The maxima in the barrier height correspond with maxima in the topographical image, suggesting that the wavefunction decay rate is greater over B sites than A sites. A "zoomed" constant current image of HOPG approximately 32 Å on a side is provided in Figure 4. Each of the bright features in this grayscale image is a carbon atom, generally believed to be B site atoms. The threefold symmetry is quite evident in this image. However, tip asymmetries often lead to asymmetrically resolved images, in which apparent resolution is higher in one direction (relative to the scan direction) than another, leading to the appearance of prominent atomic rows in the data. An example of an image obtained using an asymmetric tip is provided in Figure 5. The top-view image (left) in Figure 5 has prominent horizontal atomic rows; the data is also plotted in two 3-D solid-modeled projections, one whose brightness is keyed to height (top right) and one whose brightness is keyed to local slope (bottom right).

HOPG as a Substrate

The basal plane of HOPG is commonly used as a substrate for the deposition of a variety of adsorbates, most frequently biological molecules like DNA. The main reasons for its popularity are its ease of preparation and its atomic flatness. However, defect-free HOPG is also chemically inert, which makes stable attachment of materials difficult. Attempts to make the basal plane of HOPG more reactive by chemical or physical (usually by oxidation via exposure to glow discharge) means result in unacceptable roughening of the surface. We have found in our studies that molecular adsorbates,

especially DNA, have a greater affinity for themselves than for the HOPG substrate to such an extent that there is considerable molecular "clumping." These observations are discussed in chapter 5 of this thesis. In addition, there have been recent reports[31,32] which have claimed that there exist, in air and electrochemical environments, surface features which could be mistaken for biomolecules. The authors of these papers report that steps and defects caused by poor cleavage can produce confusing features in STM images, especially when contamination accumulates at these features. Consequently, these authors question the usefulness of HOPG as a substrate for biomolecular adsorbates. These studies are discussed in detail in chapter 5, in addition to alternate substrate suggestions.

***Conclusion***

Imaging of HOPG with STM in UHV reveals that the surface is atomically flat over areas thousands of square ångströms in size. The HOPG surface appears to be clean by Auger and STM analysis after brief air exposure and to remain clean in UHV. In UHV, we have observed neither "giant" atomic corrugation nor accumulation of contamination at step edges nor features that could be mistaken for biomolecular adsorbates like DNA. However, these features have been encountered in STM images acquired in air on "dirty" HOPG samples, which had not been freshly cleaved. Therefore, it seems that HOPG is still a rather good substrate for molecular adsorbate studies when performed in UHV, even when one takes into account its lack of reactivity. These issues are addressed in more detail in chapter 5. It has been shown also that the tip structure, more specifically tip asymmetry and multiple tipping, can contribute to a wide variety of appearances for the HOPG surface atomic arrangement. Tip preparation unfortunately remains

for the most part a "hit-or-miss" proposition, in which the effectiveness of a tip is judged by using it in a STM. There have been efforts[33] to evaluate the termination structure of the tip using a recently installed field emission microscope (FEM) apparatus in order to understand and perhaps control the tip structure necessary for successful STM imaging.

## *B. Titanium Disulfide, $TiS_2$*

### *Background*

Physical Properties of $TiS_2$

Most of the early STM studies focussed on elemental surfaces. However, more recent investigations have included compound surfaces, including most notably the III-V semiconductors like GaAs and the family of transition metal dichalcogenides, e.g., $MoS_2$, which include numerous CDW materials. Titanium disulfide ($TiS_2$),[34] a transition metal dichalcogenide, is a layered compound semimetal[2] composed of alternating layers of titanium and sulfur atoms. Therefore, there are two types of surface atoms accessible to investigation by STM, with titanium atoms comprising the outermost surface layer. The in-plane bonding is covalent while there exist only weak van der Waals bonds between sandwich layers.

The cleavage plane of $TiS_2$ is atomically flat and relatively inert chemically. The structure of $TiS_2$ is provided in Figure 6; views both along and perpendicular to the *c* axis are shown. The Ti-S bond length is 2.42 Å and the S-S or Ti-Ti intralayer bond length is 3.39 Å. The cleavage plane remains unreconstructed from the bulk structure. Unlike the more familiar transition metal dichalcogenide, molybdenum disulfide ($MoS_2$), which is a semiconductor with trigonally prismatic coordination, $TiS_2$ has octahedral

cation coordination. In addition, $TiS_2$ has only one layer per unit cell, while $MoS_2$ has two layers. Titanium disulfide is officially classified as a 1T polytype hexagonal compound, characterized by the layered 1T-$CdI_2$ structure. Since the packing is hexagonal and there are equal numbers of Ti and S atoms, an image of either Ti or S atoms would show the same hexagonal symmetry with 3.4 Å lattice spacing. If both the top S layer and the Ti layer are visible, then the image will possess threefold symmetry. The close packed Ti layers are sandwiched between the two close packed S layers. At stoichiometric composition, the Ti cations are believed to occupy all the octahedral interstices between two layers of polarized S anions.

The pseudo-two-dimensional character of these materials contributes to a wide range of interesting physical and chemical properties:[35,36] interlayer intercalation of molecules, superconductivity, and charge density waves. It is expected[37,38] that the $TiS_2$ has a relatively high density of surface point defects, "missing" Ti atoms which are displaced into intersandwich sites, with S-S pair bonding around the sandwich vacancy. At near-stoichiometric compositions, the existence of displaced Ti atoms has been suggested,[39] i.e., Frenkel defects consisting of a Ti vacancy and an interstitial in the van der Waals' gap; an excess of Ti atoms up to 10 % can be accomodated in this gap.

The in-plane conductivity of $TiS_2$ is approximately 5000 $\Omega^{-1}cm^{-1}$ and the carrier density is ~ $10^{20}$ carriers/$cm^3$. There remains a controversy over whether titanium disulfide is a small band overlap semimetal with metallic characteristics or an extrinsic small bandgap semiconductor which is degenerate or nearly so. There are numerous references for both sides of the argument, reporting both semimetallic[40,41] and semiconducting[42,43] behavior. More recent investigations[44,45] however support more strongly the

contention that it is a semiconductor. The latter authors have reported the indirect bandgap to be ~ 0.2 to 0.3 eV and the direct bandgap to be ~ 0.8 eV.

STM Studies of $TiS_2$

There is only one published report on the imaging of $TiS_2$ with STM,[39] a structural study performed in air. Those authors reported that in addition to the trigonal lattice symmetry, they observed triangular-shaped features associated with defects at both 1T-$CdI_2$ structure sites and tetrahedral sites, caused presumably by displaced Ti atoms. The authors used a low sample bias of 25 mV and a moderate 1.3 nA tunneling current for constant current imaging. Their images consisted of an atomic lattice with triangular symmetry and 3.4 Å spacing. The "lower" layer atoms that were observed could be attributed to either multiple-tipping or to Ti atoms below the S surface layer. The prominent defect structures appeared as highlighted triangles with a singular orientation consisting of from 6 to 15 sites and randomly distributed on the surface. The defects were proposed to be Ti atoms displaced within the sandwich interstitially during the crystal growth process.

***Experimental***

The $TiS_2$ sample was a synthetically prepared single crystal,[46] obtained by iodine vapor phase transport in quartz tubes. In the synthetic process, powder is placed at the hot end (~ 850°C) of an evacuated quartz tube. Iodine is used as a transport agent and a small amount of excess S is added to ensure near-stoichiometric crystals. The sample was of good quality, shiny yellow-golden in color, and easily cleaved by adhesive tape. The sample was ~ 5 x 5 mm and was mounted on a stub by indium solder. The sample was cleaved in a nitrogen flow and immediately introduced into vacuum. No Hall probe

measurements were performed on the sample to determine the carrier concentration of the particular sample. In addition, no thermoelectric power or Seebeck coefficient measurements were carried out to characterize the sample. The STM experiments were performed at a pressure below $10^{-9}$ torr using ac electrochemically etched tungsten tips. The surface was investigated using constant current, constant height, and barrier height imaging techniques and their results are reported in the following section. The tunneling conditions are provided with the individual figures.

***Results and Discussion***

Comparison of Imaging Modes

Large-area STM images of $TiS_2$ confirmed that the surface is atomically flat over vast regions, often showing no roughness or step structure in the maximum scanning range of the piezoceramics (0.5 μm on a side). Atom-resolved images of the $TiS_2$ surface were obtained using three modes: constant height, constant current, and barrier height techniques. The constant height image, shown in Figure 7, is cropped to ~ 15 x 15 Å from a larger image to emphasize the threefold symmetry and the hexagonal arrangement of atoms in the unit cell. The atom centers are spaced 3.4 Å apart, consistent with imaging of either the Ti or S atomic lattice. Figures 8 and 9 show simultaneously acquired constant current and barrier height images, respectively. The images have both been presented in 3-D projections, but appear different due to slightly different display orientation and cropping. However, they represent nearly identical areas on the surface; the bottoms and sides of the two figures are consistent. The constant current image in Figure 8 shows typical point defects observed on the $TiS_2$ sample, which are apparently missing atoms or vacancies. The corresponding barrier

height image shows no similar companion vacancies. The images are discussed in the subsection immediately following.

Imaging of Point Defects

The constant current image in Figure 8, ~ 35 x 25 Å in size, shows two distinct vacancies whose positions are consistent with the atomic lattice of bright spots. This image is representative of the surface, which typically contained ~ 1 to 2 % vacancies. Since it is known that Ti atoms are displaced into interstitial sites, it can be assumed that these observed "holes" are displaced or "missing" Ti atoms. It is unlikely that they are S atoms, even though S atoms comprise the outermost surface layer in $TiS_2$; sulfur vacancies are not believed to occur with this frequency.

The corresponding barrier height image (Figure 9) shows a slightly decreased response over these vacancy sites, but there exists no clear indication of any missing atoms. The lack of a "hole" in the barrier height indicates that the sulfur lattice may contribute more strongly to the barrier height than to the "topography." The barrier height may "feel" the sulfur lattice as well or may be a less localized measurement than that of the atomic topography.

***Conclusion***

This STM imaging investigation of $TiS_2$ revealed that although the surface was atomically flat over regions up to nearly a square micron in size, it indeed also contained a large density of point defects. Unlike the published report performed in air, no raised or laterally enhanced defect structures were observed. No triangular features were encountered, only missing atoms probably due to Ti atoms displaced into interstitial sites in the van der Waals structure. This conclusion is obtained since only Ti atoms are known to form

these defect structures and the remainder of the atomic lattice was consistent with the vacancies. Therefore, it also seems that under the tunneling conditions used for the constant current images that the bright spots correspond with Ti atoms in the underlying layer rather than surface S atoms. The fact that there was not a corresponding "hole" observed in the barrier height image leads one to believe that the electronic structure, especially the local "work function," is relatively unaffected by the single vacancy. It is possible that the barrier height image, which probes the rate of decay of the local surface wavefunction, is more sensitive to contributions from neighboring and subsurface (or true surface) atoms. A surface such as this with a high density of defects offers the opportunity to study the local electronic effects of vacancies.

## *C. Boronated Pyrolitic Graphite, BPG*

### *Background*

Historical Background

Graphite is generally considered to be both atomically flat (over areas up to square microns) and defect-free, especially when highly-oriented. There are several grades of HOPG, graded ZYA, ZYB,...ZYH, in order of decreasing quality, as mentioned earlier in this chapter. Graphite, especially the higher grades, contains very few point defects, estimated from STM oxidation studies[47] to be on the order of 1 $\mu m^{-2}$. In order to study the effect of point defects on the STM imaging of graphite, one can introduce substitutional point defects.

Graphite reacts with many elements and compounds to form intercalation compounds,[48] in which the reactant occupies an interstitial

position between the layer planes. Boron is the only impurity known with certainty to act as a substitutional dopant in graphite,[49,50] rather than an intercalant or interstitial dopant. Boronated pyrolitic graphite (BPG) is usually prepared by heating graphite to ~ 2500°C in the presence of boron. In this way, up to ~ 1% of the carbon sites can be substituted by boron atoms. Boron is a natural impurity in graphite (on the order of 10 ppm[51]) and is ordinarily removed in order to obtain pure graphite.

In the 1960's there was much interest in BPG, especially its defect structure following radiation, since it was commonly used in nuclear reactor cores. There were numerous electron microscopy (EM) experiments which investigated the density and appearance of defects, especially basal plane dislocations and vacancies. These experiments typically involved indirect observation of these surface features with EM following gold decoration.[52,53] Gold evaporated onto the surface preferentially aggregates at irregularities which consequently become visible under EM. Oxidation of BPG by oxygen, ozone, or carbon dioxide, causes vacancies that can then be decorated for EM observation. However, with the limited resolution of EM, only the relative defect density could be obtained. No detailed analysis of the structure of BPG and its associated surface defects was possible.

Physical and Electronic Properties of BPG

Boron contained in graphite acts very similar to a dopant in a semiconductor. Even in extremely small concentrations, boron has profound effects on the physical and electronic characteristics of graphite.

Boron, an electron acceptor, is small ($B^{+3}$ ion diameter: 0.40 Å) and has one fewer valence electron than carbon. Since the boron atom has one less valence electron than carbon, its substitution in the graphite lattice probably

causes the trapping of an electron from the conduction band. The expected electronic effects are therefore twofold: the predominant one at low concentrations is lowering of the Fermi level within the normal band structure. Dilute doping is important in a semimetal like graphite because of its small band overlap (0.035 eV). In addition, the degeneracy of the $\pi$-bands around the Fermi level is broken. At higher concentrations, carrier scattering is greatly increased and eventually a highly defective type of conduction is established. Turnbull *et al.*[51] observed by x-ray crystallography that in BPG the *a*-spacing was increased by 0.0031 times the boron atomic concentration and the *c*-spacing reduced by 0.00594 times, compared to pure graphite. This lattice distortion results in line dislocations and strong twinning in regions of large concentration gradients. This lattice strain is known to produce dislocation loops, visible by EM.

It is known that in the oxidation "stripping" reaction of graphite there is considerable chemical anisotropy. In fact, oxygen reacts up to $10^{13}$ times faster at edges (and defects) than at perfect basal plane faces.[54] The cleavage surface is not appreciably attacked at 700°C unless it contains vacancies or other defects. The carbon atoms surrounding a vacancy react at nearly the same high rate as edge atoms, presumably due to their unoccupied $sp^2$ orbitals, and are therefore rapidly removed, thus converting the vacancy into a roughly circular monolayer deep depression (etch pit). In BPG, the carbon atoms surrounding a boron atom in the surface are as reactive chemically as the atoms surrounding a lattice vacancy in graphite.[55] This effect may be due to the fact that boron atoms are rapidly oxidized or hydrolyzed (in moist air). When gently oxidized, the enhanced reactivity at vacancies and at boron atoms causes these defects to expand into monolayer etch pits, which were

typically detected by EM following gold decoration. Therefore, BPG is believed to be considerably more reactive (around boron sites) than pure graphite.

STM Observations of HOPG Defects

To date there have been no published articles on either STM or AFM of boronated graphite. However, there has been two theoretical studies[56,57] on the effect of point defects, including in the former, boron substituents, on STM images of graphite, and several reports of the observation of defects, including etch pits, on HOPG.

Mizes and Harrison[57] attempted to predict with theory the appearance of STM images of impurity sites in graphite, following observation of a "point defect" on carbon-doped boron nitride. The authors predicted that an impurity atom would cause a "bright" (enhanced tunneling) triangular-shaped feature centered on the impurity, in which the 3 neighboring carbon atoms would also appear bright. They also theorized that the brightness of the feature would be highly dependent on the tip-sample distance. They calculated this distance dependence for boron and nitrogen impurity atoms in graphite. Soto,[56] using an extended Huckel band method,[58] predicted that a point defect like boron would create a charge enhancement in the atoms directly surrounding it and should act as a perturbation to distinguish the two sublattices (A and B sites) found in graphite. Soto also calculated the altitude dependence of the charge density directly over the defect and found that it should be characteristic of the defect's chemical nature. The author used an 18-site single-layer unit cell with one boron substituent; the lattice thus formed is composed of 5% boron. It was found that at low altitude over the surface, the charge density over the boron is similar to other atoms but at

higher altitudes it becomes a maximum. There are also maxima over the first and third nearest neighbors to the boron, and there is a charge enhancement around the defect. The difference in charge density over the first and second neighbors to the defect was attributed to the alternant nature of the graphite lattice. In such an alternant system, there are two equivalent sublattices until one of them is perturbed; the boron substituent suppresses the charge on the sublattice that contains it. The variation in charge density over the defect with altitude change was attributed to the difference in nuclear charges of carbon and boron. As a result, the boron wavefunction decays more slowly than that for carbon, and therefore at high altitude, the charge density of the boron should appear as a maximum with respect to the other carbons. In addition, the barrier height measured over the boron defects should be lower than that for the surrounding carbon lattice. Finally, it was found that the altitude dependence and charge density for a nitrogen defect are different from those for a boron.

Although steps are known by STM to occur on HOPG, especially if the samples are poorly cleaved or if lower grades of graphite are used, line or edge dislocations[59] and tilt boundaries[18] have rarely been reported. Moiré-type patterns[18] and superperiodicity,[60,61] caused probably by multiple-tipping or by sliding graphite planes across one another, have also been reported. More recently, there have been reports[30,31] of relatively large-scale step-related structures occasionally observed by STM in air. These observed structures have brought HOPG under attack as a substrate for biological adsorbates since they may be mistakenly interpreted as the molecules themselves. This issue is discussed further later in this chapter as well as in chapter 5. The latter

discussion focuses on the interpretation of STM images where biomolecules have been adsorbed on HOPG.

***Experimental***

The BPG samples used in these experiments were obtained from Arthur Moore (Union Carbide, Cleveland, OH). The boron atomic concentration was ~ 0.5%, such that approximately 1 in every 200 lattice sites contained a boron rather than a carbon atom. The samples varied in quality between ZYB and ZYH grade, but those used in these experiments were probably ZYB or ZYC. These latter quality designations have 0.8° and 1.5° mosaic spreads, respectively (or 2 and 4 times the average grain orientational misalignment of ZYA grade, respectively). The samples did not cleave (with adhesive tape) as "cleanly" as ZYA grade HOPG, and were not as shiny, exhibiting a pronounced hazy, "orange-peel" appearance.

Some of the studies were performed in UHV (pressure ~ $10^{-10}$ torr) using the Caltech STM and some were carried out in air using commercial STM instruments.[62] For studies performed in UHV, the samples were cleaved in air and mounted to stubs using indium solder, and a tunneling current of 100 pA was used. The samples were not "secured" for air studies, and a tunneling current of 1 nA was used typically. The tip was either ac-etched W or mechanically cut Pt for any experiment and a sample bias between 10 and 500 mV was usually applied; the exact experimental parameters are provided with the particular figure or data. For UHV studies, constant current and simultaneous barrier height imaging were most common, while constant height was most common for atomic resolution air studies and constant current for larger areas. The z-piezoceramic modulation for the barrier height studies was 0.3 Å rms at 1 kHz. Unless otherwise

specified, raw data are shown in the figures immediately following this chapter.

***Results and Discussion***

The ability to use STM to image and investigate single boron atom "defects" represents significant progress, since other methods that have been used to date to study the effects and appearance of boron substitution on graphite possess serious limitations. Etch-decoration (with Au) techniques, combined with SEM, do not have sufficient resolution or discrimination to image individual defects or boron atoms. As a result, these methods are not able to distinguish between single defects, defect aggregates, and closely spaced defects. On the other hand, STM provides "real" height information and can resolve individual defects at atomic resolution, without the need for chemical etching or metal decoration.

Long-Range Morphology

The long-range morphology of BPG, as revealed by STM, was found to be very similar to pure HOPG (see section A earlier this chapter). Additionally, no observable difference was noticed between images acquired in air and UHV. There were no changes observed with sample bias polarity or bias values between 10 mV and 1 V. The cleaved surface was atomically flat over the maximum scan range, with occasional small steps (< 10 layers) at a density similar to pure ZYA grade HOPG. The only noticeable difference on this scale was that the steps were less linear than those for ZYA HOPG. The steps were often curved and were usually not at 120° with respect to one another, as is found with ZYA HOPG. In addition, it seemed that some of these features, especially overlapping "steps," were not true "steps" but rather may have been associated with subsurface steps, grain boundaries, or bulk

dislocations which consequently gave rise to atomic-scale surface "buckling." These features are often measured to have less than a single atom layer height, yet are clearly visible in the image. A $(1\mu m)^2$ image representative of the long-range morphology of BPG is provided in Figure 10. This image was obtained in air with a commercially-available TopoMetrix STM using a mechanically cut Pt tip. A zoomed-in image, acquired with nearly identical conditions, showing the individual boron sites is provided in Figure 11. A more extensive investigation of the boron substituents was performed using the Caltech UHV-STM and is described in the following subsection.

Atom-Resolved Imaging of Boron Sites

The BPG surface was imaged both in air and UHV (using the Caltech UHV-STM) with atomic resolution, using both ac-etched W and mechanically cut Pt tips. No changes were observed over the sample bias range of 10 mV to 1 V or with bias polarity. In addition, exposure to air did not appreciably change the appearance of the surface. The boron sites appear as protrusions 2 to 5 Å in diameter (depending on the tip sharpness) and 1 Å in height (relative to surrounding carbon atoms), with a density consistent with the assumed atom concentration of 0.5%. However, the boron atoms were not randomly distributed on the surface; many of them were aggregated into clusters or occasionally into straight lines which often gave rise to associated defects such as edge dislocations (see the following subsection for additional details on these observations).

A constant current image ~ 120 Å on a side acquired in air using a mechanically cut Pt tip is provided in Figure 12. The image reveals a cluster of boron atoms at bottom center. The overall boron atomic concentration seems consistent with the assumed 0.5% value. The carbon lattice of the

graphite is not visible, presumably because of a relatively "dull" tip. Figure 13 shows a "zoomed" image on the same sample, which provides some information on the registry of boron atoms with the graphite lattice. This image is about one-quarter the size of the previous figure and again shows boron aggregation into small clusters. There appears to be a significant density of vacancies and appreciable lattice distortion at areas of locally high boron concentration. The row-like appearance of the graphite lattice is probably due to an asymmetric tip. The quality of images obtained using an ac-etched W tip in UHV was considerably better.

Many atom-resolved images of the BPG surface were obtained in UHV using W tips. Some of these reveal defects and etch pits which are described in subsections immediately following. The boron sites in the images taken with a W tip appear smaller than those obtained using Pt tips, probably because the W tips are sharper. This conclusion is further substantiated by the better overall resolution of these images. Figure 14 is a typical image, 60 by 50 Å in size, showing randomly distributed boron atoms on the BPG surface. The boron sites appear as "bumps" in both the constant current (left) and barrier height (right) images. Occasionally, the boron sites are less randomly distributed and are more highly concentrated in certain areas on the surface, separated by regions free of boron sites. An example of this is provided in Figure 15. In these cases, the regions of high boron concentration have a "cloudy" or "halo-like" appearance, in which these areas are slightly brighter than the neighboring boron-free regions. It is difficult to interpret this effect, but it is likely due to a slightly spatially-delocalized perturbation of the surface electronic structure which changes the ease with which electrons can tunnel from areas in close proximity to groups of boron atoms. The effect

is more pronounced in the constant current images than in the corresponding barrier height images.

These observations were not successfully predicted by theoretical calculations.[56,57] The boron sites were round, not triangular in appearance as predicted by Mizes and Harrison.[57] No charge enhancement in the atoms surrounding the boron substituent, permitting the A and B sublattices to be distinguished, as theorized by Soto,[56] was observed. In addition, the barrier height was found to increase over the boron atoms (relative to the surrounding carbon lattice), opposite to the decrease predicted by Soto's model.

Surface Defects

In some images, concentrated clusters of boron substituents are observed to cause pronounced surface defects. The most common defects observed were edge dislocations and localized atomic disorder. In the former, clusters of adjacent or closely spaced boron atoms seem to induce dislocations evidenced by a lateral shift in atomic registry by as much as half a unit cell. An example of a relatively well-ordered edge dislocation is provided in Figure 16. Associated with the dislocation located at the region of high boron concentration (slightly brighter region in Figure 16) is a shift of the atomic lattice approximately half a unit cell at the bottom left relative to the carbon lattice at the upper right. This dislocation probably results because of the high lattice strain introduced by such a cluster of boron atoms. In an attempt to reduce the overall strain imposed by the localized boron "lattice," the adjacent carbon lattices shift relative to one another. Additional examples of this type of defect are shown in Figures 17 and 18. Figure 17 is a barrier height image which reveals a boron cluster in the lower right corner. Again, the presence

of the boron atoms induces sufficient strain to cause a dislocation and a shift in atomic registry. Figure 18 presents a series of barrier height images of a similar region to that shown in Figure 17. The borons apparently assume out-of-registry positions in the overall lattice due to their different size and valence structure.

Often associated with these regions of high boron concentration are disordered boron "patches." In these cases, the boron atoms have no apparent registry with the adjacent carbon lattice. In addition, the boron atoms cause disordered atomic arrangements similar to that shown in Figure 19. In this image, no familiar hexagonal graphite lattice is discernible. This result is not surprising, since one would not expect the boron atoms to be able to adopt a lattice consistent with the surrounding carbon framework. These amorphous patches make obvious the polycrystalline nature of the BPG material.

Etch Pits

Etch pits of monolayer depth (3.35 Å) were occasionally found on the BPG surface. These etch pits were typically round or oval in shape and between 20 and 80 Å in diameter. These etch pits are presumably formed by oxidation or hydrolysis (in moist air) of carbon atoms surrounding boron atoms. As mentioned previously, the atoms adjacent to boron defects are substantially more reactive than basal plane atoms and that this oxidation "stripping" reaction is highly anisotropic. These etch pits were probably caused by mild heating of the sample in air, following sample mounting by indium solder to the sample stub.

Etch pits have been previously observed in two reported STM studies on graphite. Hexagonal etch pits between 500 and 2000 Å in width and 30 and 100 Å in depth were observed[63] on graphite flakes synthesized from a benzene

precursor. Chang and Bard[47] used STM to study the oxidation of HOPG in air at elevated temperatures. The authors found that etch pits were formed on preexisting defects or generated vacancies by heating at 650°C. The density of the pits was on the order of 1 $\mu m^{-2}$, indicative of the density of intrinsic vacancies on the HOPG surface. Both the size and number of these vacancies were found to increase with higher reaction temperature and longer heating time.

Figure 20 shows two distinct etch pits, each of monolayer depth and about 30 Å in diameter. These etch pits are visible in both constant current and barrier height images. It is often possible to resolve individual boron defects within the etch pit boundary on the bottom surface of the etch pit. Figure 21 reveals three boron atoms within the etch pit; atomic resolution was obtained at both levels of the pit. It is probable that these boron atoms are responsible for the formation of the pit, in which adjacent carbon atoms have been abstracted by mild oxidation.

Imaging of BPG with a Graphite Tip

It is commonly believed that the probable mechanism for imaging graphite involves "sliding graphite planes,"[17,24] as described earlier. In these theories, the ease with which graphite is imaged with atomic resolution, the lack of observed defects, and the observation of asymmetric or dynamic images and low barrier heights have been explained by tip-surface contact. This contact subsequently results in the "rubbing" of one plane of graphite, most likely from a microscopic flake of graphite picked up by the tip, across another during STM scanning. The intimate contact of graphite planes causes defects to be "smeared" or "averaged" out and provides an "amplified" and more stable junction for providing atomic resolution. The deformability of

the graphite surface also gives rise to decreased barrier height measurements. Asymmetric or dynamic images result due to the variable orientations with which the graphite planes could be scanned relative to one another. This theory has been tested by simulating "sliding graphite planes," using a graphite-graphite junction with a pencil lead tip and an HOPG surface.[17] However, it is important to test whether this type of junction adequately simulates "sliding graphite planes." In these experiments, a number of "anomalous" imaging characteristics were found, including asymmetric patterns, a weak tip-sample separation dependence, and a lack of observed defects. These anomalies were attributed to tip-surface contact and the intervention of graphite flakes in the junction. As a result, it was determined that graphite pencil leads were a good experimental simulation of the theory of sliding graphite planes.

We have attempted to evaluate the validity of this experimental simulation by using a pencil lead to image BPG. Our attempts to resolve the individual boron defects which cover the BPG surface were surprisingly successful. A line-scan current image of the BPG surface using a mechanically sharpened graphite pencil lead tip is provided in Figure 22. This image was acquired in air using a Digital Instruments' Nanoscope II STM with typical tunneling conditions (shown on figure). The image reveals the expected distribution and concentration of boron substituents, as shown by the small bumps. The significance of these results is explored in the following subsection.

Evaluation of "Sliding-Planes" Mechanism

Based on the results of previous work of our labs and others, a theory of graphite imaging based on the notion of sliding planes has been adopted by

the STM community. This theory was based on experimental evaluations using pencil lead tips for imaging graphite. However, this experimental approach may not adequately simulate the sliding of graphite planes across one another.

The ability to resolve individual boron defects on the BPG surface using a pencil lead tip brings into serious question whether such an approach is valid for simulating sliding graphite planes. If graphite planes, rather than at most several points of tunneling, are responsible for graphite imaging, then isolated defects such as the boron atoms in BPG would not be resolved since they would be averaged out. As a result, only the overall lattice registry would be imaged. The appearance of Figure 22 suggests a single tunneling point (or multiple tunneling points separated by appreciable distances) and not simply graphite planes. Therefore, in order to test theories of sliding graphite planes, another experimental approach would have to be adopted. These results do not bring into question the validity of the theories themselves, but rather just the experimental methods that have been used to evaluate them to date.

However, these results suggest that the "sliding planes" mechanism is not always active and is not the reason for the lack of defects that are reported in STM experiments on HOPG. The latter is most likely due to the fact that well-cleaved high-quality HOPG indeed has very few surface defects. In addition, it seems that tip-surface contact or tip "crashing" is probably unnecessary for imaging graphite with atomic resolution.

BPG as a Substrate

As mentioned earlier in this chapter, graphite (specifically, HOPG) has recently come under considerable fire as a substrate for adsorbates, especially

biological samples like DNA. These reports[31,32] suggest that there exist on the HOPG surface native structures resulting from cleavage which may be confused with true biomolecular structure. Although otherwise ideal, because of its ease of preparation and its atomic flatness, these structural features combined with the chemical inertness of the basal plane make HOPG less than perfect as a substrate for adsorbates.

However, one disadvantage of HOPG as a substrate, namely its inertness, may be eliminated by using BPG. The boron sites presumably would be much more highly reactive for the attachment of biomolecular adsorbates, acting much like anchors to the deposited molecules. However, the same "confusing" structures observed on HOPG would also be present on BPG. This limitation though is not fatal since it is quite straightforward with experience to distinguish between features associated with the substrate and those of the adsorbate. Other common substrates such as gold evaporated or epitaxially grown on mica suffer from similar confusing microstructure and are more difficult to prepare. With its greater expected reactivity (relative to HOPG), BPG should then be considered to be a good STM substrate for adsorbate attachment.

***Conclusion***

This STM study of BPG illustrated the possibility of imaging and distinguishing individual boron substituent sites in a carbon lattice. The boron atoms appear brighter than the surrounding carbon atoms in both constant current and barrier height images. In constant current images, the boron defects appear as bumps ~ 1 Å high (relative to adjacent carbon atoms) and between 2 and 5 Å in diameter, depending on tip sharpness. The positions of isolated boron defects were found to be largely aligned with the

carbon lattice, as expected from the substitutional nature of the boron impurity. The density of these boron sites was consistent with the expected atom concentration. The boron atoms were often not randomly distributed, sometimes being clustered into small "islands" which gave rise to associated defects such as edge dislocations and amorphous regions. The results of this imaging study were evaluated with respect to prior theoretical predictions, and were found to be largely inconsistent with calculations. The long-range morphology of the BPG surface was found to be similar to that of HOPG. However, the steps were commonly neither straight nor aligned with the principal axes of the graphite lattice.

STM provides a highly improved method for investigating BPG over traditional electron microscopy studies using decoration techniques. With STM, single boron defects can be resolved without the need for chemical etching or metal decoration. It was also possible for the first time to study in detail amorphous regions and dislocations in the BPG surface. Monolayer-deep etch pits, formed by the mild oxidation of boron defects and their surrounding carbon atoms, were observed. Etch pits as small as 20 Å in size were resolved, about ten times smaller than those resolvable by EM.

The increased reactivity of the boron sites relative to the basal plane of graphite makes BPG a good substrate for deposition of adsorbates, including biologically important molecules like DNA. Although susceptible to the same criticisms concerning confusing structural features which plague HOPG, the other benefits of its use as a substrate probably outweigh its weaknesses.

Our results demonstrating the ability to resolve individual and isolated boron defects with a graphite tip made up of a sharpened pencil lead introduce significant doubt about the validity of such an approach for

simulating sliding graphite planes, the mechanism assumed to be responsible for HOPG imaging. In addition, these results suggest that the sliding planes mechanism is not always active and is not necessarily the reason for the reported lack of observed defects on HOPG. Consequently, tip-surface contact or "crashing" is probably unnecessary for imaging HOPG. Conclusions made about previous experiments employing this approach may require reevaluation.

**Figure 1**

A top-view drawing of the structure of the basal plane of graphite. The hexagonal unit cell is made up of three different atomic sites, labeled A,B, and C. Site A is a surface carbon atom with a neighboring atom in the underlying layer, site B is a surface carbon atom without an atom beneath it, and site C is a surface hollow. The interatomic spacing is 1.42 Å, the interlayer spacing is 3.35 Å, and the unit cell spacing (used in STM calibration) is 2.46 Å. The dotted line represents the underlying layer lattice. It is believed from theoretical considerations (Ref. 16) that the B sites are imaged in STM experiments. Figure is taken from Ref. 11.

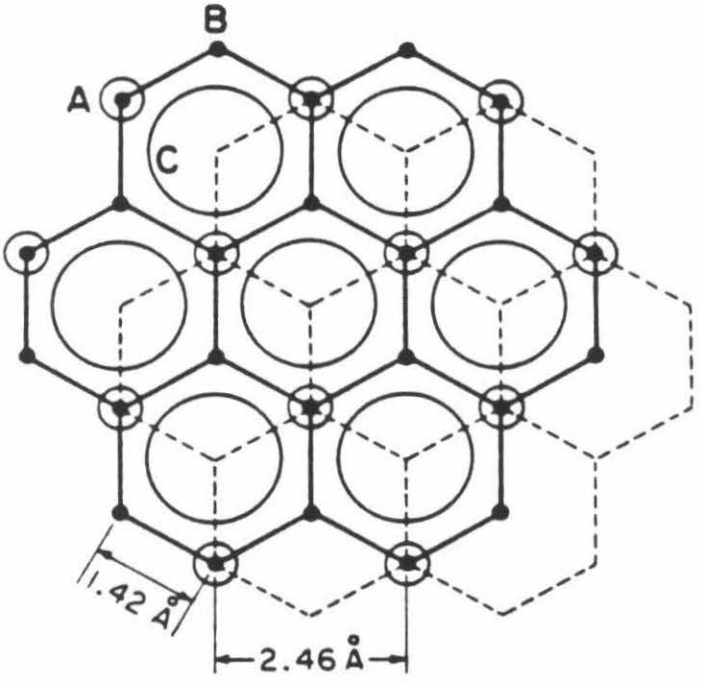
B
A
C
1.42 Å
2.46 Å

**Figure 2**

A constant height image approximately 10 x 13 Å is shown here in both a top-view grayscale (left) and a solid-modeled three-dimensional projection (right). The hexagonal "honeycomb" pattern is probably a result of multiple-tipping. The experimental conditions are as follows: tunneling current = 100 pA and bias voltage (sample) = +0.10 V. The image is 100 data pixels in $x$ by 128 pixels in $y$ and was obtained at a pressure of $< 10^{-9}$ torr using an ac etched tungsten tip. The data have been smoothed using a binomially weighted sliding window average corresponding to a two-dimensional Gaussian of ~ 0.2 Å FWHM.

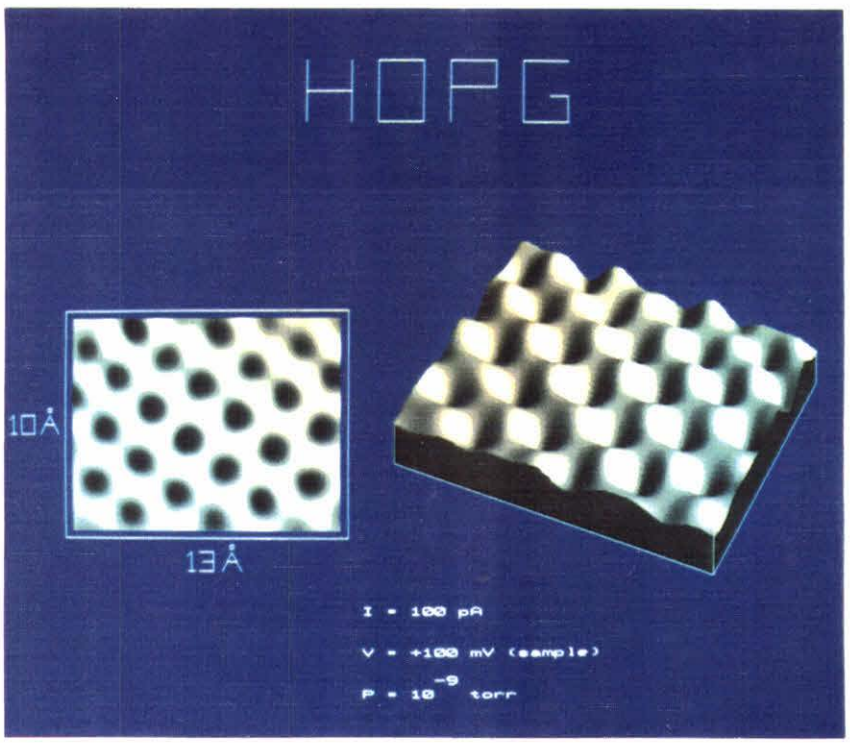
HOPG
10Å
13Å
I = 100 pA
V = +100 mV (sample)
P = 10^-9 torr

**Figure 3**

A pair of simultaneously obtained images: at top is a constant current image, and at bottom, a barrier height image. The images are each roughly 120 x 100 Å and contain 500 data pixels in $x$ by 200 in $y$. Both are shown in top-view grayscale presentations. The tunneling current was 100 pA and the sample bias was 1 V; the corresponding gap resistance was 10 GΩ! The $z$ modulation used for the barrier height was ~ 0.5 Å at 1kHz; the barrier height at the local maxima was ~ 1 eV. Raw data is shown. The curvature of the atomic rows is due to piezoceramic creep. This represents an atomically resolved image of HOPG acquired with both one of the largest reported scan areas and gap resistances.

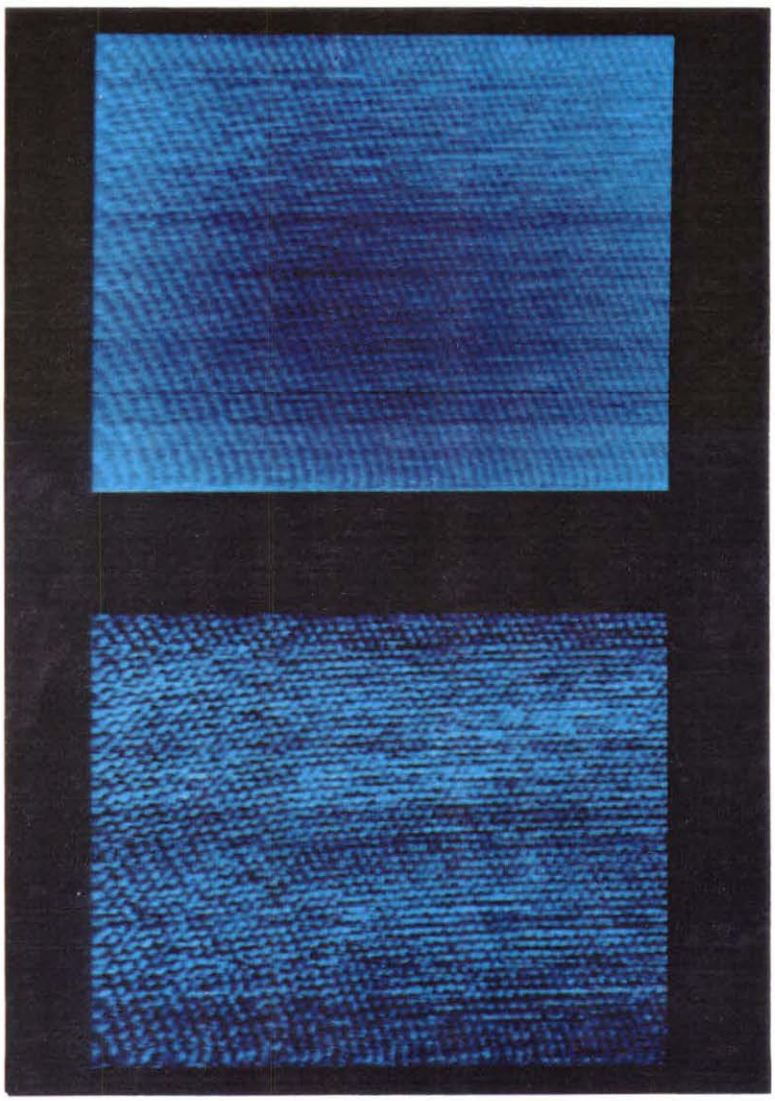

**Figure 4**

A constant current image of HOPG 32 Å on a side. The tunneling current was 100 pA and the sample bias was +0.01 V. There are 500 pixels in $x$ and 126 pixels in $y$. The image has been low-pass Fourier filtered to remove features below ~ 0.7 Å in size.

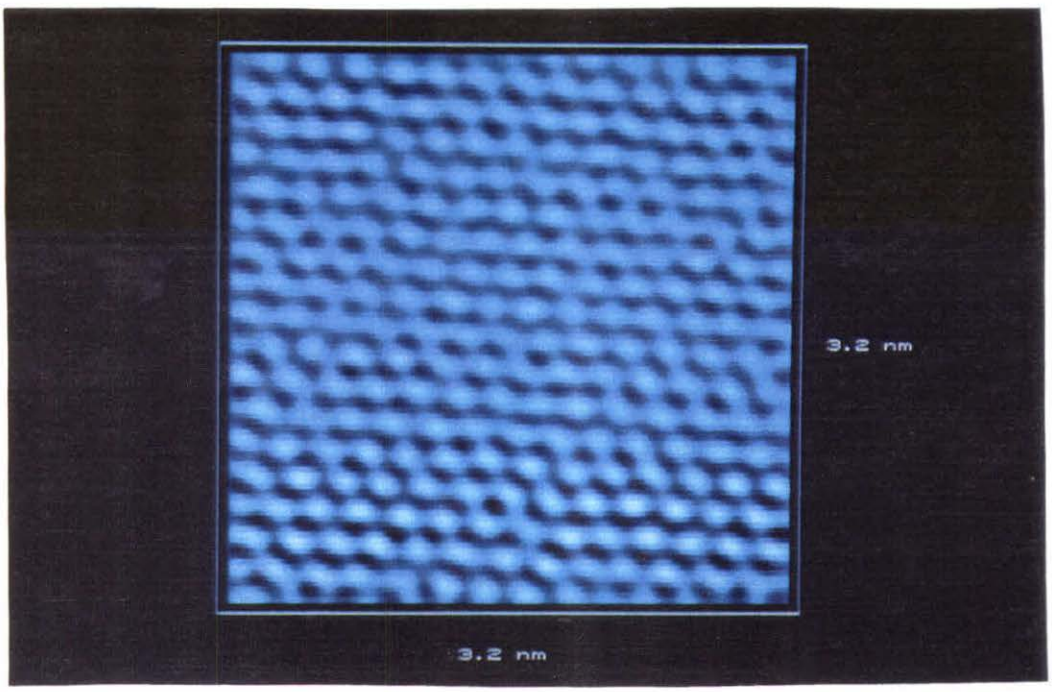
3.2 nm
3.2 nm

**Figure 5**

An example of tip asymmetry is illustrated in this constant current image of HOPG acquired in UHV. The image is ~ 16 x 16 Å with 500 and 125 data pixels in $x$ and $y$, respectively. The most striking features of this image are the horizontal atomic rows, caused by an asymmetric probe tip. This asymmetry leads to better lateral resolution in the image vertically than horizontally. The tunneling current was 1 nA and the bias applied at the sample was +0.01 V. The top-view image at left shows prominent horizontal atomic rows. The data is also plotted in two 3-D solid-modeled projections, one whose brightness is keyed to height (top right) and one whose brightness is keyed to local slope (bottom right).

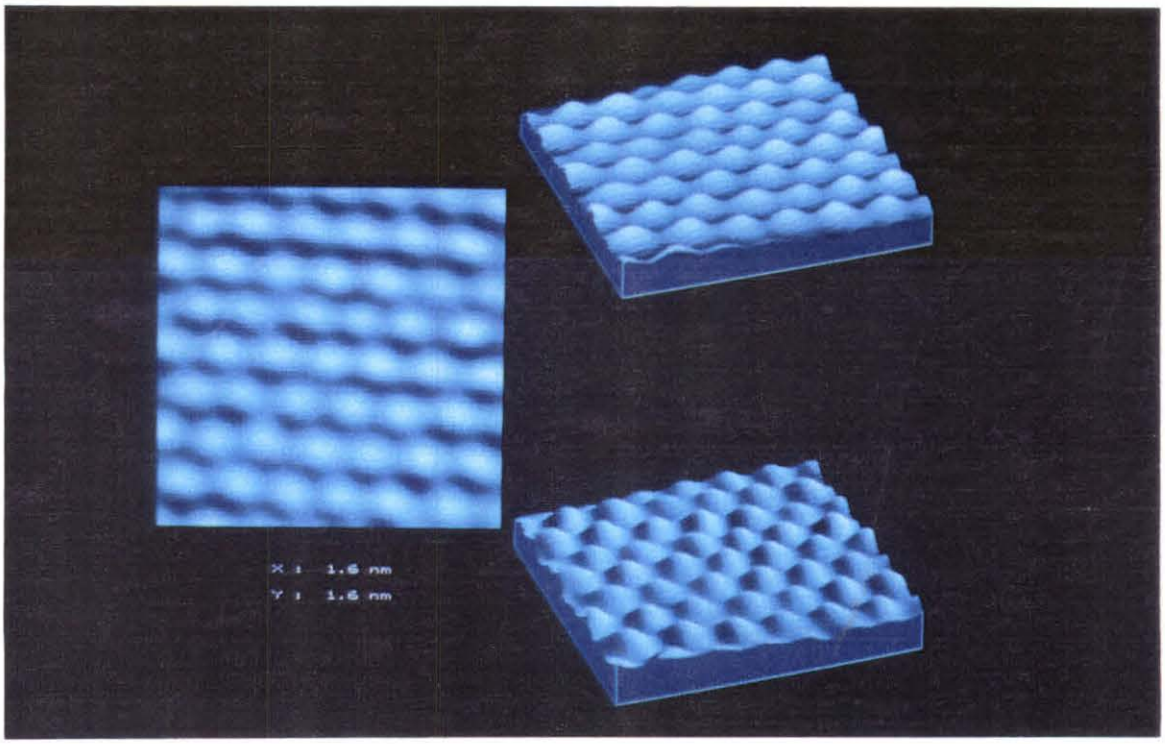
X : 1.6 nm
Y : 1.6 nm

**Figure 6**

The structure of $TiS_2$ is provided here, in both top-view, along the *c* axis in (a) and side-view, perpendicular to the *c* axis in (b). In (a) the second-order prismatic plane (1120) of the $TiS_2$ structure showing the van der Waals gap and the stacking order is shown. $T_1$ and $T_2$ are the two inequivalent tetragonal sites. Solid lines connect the Ti lattice. In (b) the basal plane of the 1T structure is shown; again, solid lines connect the Ti lattice. The open circles are sulfur atoms and the filled circles are titanium atoms. The Ti-S bond length is 2.42 Å and the S-S or Ti-Ti bond length is 3.39 Å. The topview reveals a hexagonally arranged topmost sulfur layer with a similarly arranged underlying lattice of titanium atoms. Figure is taken from Ref. 39.

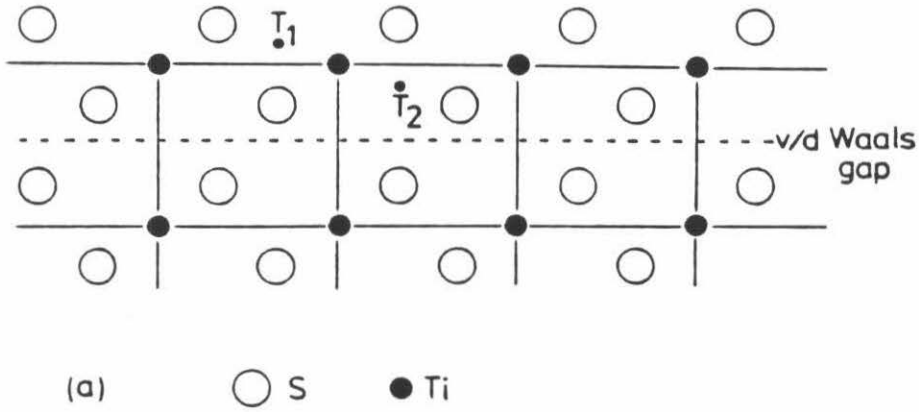
T1
T2
v/d Waals gap
(a)
S
Ti

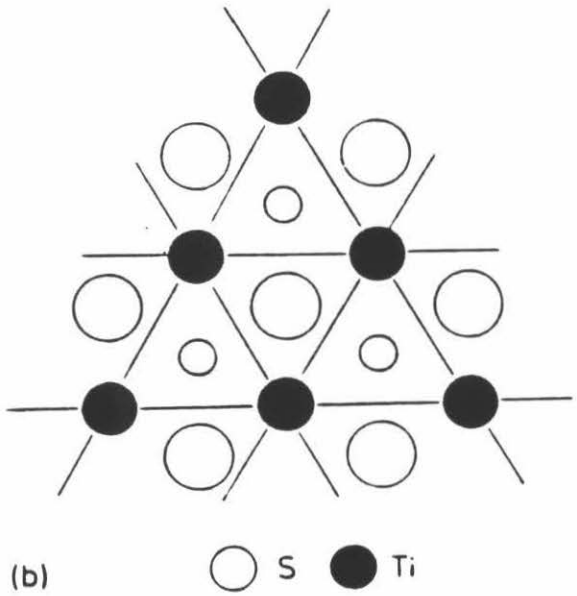
(b)
S
Ti

**Figure 7**

A constant height image of $TiS_2$ ~ 15 x 15 Å clearly reveals the threefold symmetry and hexagonal arrangement of surface atoms. The data are presented in a 3-D projection with features keyed to current (brighter = higher current). An ac electrochemically etched tungsten tip was used with a sample bias of +0.10 V, a tunneling current of 1nA, and a vacuum < $10^{-9}$ torr. The image has been low-pass Fourier filtered to remove features below ~ 1 Å in size. The image is "ribbed" due to the relatively low pixel density (50 x 50); the figure has been cropped from a larger image to emphasize the unit cell arrangement.

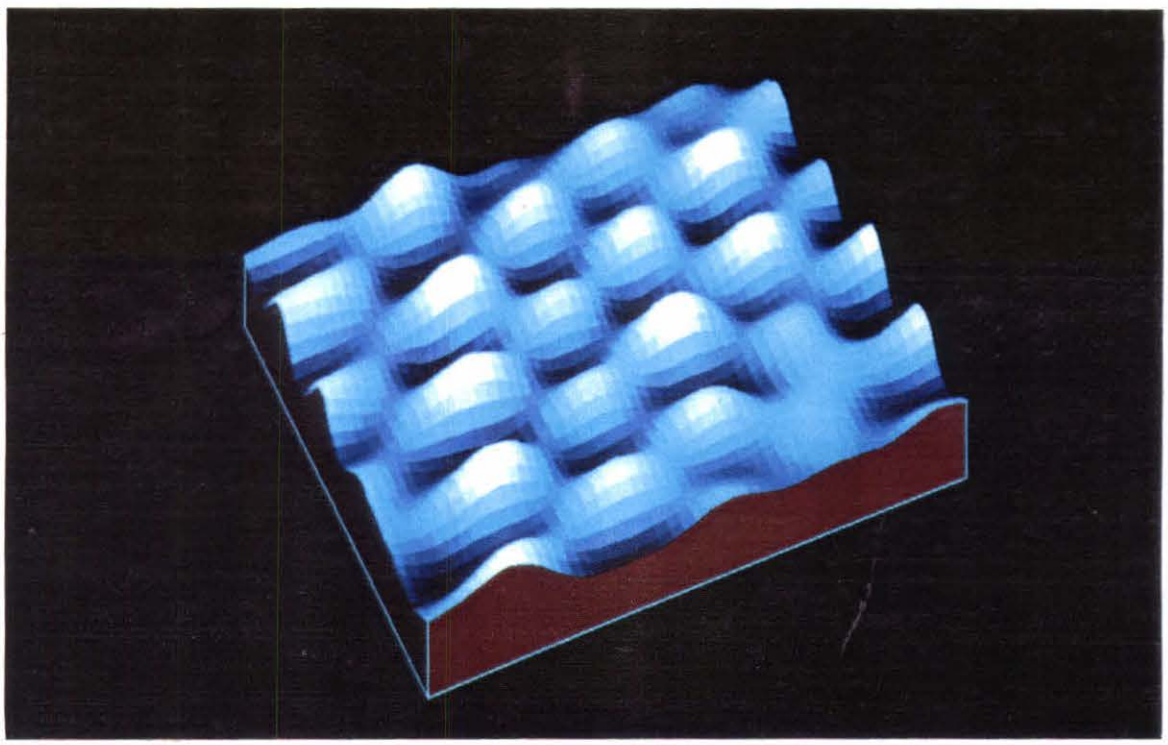

**Figure 8**

A constant current image of $TiS_2$ ~ 35 x 25 Å reveals two vacancies (missing atoms) typical of the appearance of the surface. The vacancies are probably displaced Ti atoms (see text). The data were acquired simultaneously with a barrier height image (shown in Figure 9), in UHV using an ac etched W tip, a sample bias of +0.05 V, and a tunneling current of 1 nA. The image contains ~ 500 by 90 pixels and has been low-pass Fourier filtered to remove features below ~ 1 Å. The topmost ~ 35 data lines in $y$ have been cropped from this presentation.

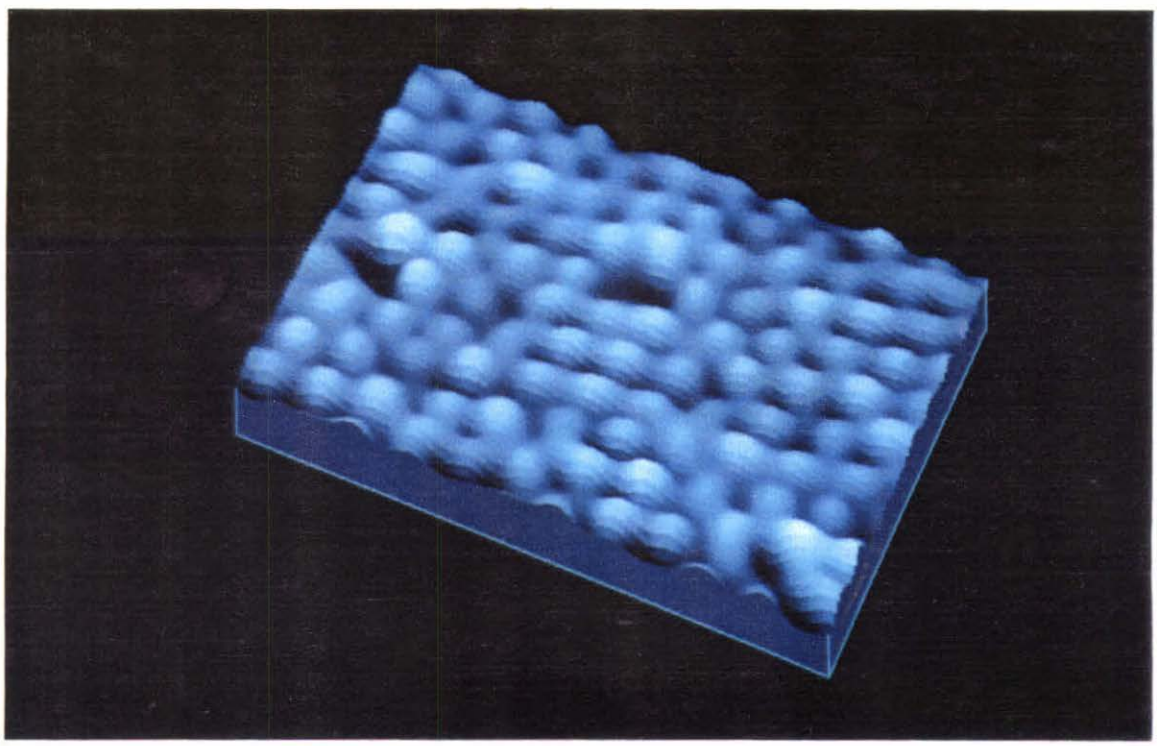

**Figure 9**

The corresponding barrier height image of $TiS_2$ acquired simultaneously with the constant current image shown in Fig. 8. The z piezoceramic was modulated ~ 0.8 Å p-p at 1 kHz during scanning. The barrier height maxima are ~ 1.5 eV. The image is ~ 35 x 35 Å and represents a nearly identical region to that of Fig. 8, except that it is uncropped (contains a complete ~ 500 by 125 pixels). Therefore, the bottom and sides of the image are identical. The locations of the vacancies in Fig. 8 show a very slightly diminished response, but clearly do not exhibit associated "holes" in the measured barrier height. This image was obtained using the same experimental conditions and has been filtered similarly.

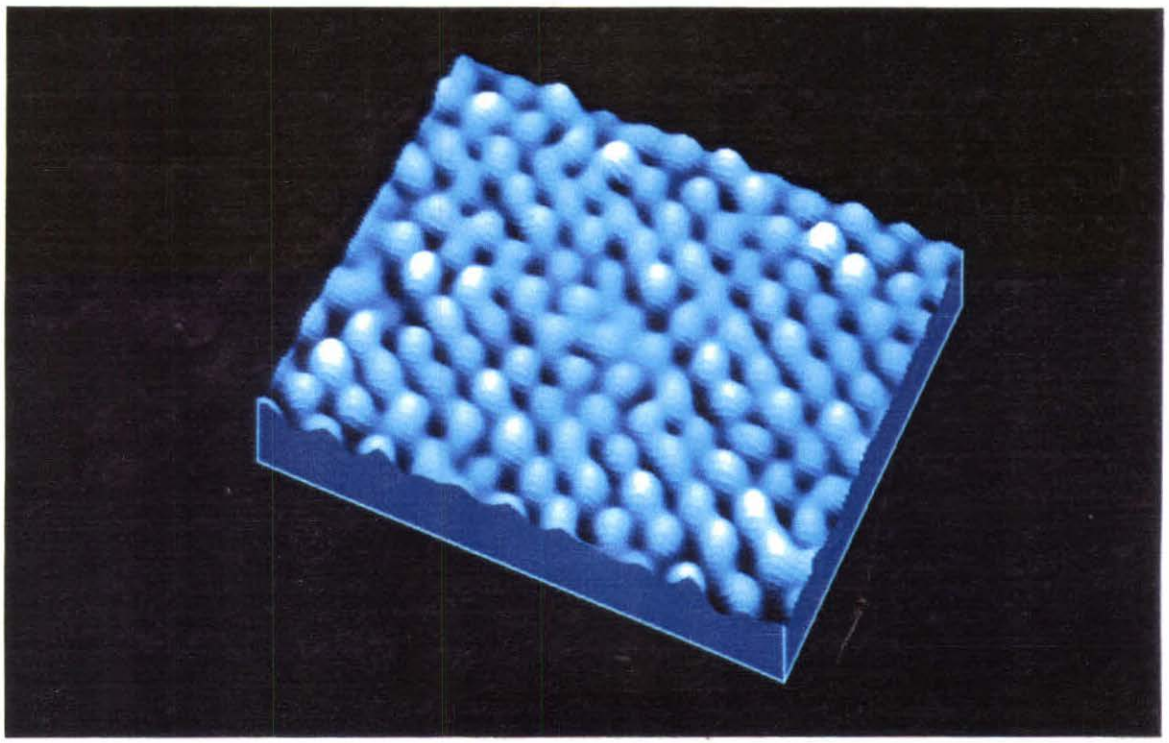

**Figure 10**

A constant current image of BPG 1μm on a side reveals an atomically flat surface with small steps (primarily single or double layer height) sloping upward from upper left to lower right. The total height variation is ~ 30 Å and is evidenced by the variation in brightness from dark to light in this height-keyed presentation. Note that the steps are not linear and that some of the overlapping "steps" measure less than a single-layer step in height and are probably the surface manifestation of subsurface features such as bulk dislocations or grain boundaries. This image was obtained in air using a TopoMetrix STM with a mechanically cut Pt tip.

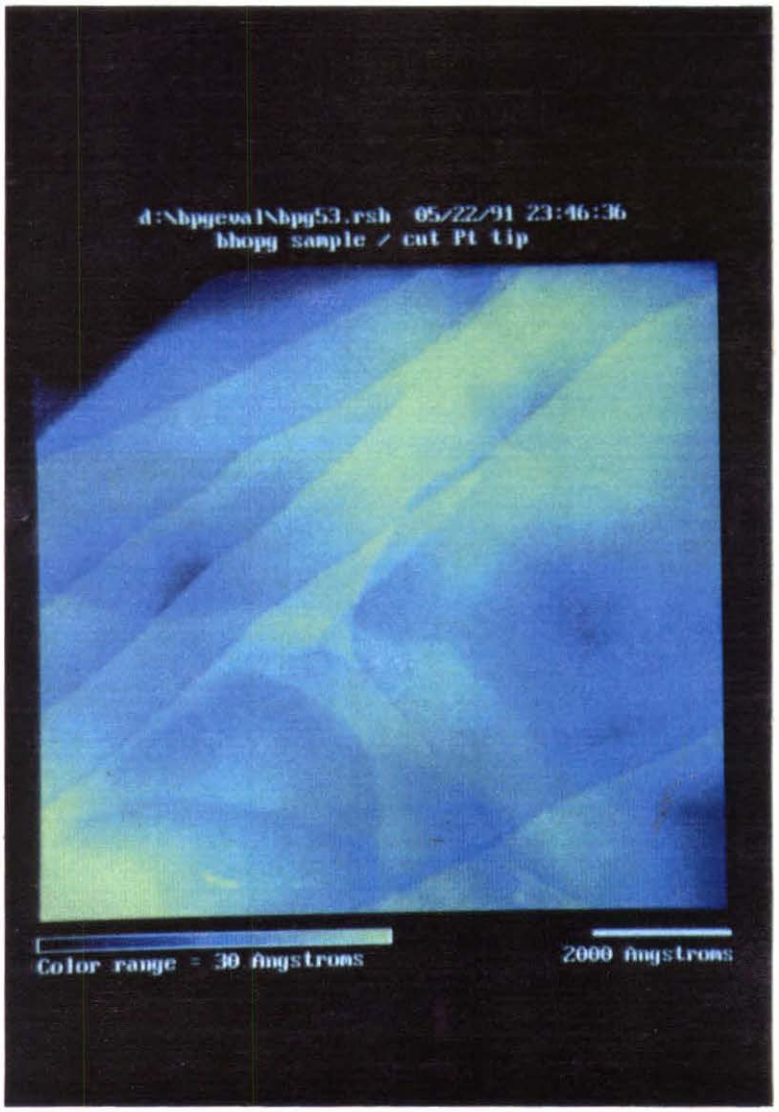
d:\bpgeval\bpg53.rsh 05/22/91 23:46:36
bhopg sample / cut Pt tip
Color range = 30 Angstroms
2000 Angstroms

**Figure 11**

An image of the individual boron sites on the BPG surface at higher magnification than Fig. 10. The image is ~ 250 Å on a side and was acquired in air using a TopoMetrix STM with a mechanically cut Pt tip. The boron sites appear as small bumps (white dots) ~ 5 Å in diameter and 1 Å in height. The boron substituents appear smaller (~ 2 or 3 Å) if the tip is sharp. The borons in this image appear to be randomly distributed, but this is not always the case.

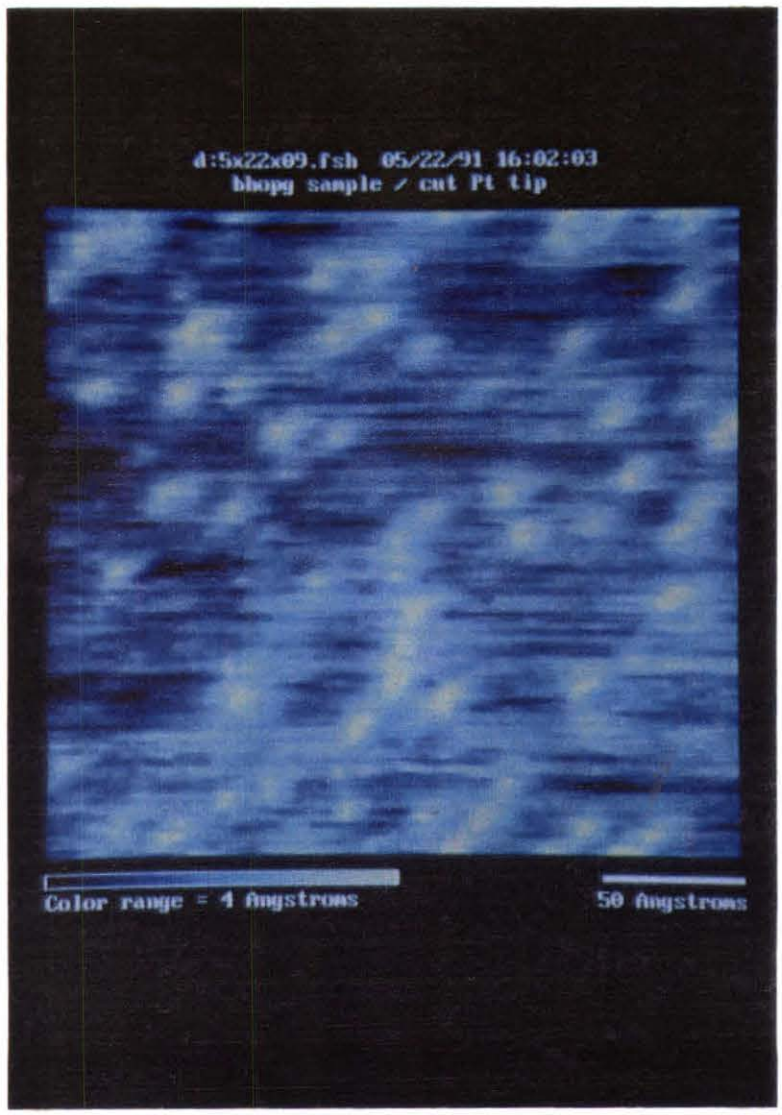
d:5x22x09.fsh 05/22/91 16:02:03
bbopg sample / cut Pt tip
Color range = 4 Angstroms
50 Angstroms

**Figure 12**

The boron sites in the surface of BPG are revealed in this 120 Å x 120 Å constant current image obtained in air using a mechanically cut Pt tip. The boron atoms are not evenly distributed, clustered in certain sections of the image (note especially the cluster at bottom center). The carbon lattice is not visible due to a combination of the large image size and a "dull" tip.

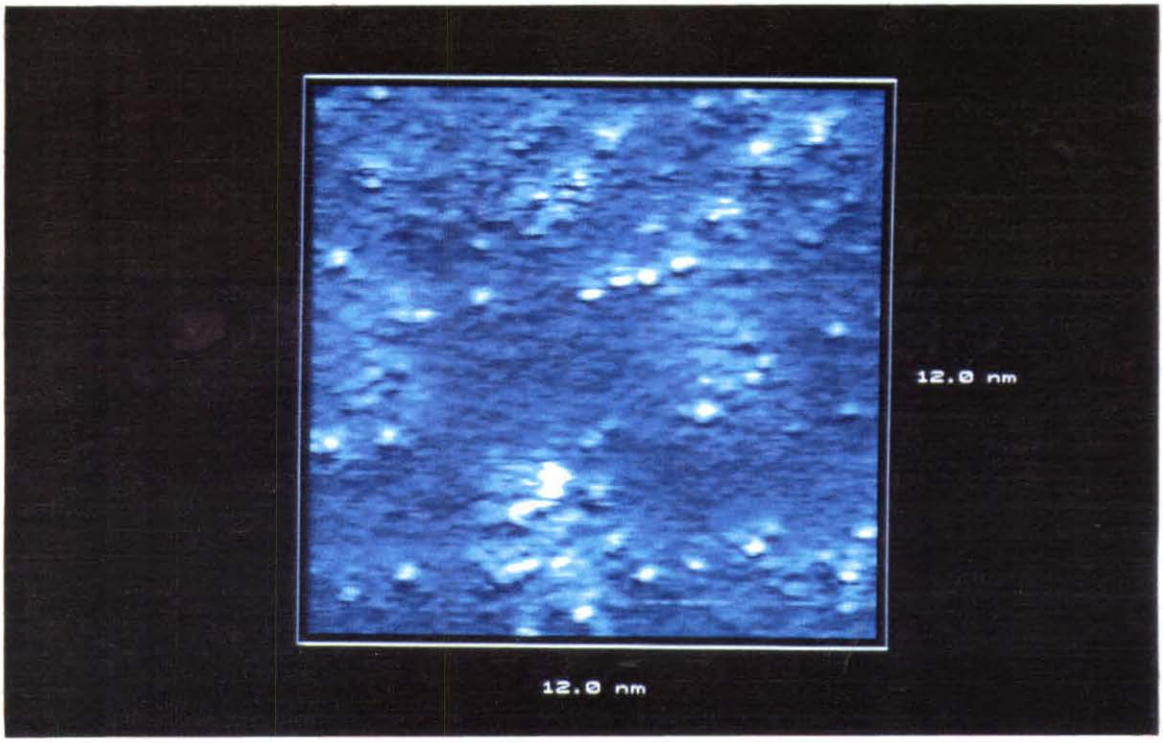
12.0 nm
12.0 nm

**Figure 13**

A "zoomed" image on the same sample as in Fig. 12, using nearly identical conditions. This image is ~ 55 Å on a side and shows small clusters of boron atoms and their registry with the surrounding graphite lattice. The resolution of the carbon atoms is relatively low, such that the lattice appears as diagonal rows. This effect is probably due to an asymmetric tip. Some evidence of vacancies and lattice distortion near areas of locally high boron concentration is visible.

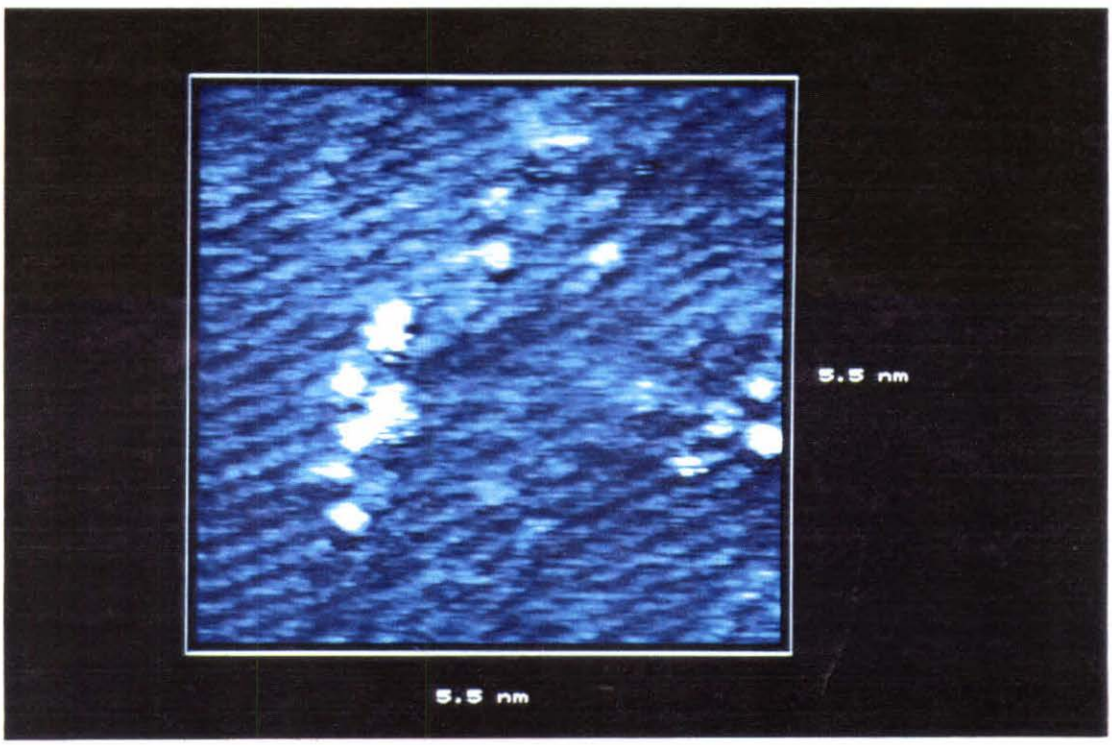
5.5 nm
5.5 nm

**Figure 14**

An image of the BPG surface 60 x 50 Å reveals a randomly distributed arrangement of surface boron sites. The constant current image is shown at left and the corresponding barrier height image at right. These images were obtained in UHV using an etched W tip. The tunneling current was 1 nA and the sample bias voltage was +250 mV.

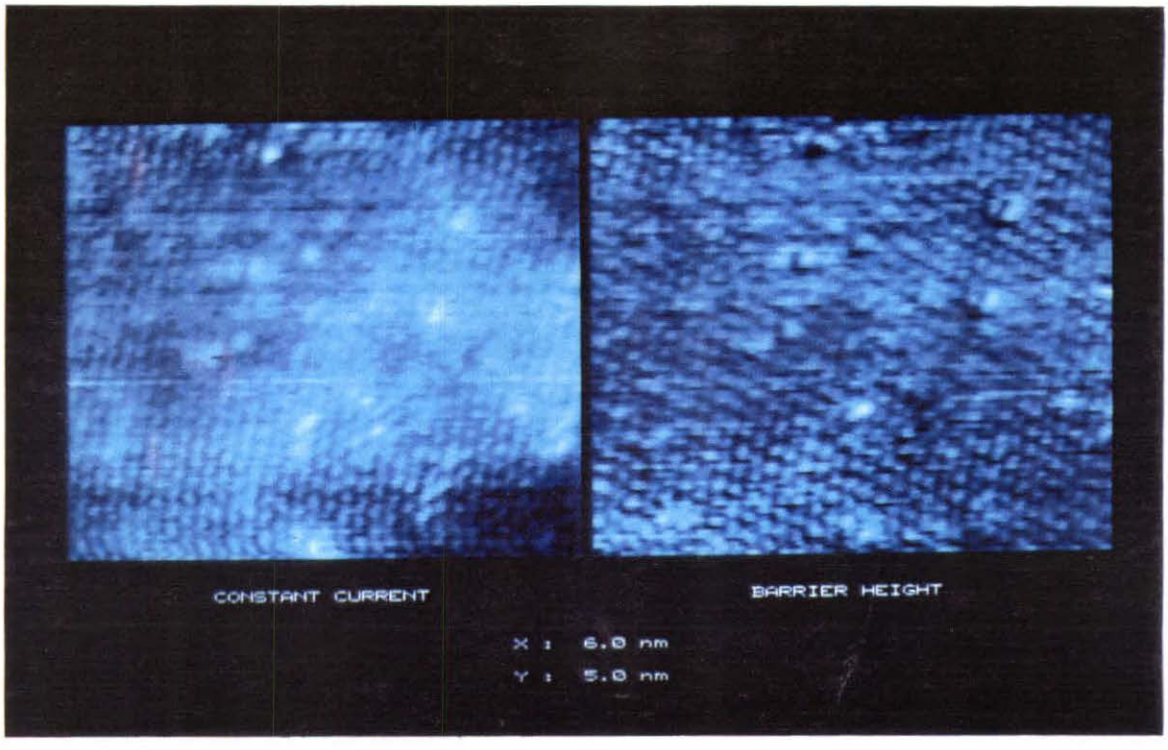
CONSTANT CURRENT
BARRIER HEIGHT
X : 6.0 nm
Y : 5.0 nm

**Figure 15**

The concentration of boron sites on certain regions of the BPG surface gives rise to localized "cloudy" regions which appear slightly brighter than the neighboring boron-free areas. This phenomenon is seen here in this pair of simultaneously-obtained constant current (left) and barrier height (right) images. This effect is more pronounced in the constant current image. This (60 Å)$^2$ image was obtained in UHV with an etched W tip using a tunneling current of 1 nA and a sample bias of +250 mV.

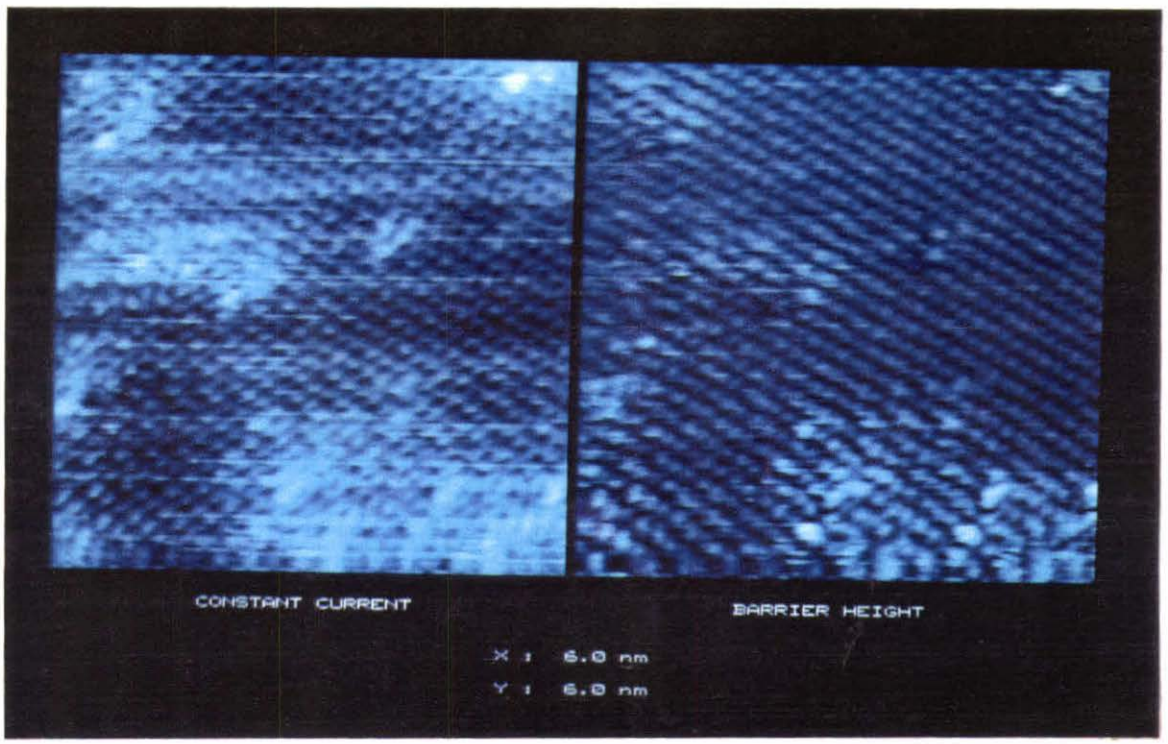
CONSTANT CURRENT
BARRIER HEIGHT
X : 6.0 nm
Y : 6.0 nm

**Figure 16**

A constant current STM image of BPG ~ 30 Å on a side revealing a microscopic edge dislocation at an area of high boron concentration. The carbon lattice at the upper right is shifted diagonally approximately one-half of an unit cell relative to the lattice in the lower left. The area of high boron concentration is evidenced by the slightly brighter region in the lower left quadrant of the image. The image was obtained using a tunneling current of 1 nA and a sample bias of +100 mV. The image is Fourier-filtered to remove frequencies corresponding to features less than 1 Å in size.

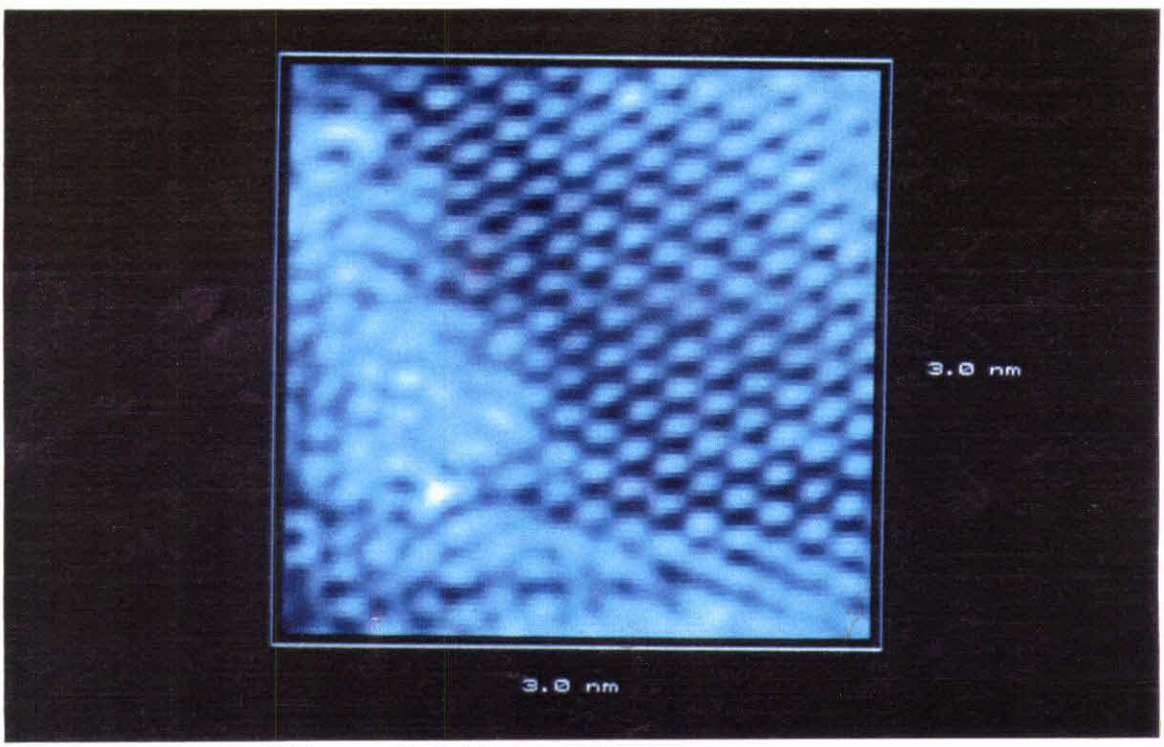
3.0 nm
3.0 nm

**Figure 17**

A cluster of boron atoms in the lower left corner (bright region) of this barrier height STM image ~ 30 Å on a side gives rise to an edge dislocation, causing a lattice registry shift in the surface atomic arrangement. The boron atoms also appear slightly larger than their adjacent carbon atom counterparts. Raw data are shown.

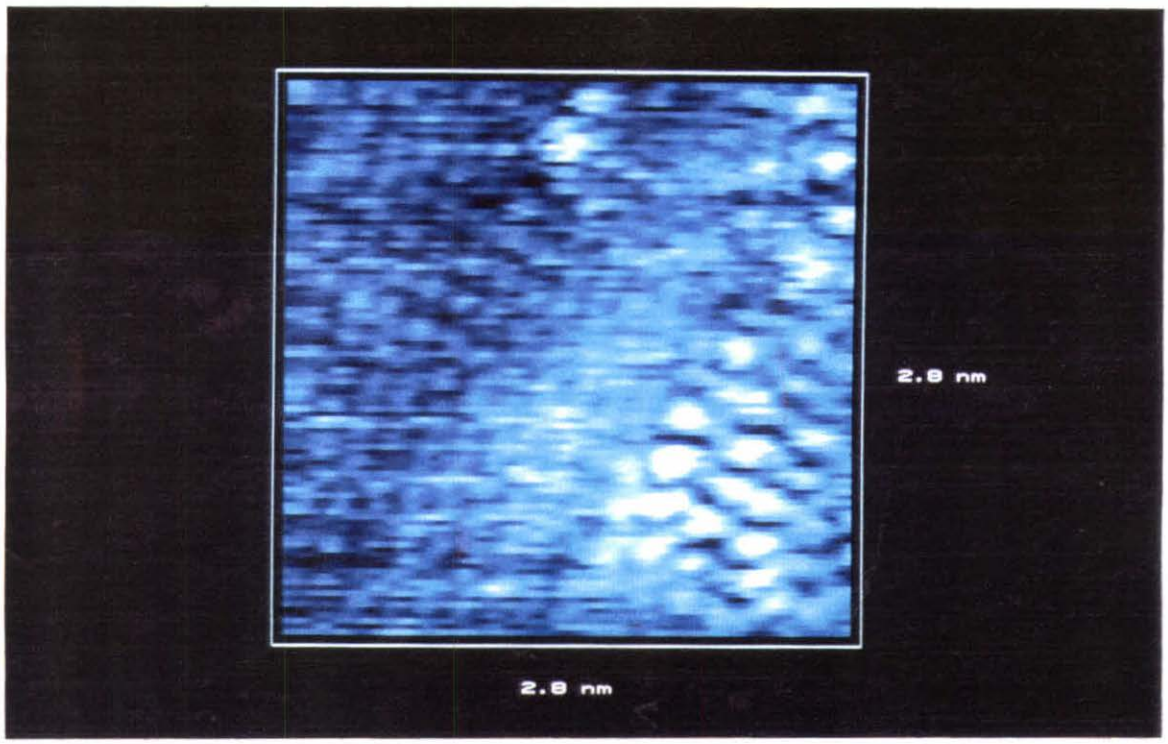
2.8 nm
2.8 nm

**Figure 18**

A series of four STM barrier height images of a similar region to Figure 17 is provided here. Each of these images illustrates the edge dislocation and the boron cluster which induces it. The boron atoms presumably introduce sufficient strain into the lattice to cause a registry shift of atoms.

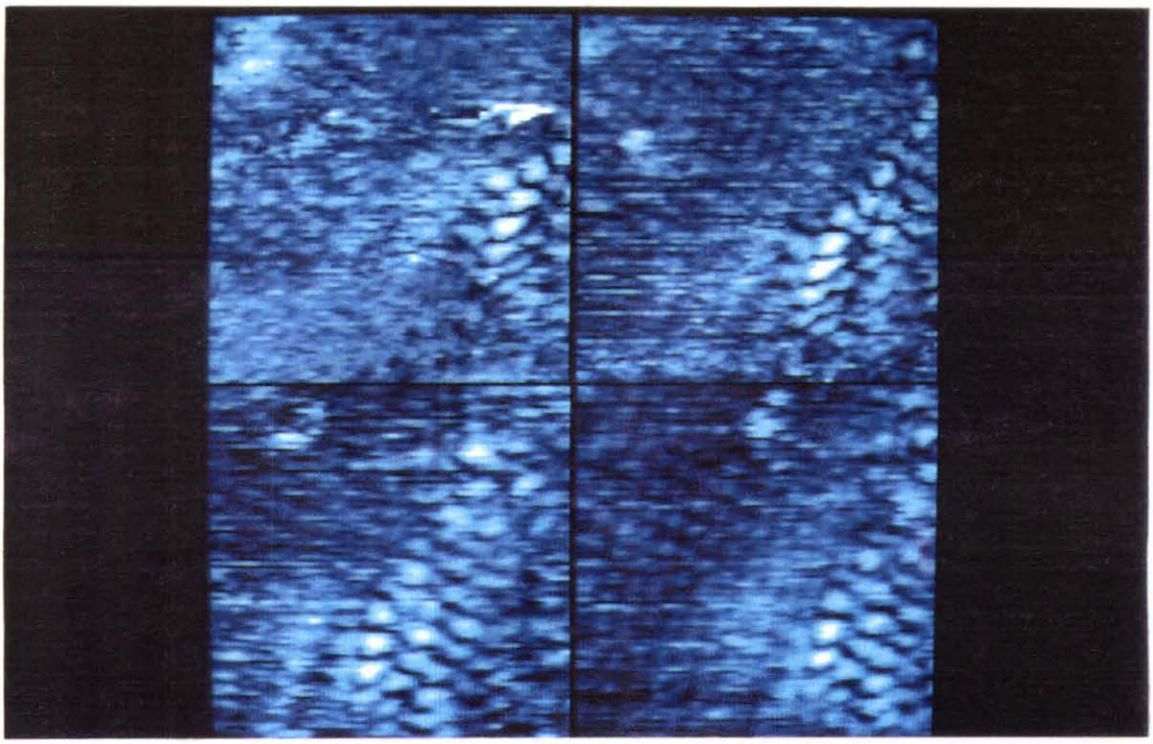

**Figure 19**

A pair of simultaneously-obtained constant current (left) and barrier height (right) images, each 28 Å on a side, show an area of disordered ("amorphous") atomic arrangement on the BPG surface. These amorphous regions occur in areas of high boron concentration.


CONSTANT CURRENT
BARRIER HEIGHT
X : 2.8 nm
Y : 2.8 nm

**Figure 20**

Monolayer (3.35 Å) deep etch pits ~ 30 Å in diameter are occasionally found on the BPG surface. This pair of simultaneously-obtained constant current (left) and barrier height (right) images are each ~ 60 Å on a side and reveal two distinct etch pits. These etch pits are presumably formed by the hydrolysis of boron sites during heating in moist air.

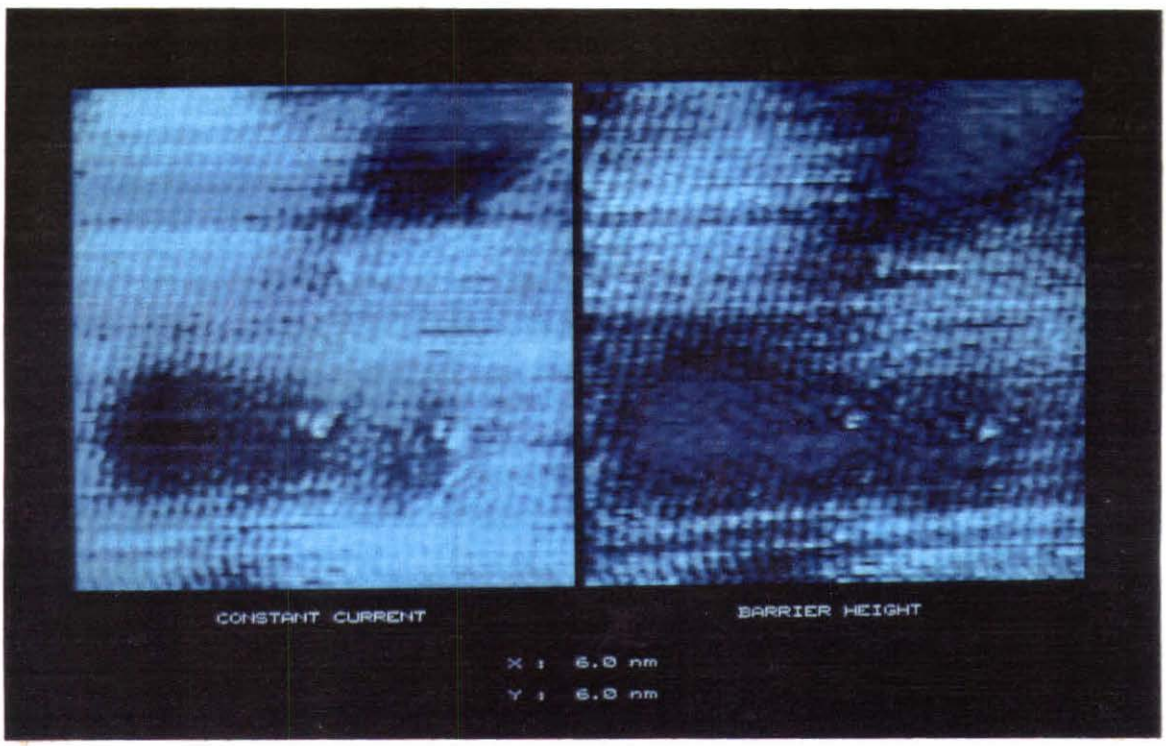
CONSTANT CURRENT
BARRIER HEIGHT
X : 6.0 nm
Y : 6.0 nm

**Figure 21**

Another example of an etch pit similar to that shown in Figure 20 is provided here. The pit is again one layer deep and is similar in size to others observed. There are three distinct boron sites visible on the bottom surface of the etch pit region. Both constant current and barrier height images are provided and are ~ $(30\ \text{Å})^2$ in size.

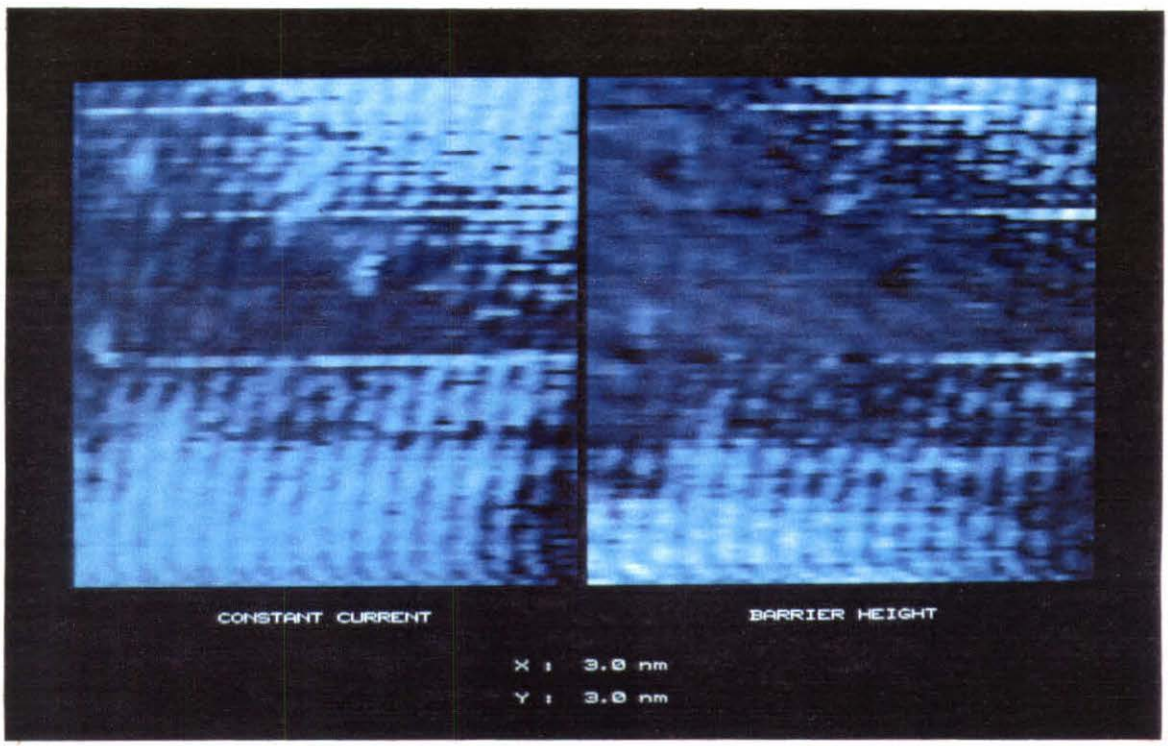
CONSTANT CURRENT
BARRIER HEIGHT
X : 3.0 nm
Y : 3.0 nm

**Figure 22**

A line-scan representation of a current image of BPG obtained using a graphite tip is provided here. A graphite tip was used to evaluate the validity of such an approach in simulating sliding graphite planes in HOPG imaging. The image reveals the ability of a graphite tip to resolve the individual boron sites on the BPG surface. It would be expected that these features would be "smeared out" if the imaging mechanism involved sliding graphite planes. The image was obtained on a Digital Instruments' Nanoscope II STM using a mechanically sharpened graphite tip. The image size is ~ (275 Å)$^2$ and other experimental parameters are provided with the figure.

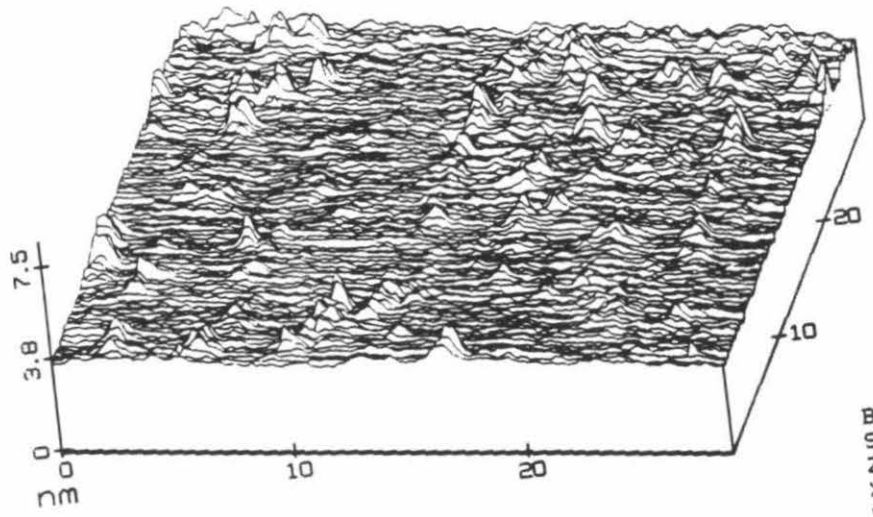


Data taken Wed Mar 06 15:56:57 1991
Buffer 3(BGHGT.001(F)(F)), Rotated 0°, XY axes [nm], Z axis [nm]

## *REFERENCES*


1. C. Kittel, in *Introduction to Solid-State Physics*, 6th edition (John Wiley and Sons, New York, 1986), p. 212.

2. it remains under some debate whether $TiS_2$ is a semimetal or a semiconductor.

3. E. Clar, in *Polycyclic Hydrocarbons* (Academic Press, New York, 1964), Vol. 1.

4. R. Bowling, R. Packard, and R.L. McCreery, *J. Am. Chem. Soc.* **111**, 1217 (1989).

5. Union Carbide, Advanced Ceramics Division, Cleveland, OH.

6. A.W. Moore, *Chem. and Phys. of Carbon* **11**, 69 (1973).

7. A.W. Moore, Union Carbide, personal communication.

8. R.S. Robinson, K. Sternitzke, M.T. McDermott, and R.L. McCreery, *J. Electrochem. Soc.* **138**, 2412 (1991).

9. G. Binnig, H. Fuchs, Ch. Gerber, H. Rohrer, E. Stoll, and E. Tosatti, *Europhys. Lett.* **1**, 31 (1986).

10. G.S. Painter and D.E. Ellis, *Phys. Rev. B* **1**, 4747 (1970).

11. S.-I. Park and C.F. Quate, *Appl. Phys. Lett.* **48**, 112 (1986).

12. J. Schneir, R. Sonnenfeld, P.K. Hansma, and J. Tersoff, *Phys. Rev. B* **34**, 4979 (1986).

13. A. Selloni, P. Carnevali, E. Tosatti, and C.D. Chen, in *Proceedings of the 17th International Conference on the Physics of Semiconductors*, ed. J.D. Chadi and W.A. Harrison (Springer Press, New York, 1985), p. 11; *Phys. Rev. B* **31**, 2602 (1985).

14. R. Sonnenfeld and P.K. Hansma, *Science* **232**, 211 (1986).

15. H.J. Mamin, E. Ganz, D.W. Abraham, R.E. Thomson, and J. Clarke, *Phys. Rev B* **34**, 9015 (1986).

16. D. Tomanek, S.G. Louie, H.J. Mamin, D.W. Abraham, R.E. Thomson, E. Ganz, and J. Clarke, *Phys. Rev. B* **35**, 7790 (1987).

17. R.J. Colton, S.M. Baker, R.J. Driscoll, M.G. Youngquist, W.J. Kaiser, and J.D. Baldeschwieler, *J. Vac. Sci. Technol. A* **6**, 349 (1988).

18. T.R. Albrecht, H.A. Mizes, J. Nogami, S.-I. Park, and C.F. Quate, *Appl. Phys. Lett.* **52**, 362 (1988).

19. R.J. Driscoll and M.G. Youngquist, unpublished results.

20. J.H. Coombs and J.B. Pethica, *IBM J. Res. Develop.* **30**, 455 (1986).

21. J. Tersoff, *Phys. Rev. Lett.* **57**, 440 (1986).

22. J.M. Soler, A.M. Baro, N. Garcia, and H. Rohrer, *Phys. Rev. Lett.* **57**, 444 (1986).

23. H.A. Mizes, S.-I. Park, and W.A. Harrison, *Phys. Rev. B* **36**, 4491 (1987).

24. J.B. Pethica, *Phys. Rev. Lett.* **57**, 3235 (1986).

25. R.J. Colton, S.M. Baker, W.J. Kaiser, and J.D. Baldeschwieler, *Appl. Phys. Lett.* **51**, 305 (1987).

26. in some cases, a commercial STM instrument was used. Either a Nanoscope II (Digital Instruments, Santa Barbara, CA) or a TMX 2000 (TopoMetrix, Santa Clara, CA) was used. When using the TMX 2000, David Baselt usually assisted and provided the D-BOSS operating system and software for the instrument. These experiments were performed in air.

27. Platinum or platinum-iridium tips were generally used for experiments performed in air.

28. D.R. Baselt, personal communication.

29. J. Xhie, K. Sattler, U. Müller, N. Venkateswaran, and G. Raina, *Phys. Rev. B* **43**, 8917 (1991).

30. C. Liu, H. Chang, and A.J. Bard, *Langmuir* **7**, 1138 (1991).

31. C. Clemmer and T. Beebe, Jr., *Science* **251**, 640 (1991).

32. H. Chang and A.J. Bard, *Langmuir* **7**, 1143 (1991).

33. developed by M.G. Youngquist, with assistance from S.M. O'Connor.

34. for a general reference on layered materials, see Doni and Girlanda, in *Electronic Structure and Electronic Transitions in Layered Materials*, ed. V. Grasso (Dordrecht, Netherlands, 1986).

35. R.H. Friend and A.D. Yoffe, *Adv. Phys.* **36**, 1 (1987).

36. J.A. Wilson, *Phys. Status Solidi B* **86**, 11 (1978).

37. W.J. Kaiser and M.B. Weimer, personal communication.

38. A. Zunger and A.J. Freeman, *Phys. Rev. B* **16**, 906 (1977).

39. G.P.E.M. van Bakel, J.Th.M. De Hosson, and T. Hibma, *Appl. Phys. Lett.* **56**, 2402 (1990).

40. S. Takeuchi and H. Katsuda, *J. Jpn. Inst. Met.* **34**, 758 (1970).

41. A.H. Thompson, F.R. Gamble, and C.R. Simon, *Mater. Res. Bull.* **10**, 915 (1975).

42. J.A. Wilson, *Solid State Commun.* **22**, 551 (1977).

43. R.H. Friend, D. Jerome, W.Y. Liang, J.C. Mikkelsen, and A.D. Yoffe, *J. Phys. C* **10**, L705 (1977).

44. C.H. Chen, W. Fabian, F.C. Brown, K.C. Woo, B. Davies, B. Delong, and A.H. Thompson, *Phys. Rev. B* **21**, 615 (1980).

45. E.M. Logothetis, W.J. Kaiser, C.A. Kukkonen, S.P. Faile, R. Colella, and J. Gambold, *J. Phys. C* **12**, L521 (1979); C.A. Kukkonen, W.J. Kaiser, E.M. Logothetis, B.J. Blumenstock, P.A. Scroeder, S.P. Faile, R. Colella, and J. Gambold, *Phys. Rev. B* **24**, 1691 (1981).

46. the $TiS_2$ samples were courtesy of W.J. Kaiser of the Jet Propulsion Laboratory.

47. H. Chang and A.J. Bard, *J. Am. Chem. Soc.* **113**, 5588 (1991).

48. A.R. Ubbelohde and F.A. Lewis, *Graphite and its Crystal Compounds* (Clarendon Press, Oxford, 1960).

49. D.E. Soule, *Proceedings of the Fifth Carbon Conference*, Vol. 1 (Pergamon Press, Oxford, 1962), p. 13.

50. D.E. Soule, J.W. McClure, and L.B. Smith, *Phys. Rev.* **134**, 8468 (1964).

51. J.A. Turnbull, M.S. Stagg, and W.T. Eeles, *Carbon* **3**, 387 (1966).

52. G.A. Bassett, *Phil. Mag.* **33**, 1042 (1958).

53. G.R. Hennig, *Appl. Phys. Lett.* **4**, 52 (1964).

54. G.R. Hennig, *J. Chem. Phys.* **40**, 2877 (1964).

55. G. Hennig, *J. Chem. Phys.* **42**, 1167 (1965).

56. M.R. Soto, *Surf. Sci.* **225**, 190 (1990).

57. H.A. Mizes and W.A. Harrison, *J. Vac. Sci. Technol. A* **6**, 300 (1988).

58. R. Hoffmann, *Rev. Mod. Phys.* **60**, 601 (1988).

59. H.W.M. Salemink, I.P. Batra, H. Rohrer, E. Stoll, and E. Weibel, *Surf. Sci.* **181**, 139 (1987).

60. M. Kuwabara, D.R. Clarke, D.A. Smith, *Appl. Phys. Lett.* **56**, 2396 (1990).

61. J.F. Womelsdorf, W.C. Ermler, and C.J. Sandroff, *J. Phys. Chem.* **95**, 503 (1991).

62. either TopoMetrix's TMX 2000 or Digital Instruments' Nanoscope II, as noted.

63. D.P. Kim, M.M. Labes, and L.M. Siperko, *Mat. Res. Bull.* **25**, 1461 (1990).

# *Chapter 3*

# *SCANNING TUNNELING MICROSCOPY OF A CLEAVED SEMICONDUCTOR, GALLIUM ARSENIDE, GaAs(110)*

## *INTRODUCTION*

### *Motivation for Studying GaAs with STM*

Gallium arsenide (GaAs) is a member of an important class of materials known as III-V compound semiconductors. GaAs is the prototypical example of such materials and is ideally suited for numerous optoelectronic and electronic applications. GaAs is the most investigated compound semiconductor because of its many applications,[1] which include light-emitting and light-detecting devices such as solid-state lasers, solar cells, photocathodes, and a variety of transistor devices and integrated circuits. Much of the interest in studying GaAs is due to its "speed" in electronic devices, resulting from the decreased electronic effective mass for GaAs relative to that for other semiconductors such as Si. There is also considerable effort being applied towards improving molecular beam epitaxy (MBE) methods involving GaAs films.

Prior to scanning tunneling microscopy (STM), the GaAs surface was studied primarily by low-energy electron diffraction (LEED) and reflection high-energy electron diffraction (RHEED) techniques, which provided information on surface ordering and reconstruction. However, no real-space imaging of the surface atomic positions was possible and only limited, broad-range information was obtained. The introduction of STM has made it possible to study the atomic arrangement of surfaces in real-space. In addition, it is possible to investigate the electronic structure of these surfaces with atomic precision.

The technologically important crystal face of GaAs is the (100) surface; however, much attention has been focussed on the (110) face because it is the cleavage face of the GaAs crystal. The (110) cleavage face is easily prepared

and remains largely unreconstructed (except for some minor surface relaxation) upon cleavage. The cleaved surface, when prepared in UHV, is clean and pristine and is atomically flat with a relatively low defect density. In addition, it is electronically simple, having no surface states in the forbidden band gap.[2] The surface states are found in the valence and conduction bands.[3] The GaAs(110) surface contains equal numbers of cations (Ga) and anions (As), allowing two physically, chemically, and electronically distinct atomic species to be probed by STM.

***Physical Properties of GaAs(110)***

Most semiconductor surfaces tend to reconstruct their atomic arrangement, driven by the minimization of the surface free energy. This results in an atomic registry which differs from that of the bulk. The most famous reconstructed surface is the (7x7) reconstruction of the Si(111) surface. The GaAs(110) surface has a simple geometry, which is not reconstructed, experiencing only a slight relaxation in the Ga-As bond upon cleavage. The unrelaxed GaAs(110) cleavage surface consists of alternating rows of Ga and As atoms, and exhibits a 1x1 LEED pattern. Since the (110) surface is usually prepared by cleavage in UHV without any heat treatment, its cleanliness and ideal stoichiometry are known with certainty. The (110) is by far the best understood of all semiconductor surfaces, both electronically and structurally. The GaAs(110) surface unit cell contains two atoms, one cation (Ga) and one anion (As) and is 4.00 by 5.65 Å in size. The Ga and As atoms are linked in zig-zag chains parallel to the [110] direction. Each Ga and As atom binds a single electron in a half-filled dangling bond. In the case of the ideal truncated structure, the underlying layers consist of identical chains. The

interlayer spacing is 2.00 Å. Figure 1 provides a schematic showing the atomic structure of the GaAs(110) surface.

The surface distortion caused by relaxation was first detected by electron paramagnetic resonance (EPR) measurements.[4] The first quantitative determination of the relaxed surface atomic geometry of GaAs(110) was made using dynamical LEED data analysis.[5] The surface maintains its (1x1) periodicity but the relaxation causes the surface Ga atoms to be pulled towards their three nearest neighbors (two in the surface plane, one in the second layer) and the surface As atoms to tilt up from the ideal surface plane, resulting in a bond rotation between a line connecting surface Ga and As neighbors and the (110) plane. The electrons in the Ga dangling bonds transfer to the As, forming as a result, fivefold-coordinated As atoms and threefold-coordinated Ga atoms. Consequently, the surface As atoms are 0.65 Å higher than their adjacent Ga atoms.[6]

***STM Studies of GaAs(110)***

The STM has been used since its invention to investigate the surface morphology of semiconductor materials.[7] In 1985, with the first STM study of GaAs(110) by Feenstra and Fein,[8] came the first STM observations of the topography of a *cleaved* semiconductor surface. In fact, it was the first report of a STM study on *any* cleaved surface. Their STM results were consistent with what was known about the surface from LEED studies. The authors observed atomic rows made up of zig-zag chains of alternating Ga and As atoms with a (1x1) periodicity. The corrugation amplitude in the [001] direction was found to be between 0.2 and 0.5 Å, and that in the [110] direction ~ 0.05 Å. Point defects, typically 0.7 Å deep, resulting from missing atoms, were also observed.

The compound nature of GaAs makes it possible to probe two physically and electronically distinct atoms. Feenstra *et al.*[9] later demonstrated for the first time atom-selective (voltage-dependent) imaging of a surface by STM. Their images revealed either only Ga atoms or only As atoms, depending on the polarity of the bias voltage. As a result, they were able to identify chemically the different atoms comprising the unit cell. This experiment was possible because STM probes the *electronic* properties of a surface, with the images corresponding to contours of constant state density, which for semiconductors, are often spatially localized on specific atoms or bonds. For the GaAs(110) surface, the unit cell is characterized by a single maximum, which corresponds to only one of the atoms in the unit cell. This observation is due to the electronic structure of GaAs(110), in which the two dangling bonds broken at the surface combine into one lone pair of electrons localized on the As atom, while the fourth valence orbital of Ga is empty.[10] A projection of the surface density of states then has occupied states concentrated preferentially on the surface As atoms and unoccupied states on the Ga atoms.[11] Therefore, STM images acquired with a negative sample bias (electrons tunneling from sample to tip, probing the filled states of the surface) reveal the As atoms, and images using a positive sample bias (electrons tunneling from tip to sample, probing empty surface states) reveal the Ga atoms.

The observed effect of adsorbed oxygen atoms on the GaAs(110) surface was reported by Stroscio *et al.*.[12] The images displayed a significant voltage dependence, arising from the energy dependence of the local state density. In addition to this short-range behavior, a long-range coulombic screening was observed at low oxygen coverages in the surrounding bare surface region.

This screening was evidence of local band bending at the surface and had a characteristic screening length of ~ 50 Å on *n*-type GaAs. The oxygen atoms were found to be protrusions at negative sample bias (tunneling out of valence states) and depressions at positive sample bias (tunneling into conduction band states).

More recently, GaAs(110)-adsorbate systems have become very popular for study by STM. The adsorbates have usually been metals, due to the interest in metal-semiconductor interfaces. The metals used to date in STM studies include bismuth,[13] gold,[14] iron,[15] chromium,[16] antimony,[17] tin,[18] samarium,[19] and aluminum.[20] Cesium[21,22] atoms have also been deposited on GaAs(110) to produce linear one-dimensional atomic chains or "wires." There have also been STM studies which have focussed on the imaging of point defects and microfaceting,[23] as well as crystal dislocations (both screw and edge type) induced by plastic deformation.[24] In the former investigation, STM imaging of *n*-GaAs(110) showed terraces with different step orientations and point defects along the Ga and As rows. In the latter study, atomically resolved images of perfect and partial dislocations penetrating the cleaved (110) surface were obtained. The samples were deliberately deformed by 3.7 % in compression at 400°C. The dislocations were found to be mobile over nanometer distances.

## *EXPERIMENTAL*

The STM used in these experiments was the same Caltech-built UHV instrument described in chapter 1. The typical constant current image was ~ 100 x 100 Å in size and contained 500 data points in $x$ and 100 data points in $y$. The typical current image was ~ 20 x 20 Å in size and comprised 125 data

points in both $x$ and $y$ directions. Any post-acquisition smoothing or filtering is described in the caption accompanying the particular figure. A least-squares-fit plane has been subtracted from all data. The sample bias was usually between 2 and 3 volts, the polarity of which depended on whether Ga or As atoms were being imaged. The tunneling current used for all data presented here was 100 pA. Attempts at using tunneling currents on the order of 1 nA were unsuccessful in obtaining high-quality atomically resolved images.

The tips were prepared from 0.5 mm diameter tungsten wire, electrochemically etched using standard 6V-ac techniques with hydroxide solutions. No special tip pre-cleaning procedures were employed prior to imaging. The tips however were sometimes cleaned *in situ* by field emission at μA-range currents to remote areas of the GaAs surface. These tips were not particularly stable, causing frequent $z$-level changes due to tip changes and/or resolution changes during imaging. "Current spikes" were also occasionally observed and were probably due to transient tip changes. The samples were $n$-type (Si-doped) GaAs wafers with a carrier concentration > $10^{18}$ $cm^{-3}$. The type and concentration of the doping were confirmed by Seebeck coefficient and four-point van der Pauw resistivity and Hall coefficient measurements,[25,26] respectively. The 0.5 mm thick wafers were scored using a standard hand-held diamond-tipped scribe and were cleaved *in vacuo* in the [100] direction, exposing a (110) crystal face. The wafers were cleaved by tapping the scored sample with the blunt tip of the vacuum chamber's wobble stick and were then immediately mounted on the STM louse sample stub holder. The quality of the cleave was determined by visual inspection (through a quartz window) with a long focal-length microscope prior to

introduction to the STM stage. Poorly cleaved samples, evidenced by visibly rough surface morphology, were discarded. The pressure of the vacuum chamber was maintained below $10^{-10}$ torr during the experiments. The GaAs wafers were mounted edge-on in sample stubs using melted indium for electrical contact. The resistance of the contact was found to be negligible compared to the tunneling junction resistance. The samples were mounted with the [110] direction at ~ 45° to the scan direction, such that the [110] atomic rows would be diagonal with positive slope in STM images.

## *RESULTS AND DISCUSSION*

### *Atom-Resolved Imaging*

The GaAs(110) surface was found to be quite difficult to image with atomic resolution. The reason for this difficulty is three-fold. Firstly, the apparent atomic corrugation on the GaAs(110) surface was usually very small, ~ 0.1 Å or less in the [001] direction and on the order of 0.01 Å in the [110] direction. These small values required very good isolation from both electrical and vibrational noise for atomic features to be discerned. This condition was further challenged because of the necessity to operate at lower tunneling currents (100 pA) for high-quality imaging. In addition, good cleaves of GaAs wafers were not always possible, due to the fact that the *in vacuo* mechanical setup and geometry were far from ideal. The scoring of the wafers also often produced long-range damage which prevented smooth wafer cleavage. It is known[27] that diamond-scribe scoring damage can propagate for relatively long distances (~ 1 mm or more). Lastly, the ac-etched W tips were often insufficiently sharp to provide high measured corrugation, unstable during scanning (numerous tip changes were observed, usually

preventing consistent atom-resolved imaging), and "dirty" upon initial approach (probably from residual oxide coating of the tip following hydroxide etching), thereby necessitating field-emission cleaning before good and stable experimental conditions could be achieved and maintained.

The long-range morphology of the cleaved GaAs(110) consisted of large atomically-flat terraces extending thousands of ångströms laterally, separated by occasional small steps and similarly large rough regions. The structure of these steps, often monatomic, are discussed in the following subsection. In Figure 2, we show an atomically resolved constant current STM image of an atomically flat region of *n*-type GaAs(110). The negative sample bias used in acquiring this image makes the arsenic atoms selectively appear. The atomic rows (in the [110] direction) are arranged diagonally in the image as expected from the deliberate orientation of the sample. The surface is perfectly terminated, devoid of any visible point or edge defects. However, defects were occasionally observed and are discussed in the following subsection. A "zoomed" image (acquired with the same pixel density) from the same sample shown in Figure 2 is provided in Figure 3. Again, As atoms are imaged, but the atoms are more clearly resolved. In both images, the unit cell appears almost square in shape, approximately 5.4 Å x 5.6 Å in size. The unit cell is expected to be rectangular in shape and about 4.0 Å x 5.6 Å in size. Any deviations from the expected geometry and dimensions of the unit cell are a result of a combination of the following: piezo non-orthogonality, unequal piezo expansion, and thermal drift. The major atomic corrugation in Figure 3, in the [001] crystal direction (between atomic rows), was measured to be ~ 0.03 Å peak-to-valley. The corrugation in the orthogonal [110] direction (along the rows) was ~ 0.01 Å. These values are extremely small and test the

limits of vertical resolution of STM. Such values require very quiet instrumental operation, with little interference from vibrational and electrical noise. The atomic corrugation values are an order of magnitude less than can be expected under ideal conditions,[28] and are probably due to a "dull" tip unable to sense the full vertical surface topographical variations. The [001] corrugation is graphically illustrated with a cross-sectional linecut in Figure 4. Although the data have been slightly smoothed (see figure caption), the quietness and sensitivity of the STM system is evident.

It was found that atom-resolved constant current images with negative sample biases (imaging As atoms) were considerably easier to obtain than those with positive sample biases (imaging Ga atoms). The tunneling junction became unacceptably noisy when tunneling from the tip to the sample at positive sample biases. Often, current spikes, probably arising from transient tip changes, made consistent atomic resolution imaging impossible. The reason for this behavior is unknown; other researchers have not reported similar behavior. An example showing Ga atoms is provided later in Figure 8. In addition, high-quality constant height or current images were more difficult to acquire than their feedback-mediated counterparts. Although several atom-resolved current images were obtained at both bias polarities, little success was made in acquiring a high-quality set of "concurrent" constant height images at opposite polarities. Consequently, it was not possible to compare such results with the results of Feenstra and coworkers[9] involving constant current atom-selective imaging. The unit cell dimensions derived from the constant height images were 5.1 x 5.7 Å, closer to the expected values. This may be due to the fact that thermal drift would have a less pronounced effect on these "fast scan" image dimensions.

*Point Defects and Steps*

Occasionally, point and edge defects, in the form of vacancies and steps, were observed on the GaAs(110) surface. The vacancies typically consisted of ~ 0.6 Å deep depressions along the atomic row, with lateral dimensions of one unit cell in the [001] direction and about two unit cells in the [110] direction. An example illustrating surface point defects is provided in Figure 5, which contains two vacancies (missing As atoms), shown by the small dark holes. The vacancy at top-right in Figure 5 has adjacent to it a displaced atom, presumably the "missing" As atom which has come to rest next to its original position. Since the atomic lattice is aligned both vertically and laterally on all sides around the depression, the defect is a point defect rather than a dislocation. No statistics were obtained to provide information on the density of these defects, but they are observed at a frequency considerably larger than that expected for the dopant, considering the bulk doping level of the sample.

Small steps, occasionally monatomic in height, were observed separating otherwise flat terraces on the surface. The monatomic steps were measured to have heights between 1.8 and 2.0 Å; the expected value is 2.0 Å. The steps were irregular and rough, but generally aligned along the [112] crystal orientation. Figures 6 and 7 are constant current images showing isolated monatomic steps. In each case, the upper terrace, showing As atomic rows, is located at the upper right of the figure. The sample used for these images had been stored in the vacuum chamber ($10^{-10}$ torr) for two weeks following cleavage prior to imaging. This may account for the observed contamination on the lower terrace in these images. In Figure 7 however, it is possible to discern three rows of As atoms at the bottom right of the lower

terrace interdigitated with the As atomic rows of the upper terrace. This interdigitation (shift by one-half an unit cell) is expected from the structure of GaAs(110), shown in Figure 1. In addition, the upper terrace of Figure 7 shows several vacancies, as well as "extra" atoms laying on the surface. These atoms seem to be displaced out of the vacancies, from which they probably originate.

***Coulombic Screening by Adsorbed Atoms***

On a particular sample which had been stored for five weeks in the vacuum chamber after cleavage, the presence of adsorbates is clearly seen. Figures 8 and 9 show the effect of charged adsorbates on the appearance of the *n*-GaAs(110) surface at positive sample bias. In addition to the well-resolved Ga atomic lattice, one observes large surface features in Figure 8, the dominant of which is a depression at the center. This depression is isolated in a cropped version shown in Figure 9. The adsorbate responsible for this round "hole" is probably an oxygen atom, judging by its appearance[29] and the fact that molecular oxygen is one of the most prevalent components of our vacuum system.[30] A STM analysis of this system provides a means to investigate adsorbate-induced surface states on semiconductors.

At positive sample biases, the adsorbate appears as a negative STM displacement, indicating a decrease in the local density of states (LDOS) in the conduction band. The adsorbate contour is provided by a cross-sectional linecut in Figure 10. The linecut shows that the depression measures ~ 15 Å FWHM and extends ~ 40 Å laterally (diameter) across the surface. This behavior is probably due to a negatively charged adsorbate-induced acceptor state on the GaAs(110) surface. Theoretical calculations show that a negative charge located on the semiconductor surface modifies the LDOS, producing a

combination of an increase in the DOS near the valence-band edge and a corresponding decrease in the conduction band.[28] The occupied acceptor state induced by the electronegative adsorbate results in charge transfer from the conduction band, producing a compensating positive space-charge layer. This results in long-range surface band bending and coulombic screening. In other words, the negative charge of the adsorbate repels the conduction-band electrons, and a charge depletion region is formed in the bare region surrounding the adsorbate. Outside the depletion region, the field from the charged defect is screened by the conduction electrons with a characteristic Coulombic screening length. The observed 40 Å extent of the depression is in agreement with the expected Coulombic screening length.[12] The large lateral extent of the feature is due to an inefficient screening of the adsorbate's negative charge by the semiconductor's gas of conduction electrons. Note that the atomic corrugation is observed to continue through the depression, as expected for an electronic rather than topographical effect. It also suggests that the underlying lattice is not significantly disturbed by the adsorbate. The surface contours around the defect can be interpreted as a real-space view of the local band bending induced by the adsorbate. Stroscio *et al.*[31] have shown no evidence of band bending for *p*-type GaAs(110) with adsorbed oxygen.

***Fourier Transform Power Spectrum***

A two-dimensional (2-D) Fourier transform analysis of STM data can yield valuable information about the dominant frequencies comprising the image (and reciprocally, the spacing of major periodic features of the image) as well as their relative orientations, which subsequently may be correlated with the crystal orientational directions of a single-crystal sample. The 2-D power spectrum directly illustrates these data (the spacing and orientation of

image features) in reciprocal-space as well as their relative power intensities. One can directly count the relative number and sizes of various structures and defects on the surface.[32] The stronger the peak (seen as a dot or cluster of dots in typical spectral presentations), the easier the features are seen in the real-space STM image. It is often possible though to "discover" additional repetitive features by Fourier analysis not readily seen by the naked eye in a STM image. Fourier analysis is most applicable to periodic atomic resolution images, preferably as large as is manageable for the most accurate statistical analysis. The power spectrum often provides more accurate, i.e., averaged, measurement of spacings, e.g., unit cell dimensions, than simple measurements directly obtained from the real-space STM image. The 2-D power spectrum is especially valuable in analyzing large atom-resolved STM images, since they can be directly compared to diffraction images, such as LEED patterns. The 2-D Fourier transform power spectrum is essentially a diffraction pattern from the STM corrugation and should correspond most closely to a helium-diffraction experiment.[33] The same Fourier power spectrum makes it a straightforward process to choose which image frequencies to "filter out" prior to inverse-transforming the data. In this way, one can obtain a Fourier-filtered version of the STM image. The 2-D transform of an image identifies the spatial frequency components, and by eliminating or attenuating suspected noise components in the transform, then taking the inverse transform, a filtered image can be obtained. This type of filtering is especially useful when there exists extraneous data "noise" which is periodic in nature.

The 2-D power spectrum of the data from the STM image of GaAs(110), shown in Figure 2, is provided in Figure 11. The power spectrum is shown

with high power intensities being bright in a histogram-clipped linear grayscale. The dc components have not been attenuated in this presentation, giving rise in part to the bright central region. This feature arises also as a result of low-frequency system noise, which is primarily composed of vibrational and seismic coupling. There are two dominant features in the 2-D power spectrum arising from atomic corrugation in the STM image, the pairs of which are located roughly along the two diagonal axes. The rectangular-shaped unit cell of the GaAs(110) surface and the intentional diagonal orientation of the sample are evident. The major corrugation with wave vector in the [001] crystal direction gives rise to the brighter peak labeled (10) in the figure and the smaller corrugation along the [110] direction gives rise to the orthogonal (01) peak. The intense line at $k_x = 0$ arises from the discrete z-level changes (bands of lighter and darker topography) between scan lines, due primarily to tip changes during scanning. The unit cell dimensions (for the image in Figure 2) deduced from the peaks observed in the power spectrum (Figure 11), 5.4 x 5.6 Å, are in agreement with those obtained directly from the STM image.

## *CONCLUSION*

The GaAs(110) surface was imaged by STM in UHV to reveal selectively either Ga or As atoms, depending on the polarity of the sample bias used. Atom-resolved constant current images were obtained with measured atomic corrugation on the order of 0.01 Å! The unit cell dimensions derived from both direct image analysis and Fourier transform power spectrum measurements, 5.4 x 5.6 Å, are in general agreement with the expected dimensions. It was found that constant current images were easier

to obtain than their constant height counterparts, and that it was easier to acquire high-quality images at negative sample bias than at positive sample bias. In addition, tunneling currents significantly above 100 pA yielded poor images.

Point defects in the form of vacancies (or missing atoms) and edge defects in the form of steps were occasionally observed. The point defects were generally ~ 0.6 Å deep and extended laterally approximately 1 unit cell in the [001] direction and 2 unit cells in the [110] direction. The vacancies were sometimes associated with "extra" atoms located adjacently on the surface, which presumably originated from the vacancy locations. Small steps, many of which were monatomic, separated large terraces of atomically flat regions. These single-layer steps, 2 Å in height, were usually rough and irregular but were generally oriented in the [112] crystal direction. In one instance, atomic rows on the lower terrace adjacent to a monatomic step interdigitated with those of the upper terrace, as expected from the general structure of GaAs(110). Some evidence of contamination on samples stored for extended periods of time in the vacuum chamber was noted.

The real-space manifestation of surface electronic band-bending was observed on *n*-type GaAs(110) with isolated charged adsorbates. These adsorbates, presumably oxygen atoms, because of their electronegativity induce long-range Coulombic screening effects on the semiconductor's surface. As a result, images of the surface acquired at positive sample biases show large depressions with an apparent depth of ~ 0.6 Å but a lateral extent almost 50 Å in diameter. This effect arises because of the inefficient screening of the adsorbate's charge by the semiconductor's conduction electron gas. The atomic corrugation is seen to continue through the defect region, suggesting it

is an electronic rather than geometric "hole" and that the underlying semiconductor structure is not significantly affected.

A 2-D Fourier transform power spectrum derived from an atom-resolved GaAs(110) STM image reveals valuable information on the spatial frequency components of the data. From this spectrum, one can deduce the orientation of the crystal, the spacing of atomic features, i.e., the unit cell dimensions, and the relative intensities (power) of these features. The power spectrum provides a pattern directly comparable to patterns obtained from diffraction experiments, such as LEED.

**Figure 1**

The GaAs(110) surface is illustrated in this schematic showing the atomic arrangement of both Ga and As atoms in both a top-view in a), and a side cross-sectional view in b). The dimensions of the unit cell, 4.00 x 5.65 Å, are shown. The separation $h$ of the top two atomic layers is 2.1 Å. The Ga atoms are represented by the filled circles and the As atoms are the unfilled circles. The figure is taken from Feenstra and Fein.[34]

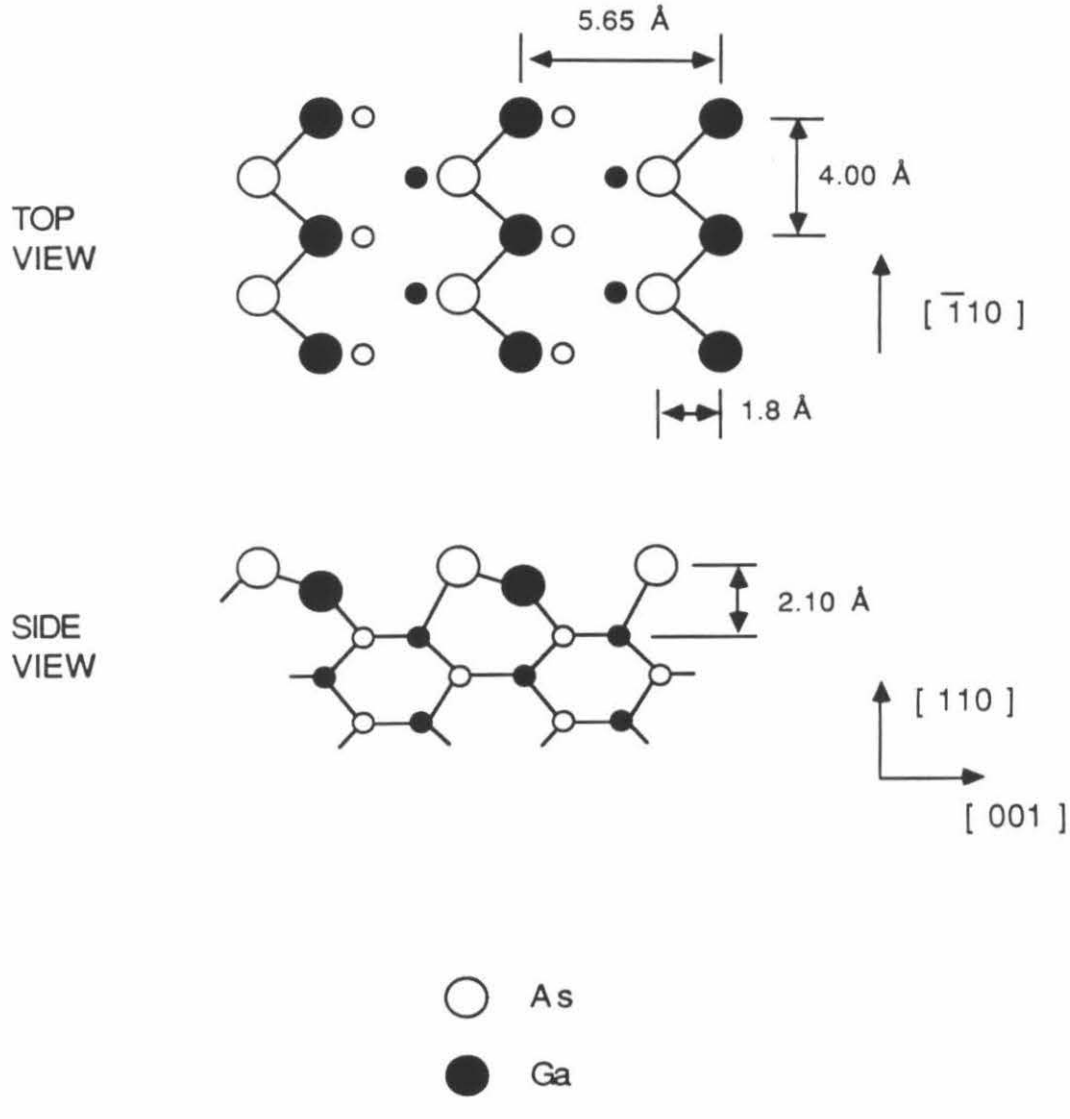
5.65 Å
4.00 Å
TOP
VIEW
[ $\bar{1}$10 ]
1.8 Å
2.10 Å
SIDE
VIEW
[ 110 ]
[ 001 ]
As
Ga

**Figure 2**

The As atoms terminating the *n*-type GaAs(110) surface are shown here in this 130 x 130 Å constant current image, acquired at a sample bias of -2.0 V. This solid-modeled projection was obtained in UHV ($< 10^{-10}$ torr) using a tunneling current of 100 pA with an ac-etched tungsten tip. The surface is atomically flat over this area and perfectly terminated, with no point or edge defects.

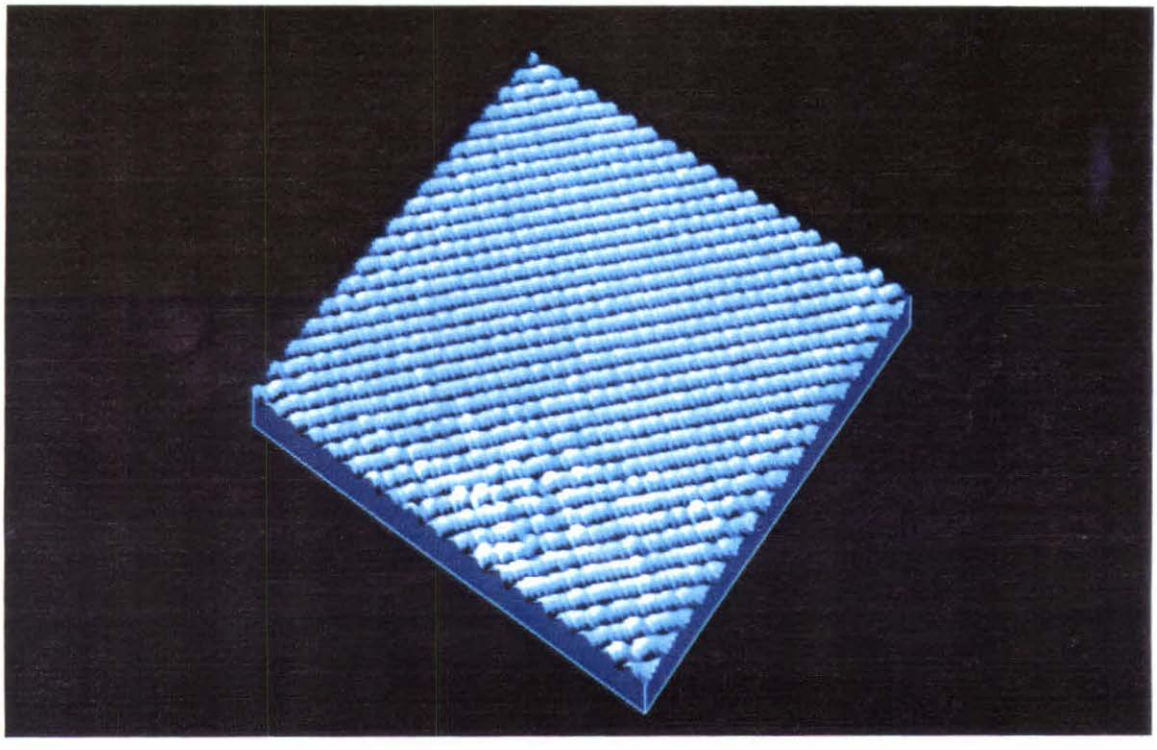

**Figure 3**

A "zoomed" constant current image of *n*-GaAs(110), taken on the same sample (similar area) as that shown in Figure 2. This (65 Å)$^2$ image was acquired at a sample bias of -2.0 V; consequently, arsenic atoms are shown. The rectangular-shaped unit cell is evident. Again, there are no defects observed in this area. The peak-to-valley atomic corrugation in the [001] direction is less than 0.04 Å; the corrugation in the orthogonal [110] direction is ~ 0.01 Å. The [001] corrugation is shown graphically in a cross-sectional linecut in Figure 4.

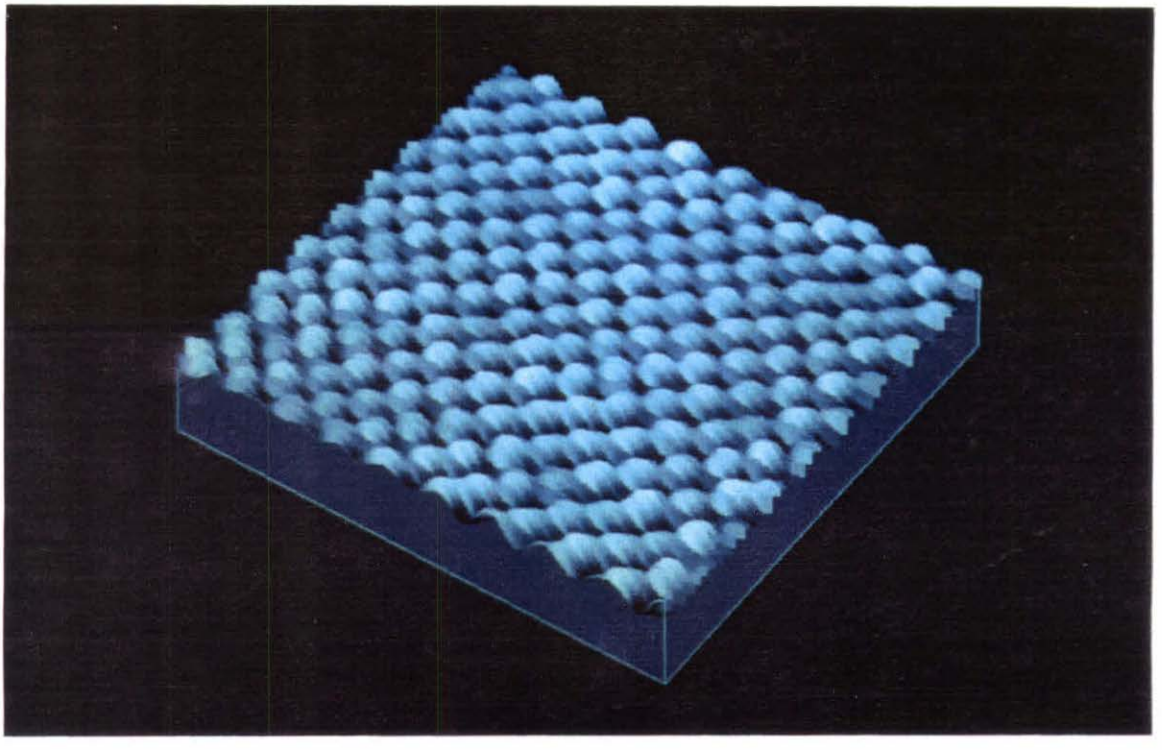

**Figure 4**

The major atomic corrugation, in the [001] direction, is shown plotted in this graph. This cross-sectional linecut reveals that the peak-to-valley amplitude is approximately 0.03 Å (3 pm). Each peak represents an As atom, separated from its neighbor by 5.65 Å. The data have been smoothed using a binomially weighted sliding window average corresponding to a Gaussian of ~ 1 Å FWHM.

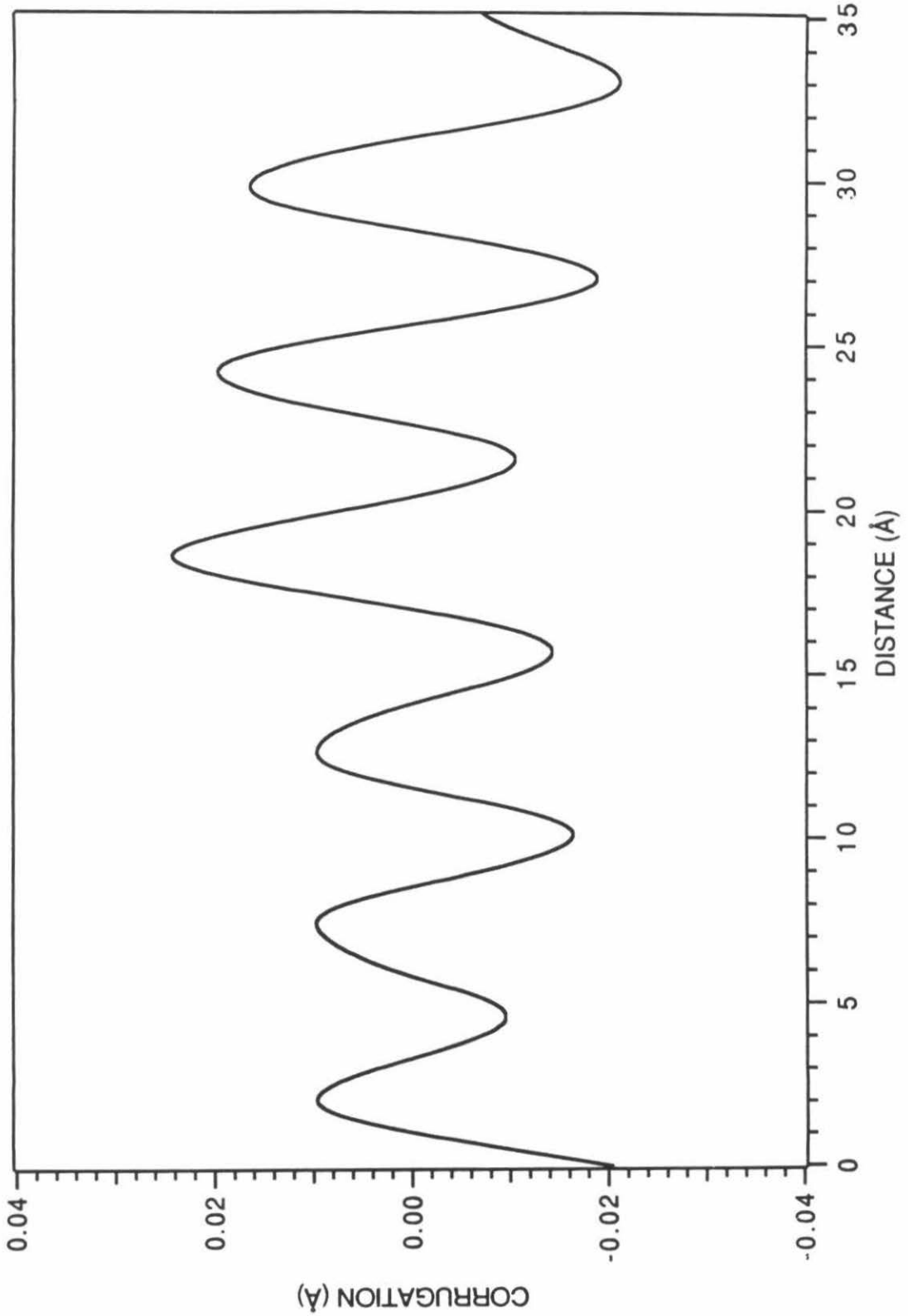
0.04
0.02
0.00
-0.02
-0.04
CORRUGATION (Å)
0
5
10
15
20
25
30
35
DISTANCE (Å)

**Figure 5**

This (130 Å)$^2$ constant current image of *n*-GaAs(110) shows the As atoms in diagonal rows. There are two point defects or vacancies (missing As atoms), shown by the dark holes. The vacancy at top right has an adjacent displaced atom (presumably the vacant As). The point defects are ~ 0.6 Å deep. The tunneling current was 100 pA and the sample bias was -2.0 V. An etched tungsten tip was used and the pressure was kept below $10^{-10}$ torr.

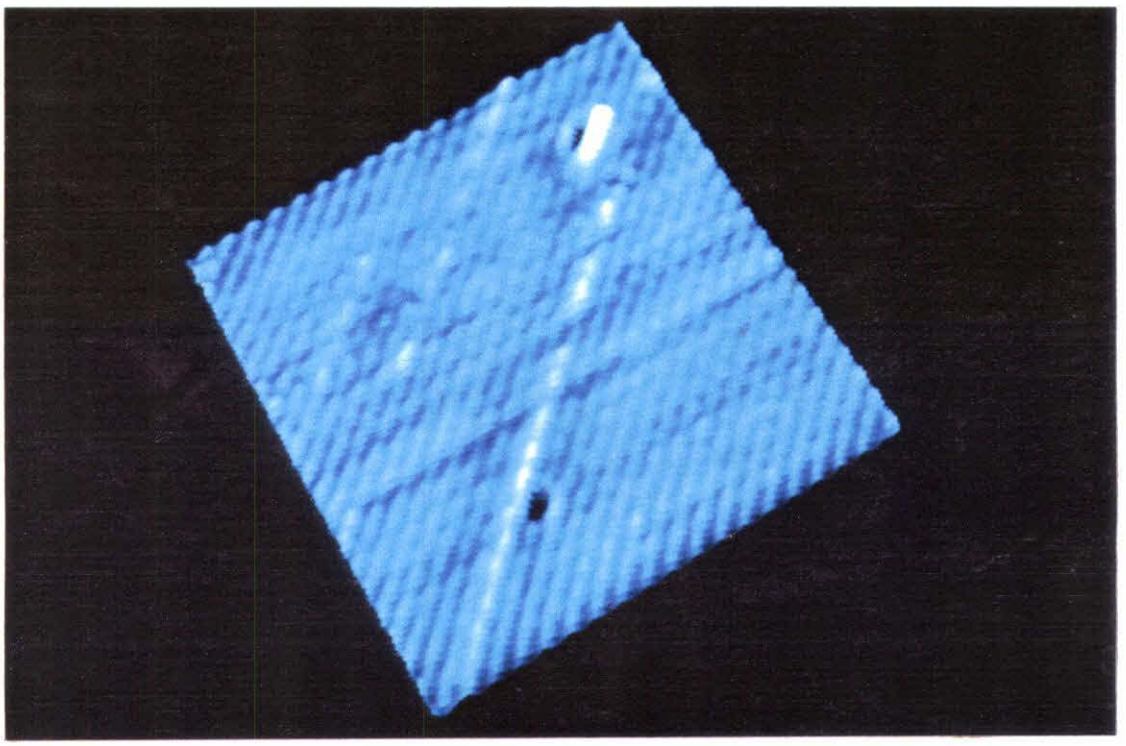

**Figure 6**

A single-height step 2 Å high is illustrated here in this 130 Å x 80 Å constant current STM image of *n*-GaAs(110). The -2.0 V sample bias reveals the As atoms which terminate the surface. The lower terrace at bottom left has visible contamination; the sample was stored two weeks after cleavage prior to imaging.

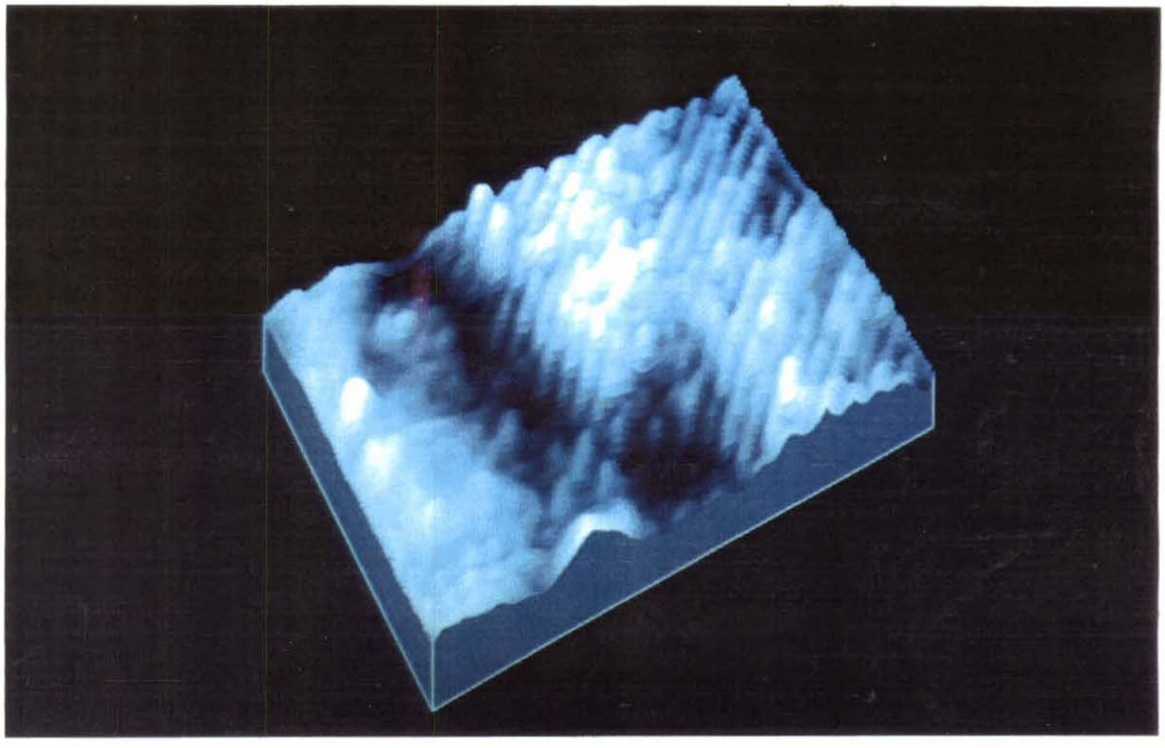

**Figure 7**

This (130 Å)$^2$ constant current image of the *n*-GaAs(110) surface reveals a single atomic layer step (2Å high). The upper terrace has several point defects and the step edge is irregular. The lower terrace is slightly contaminated; the same two week old sample used in Figure 6 is imaged here. The bottom right portion of the lower terrace faintly shows three rows of As atoms interdigitated with the As atomic rows of the upper terrace, as expected from the GaAs(110) structure (see Figure 1). The image was acquired using an etched W tip, a tunneling current of 100 pA, and a -2.0 V sample bias.

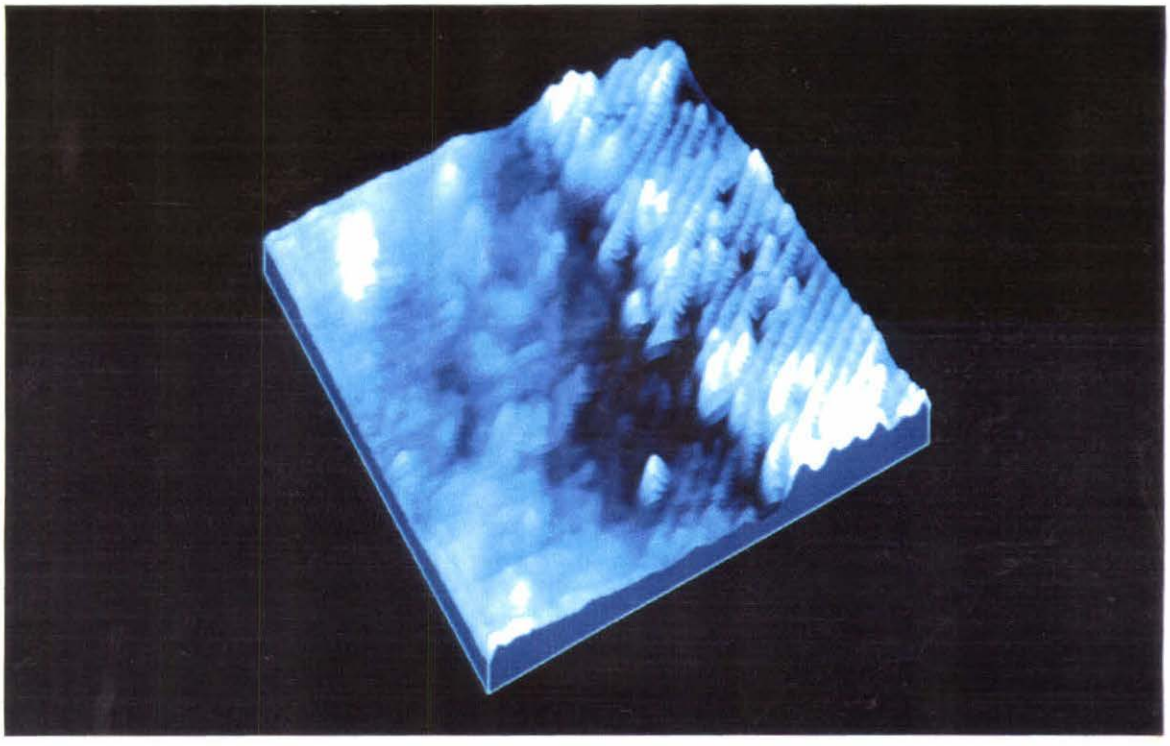

**Figure 8**

A month-old cleaved *n*-type GaAs(110) surface is shown here in a constant current image acquired at +2.5 V. Consequently, Ga atoms are imaged. This (130 Å)$^2$ image is provided in both line-scan (left) and top-view colorscale (right) presentations. Charged adsorbate species cause large features on the surface; the dominant dark feature ("hole") in the center is probably caused by an adsorbed oxygen atom. This "hole" is shown in greater detail in Figure 9. An etched W tip was used and the tunneling current was 100 pA. The data have been low-pass Fourier filtered to remove features below ~ 1.5 Å in size, and current "spikes" deviating by > 2.5 $\sigma$ (standard deviations) from their scan-line average have been substituted by corresponding interpolated values (averages of their adjacent scan-line pixel values).

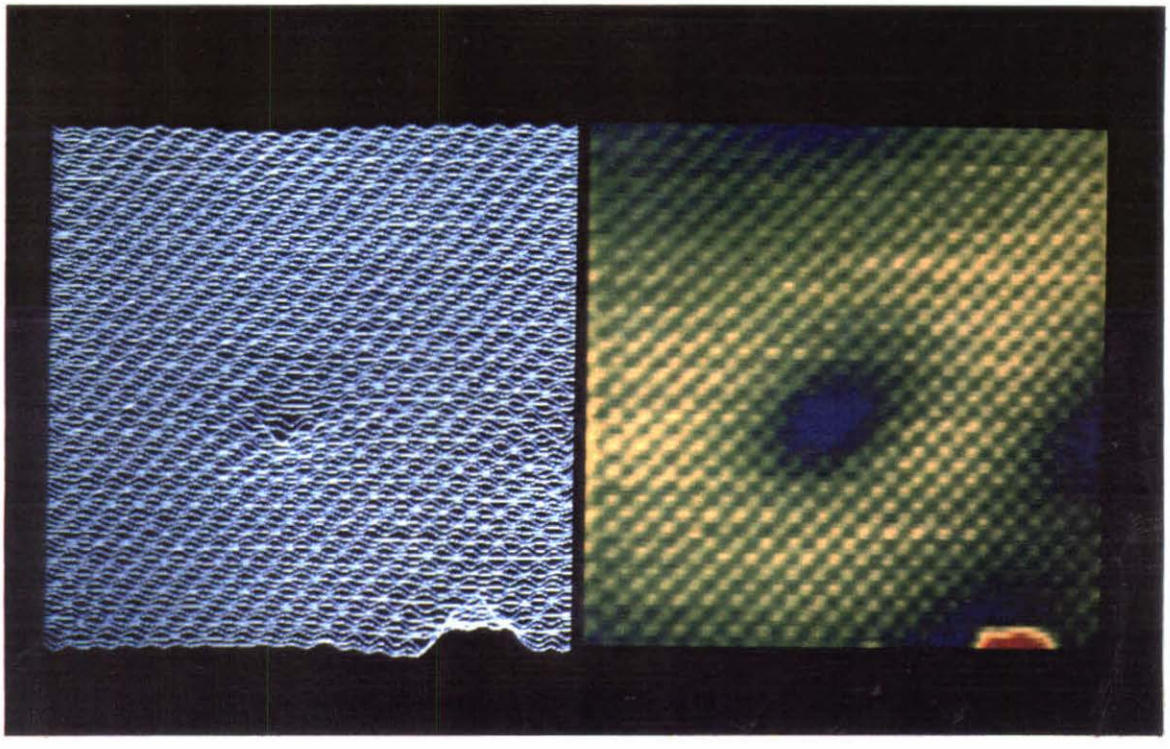

**Figure 9**

An electronic "hole" caused by a negatively charged adsorbate, presumably an oxygen atom, is shown here in a cropped version of the previous figure. The adsorbate causes charge depletion in the surrounding bare surface region. This coulombic screening extends nearly 50 Å across the *n*-type GaAs(110) surface. The FWHM is ~ 15 Å and is graphically illustrated in a cross-section shown in Figure 10.

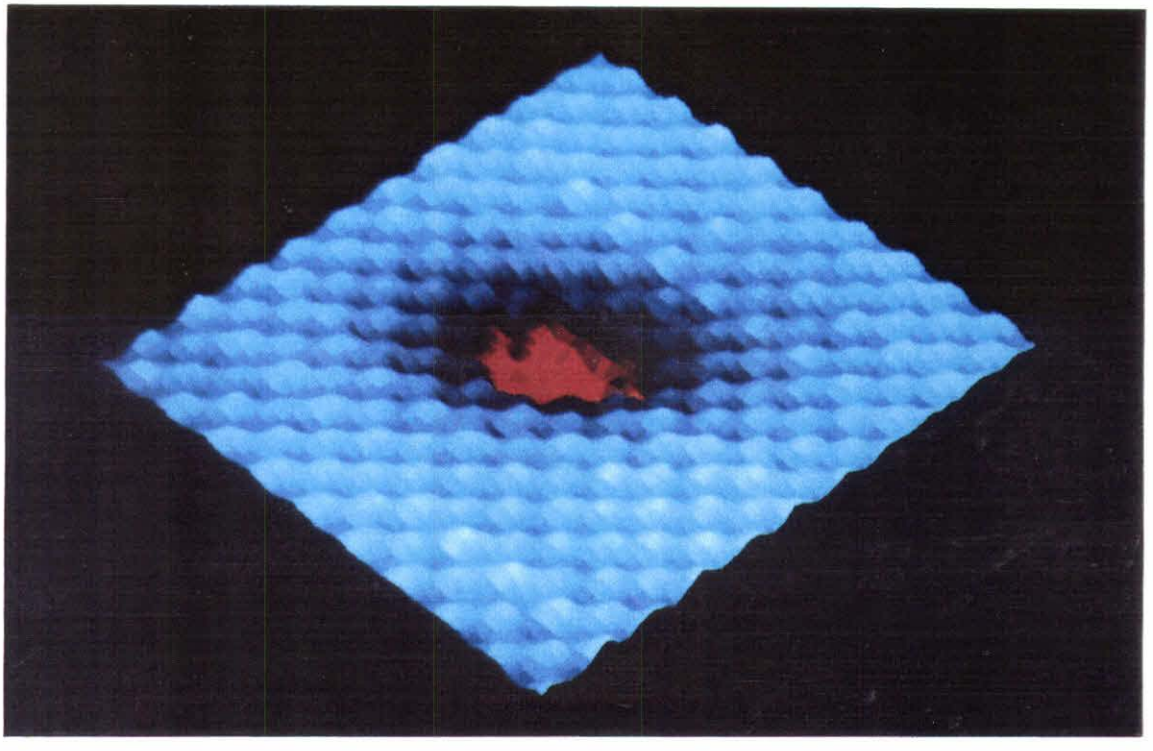

**Figure 10**

A cross-sectional linecut through the electronic "hole" shown in Figure 9 reveals that the screening length extends ~ 40 Å and that the FWHM is ~ 15 Å. The adsorbate causes a long-range screening feature with an apparent depth of ~ 0.6 Å. Note that the atomic corrugation extends through the feature. Each of the small peaks is an individual Ga atom. The vertical dotted lines represent the positions of atoms in the Ga lattice.

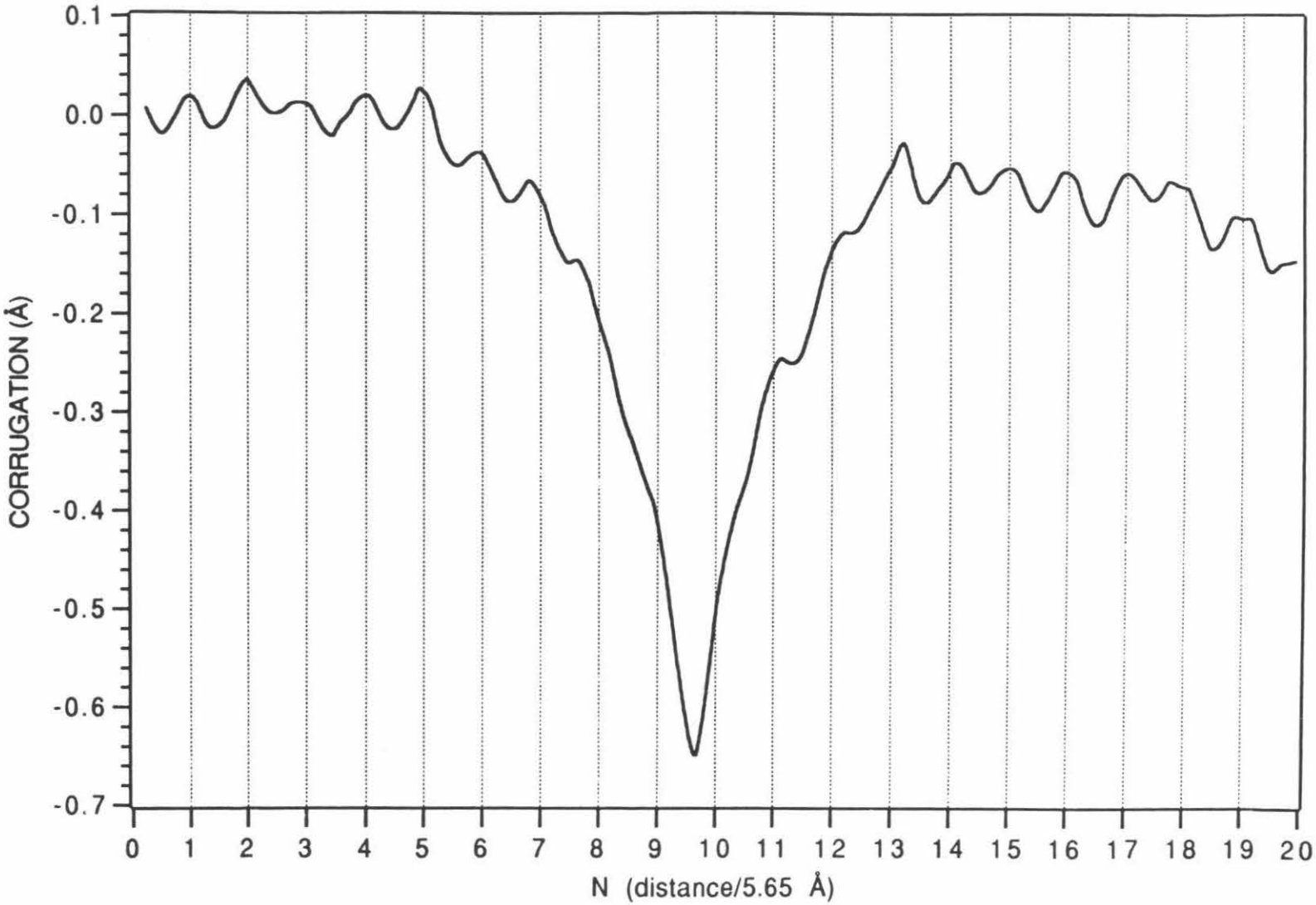
0.1
0.0
-0.1
-0.2
-0.3
-0.4
-0.5
-0.6
-0.7
CORRUGATION (Å)
0 1 2 3 4 5 6 7 8 9 10 11 12 13 14 15 16 17 18 19 20
N (distance/5.65 Å)

**Figure 11**

The two-dimensional (2-D) Fourier power spectrum for the data shown in Figure 2, is shown here. The power spectrum is presented with brightness corresponding with power intensity. The histogram has been clipped in order to provide greater contrast. The dc components have not been attenuated and the "noise" along $k_x = 0$ is a product of the $z$-changes between scan lines. These tip changes give rise to subtle bands of lighter and darker topography in the STM image. The major atomic corrugation along the [001] crystal direction gives rise to the brighter "pair" of peaks labeled (10) in the figure, and the smaller corrugation along the [110] direction gives rise to the orthogonal (01) peak. The distortion of the geometry from the expected geometry is a result of a combination of piezo non-orthogonality, unequal piezo expansion, and thermal drift.

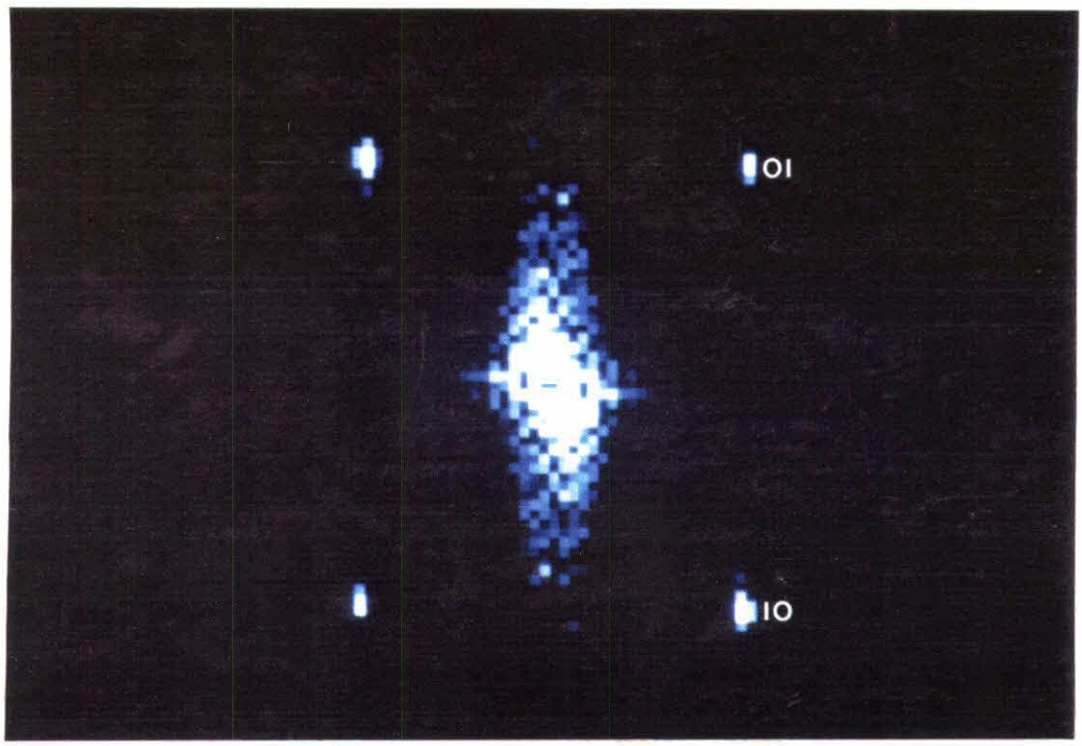
01
10

## *REFERENCES*


1. F. Bechstedt and R. Enderlein, in *Semiconductor Surfaces and Interfaces: Their Atomic and Electronic Structures* (Akademie-Verlag, Berlin, 1988), p. 250.

2. S.B. Zhang and M.L. Cohen, *Surf. Sci.* **172**, 754 (1986).

3. B. Reihl, T. Riesterer, M. Tschudy, and P. Perfetti, *Phys. Rev. B* **38**, 13456 (1988).

4. D.J. Miller and D. Haneman, *Phys. Rev. B* **3**, 2918 (1971).

5. A.R. Lubinsky, C.B. Duke, B.W. Lee, and P. Mark, *Phys. Rev. Lett.* **36**, 1058 (1976).

6. S.Y. Tong, W.N. Mei, and G. Xu, *J. Vac. Sci. Technol. B* **2**, 393 (1984).

7. G. Binnig, H. Rohrer, Ch. Gerber, and E. Weibel, *Phys. Rev. Lett.* **50**, 120 (1983).

8. R.M. Feenstra and A.P. Fein, *Phys. Rev. B* **32**, 1394 (1985).

9. R.M. Feenstra, J.A. Stroscio, J. Tersoff, and A.P. Fein, *Phys. Rev. Lett.* **58**, 1192 (1987).

10. W.A. Goddard III, J.J. Barton, A. Redondo, and T.C. McGill, *J. Vac. Sci. Technol.* **15**, 1274 (1978).

11. J. Tersoff and D.R. Hamann, *Phys. Rev. Lett.* **50**, 1998 (1983).

12. J.A. Stroscio, R.M. Feenstra, and A.P. Fein, *Phys. Rev. Lett.* **58**, 1668 (1987).

13. R. Ludeke, A. Taleb-Ibrahimi, R.M. Feenstra, and A.B. McLean, *J. Vac. Sci. Technol. B* **7**, 936 (1989).

14. R.M. Feenstra, *J. Vac. Sci. Technol. B* **7**, 925 (1989); *Phys. Rev. Lett.* **63**, 1412 (1989).

15. P.N. First, J.A. Stroscio, R.A. Dragoset, D.T. Pierce, and R.J. Celotta, *Phys. Rev. Lett.* **63**, 1416 (1989).

16. B.M. Trafas, D.M. Hill, P.J. Benning, G.D. Waddill, Y.-N. Yang, R.L. Siefert, and J.H. Weaver, *Phys. Rev. B* **43**, 7174 (1991).

17. P. Martensson and R.M. Feenstra, *Phys. Rev. B* **39**, 7744 (1989).

18. C.K. Shih, E. Kaxiras, R.M. Feenstra, and K.C. Pandey, *Phys. Rev. B* **40**, 10044 (1989).

19. B.M. Trafas, D.M. Hill, R.L. Siefert, and J.H. Weaver, *Phys. Rev. B* **42**, 3231 (1990).

20. M. Suzuki and T. Fukuda, *Phys. Rev. B* **44** , 3187 (1991).

21. P.N. First, R.A. Dragoset, J.A. Stroscio, R.J. Celotta, and R.M. Feenstra, *J. Vac. Sci. Technol. A* **7**, 2868 (1989).

22. L.J. Whitman, J.A. Stroscio, R.A. Dragoset, and R.J. Celotta, *Science* **251**, 1206 (1991).

23. G. Cox, K.H. Graf, D. Szynka, U. Poppe, and K. Urban, *Vacuum* **41**, 591 (1990).

24. G. Cox, D. Szynka, U. Poppe, K.H. Graf, K. Urban, C. Kisielowski-Kemmerich, J. Krüger, and H. Alexander, *Phys. Rev. Lett.* **64**, 2402 (1990).

25. L.J. van der Pauw, *Phillips Res. Rep.* **13**, 1 (1958).

26. M. Levy and M.P. Sarachik, *Rev. Sci. Instrum.* **60**, 1342 (1989).

27. W.J. Kaiser and M. H. Hecht, Jet Propulsion Laboratory, personal communication.

28. J.A. Stroscio, R.M. Feenstra, D.M. Newns, and A.P. Fein, *J. Vac. Sci. Technol. A* **6**, 499 (1988).

29. J.A. Stroscio and R.M. Feenstra, *J. Vac. Sci. Technol. A* **6**, 577 (1988).

30. using a Dycor M100 quadrupole mass spectrometer.

31. J.A. Stroscio, R.M. Feenstra, and A.P. Fein, *Phys. Rev. B* **36**, 7718 (1987).

32. U.K. Koehler, J.E. Demuth, and R.J. Hamers, *Phys. Rev. Lett.* **60**, 2499 (1988).

33. J.E. Demuth, U. Koehler, and R.J. Hamers, *J. Microsc.* **152**, 299 (1988).

34. R.M. Feenstra and A.P. Fein, *IBM J. Res. Develop.* **30**, 466 (1986).

# *Chapter 4*

# *SCANNING TUNNELING MICROSCOPY AND SPECTROSCOPY OF ANNEALED AND STRESSED SILICON(111)-(7x7)*

## *INTRODUCTION*

### *Motivation for Studying Silicon with STM*

Silicon, the most popular and well-known semiconductor, is probably the most important technological material in the world, particularly with respect to electronics and computers. Despite intense effort to develop alternative semiconductor systems, the dominant position of silicon in semiconductor device technology remains nearly unchallenged. A large majority of modern electronics depends on the utilization of silicon, especially in applications involving photovoltaics and integrated circuitry. Nearly every electronic device or "chip" relies enormously on silicon manufacturing technology. The structure of the silicon surface, as small as the atomic scale, is of special interest to researchers attempting to increase device quality.

An enormous research effort has been focussed on silicon, because of its great practical importance as well as fundamental interest. Although its bulk structure is very well understood, the structure of its clean low-index faces have been particularly difficult to solve, especially the well-known (7x7) reconstruction of Si(111). The (111) face has received particular attention because silicon cleaves along (111) planes and since early silicon devices were fabricated with (111) oriented slices; today, integrated circuits use silicon wafers with (100) surfaces. In 1959, Farnsworth *et al.*,[1] using low energy electron diffraction (LEED), first reported the observation of a (7x7) unit cell, seven times larger than the (1x1) bulk structure, on a Si(111) surface cleaned by ion bombardment and annealing. Nearly thirty years of intense and highly sophisticated research were invested in efforts to obtain a structural solution to this surface before the invention and introduction of the scanning

tunneling microscope (STM) to the world of surface science. The ability of STM to provide real-space three-dimensional data on semiconductor surfaces with atomic resolution makes it an invaluable tool for structural analysis. In fact, STM was largely responsible for the elucidation of the structure of the Si(111)-(7x7) reconstructed surface. The generally accepted dimer-adatom-stacking fault (DAS) model by Takayanagi *et al.*[2,3] was based largely on the original STM experiments by Binnig and coworkers.[4] This DAS model is discussed in detail in the following section. A brief history of STM studies on the Si(111)-(7x7) is also provided later in this introductory section.

Until recently, solving surface structures has been difficult since one needs techniques that are selectively sensitive to the first few atomic layers rather than the underlying bulk. Before STM, the most powerful and popular technique for structural determination was LEED where the incident electrons (with energies of ~ 100 eV) were strongly scattered by the first few layers. Due to the complex multiple scattering that can take place, especially on a complex surface such as the (7x7) reconstruction, LEED could not provide a definitive solution for any Si surface structure, much less the (7x7). The STM's unique sensitivity to surface structure makes it the ideal choice for evaluating even subtle details of atomic arrangements. With STM, one can image local structures and individual defects such as vacancies, atomic displacements, dislocations, and steps, which are difficult or impossible to study by other experimental techniques that provide information averaged over macroscopic surface areas. As semiconductor devices become smaller, the properties of the surfaces and interfaces may eventually dominate the bulk properties. Consequently, surface structure determination by STM may be a first step towards understanding surface properties.

*Physical Properties of Si(111)-(7x7)*

Like most semiconductor surfaces, the silicon atoms at the vacuum interface rearrange to minimize the surface free energy. This rearrangement, known as reconstruction, results in the terminated surface having a structure which differs from the bulk material. In addition, the clean, cleaved Si(111) surface shows different geometric structures depending on the preparation method, the thermal history, and the temperature of the sample. When freshly cleaved in UHV at liquid nitrogen temperature and above, a metastable (2x1) unit cell is observed. Upon annealing to approximately 250°C, the (2x1) transforms irreversibly to a (7x7) structure,[5] which is thermodynamically stable at room temperature. Upon further heating to 900°C, the (7x7) surface transforms reversibly to a (1x1) structure.[6] If the surface is quench-cooled, a (1x1) pattern is observable at room temperature.[7] If it is slowly cooled below 830°C, the stable (7x7) reconstruction is produced. The (7x7) periodicity was confirmed by LEED and reflection high energy electron diffraction (RHEED).[8,9] as well as UHV-reflection electron microscopy (REM),[10] UHV-transmission electron microscopy (TEM),[11] and UHV-low energy electron reflection microscopy (LEERM).[12]

The (7x7) reconstruction on Si(111) is produced on surfaces that have been mechanically and/or chemically polished, or simply cleaved, and then cleaned in UHV by heat treatment alone at about 950°C (recall lower temperatures are required for cleaved surfaces), or by ion bombardment followed by similar heat treatment. A number of structures were proposed prior to STM, based largely on LEED data, none of which were consistent with all experimental observations. A review of the history of the experiments on

Si(111)-(7x7) and subsequent proposed structures is given by Haneman and Haydock.[13]

The data of Binnig *et al.*[4] showed the real-space arrangement of the (7x7) reconstruction. The unit cell was seen to be diamond-shaped and consist of twelve adatoms. The two triangular halves of the unit cell, each containing six adatoms, were asymmetric with respect to height. The authors proposed a model to explain their observations: an array of 12 adatoms on an unmodified substrate. However, this model did not account for the unit cell asymmetry. In response, Chadi[14] in 1984 suggested sub-surface bond breaking in addition to the 12 adatoms. Numerous alternative models were proposed before the DAS model[2,3] was introduced in 1985, which is now generally accepted to be correct. A review of these models is provided by Haneman.[15]

The DAS model by Takayanagi was based on extensive data from LEED and transmission electron diffraction (TED)[16] data. The DAS model featured (1) different stacking in the two halves of the unit cell, (2) nine atom pairs, or dimers, on the sides of these two triangular subcells, and (3) twelve adatoms over the cell. The DAS model for the Si(111)-(7x7) surface is shown in both top-view and side-view in Figure 1, with the different surface atom types identified. The surface adatom layer consists of triangular subunits that each contain six silicon adatoms arranged locally in a (2x2) structure, leaving three unsaturated rest atom dangling bonds in each.[17] Each of the triangular subunits is surrounded by nine silicon dimers. The adatoms lie along or parallel to lines that bisect the triangular subunits of the cell. Each silicon in the adatom layer is triply coordinated with three backbonds to the underlying rest layer atoms and occupy three-fold closed sites ("hollows") formed by the rest atoms. The remaining silicon adatom bonding orbital constitutes the

adatom dangling bond, which points out from the surface. The triangular subunits are alternately faulted and unfaulted with respect to the underlying bulk. In the unfaulted half, the crystal maintains the cubic diamond structure up to the last complete atomic layer. The stacking fault in the faulted half is due to a rotation of the bond directions in the outer layer by 60°. These subunits are bounded by dimer rows which intersect to produce "vacancies" at the corners of the unit cell, known as corner holes. These corner holes are actually 12-membered rings formed as a result of the partial dislocations at the border of the triangular subunits.

As with most semiconductors, the Si(111) surface reconstructs to create a structure which differs markedly from that of the corresponding bulk-terminated surface. The driving force behind the reconstruction is minimization of the surface free energy, primarily through a reduction in the number of surface dangling bonds. The bonding in semiconductors is largely covalent, in which atoms contain directional bonding orbitals. Reconstruction often results in the formation of bonds which are strained and consequently weaker than those of the bulk. The energy cost in forming such bonds however is more than compensated by the reduction in the number of dangling bonds. In the DAS model, the number of dangling bonds is decreased from 49 per unit cell to 19 per cell, 12 on the two types of adatoms, 6 on the rest atoms, and 1 on the bottom of the corner hole.

***STM Studies of Si(111)-(7x7)***

Although STM has been used to investigate a wide variety of materials science problems, the greatest amount of STM effort has been applied to the study of semiconductor surfaces. The reason for this is due to the fact that semiconductor surfaces exhibit complex and interesting atomic

reconstructions, and because many important properties of semiconductor surfaces are dependent on defects and other surface imperfections with atomic dimensions. The ability of STM to do just this makes it the ideal choice for such studies.

Historically, the first surface to be atomically resolved with the STM was the (7x7) reconstruction of the Si(111) surface.[4] Since then, Si(111)-(7x7) has become the *de facto* standard for UHV-STM calibration.[18] Demuth[18] provides a history of the measured resolution on the (7x7) surface, chronicling the quest towards achieving higher resolution. Becker *et al.*[19] in 1985 showed that the (7x7) reconstruction persists essentially undistorted right up to monatomic step edges, and that the upper step edge passes through the corner holes. Swartzentruber *et al.*[20] reported on structural disorder and step bunching in the equilibrium crystal shape phase transition on vicinal Si(111). The authors also discussed the effect of cleaning (and annealing) temperature and environment on the "quality" (roughness, disorder, and cleanliness) of prepared surfaces, including the (7x7) reconstruction. Recently, Kitamura and coworkers[21] were successful in obtaining atomic resolution STM images of the (1x1) <--> (7x7) surface reconstruction of a silicon (111) thin film at about 860°C.

Binnig and Rohrer[22] showed that the STM is a spectroscopic as well as a topographic tool. They used scanning tunneling spectroscopy (STS) in the form of current-voltage (*I-V*) spectra to investigate the electronic structure of the (7x7) surface states. Later, Tromp, Hamers, and Demuth[23] developed a localized STS technique known as current imaging tunneling spectroscopy (CITS)[24] to study localized surface states in real-space, spatially resolved and correlated with the (7x7) structure. This method of obtaining real-space

images of the surface electronic structure is described in chapter 1. A review of the history of STS applied to semiconductors, including the (7x7) surface, is provided by Tromp.[25]

There have been dozens of publications involving the evaporation or epitaxial growth of materials, primarily metals, on the Si(111)-(7x7) surface. The former studies have largely investigated the structural effects induced by evaporated material, including the formation of overlayers and new reconstructions.[26,27] There has been particular interest in the structure of alkali metals on the (7x7) surface.[28] The latter group of investigations have focussed on systems appropriate for molecular beam epitaxy (MBE).[29] More recently, there have been several attempts at using STM and STS to study atom-resolved surface chemistry. Avouris and Wolkow[30] studied the reaction of Si(111)-(7x7) with ammonia, $NH_3$. The authors were able to selectively image reacted and unreacted surface sites using topographs obtained at different energies in combination with atom-resolved spectra. In essence, they mapped the spatial distribution of the surface reaction on an atom-by-atom basis, and found significant differences in reactivity between the various surface sites on the (7x7) surface. Boland[31,32] has investigated individually the reactions of the (7x7) surface with chlorine and hydrogen.

***STM Studies of Stressed Silicon***

Stress and strain play major roles in the physical properties of bulk materials. The role of stress on surface and near-surface structure has been addressed both theoretically and experimentally. However, there have been to date only two published reports, by Swartzentruber *et al.*[33] and Packard *et al.*,[34] of STM experiments on strained silicon samples. The former set of authors used STM to evaluate the influence of externally applied uniaxial

strain on the Si(001) surface, and found that the strain induced modification of the relative areas of the (1x2) and (2x1) domains. These results were in agreement with previous LEED studies.[35] The samples were "pushed" or "pulled" through a variable displacement at one end of a sample with the other end held fixed in a clamp. The uniaxial strain field introduced by this method varied linearly along the length of the sample. The strain was applied during sample heating and was removed after cooling. The strain was shown to lift the orientational degeneracy of the surface energy for (2x1) and (1x2) domains and to produce a striped phase of majority and minority domains with the ratio of domain areas depending on the magnitude of the strain. The latter group applied uniaxial strain to Si(100) and found similar results.

No reports of similar experiments performed on Si(111)-(7x7) have been published. The silicon(111) wafers used in the experiments described in this chapter were subjected to uncalibrated stress (largely anisotropically) during heating on two sides of a square-shaped sample by screws used to hold the sample. The results are described in the following sections.

*EXPERIMENTAL*

All of the STM images shown in this chapter were acquired using a tunneling current of 1 nA. This value provided consistently quiet, high-quality images, as long as the tip was sufficiently sharp. The images typically comprised 500 data pixels in $x$ by between 100-500 data pixels in $y$. The pixel density had to be at least one per Å in order to provide clearly discernible atom-resolved images. The $z$-piezo modulation for barrier height imaging

was typically 1 Å p-p. The sample and tip preparation procedures are described following.

***Sample Preparation***

The silicon samples used in these experiments[36] were prime-grade *n*-type (antimony doped) wafers cut 4° off the (111) orientation, with a nominal resistivity of 0.01 Ω-cm. The wafers were scored with a standard hand-held diamond-tipped scribe with the polished side of the wafer face-down in contact with lint-free paper. The scored wafer was then cleaved into square-shaped samples of appropriate size (~ 0.5 cm on a side) for the sample holder. The surface of the wafer was rinsed with anhydrous ethanol (USP grade) and wiped dry with lint-free paper until visibly shiny and free of debris. Efforts were made to keep the samples free of contact with metals, especially nickel-containing materials, which are known[20] to inhibit silicon reconstruction. The samples were handled only with teflon tweezers or polyethylene, with special attention to avoid touching the surface of the sample, handling only by the edges.

The samples were mounted on stubs designed for resistive sample heating.[37] The samples were held down on opposite sides by screws using considerable torque, sufficient to cause visible strain (bowing) of the sample. The sample was immediately placed in the fast-entry vacuum load lock and transferred to the STM vacuum chamber, which also housed the resistive heater. The sample holder was placed into the heater to provide good electrical contact, and current was applied across the sample to provide resistive heating. The samples were typically annealed and cleaned by heating the sample to above 1200°C, estimated by an optical pyrometer. The pyrometer was external to the vacuum chamber; a quartz window on the

vacuum chamber was used for sample viewing. The base pressure of the vacuum chamber at this time was roughly $3 \times 10^{-10}$ torr. The pressure during heating was maintained below ~ $3 \times 10^{-9}$ torr to minimize contamination. The chamber's cryopanel was cooled with liquid nitrogen during heating to increase the pumping speed of the system. The sample and holder were outgassed for several hours at temperatures between 500°C and 600°C prior to annealing. The sample was then heated quickly to just below 900°C, followed by several "flashes" (lasting several seconds at elevated temperatures) to temperatures as high as 1200°C or 1250°C. In each flash, the pressure was monitored and heating was discontinued when the pressure exceeded ~ $10^{-9}$ torr. This procedure was repeated until a few "flashes" above 1200°C could be maintained for several seconds with the pressure remaining below $3 \times 10^{-9}$ torr. The sample was then cooled quickly (within a few seconds) to ~ 950°C, followed by slow cooling (15°C per minute) through the (7x7) phase transition region (about 830°C) to about 650°C, followed by quicker cooling (decrease of the heating current to zero over a period of a few minutes). The sample was allowed to cool undisturbed to nearly room temperature before mounting on the louse for STM analysis. One sample was annealed at low temperature (about 900°C) for several minutes and cooled similarly slowly. The results of this experiment are also discussed later in this chapter. Following the initial annealing and cleaning process, it was found to be sufficient to quickly heat by flash-annealing and quickly cool the samples to remove adsorbed contamination (which can collect over a period of hours or days with storage at typical vacuum pressures) and obtain a well-ordered and clean (7x7) reconstruction. The surfaces which resulted from these quick anneals were only slightly less well-ordered than the initial surfaces.

*Tip Preparation and Cleaning*

The tips used in this study were primarily ac-etched 20 mil diameter tungsten tips. The tips were rinsed with water and ethanol prior to vacuum introduction. These tips are known[38] from SEM studies to have a gross radius of curvature of ~ 1000 Å and a 10° half-angle. A few dc-etched tips were also used; the radius of these tips is ~ 100 Å and the half-angle is 6°. No mechanically prepared tips were tried and no other tip materials were tested.

The tips typically did not provide atom-resolved images upon initial tunneling approach. The tips usually required controlled crashing by oscillating the tip into the surface, or needed to be "pulsed" before high quality atomic resolution could be obtained. The former process involved deliberately setting the feedback's time constant at a small enough value to induce feedback oscillation, leading to tip-surface contact. This procedure presumably either removes the surface oxide on the tip remaining after etching or causes the tip to pick up silicon atoms. The latter method involved raising the bias voltage to a specified voltage (usually 10 volts) for a short "pulse" typically ranging μsec - msec in duration. This form of "field emission" was a reasonably reliable method of regaining atomic resolution after "catastrophic" tip changes.

The ac-etched tips were found to be more stable under repeated scanning than their dc-etched counterparts. This behavior was probably due to the larger aspect ratio of the ac-tips which imparted them with a more robust structure. The ac-tips were also more amenable to the "crashing" and "pulsing" procedures than the dc-tips. The dc-tips suffered invariably from a high frequency of tip changes and rarely provided high quality atom-resolved images. In a few cases, tips heated *in vacuo* to ~ 600°C, in an attempt to

remove surface oxides, were tested. These tips provided neither a higher frequency of successful atomic resolution imaging nor fewer tip changes during STM scanning. Scanning electron micrographs of the heated tips did not show any appreciable differences caused by heating. Further efforts are being made in our labs to investigate tip cleaning procedures.

## *RESULTS AND DISCUSSION*

### *Step Pinning by SiC Islands*

Surface structural disorder, defined as any disruption of perfect order in the surface, influences a wide variety of surface thermodynamic and kinetic processes, surface electronic properties, and surface chemistry. The cleaning of surfaces is an example of the interrelationship of disorder and surface chemistry.[20] The long-range atomic order, smoothness, and cleanliness of the Si(111)-(7x7) surface are strongly dependent on the annealing/cleaning temperature.[39] Low-temperature anneals of Si(111) are known[20,40] to produce surfaces which typically possess poor long-range atomic order and cleanliness. Although temperatures as low as about 850°C are required to remove the native oxide layer on the silicon surface, considerably higher temperatures (1250°C)[20] are necessary to prepare clean and well-ordered (7x7) surfaces. At lower cleaning temperatures (below approximately 1200°C), carbon contamination remains evenly dispersed on the surface, disrupting the long-range atomic order.[41] The increased order at higher temperatures is probably due to the diffusion of carbon contamination, which coagulates into precipitates of silicon carbide (SiC), leaving surrounding regions extremely clean and well-ordered. The minimum temperature required for the removal of carbon contamination then is 1200°C, at which the diffusivity and

solid solubility of carbon in silicon are high enough to enable it to diffuse into the bulk and not precipitate as SiC at the surface.[42,43] The cleaning process of the Si(111)-(7x7) surface during annealing was observed directly by UHV-SEM.[40] These authors observed that oxygen was removed at temperatures above 700°C, the temperature at which a SiC layer started to grow on the surface. At 900°C, SiC coalesced into islands, which are removed only above 1200°C, the point at which the surface became smooth and clean. In addition, since the SiC islands which had acted as step pinning sites against step movement are removed, the wavy, curved steps straighten out and became regular and parallel. Care must also be taken to maintain the vacuum pressure low enough ($10^{-9}$ torr range) during sample heating to prevent contamination of the surface.

These observations described above were borne out in our STM experiments on Si(111). One silicon wafer was cleaned by a low-temperature annealing procedure:[44] heating at ~ 950°C for about 5 minutes at a pressure below $3 \times 10^{-9}$ torr. This low-temperature anneal was not sufficient to clean the surface of carbon contamination and provide long-range atomic order. The surface was found to contain a high concentration of contamination, presumably SiC, in the form of large islands. Figure 2 shows a representative STM image, 4000 Å on a side, of the Si(111) surface prepared in this manner. The surface is dotted with SiC islands, each ~ 50-100 Å in diameter and 50Å in height, often clustered in small groups. The SiC coverage of the silicon surface is ~ 1/3 monolayer. The islands are located almost exclusively at step edges and act as step pinning sites. At elevated temperatures, the silicon surface is "molten" and step flow is impeded by these large SiC clusters. This causes the steps to be curved following sample cooling. The step pinning and

island structures are shown at higher magnification in Figure 3, a STM image 500 Å on a side. The steps are arranged mainly in bunches of several steps, each of which is several atomic layers in height. The terraces between the steps and contamination were atomically flat, but not well-ordered. Figure 4 is a constant current STM image, ~ 130 Å x 100 Å in size, showing no clear or discernible (7x7) reconstruction. The image does not have an unreconstructed (1x1) arrangement either; the surface appears largely amorphous. Judging by the size and arrangement of the features, it is probable that the surface consists of silicon "adatoms" with a high density of vacancies. The reconstruction is inhibited, and the atomic order probably disrupted, by the presence of the SiC contamination. Silicon carbide contamination is known[41] to prevent atomic order and can inhibit reconstruction. Figure 5 shows an image obtained on a silicon sample that was subjected to a high-temperature anneal, heated to ~ 1200°C. However, the vacuum pressure was permitted to reach $10^{-8}$ torr during sample heating. As a result, the sample became contaminated, as evidenced in the STM image. Although a well-ordered (7x7) reconstruction was obtained, the surface was covered with a diffuse "spotting" of contamination of unknown composition (shown by the white cloudy features). This data illustrates the importance of maintaining a low vacuum pressure during heating, in order to prevent contamination and prepare clean silicon(111) surfaces. This contamination probably resulted from hydrocarbon "cracking" on the surface.[41]

***Step Bunching and Surface Slope***

Typically the samples were "flashed" several times to ~ 1250°C before slow cooling (approximately 15°C/min) through the (1x1) <--> (7x7) phase transition temperature of 830°C. These high-temperature anneals were

necessary to yield clean, well-ordered Si(111) surfaces, devoid of any gross contamination. No remaining SiC islands were observed on these surfaces. The surface exhibited a stepped, terraced structure; an example representative of the typical topographical appearance of the surface is provided in Figure 6. Figure 6 shows two different presentations of the same data: the left image is height-keyed where brightness corresponds to measured topographical height and the right image is slope-keyed where brightness corresponds to the local slope or derivative of the topography. The latter approach accentuates step structure; in this example, the steps are "lit" or highlighted from the left side of the image. In the (4000 Å)$^2$ image, the surface steps upward moving from bottom left to top right. The slope of the surface is attained through a combination of atomically flat terraces and large step bunches. The step bunches are well-ordered and oriented parallel to each other, separating the terraces, each of which is ~ 750 Å in width and fairly consistent in size. The main step bunches are typically between 10 and 20 Si(111) atomic double-layers high (each double-layer makes up a monatomic step 3.13 Å high), corresponding roughly to 30-65 Å in height. The terraces exhibit well-ordered (7x7) reconstructions, which are shown in a later section of this chapter. The upper terrace edges of the step bunches pass through the corner holes of the short diagonal of the (7x7) unit cell, as will be seen later in this chapter. There are few step kinks; those that are present are located on the small "zipper" steps which splinter off of and join the main step bunches. These "zipper" steps in fact suggest the way in which the step bunches form from the initial uniform distribution. The surface height varies, on average, about 275 Å over a lateral range of 4000 Å. The original slope (vicinal angle) of the sample, 4° ± 1°, is actually conserved upon stress-annealing. The sample

slope is determined by STM to be 3.9° ± 0.5°, analogous to a vicinal Si(111) surface with a corresponding miscut. The individual step bunches have a measured slope angle of 13° to 17°; recall however that the measured slope is a convolution of the actual step rise angle and the size and structure of the tip on that scale. The actual step rise angle is probably slightly larger than the measured slope. Cross-sectional linecuts through the topography of a typical area of the surface are shown in Figures 7 and 8. Figure 7 shows the surface contour as a function of lateral distance and surface height (corrugation) in Å. Figure 8 shows the same data, but now the lateral distance is plotted as a function of the number of Si(111) double-layer steps, each of which is 3.13 Å high.

The step bunches observed on these stress-annealed Si(111) surfaces are commonly seen on annealed samples with no external stress. It must be assumed then that the step bunches are more a result of the vicinal nature of the original sample than the stress applied during heating. Step bunches are known[20,45] to be associated with a morphological equilibrium crystal shape phase transition on vicinal Si(111). Si(111) miscut by a range of angles from 1.2 to 12° towards the [112] and [110] directions has been shown by LEED[45] to undergo a phase transition, in which the high temperature state is the (1x1) structure with uniformly separated steps and the low temperature state is one in which terraces of (7x7) structure coexist with facets (step bunches) of a specific orientation (~ 20° off [111]). Recall that the step bunches we measured in our experiments were oriented approximately 20° off [111], in agreement with the LEED studies performed on vicinal samples. The LEED observations were attributed to an equilibrium crystal shape phase transition, in which it becomes favorable at low temperatures to form facets of this orientation. The

resolution of LEED however was insufficient to determine the size of the terraces and facets. However, recent STM results[20,46] by Swartzentruber on vicinal Si(111) show that the facets exist as nearly uniformly spaced (terrace width ~ 750 Å) step bunches each of height ~ 10 steps, separated by sufficiently wide (7x7) terraces to maintain the nominal vicinal angle (2.5° in their case). Measurements on surfaces with different vicinal angles showed that the height of the step bunches remained relatively constant but that the width of the (7x7) terraces changed to accommodate the changes in the mean vicinal angles. This fact excluded the notion that there is a "magic" size[47] of the (7x7) terrace stabilized, for example, by strain, that controls the overall ordering in the Si(111)-(7x7) system. The appearance of the images obtained in their experiments was very similar to ours, except for the height of the step bunches. The extent of the step bunching on our stress-annealed Si(111) samples suggests that there exists very strong interactions between steps. This behavior however may be greatly influenced by the external stress. Recent UHV-reflection electron microscopy (REM)[48] and UHV-SEM[49] studies on resistively heated Si(111) samples suggest that step bunching may result from the resistive heating process. In the former study, they found that a reversible transformation from a uniform, monatomic-stepped surface to a step-bunched surface took place depending on the electric current direction and specimen temperature. Step bunching (or faceting) however has been observed on vicinal Si(111) surfaces by a variety of analysis techniques,[50,51] including those samples prepared by radiative heating,[52] i.e., without direct electrical current (dc) heating. Step bunching on these vicinal surfaces is then considered to be intrinsic. In the latter study, the authors observed that the dc-heating-induced step bunching depended on current direction and

temperature. The temperature dependence of the bunching-induced current direction on the vicinal surface was almost the same as that of nearly flat Si(111) surfaces[48] above the (7x7) <--> (1x1) phase transition temperature. An excellent overview on the subject of surface faceting on vicinal Si(111) and its relationship to the equilibrium crystal shape is given by Williams and Bartelt.[53]

*Effect of Cooling Rate on Step Orientation*

As mentioned previously in this chapter, it is known that the sample cooling rate through the phase transition temperature has a strong influence on the order of the resulting step orientation and structure (on vicinal surfaces) and of the (7x7) reconstruction on flat terraces. Slow cooling has been used for a number of years in LEED studies,[20,54] producing surfaces with a minimum of diffuse scattering. Williams and coworkers[55,56] have thoroughly explored the effect of temperature and cooling rate on the step structure and ordering of the (7x7) structure. They found that the rate of cooling through the (1x1) <--> (7x7) phase transition at ~ 850°C, where changes in step structure occur,[57] is the most crucial. It was also observed that the (7x7) reconstruction is strongly correlated across monatomic steps on slowly cooled Si(111) surfaces, where nearly all of the single-height steps exhibit the same displacement of the (7x7) reconstruction across step edges.

It can be expected that the step order and orientation of vicinal silicon(111) surfaces, even when stressed, would differ according to the cooling rate through the phase transition temperature. As evidenced in Figure 6, slow cooling rates produce parallel, well-ordered and oriented step bunches of consistent height and spacing, with few kinks and "zipper" steps. However, on samples cooled rapidly (> 100°C/sec), the step bunches are much

less regular, less consistent in height, less well-oriented, and the surface contains a greater density of kinks, smaller steps and "zipper" steps. An example of this phenomenon is provided in the image shown in Figure 9. The (4000 Å)$^2$ image, again shown in both height-keyed (left) and slope-keyed (right) presentations, illustrates vividly a marked difference in step structure and surface appearance compared to that contained in Figure 6. The magnitude and direction of the surface slope is similar, but the appearance is quite different.

***Effect of Current Direction Reversal***

The effects of electromigration and current direction on the step structure of Si(111) surfaces subjected to dc-current resistive heating have been studied using UHV-SEM.[49] The authors observed that the direction of current flow was important in determining the slope direction of step bunching (whether the steps "step up" or "step down"). They also observed the spreading ("fanning out") of large step bunches into their individual components. That is to say each of the step bunches were spread out into a larger number of finer, smaller-height steps by the action of the dc current. In addition, the (7x7) terrace widths also decreased in size. This phenomenon is presumably due to the collective electron momentum (electromigration) from the large currents (on the order of 10 A for typical sample resistivities) usually used during resistive sample heating.

A detailed illustration of electromigration effects is provided in a comparison of Figures 10 and 11. Figure 10 shows a typical (4000 Å)$^2$ STM slope-keyed image acquired on a sample subjected to "forward" current. This image is similar to that shown in Figure 6, where the dc-heating current has been applied in the same direction as the slope, causing the steps to "bunch

up," with the same average terrace widths and step bunch heights. The effect of reversing the direction of applied dc-heating current is illustrated in Figure 11, another (4000 Å)$^2$ slope-keyed STM image. On this sample, the dc-current used for resistive heating was directed in the "reverse" direction, opposite to that used initially to form the step bunches. By applying the current against the slope of the step bunches, the step bunches are effectively "fanned" out into a larger number of smaller steps. A greater number of "zipper" steps is also present. The terrace width is consequently reduced and the height of individual step bands is decreased. The overall slope of the sample however is conserved at ~ 4°. Cross-sectional linecuts comparing the slope and appearance of this image, with "reverse" current, to those for a sample with "forward" current, are provided in Figure 12. Although the appearances of the two stepped surfaces differ, the overall slopes of the samples are quite similar, showing that the slope is conserved upon reversing the direction of the dc-heating current. The step bunches are spread out into a greater number of substeps with a concurrent decrease in the terrace width. The average terrace width is reduced from about 750 Å to 200 Å, and the average step bunch height from roughly 60 Å to 20 Å. The individual terraces still contain well-ordered (7x7) reconstructions.

***Atom-Resolved Imaging of Unfilled States***

It has been shown[4,23] that the appearance of the Si(111)-(7x7) reconstructed surface is markedly different in STM imaging experiments depending on the polarity of the sample bias. That is to say the unit cell structure and geometry vary with the direction of tunneling, and depend on whether the direction of the tunneling current (and the tunneling electrons) is from tip-to-sample (positive sample bias) or sample-to-tip (negative sample

bias). This phenomenon exists because the electronic states of the surface that are being probed in each case are markedly different; the former case presumably probes the spatially-localized unfilled surface states of the (7x7) surface while the latter case probes the filled surface states.[24]

An example of a constant current STM image of the Si(111)-(7x7) surface, acquired at a positive sample bias, is shown in Figure 13. The image was obtained on a flat terrace between step bunches on an area similar to that shown in Figure 6. The image is 140 Å in $x$ by 160 Å in $y$, and a tunneling current of 1 nA and a sample bias of +2.5 V were used. Therefore, the unfilled states of the surface are probed. The atom-resolved (7x7) adatom pattern is clearly visible, and the corner holes (dark round circles) are pronounced. The short diagonal between corner holes is measured to be 27 Å and the long diagonal between corner holes, bisecting the (7x7) unit cell, is 47 Å. There are also several vacancies (missing adatoms) in this area of the surface. The threefold symmetry is visible, as are the twelve adatoms of the diamond-shaped (7x7) unit cell. The two triangular subunits of the unit cell appear to be the same height at this bias voltage and polarity. A pronounced asymmetry due to the stacking fault is visible at negative sample biases; the unfaulted half appears higher than the faulted half. This asymmetry observed at negative bias is shown in the following thesis section. A close-up, detailed view of the Si(111)-(7x7) structure, acquired with a higher pixel density, is provided in Figure 14. The constant current image is ~ (50 Å)$^2$ and reveals the complex adatom arrangement of the (7x7) unit cell. The unfilled states of the unit cell are shown in a top-view colorscale image in Figure 15. A single diamond-shaped unit cell is outlined, the four corners located at the corner holes. A slight asymmetry is visible in this image acquired at +2.0 V;

the left triangle is slightly higher (brighter) than the right triangle. The left triangle therefore is the unfaulted half of the outlined unit cell. A cross-sectional linecut through the long diagonal of a typical (7x7) unit cell is provided in Figure 16. The data again shows unfilled surface states. The linecut extends slightly beyond the corner holes (47 Å apart) and cuts through the intermediate adatoms. No asymmetry is discernible in this image at this bias. The measured atomic corrugation in this data, from adatom top to corner hole bottom is nearly 1.5 Å, suggesting that the tip was fairly sharp. A comparison of "dull" and "sharp" tips for similar linecuts is provided later in this chapter.

*Atom-Resolved Imaging of Filled States*

The filled (or occupied) surface electronic states of the (7x7) reconstruction is probed at negative sample biases in STM experiments on Si(111). At negative biases, the geometric asymmetry between the two triangular unit cell subunits, the faulted and unfaulted halves, becomes pronounced. In addition, the overall appearance of the reconstruction and the unit cell changes dramatically. Most noticeably, the diamond shape of the unit cell becomes more evident. We found it more difficult in general to obtain high-quality atomically resolved images at negative sample biases than positive sample biases.

Figure 17 provides an example of a typical STM constant current image of the Si(111)-(7x7) reconstructed surface taken at negative sample bias. This image, approximately (175 Å)$^2$ in size, reveals selectively the filled states of the sample. Although a number of vacancies and displaced Si adatoms are visible, the (7x7) unit cell is dominant. At this sample bias, -2.0 V, the unit cell asymmetry is noticeable. A close-up view of a couple of (7x7) unit cells is

provided in Figure 18, a cropped version of Figure 17. The alternate left-pointing triangles are slighter higher topographically (and brighter in the presentation) than the right-pointing triangles. The left-pointing triangles are the unfaulted halves of the (7x7) unit cells. A cross-sectional linecut along the long diagonal of these unit cells is shown in Figure 19. The overall atomic corrugation is nearly 2.0 Å peak-to-valley, suggesting a very sharp tip structure. The asymmetry of the unit cell is also evident; the left (or unfaulted) half is 0.3-0.5 Å higher than the right (or faulted) half.

***Atom-Resolved Barrier Height Imaging***

The Si(111)-(7x7) reconstructed surface was also imaged in the barrier height mode. In this mode, the z-piezoceramic was modulated at 1 kHz approximately 1 Å p-p while the tunneling current response was monitored. This imaging technique is described in detail in chapter 1. Barrier height imaging yielded consistently high-quality atom-resolved data on the (7x7) surface. In fact, it was found that atomic resolution was easier to obtain in the barrier height mode than in the standard constant current imaging. This is due to the fact that our barrier height images are frequency-limited through the use of a lock-in amplifier, making them less susceptible to noise interference. As a result, barrier height images are typically quieter and provide greater contrast than constant current images. For the most part, the two imaging modes give qualitatively similar images in appearance.

An example comparing a constant current image to a barrier height image is provided in Figure 20. The images are ~ (60 Å)$^2$ in size; the constant current image is shown at left, the barrier height image is at right. In both cases, raw data are shown. Greater contrast and apparent lateral resolution are afforded by the barrier height image. It is interesting to note that some

"vacancies" in the constant current image appear as peaks of diminished size (relative to the surrounding adatom lattice). These features are probably not true vacancies, but rather reacted adatoms (reacted with either hydrogen or oxygen). The barrier heights over the adatoms are maxima, and are minima over the corner holes; therefore, the two imaging modes exhibit the same contrast polarity over surface features. The barrier height maxima are typically about 2.8-3.0 eV; this value is slightly lower than the bulk electron work function of *p*-Si(111), which is determined to be about 4.6 eV from photoelectric measurements.[58] The measured barrier height was correlated to the condition (cleanliness?) of the tip, being highest following tip pulsing, when the tip was presumably clean. The barrier heights obtained with poor (dirty?) tips were as low as 100 meV. A cross-sectional linecut through a long diagonal of Figure 20 is shown in Figure 21. The barrier height reaches 2.8 eV over adatoms and decreases to 2.0 eV over the corner holes.

***Fourier Transform Power Spectrum***

The two-dimensional Fourier transform power spectrum of the Si(111)-(7x7) reconstructed surface provides information about the periodic nature of the surface. The 2-D power spectrum can be directly compared to diffraction patterns, such as those from LEED. A discussion of the significance of the power spectrum in providing structural information about atomic arrangement and periodicity is included in a similar section using GaAs in chapter 3.

Figure 22 provides a typical 2-D power spectrum for the Si(111)-(7x7) surface. The bright spots in the figure show the power (intensity) of spatial frequency components contained within the image being analyzed. The outermost 7th order Fourier components (faint dots in a hexagonal pattern)

indicate the periodicity of the underlying bulk Si(111)-(1x1) surface. The 3rd and 4th order components are strongest, as is found in transmission electron diffraction (TED) and LEED experiments. These components correspond to the presence of double-spaced atoms within the unit cell, i.e., the adatoms.[18]

***Line Fault Defects: Observation and Theory***

Although vacancies and displaced adatoms are common, line or edge defects have rarely been reported in STM experiments of the Si(111)-(7x7) surface. There is in fact only one report[59] of the observation of a line fault defect on Si(111). Unfortunately, a degradation of the tip prevented the authors from studying the detailed structure of the single defect they observed. In fact, they were unable to find the extent of the fault in order to determine its origin. Here we present the observation and discussion of a similar line fault defect.

Line fault defects were observed on four separate occasions in our STM studies on stressed Si(111). We will concentrate our discussion in this section on our best-resolved and most interesting line fault defect. Figure 23 is a (1000 Å)$^2$ constant current STM image of the Si(111)-(7x7) reconstructed surface, slope-keyed to accentuate step structure. Two large step bunches (facets) running vertically in the image are seen at the center and the right. The (7x7) unit cell mesh is clearly visible on the flat terraces. The "ribbed" appearance of the facet at the center is suggestive of the presence of multiple tunneling points. There is an interesting double-height step structure, with several kinks of unit cell width, located at the upper left of the image. The very top left of the image is magnified with higher pixel density in Figure 24. The top left of the image in Figure 23 is reimaged with greater pixel resolution in this ~ (200 Å)$^2$ top-view, slope-keyed constant current STM

image. Moving from bottom to top in the image, the double-height step at bottom experiences a kink of unit cell width, which causes the step to split into two single-height steps (each of these steps is 3.13 Å in height). Associated with the step kink is a line fault defect in which an extra row of adatoms is inserted into the normal (7x7) adatom structure (see white arrow in Figure 24). The fault line corresponds to an adatom registry shift of one bulk unit cell, which is 6.65 Å, in addition to the extra adatoms. This causes the corner holes along the fault line to be extended by 6.65 Å in width. The extra adatoms have the same heights as the unfaulted halves of the unit cells, which are the left-pointing triangular subunits in the images. The extra adatoms consequently have an unfaulted registry with the underlying bulk atoms. This observation suggests that the junction between the faulted and unfaulted halves of the unit cells lies between the extra adatoms and those adatoms directly above those adatoms in the images. The (7x7) reconstruction is seen to continue right to the step edge; in fact, the upper step edge passes through the corner holes of the (7x7) reconstruction. It is interesting that the structure grows undisturbed to the step edges, since these regions have been shown to be areas of considerable stress.[13] This indicates that the (7x7) structure is indeed firmly bonded. A cross-sectional linecut through the step edge is provided in Figure 25. The "doublet" step structure above the step kink in Figure 24 is analyzed by a cross-sectional linecut. The linecut reveals that each of the steps is indeed monatomic (consisting of a silicon double-layer), 3.13 Å high. The (7x7) reconstruction is seen again to persist essentially undistorted right up to the edge of the step and exists even on the intermediate step terrace, which is only ~ 20 Å wide. This observation indicates that the reconstruction itself depends on very short-range, local

interactions.[60] In addition, in contrast to the upper step edges, which pass through the corner holes, the lower terraces all have the same termination adjacent to step bunches. There is always a single additional atomic row inserted into the structure. The slope-keyed ("lit" from the right) solid-modeled presentation of Figure 24, shown in Figure 26, accentuates the detailed structure of the step. The double-height step and the step kink, leading into the splitting of the two individual monatomic steps, are visible. Also visible are the individual silicon(111) atomic layers which compose the steps. Therefore, four silicon atomic layers are discernible for the double-step and two silicon layers are seen for each of the single-height steps. Although this may be the result of a multiple tip, this would represent the first report of the imaging of the individual silicon layers which compose the steps of Si(111). The line fault defect observed in Figures 24 and 26 is explained by a structural model, a modified version of the DAS model, proposed by Hadley and Tear.[59] In this model, shown in Figure 27, the unfaulted half of the unit cell is extended by one bulk unit cell (6.65 Å) to include the extra row of adatoms. The extra row of adatoms is terminated at the extended corner hole by the formation of a dimer in the third atomic layer and by an extra dangling bond on one of the dimerized atoms. There is a subsequent increase in the areal density of dangling bonds by about 10% in the region of the interface over that of the normal (7x7) reconstruction. This increase in the surface free energy must be "stabilized" in some way; otherwise it is unfavorable that such a faulted reconstruction would exist. The line fault is either:[59] (i) stabilized by contamination, (ii) formed at the meeting of two independently growing (7x7) regions, or (iii) initiated upon cooling by some defect structure and then propagated as the (7x7) reconstruction grows. While Hadley and

Tear were unable to make a conclusion with sufficient certainty because they could not see the fault's origin, we can make such a conclusion. The first choice is unlikely since no significant surface contamination is observed in the vicinity of the fault. The second is also unlikely since the fault is well-ordered; therefore, it is quite improbable that two randomly and independently growing (7x7) regions just happened to meet at this point. The most probable mechanism is the last, since we have visual evidence of the fault's origin. The uniquely high local strain in the step kink region forces the surface to adopt a different structure, one in which an extra row of adatoms is added to the reconstruction. This conclusion is consistent with the fact that each of the line fault defects we observed (four in total) originated from a step kink. It is also possible however that such a defect may also be stabilized by the local electric-field distribution and the induced change in the surface potential or by strain fields associated with the multiple-step edges.[54] The fact that we observed several of these line faults, which are rarely seen on unstressed samples, suggests that the line defects may have resulted from the externally applied stress.

***Current Imaging Tunneling Spectroscopy (CITS)***

The technique of current imaging tunneling spectroscopy (CITS) provides spatially-resolved electronic state information about surfaces. This is accomplished by obtaining current-voltage (*I-V*) spectra at selected points during constant current STM image acquisition. In this way, in addition to the constant current topograph, one can build up current images (analogous to constant height images) at any bias voltage contained within the bias ramp used in the *I-V* spectra. The current images obtained in this manner directly reflect the spatial distribution of surface states without interference from

geometric structure considerations. The technique is described in detail in chapter 1.

The double-height step edge, shown in Figures 24 and 26, is analyzed using CITS in Figure 28. This CITS series includes: at upper left, the constant current topograph at +2.0 V sample bias; at upper right, the current image at +2.0 V; at bottom left, the current image at +1.0 V; and at bottom right, the current image at -2.0 V. Consequently, all of the images, except that at the bottom right, reveal the unoccupied states of the surface. In the topograph, protrusions are bright and depressions are dark; in the current images, bright features correspond to regions of high current and dark features to regions of low current. This technique indeed permits both the unfilled and filled surface states of the sample, anywhere within the voltage scan range, to be studied simultaneously. The energy dependence of surface states is evident; there are several adatoms which have presumably reacted that are more prominent at a specific energy (bias voltage) than at others. The left-pointing triangular subunits are the unfaulted halves of the unit cell, as seen in the image taken at negative sample bias.

***Multiple-Tipping Effects***

The structure (and sharpness) of the probe tip is of primary importance in STM imaging experiments. These tip characteristics in fact determine, to a large extent, the observed appearance of a surface, especially in atom-resolved imaging. The sharpness of the tip dictates the measured atomic corrugation, and consequently, whether or not atoms can be resolved. The overall shape of the end of the tip (which contributes to tunneling) is also essential in obtaining high-quality images, especially on rough samples or surfaces with large and/or high topographic features. It is on these types of samples that

multiple tips and tip aspect ratio come into play. The latter characteristic has a profound effect on the observed slope and sharpness of large step edges and sharp features. The former characteristic often leads to confusing and/or poor-quality images, especially involving atom-resolved images. Multiple tips or tunneling points can "smear out" atomic features and corrugation, and can produce false "ghosting" (doubling or multipling) of image features. The probability of multiple tipping increases with surface roughness or with step height.

Two examples which illustrate the effect of multiple tipping on the appearance of the Si(111)-(7x7) surface are provided in Figure 29. The images are each ~ 80 x 130 Å and were obtained in the barrier height imaging mode. The images show a couple of different patterns which can result from the contribution of multiple tunneling points to a STM image. The patterns bear little resemblance to the familiar (7x7) adatom reconstruction. The patterns resemble those reported by Nishikawa *et al.*,[61] who studied variation in images of Si(111)-(7x7), and correlated their observations with tip structure determination using field ion microscopy (FIM). The problem of multiple tipping is especially important to consider when the surface structure of the sample is not known with certainty.

Multiple tipping is also evident in the large-scale image of the (7x7) surface shown in Figure 30. The contribution of multiple tunneling points, probably separated by considerable distances, is seen in this (500 Å)$^2$ slope-keyed constant current image. Although the (7x7) unit cell mesh is visible on the large terraces, it is only "clear" and well-resolved (with good corrugation) on the three small terraces adjacent to the main step bunches. It is only in these regions that the tunneling tip is probably a single point. The large step

bunches cause other regions of the tip to contribute to tunneling, therefore blurring the atomic pattern on the large terraces. A surface with high and/or sharp surface features provides a good test of the sharpness and quality of a STM tip. The step bunches on our silicon samples were indeed a good test for evaluating tip quality. Multiple tipping is more probable with such step bunches of large height. Examples are provided in the next section.

***Evaluation of Tip Quality***

The large atomic corrugation of the Si(111)-(7x7) reconstructed surface provides a good test for evaluating the sharpness of the STM probe tip in resolving atomic-sized features. The peak-to-valley (adatom top to corner hole bottom) corrugation with a "sharp" tip can be as high as 1.5 Å or 2.5 Å, while that with a "dull" tip is typically less than 1.0 Å. Cross-sectional linecuts for the long diagonals of the (7x7) unit cells acquired with qualitatively "sharp" and "dull" tips are shown in Figure 31. The sharper tip (solid line) indeed provides a larger measured atomic corrugation than the dull tip (dashed line). The corrugation for the sharp tip is nearly 1.5 Å peak-to-valley while that for the dull tip is less than 1.0 Å.

The large step bunches on our stressed Si samples also provide an excellent test for evaluating overall tip sharpness (aspect ratio) and the presence of multiple tips. With a sharp tip, the step edges should appear sharp without "ghosting" or step "ribbing" (multiple tipping at step edges), and there should be well-resolved (7x7) on the terraces. These issues were discussed in the previous section of this chapter. Tip changes during scanning, caused primarily by unstable tip structures, are also undesirable. Tip changes for two slope-keyed constant current STM images of Si(111)-(7x7) are shown in Figure 32. The top image was acquired using a positive sample

bias, the bottom image using a negative sample bias. In each case, a tip change in the middle of the image brings about a significant decrease in atomic corrugation, and consequently, in image contrast. Even a small tip change (minor atomic reorganization which exhibit no significant z-change) can result in a dramatically different image appearance. In fact, the corrugation and atomic resolution can almost completely disappear as a result of a tip change. These images illustrate the importance of using a stable, sharp tip in order to obtain atom-resolved images. It was found that tip pulsing could often induce significant changes in tip structure, and consequently, in image contrast and symmetry. The tip was often pulsed until a stable tip, which provided symmetric atom-resolved images with good corrugation and a lack of obvious multiple tipping, was obtained. This condition usually corresponded with a high measured barrier height; a high barrier height is often associated with a clean tip.

## *CONCLUSION*

We have reported here the first STM imaging study of stress-annealed vicinal Si(111) samples. The surfaces were characterized by large flat terraces separated by oriented and parallel step bunches or facets. These step bunches, composed typically of ~ 15-20 individual steps (~ 50-65 Å) in height, were evenly spaced, separated by atomically flat terraces ~ 750 Å in width. The original slope of the 4° vicinal miscut Si(111) wafer was conserved following the stress-anneal; the sample slope was determined by large-area STM imaging to be 3.9° ± 0.5°. The flat terraces exhibited well-ordered (7x7) reconstructions, which continued essentially undistorted to the step edges. The termination of both the upper step edges and the lower terraces adjacent

to step bunches was consistent. The step edges passed through the corner holes of the (7x7) reconstruction along the short diagonal and the terraces terminated with an additional set (one row) of atoms between the step bunches and the corner holes.

The quality of the surface and the facet orientation depended strongly on the preparation of the sample. On samples subjected to low-temperature anneals, the surface was covered by silicon carbide islands which acted as step pinning sites. The intermediate terraces exhibited largely amorphous adatom arrangements. Samples cooled rapidly through the (1x1) <--> (7x7) phase transition temperature showed considerably less step ordering, the facets having a larger concentration of step kinks. In addition, the steps were less parallel and less evenly spaced than on samples with slow cooling. Electromigration effects on step structure was also observed. Step bunches were seen to spread out into a larger number of component substeps upon reversal of the direction of the heating current used for dc-resistive sample heating. Although the overall slope of the sample was conserved, both the height of steps and the width of terraces decreased as a result of current direction reversal.

Filled and unfilled states of the Si(111)-(7x7) reconstructed surface were imaged selectively with atomic resolution by STM in UHV. This was accomplished by choosing the polarity of the sample bias, and consequently, the direction of tunneling. The difference in surface appearance between the occupied and unoccupied states was evident in the STM images, especially the unit cell asymmetry which was prominent in the images acquired at negative sample bias (occupied states). The unfaulted half of the unit cell appeared 0.3-0.5 Å higher than the faulted half in these images. In addition, atom-resolved

barrier height images were obtained, with barrier heights of ~ 3 eV over the adatoms. Barrier height images, because they are bandwidth-limited, typically provided cleaner, quieter images than standard constant current topographs. A current imaging tunneling spectroscopy (CITS) image of the surface was shown, illustrating the power of this technique in obtaining spatially resolved spectroscopic information. A two-dimensional Fourier transform power spectrum of a STM image of Si(111)-(7x7) was discussed in terms of the structure and common spatial frequencies of features on the surface. The information in this technique is analogous to diffraction patterns, such as those in LEED experiments.

A rarely observed line fault defect on the Si(111)-(7x7) surface was shown. The detailed atomic structure of this defect, located at a step kink, was discussed. At the step kink, an additional row of adatoms was inserted into the (7x7) pattern, extending the corner holes by one bulk unit cell. A structural model,[59] based on a modified version of the DAS structure, explaining this line fault was described and evaluated. The origin of this defect was determined to be the local strain imposed by the step kink, rather than contamination stabilization or the random meeting of (7x7) regions. This conclusion was further substantiated by the observation of several other line faults, each of which originated from a step kink. A stressed Si(111) wafer seems to be, from our studies, an easy way of preparing samples with line defects. It would be interesting to compare the reactivity of such defect sites to normal adatom sites of the (7x7) surface.

Lastly, we discussed the image degradation caused by multiple tipping and evaluated tip quality using our highly stepped silicon surfaces. Unfortunately, tip preparation remains a "black art," with sharp, high-quality

tips obtained only through trial-and-error. As evidenced by our examples, it would be time-saving if stable and sharp tips could be routinely prepared. Further efforts toward manufacturing and cleaning tips are definitely needed.

**Figure 1**

The dimer-adatom-stacking fault (DAS) model for the Si(111)-(7x7) reconstructed surface, developed by Takayanagi,[2,3] consists of a diamond-shaped unit cell containing 12 adatoms, lying atop underlying atoms known as rest atoms. The unit cell is divided into two asymmetric triangular-shaped halves, an unfaulted and a faulted half. In the unfaulted half, the surface adatoms lie directly above underlying third-layer atoms, while those on the faulted half are offset relative to each other. As a result, the unfaulted half is slightly higher than the faulted half. The corners of the unit cell are bounded by large vacancies known as corner holes. The short distance between corner holes is 26.9 Å and the long diagonal of the unit cell is 46.6 Å. The adatoms are identified by position as either center or corner adatoms. Steps on the (7x7) surface are 3.13 Å high and consist of two silicon atomic layers.

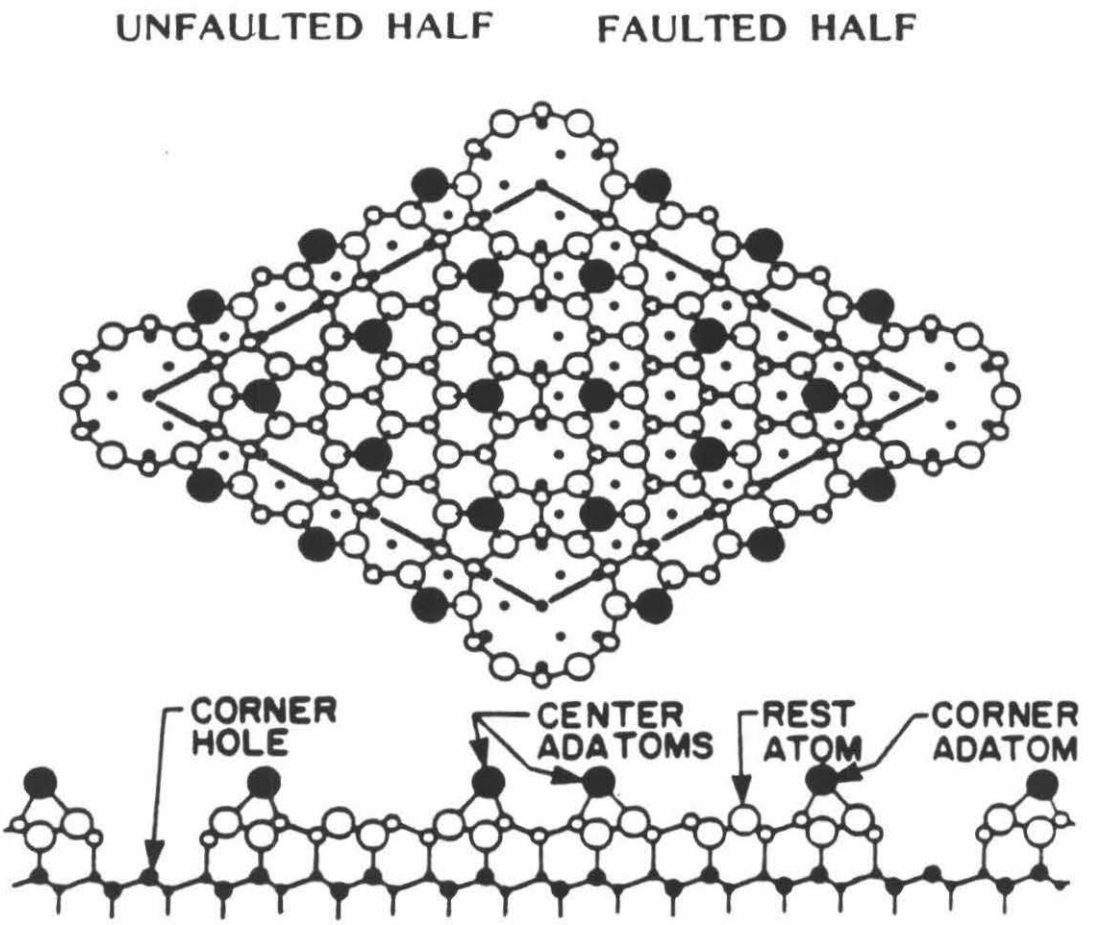
UNFAULTED HALF
FAULTED HALF
CORNER HOLE
CENTER ADATOMS
REST ATOM
CORNER ADATOM

**Figure 2**

A constant current STM image of a Si(111) wafer subjected to a long duration low-temperature anneal. The image is ~ 4000 Å on a side and shows step pinning by silicon carbide islands. Silicon carbide clusters, originating from the coagulation of carbon contamination, impede step flow at elevated temperatures, resulting in the curved step structures. Each of the SiC islands is ~ 50-100Å in diameter and ~ 50 Å in height. An image of the same sample acquired at higher magnification is provided in Figure 3.

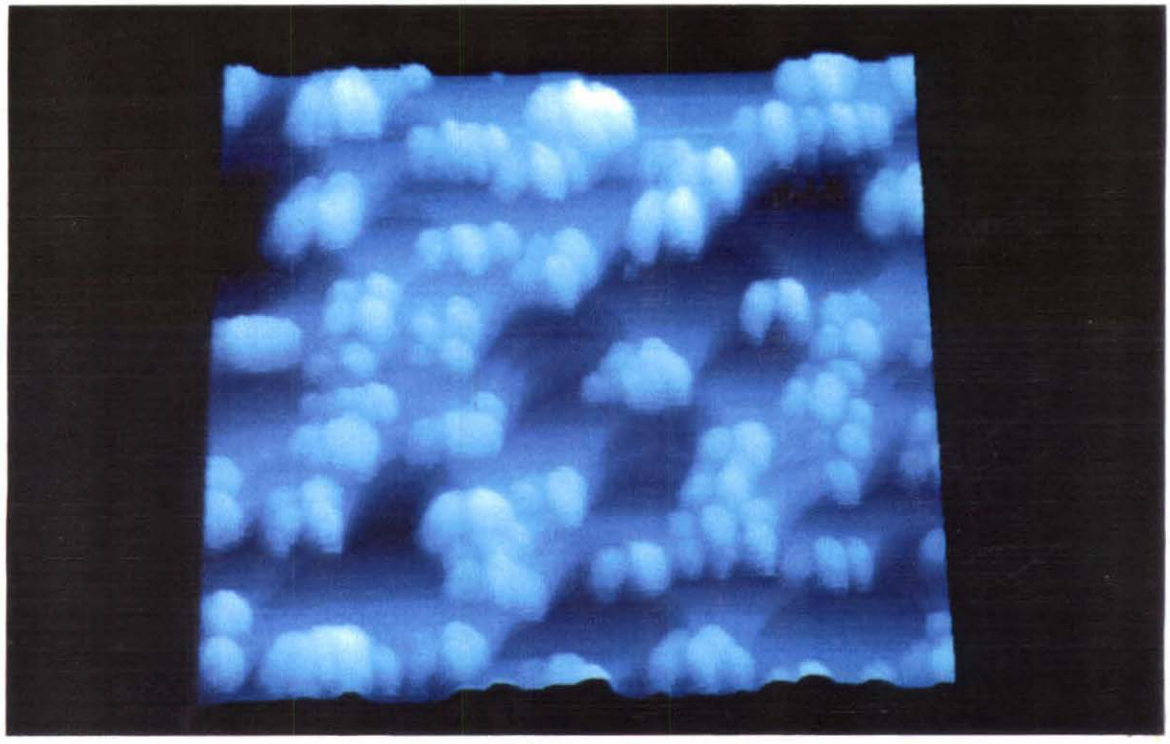

**Figure 3**

A different area of the same sample used for the image in Figure 2 is shown here at higher magnification. This image is (500 Å)$^2$ and shows the step pinning and SiC island structures with greater detail. The terraces between the multiple-height steps and islands are atomically flat. An image taken on one of these terraces is shown in Figure 4.

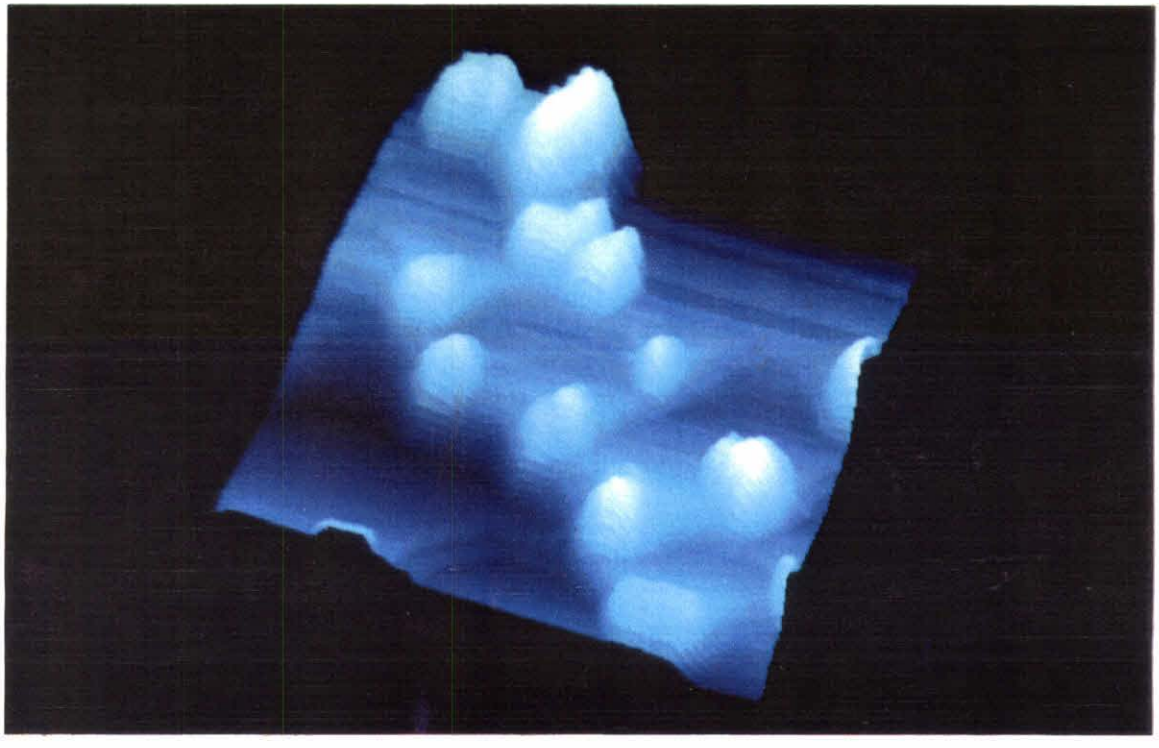

**Figure 4**

A constant current STM image acquired on one of the atomically flat terraces of the contaminated, low-temperature annealed silicon sample, as shown in Figures 2 and 3. This image, ~ 130 x 100 Å, shows a largely amorphous atomic arrangement with no clearly discernible reconstructed (7x7) or unreconstructed (1x1) structure. The atomic disorder and high density of vacancies is probably induced by the presence of SiC contamination.

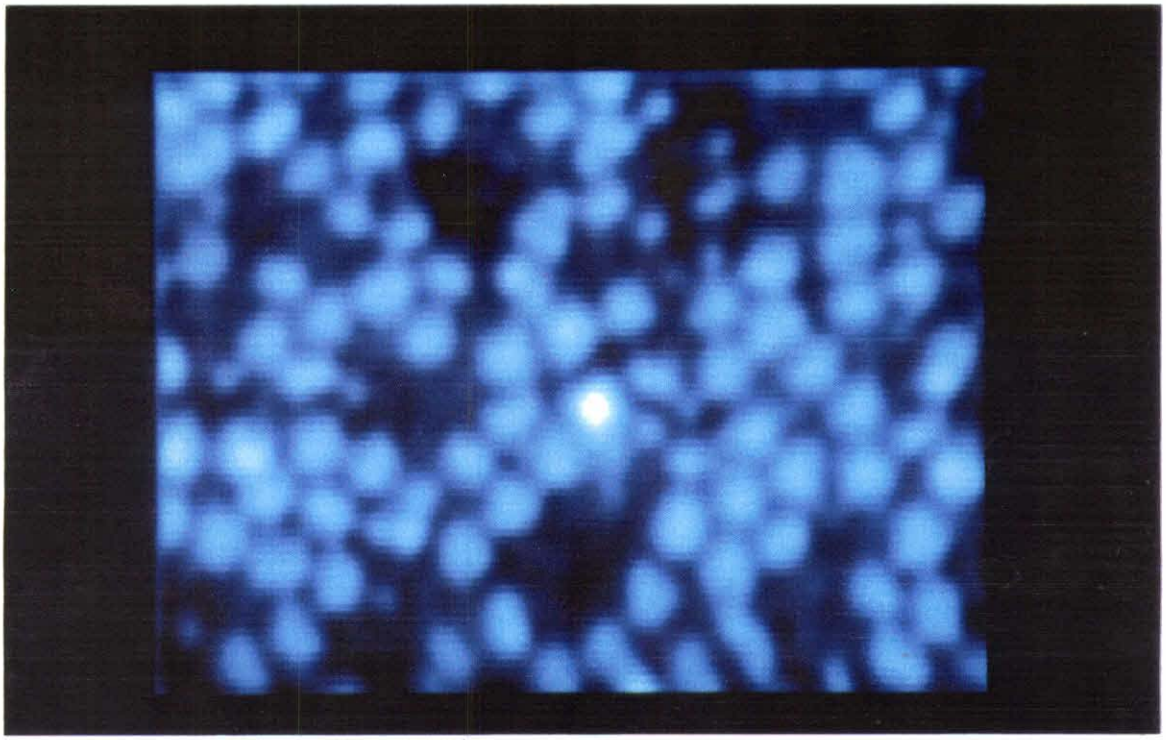

**Figure 5**

The effect of allowing the vacuum pressure to reach unacceptably high levels during high-temperature sample annealing/cleaning of a silicon(111) wafer is illustrated here in this (270 Å)$^2$ constant current STM image. The sample was heated to ~ 1200°C, sufficient to provide a well-ordered (7x7) reconstruction, but the pressure reached the $10^{-8}$ torr range during heating. This resulted in contamination of the surface, evidenced here by the diffuse cloud-like features which obscure the familiar (7x7) pattern. The probable origin of the contamination was hydrocarbon "cracking" on the surface.

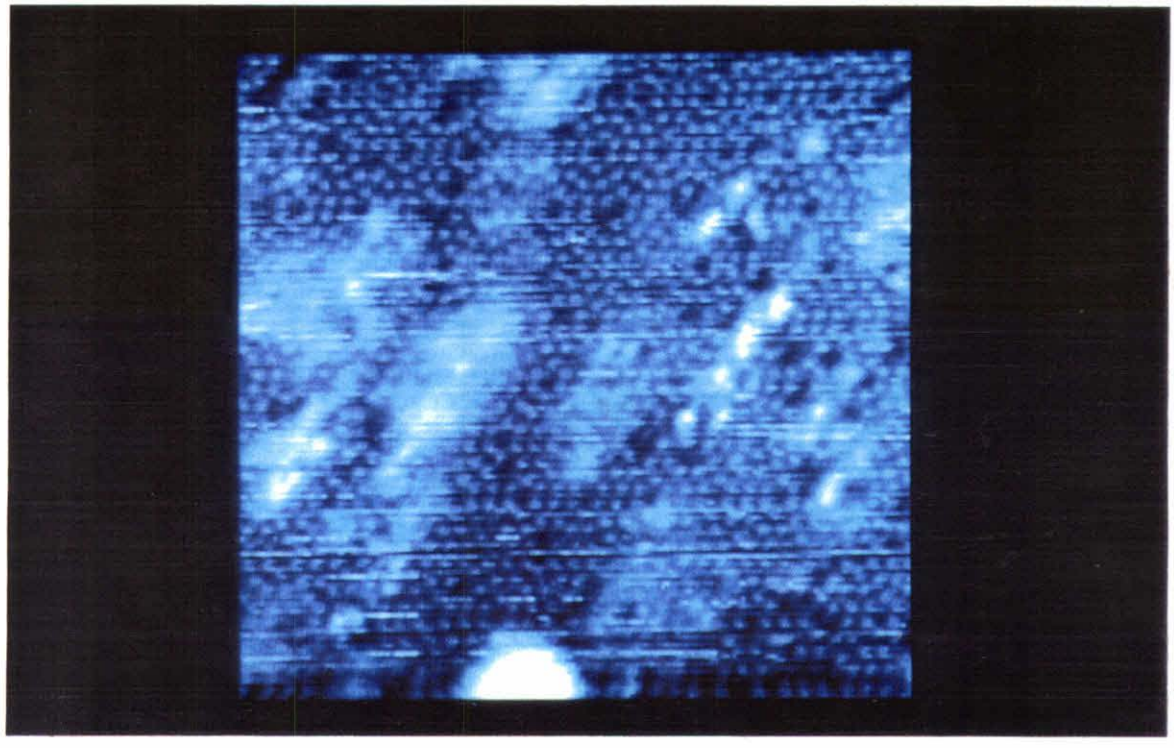

**Figure 6**

The formation of parallel, oriented step bunches (or facets) on a stress-annealed Si(111) sample heated to 1250°C is illustrated in this (4000 Å)$^2$ STM image. The left presentation is height-keyed, where brightness corresponds to topographical height, and the right image is slope-keyed, where brightness corresponds to local surface slope (derivative) and highlights step edges. The steps are seen to rise upward moving from the lower left of the image to the upper right. The step bunches are each composed of approximately 15 to 20 individual monatomic steps (each monatomic step is composed of a silicon double-layer which is 3.13 Å high). The intermediate terraces are atomically flat and exhibit well-ordered (7x7) structure. The overall slope of the surface is 3.9° ± 0.5°. Smaller "zipper" steps are seen to join the main step bunches. Cross-sectional linecuts taken through a similar set of data are shown in Figures 7 and 8.

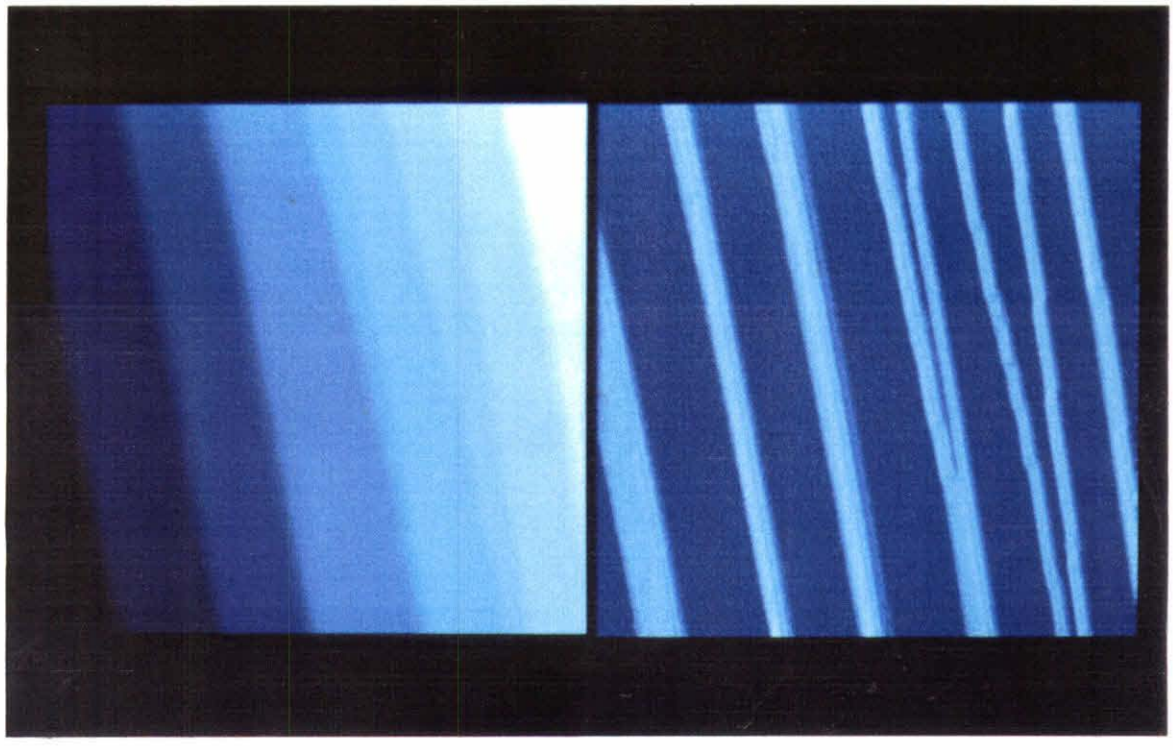

**Figure 7**

A cross-sectional linecut through a typically stepped surface of the stress-annealed Si(111) sample is shown here. The overall slope in this data is ~ 3.8°. The step bunches are uniformly spaced at roughly 750 Å intervals and are each about 50 to 60 Å in height. The slope of the individual facets is about 20° off the (111) orientation. The surface contour is plotted as a function of lateral distance and surface height.

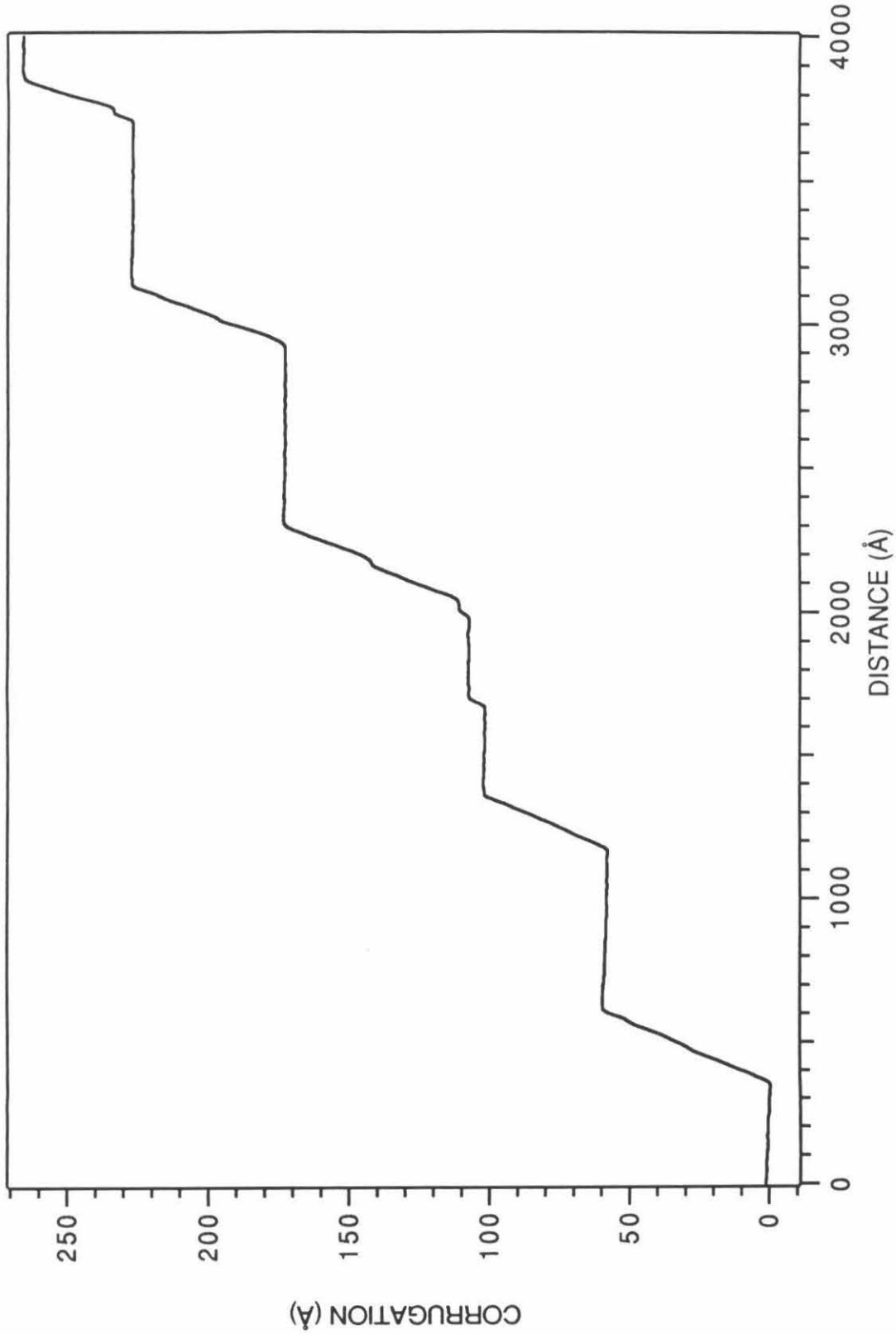
CORRUGATION (Å)
250
200
150
100
50
0
0
1000
2000
3000
4000
DISTANCE (Å)

**Figure 8**

The cross-section from Figure 7 is reproduced here, but is now plotted as lateral distance versus the number (#) of steps in height. The step bunches are typically between 15 and 20 steps in height and exhibit fairly sharp edges, indicative of a relatively sharp tip. Recall that the measured step shape in STM is a convolution of the actual step topographical shape and the tip shape and size.

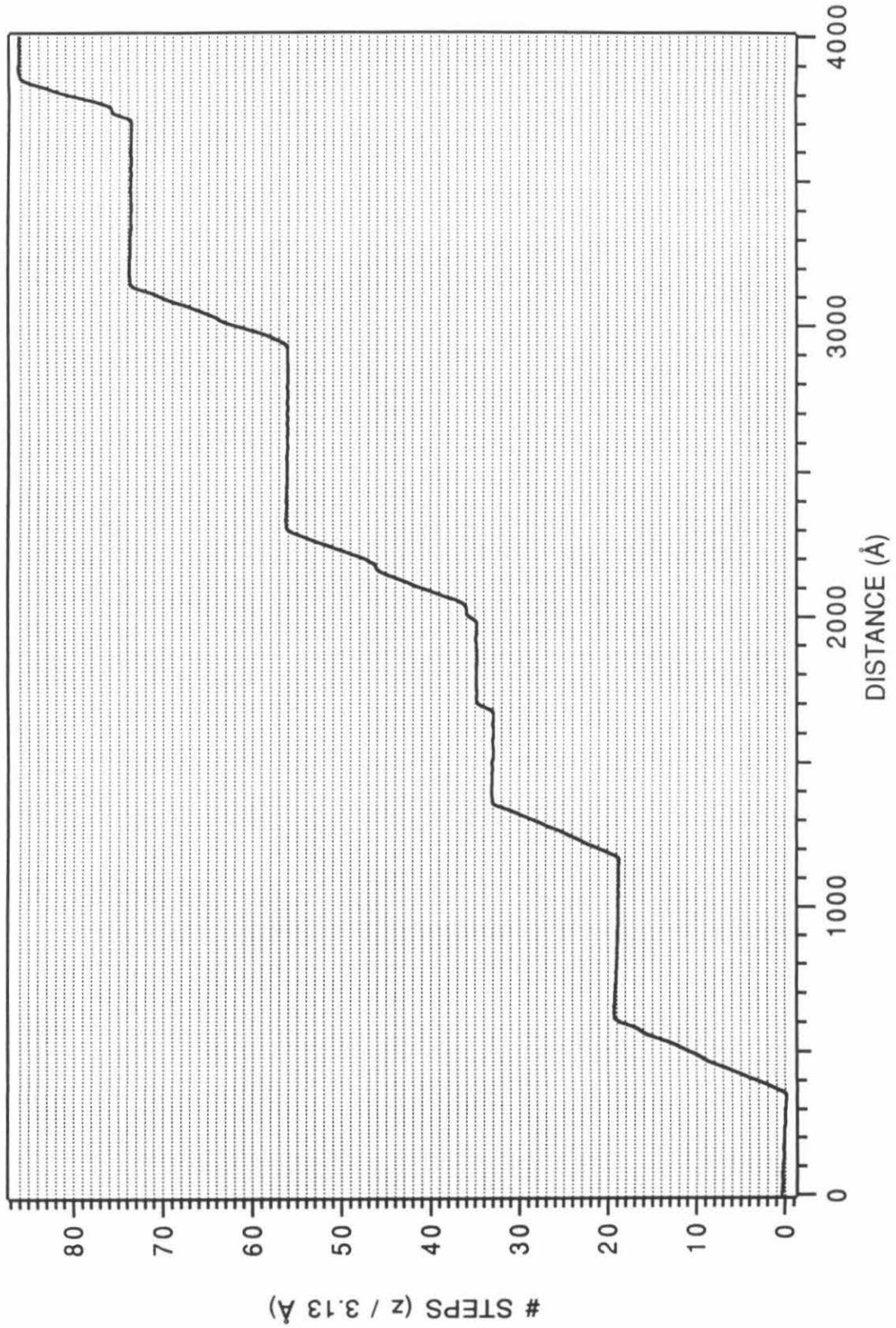
# STEPS (z / 3.13 Å)
0
10
20
30
40
50
60
70
80
0
1000
2000
3000
4000
DISTANCE (Å)

**Figure 9**

The Si(111) sample imaged here was subjected to a rapid rate of cooling (> 100°C/sec) after "flash" annealing to 1250°C. This (4000 Å)$^2$ image is shown in both a height-keyed (left) and a slope-keyed (right) presentation. The rapid cooling causes the step structure to be less ordered than that seen on slowly cooled samples. The step bunches are less clustered (greater spreading), and are less straight and regular. They are not as parallel, exhibiting less orientation and a greater density of step kinks. In addition, the terrace width (step bunch spacing) is less consistent.

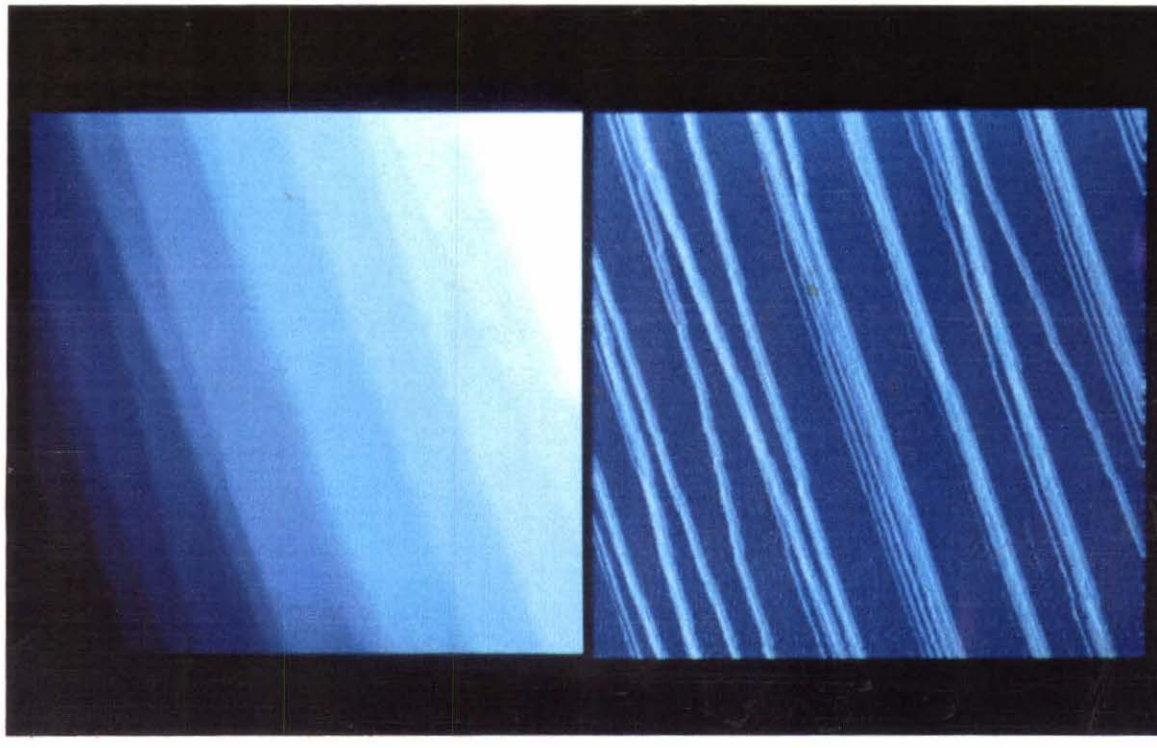

**Figure 10**

This slope-keyed (4000 Å)$^2$ STM image shows the typical appearance of the surface topography of Si(111) annealed with a dc-current applied in the "forward" direction; the "forward" direction is defined as the direction of local slope or vicinality. In this case, the electromigration causes the steps to "bunch up." This image is similar to that shown in Figure 6. An example of "reverse" dc-current direction is shown in Figure 11.

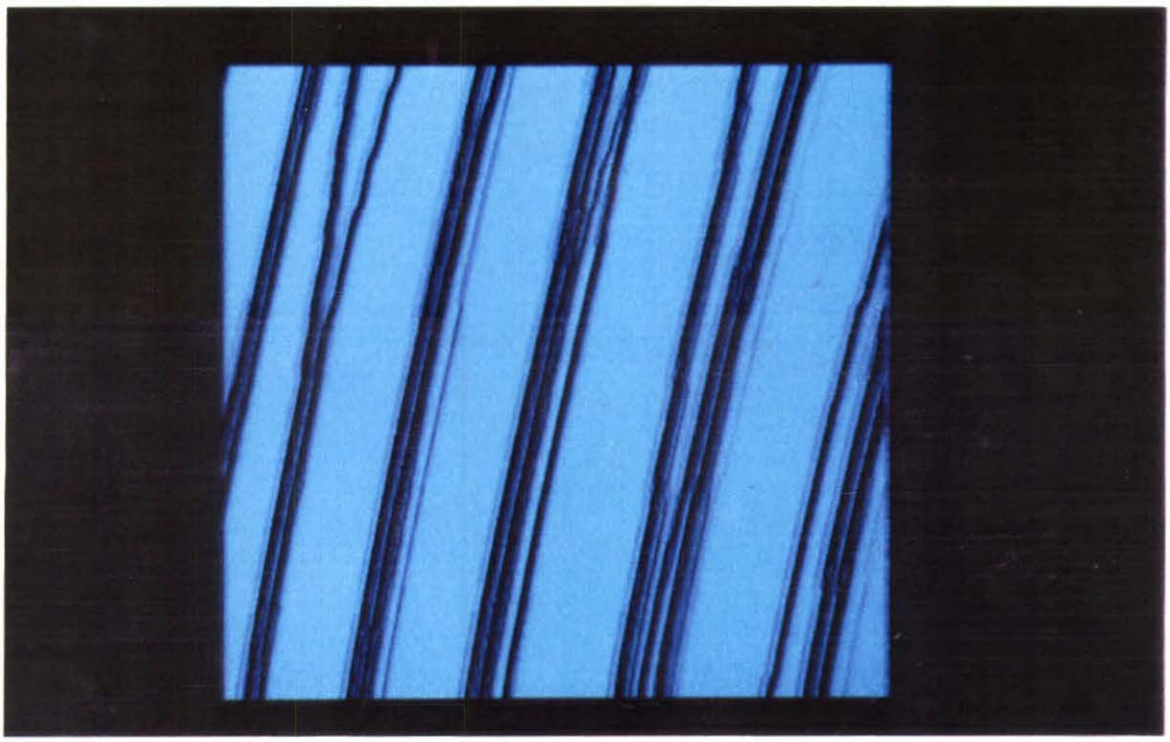

**Figure 11**

The effect of reversing the direction of applied dc-heating current is illustrated in this (4000 Å)$^2$ slope-keyed STM image. On this sample, the dc-current used for resistive heating was directed in the "reverse" direction, opposite to that used to form the step bunches initially. By applying the current against the slope of the step bunches, the step bunches are effectively spread out into a greater number of finer substeps. A greater number of "zipper" steps is also present. The terrace width is consequently reduced and the height of individual step bands is decreased. The overall slope of the sample however is conserved. Cross-sectional linecuts comparing the slope and appearance of this image with "reverse" current to those for a sample with "forward" current are provided in Figure 12.

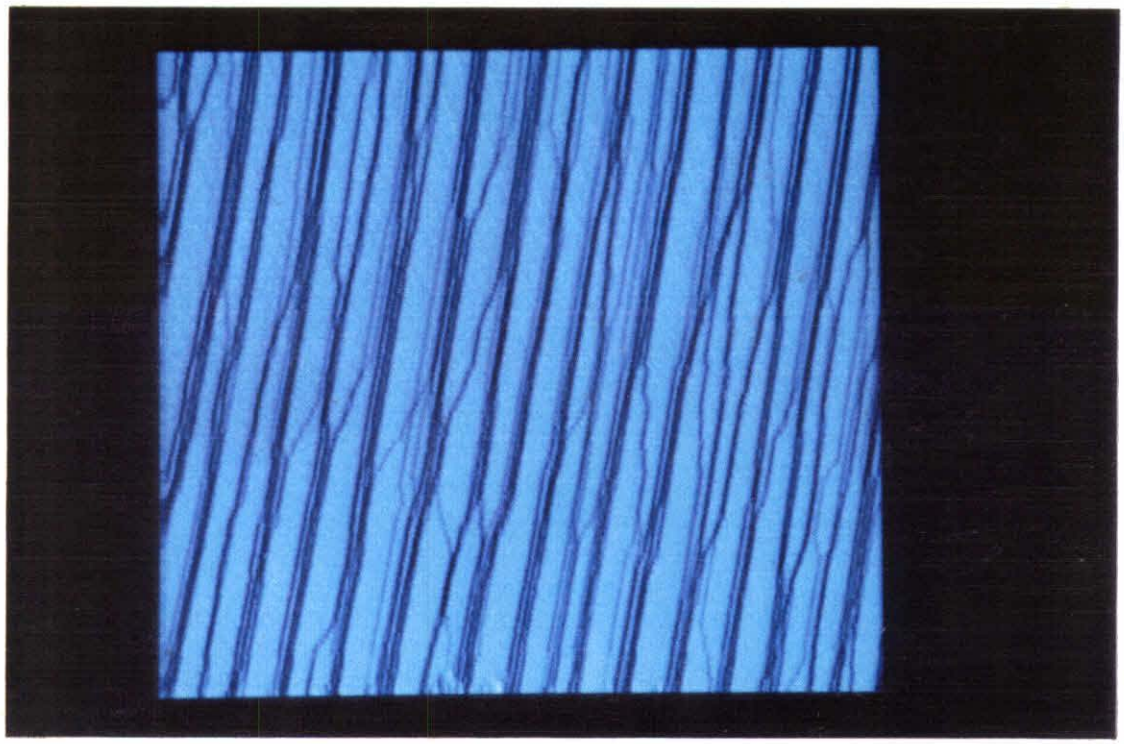

**Figure 12**

A cross-sectional linecut through Figure 11 is compared to a similar linecut for a typical "forward" current sample. Although the appearance of the stepped surfaces differs, the overall slope of the sample is conserved upon reversing the direction of dc-heating current; the slope remains ~ 4°. The step bunches are fanned out into a greater number of smaller steps with a concurrent decrease in the terrace width. The average terrace width is reduced from ~ 750 Å to ~ 200 Å, and the average step bunch height from roughly 60 Å to 20 Å. The individual terraces still contain well-ordered (7x7) reconstructions.

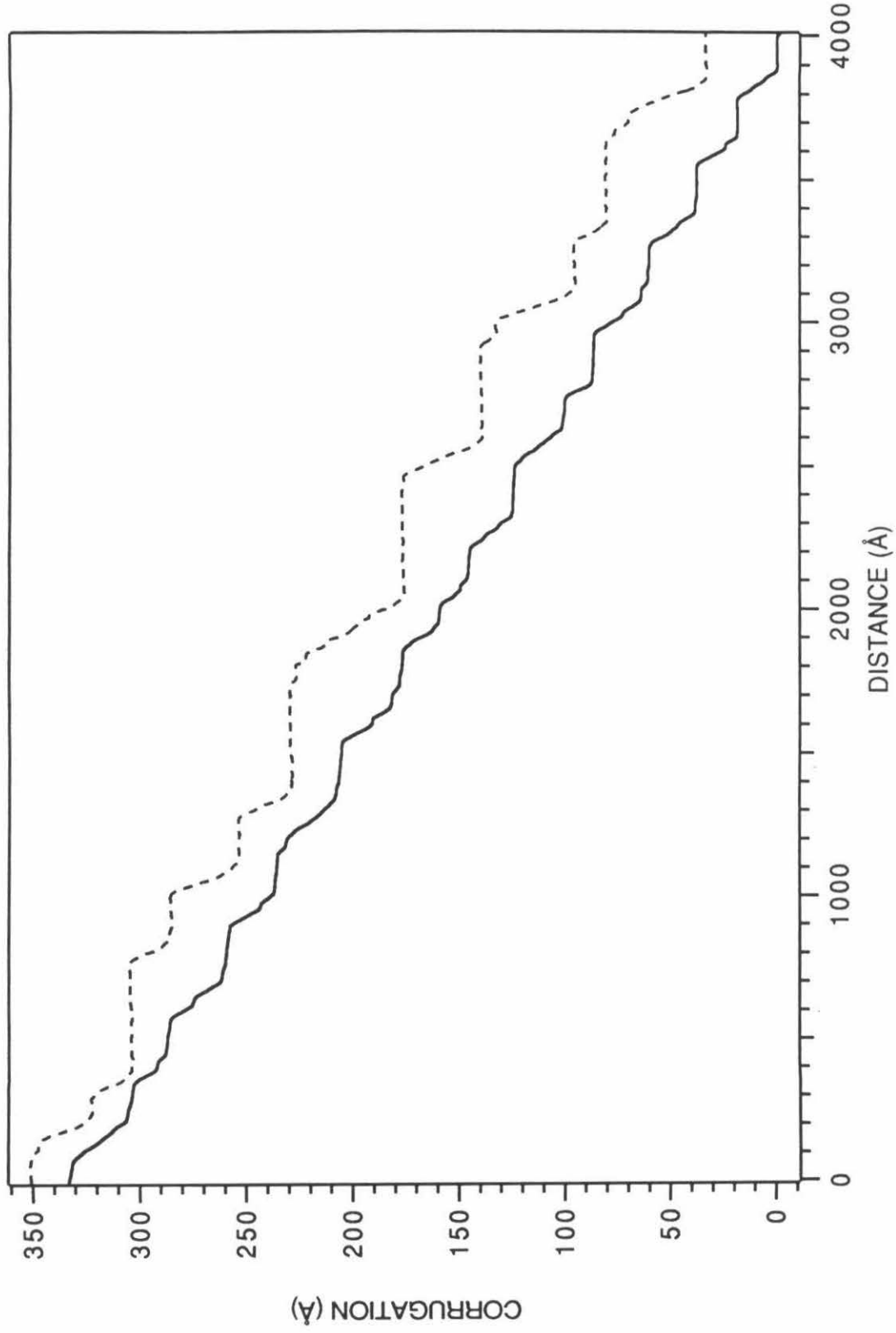
CORRUGATION (Å)
350
300
250
200
150
100
50
0
0
1000
2000
3000
4000
DISTANCE (Å)

**Figure 13**

The unfilled (unoccupied) electronic states of the Si(111)-(7x7) surface are probed at positive sample biases. This 140 x 160 Å atom-resolved constant current STM image, acquired at a sample bias of +2.5 V, shows the well-known (7x7) reconstruction. The twelve adatoms which comprise the diamond-shaped unit cell are visible, as are the corner hole vacancies. The threefold symmetry of the (111) surface is evident. The short diagonal between corner holes is 27 Å in length and the long diagonal, bisecting the triangular subunits, is 47 Å long. There are also several vacancies (missing adatoms) on this area of the sample. No visible asymmetry is observed between the two halves of the unit cell. The tunneling current was 1 nA. A close-up image, with higher pixel resolution, is provided in Figure 14.

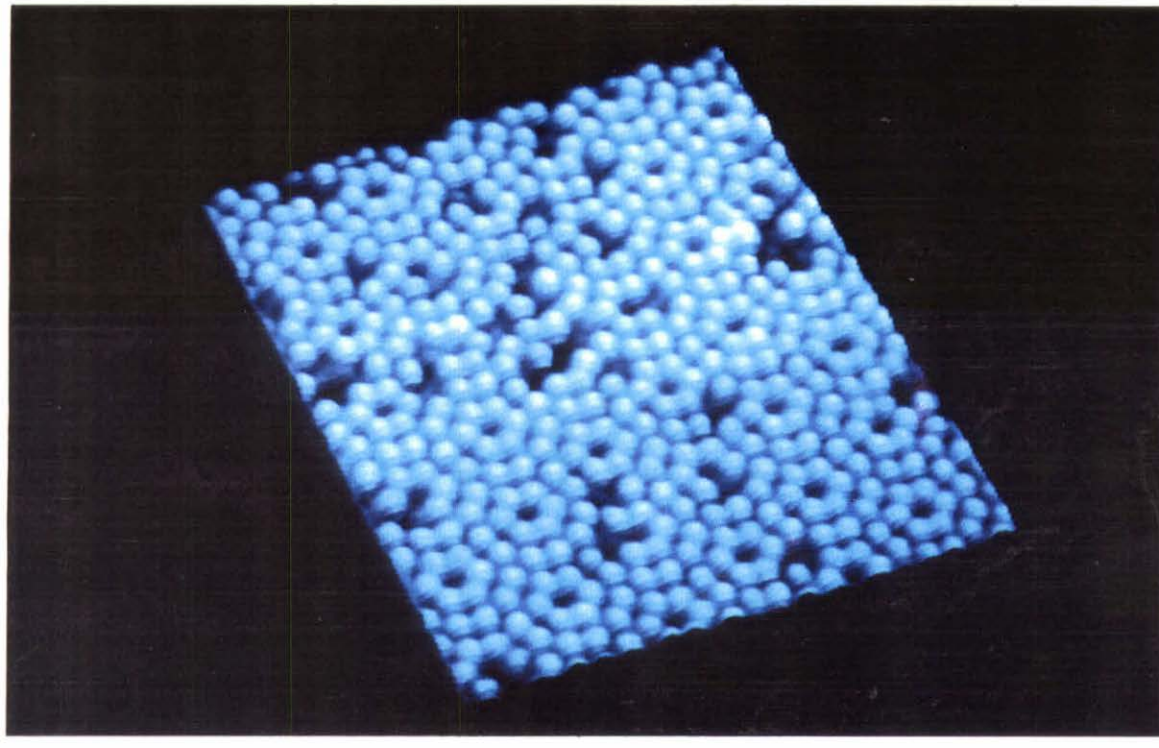

**Figure 14**

The complex arrangement of adatoms in the (7x7) reconstructed Si(111) surface is shown in this (50 Å)$^2$ constant current image. The image is similar to that shown in Figure 13 (acquired with a positive sample bias), but is taken with a higher data pixel density. The twelve adatoms appear as round bright features, and the corner holes are the dark, round depressions. Again, no unit cell asymmetry is visible. Figure 15 provides a top-view image outlining a single (7x7) unit cell and exhibits an asymmetry between the faulted and unfaulted halves of the unit cell.

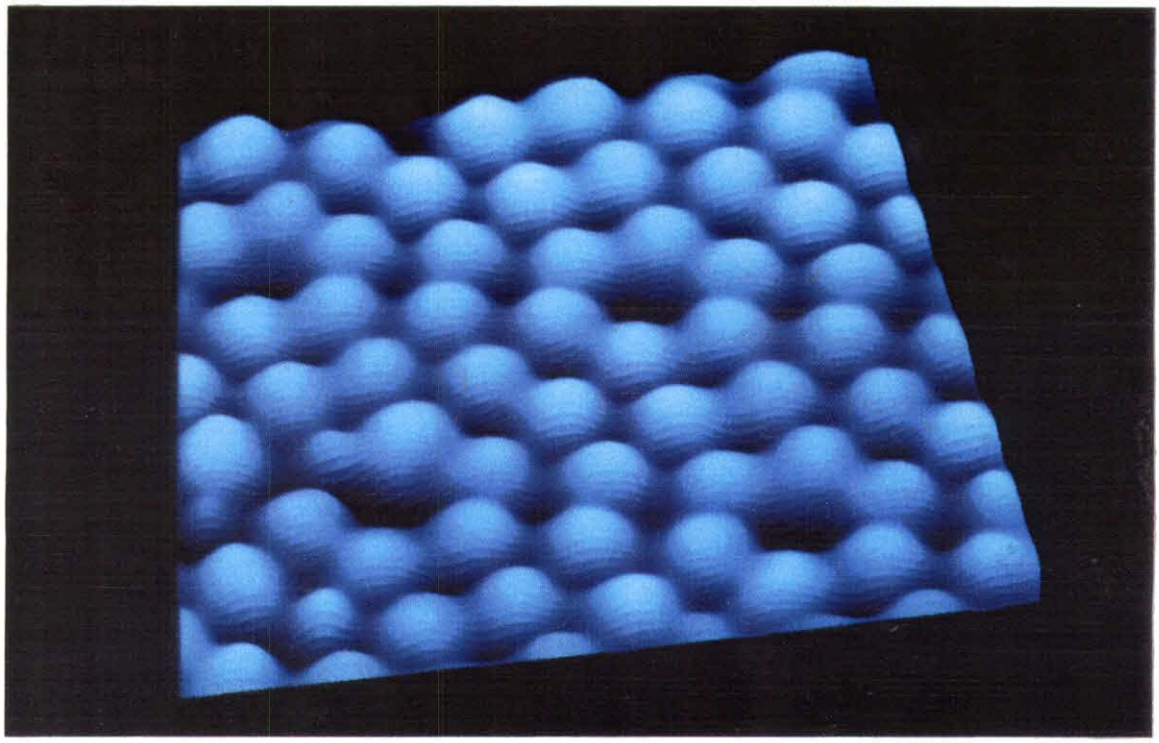

**Figure 15**

A single unit cell of the (7x7) reconstruction is outlined in this colorscale, top-view presentation. The constant current image shows topographically high areas (adatoms) as bright yellow and low areas (corner holes) as dark blue. The image was obtained using a positive sample bias; unfilled states are selectively probed. The diamond-shaped unit cell and its twelve adatoms are outlined. The two triangular subunits appear asymmetric in height. The left triangle is slightly brighter than the right triangle; the left triangle is the unfaulted half, which is slightly topographically higher. The asymmetry is more pronounced at negative sample biases.

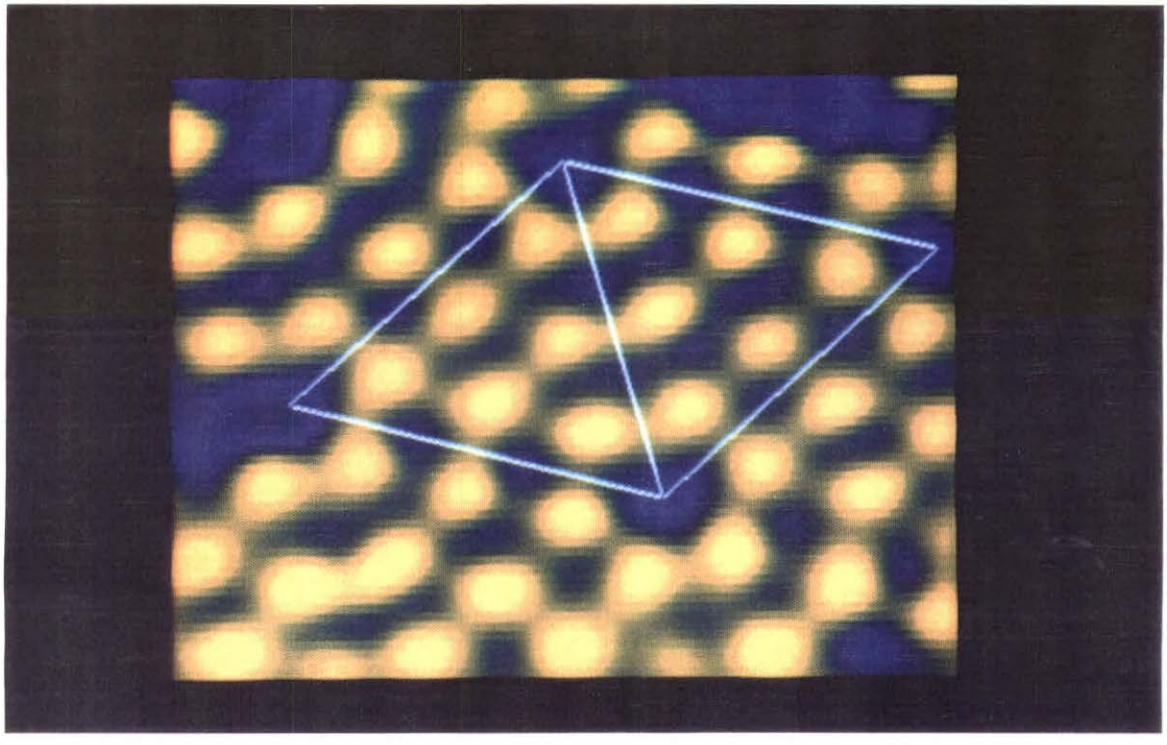

**Figure 16**

A cross-sectional linecut through a typical Si(111)-(7x7) unit cell is shown here. The linecut lies along the long diagonal of the unit cell, bisecting the triangular subunits and intermediate adatoms, and extends slightly beyond the corner holes (which are separated by 47 Å). The positive sample bias used here probes the unfilled surface states. The atomic corrugation is measured at nearly 1.5 Å peak-to-valley, indicating a fairly sharp tip. The cross-section at these tunneling parameters shows no obvious unit cell asymmetry.

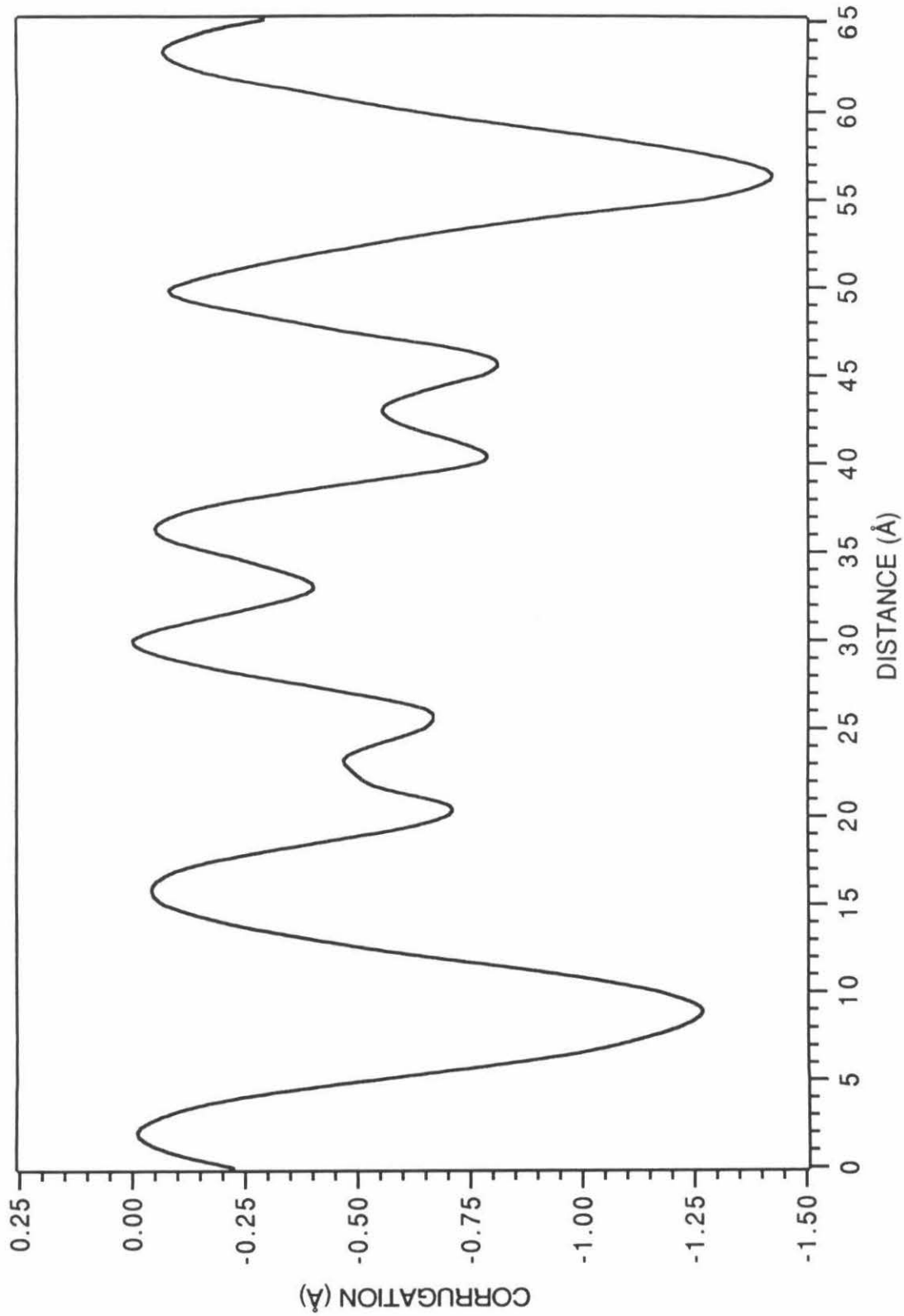
0.25
0.00
-0.25
-0.50
-0.75
-1.00
-1.25
-1.50
CORRUGATION (Å)
0
5
10
15
20
25
30
35
40
45
50
55
60
65
DISTANCE (Å)

**Figure 17**

An example of a typical STM constant current image of the Si(111)-(7x7) reconstructed surface acquired with a negative sample bias. This image, approximately (175 Å)$^2$ in size, reveals selectively the filled states of the sample. Although a number of vacancies and displaced Si adatoms are visible, the (7x7) unit cell is dominant. At this sample bias, -2.0 V, the unit cell asymmetry is noticeable. A cropped version of this image is shown in Figure 18.

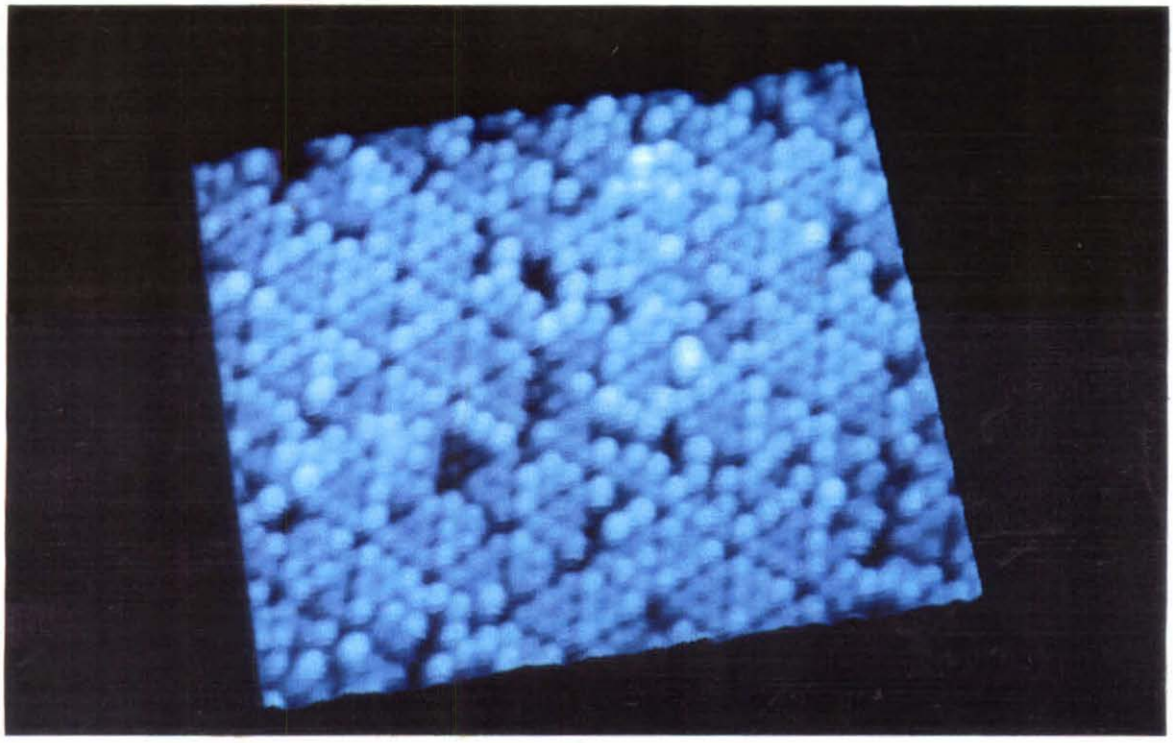

**Figure 18**

A close-up view of a couple of (7x7) unit cells is provided here, in a cropped version of Figure 17. The alternate left-pointing triangles are slighter higher topographically (and brighter in this height-keyed presentation) than the right-pointing triangles. The left-pointing triangles are therefore the unfaulted halves of the (7x7) unit cells, which are geometrically higher than the right-pointing faulted halves. A cross-sectional linecut through the long diagonal of the two unit cells is provided in Figure 19.

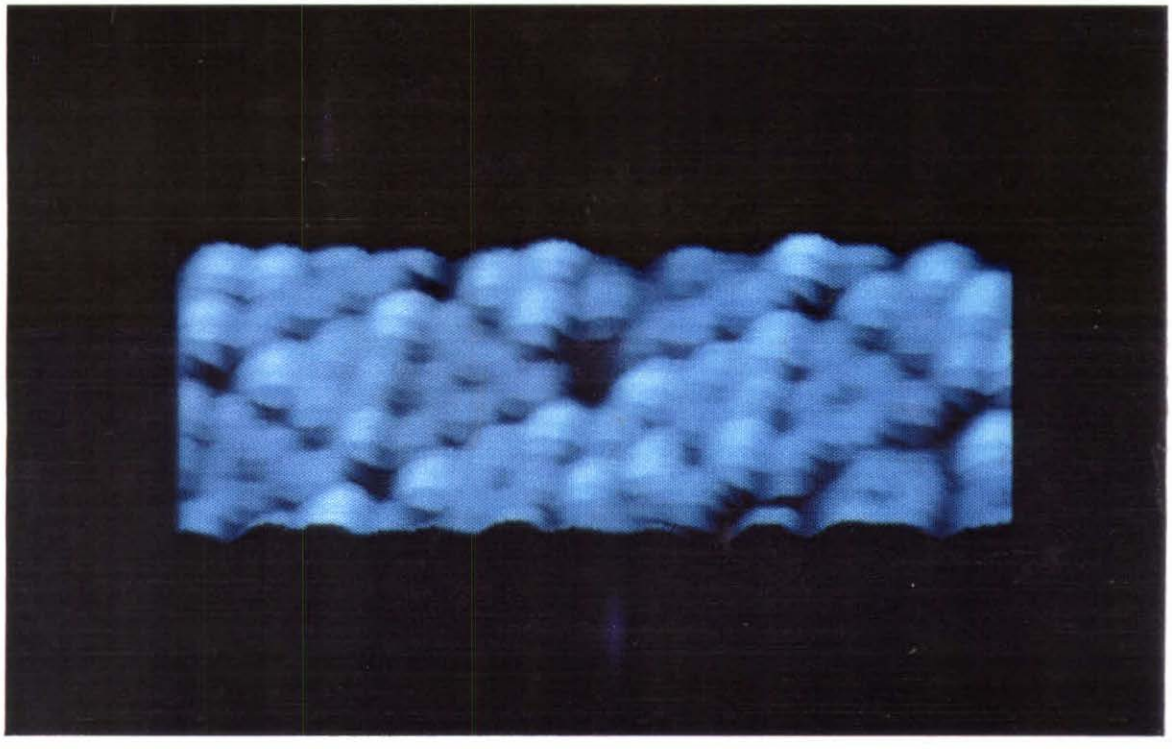

**Figure 19**

A cross-sectional linecut along the long diagonal of the two unit cells, shown in Figure 18, is shown here. The overall atomic corrugation is nearly 2.0 Å peak-to-valley, suggesting a very sharp tip structure. The asymmetry of the unit cell is also evident; the left (or unfaulted) half of each unit cell is between 0.3 Å and 0.5 Å higher than the right (or faulted) half.

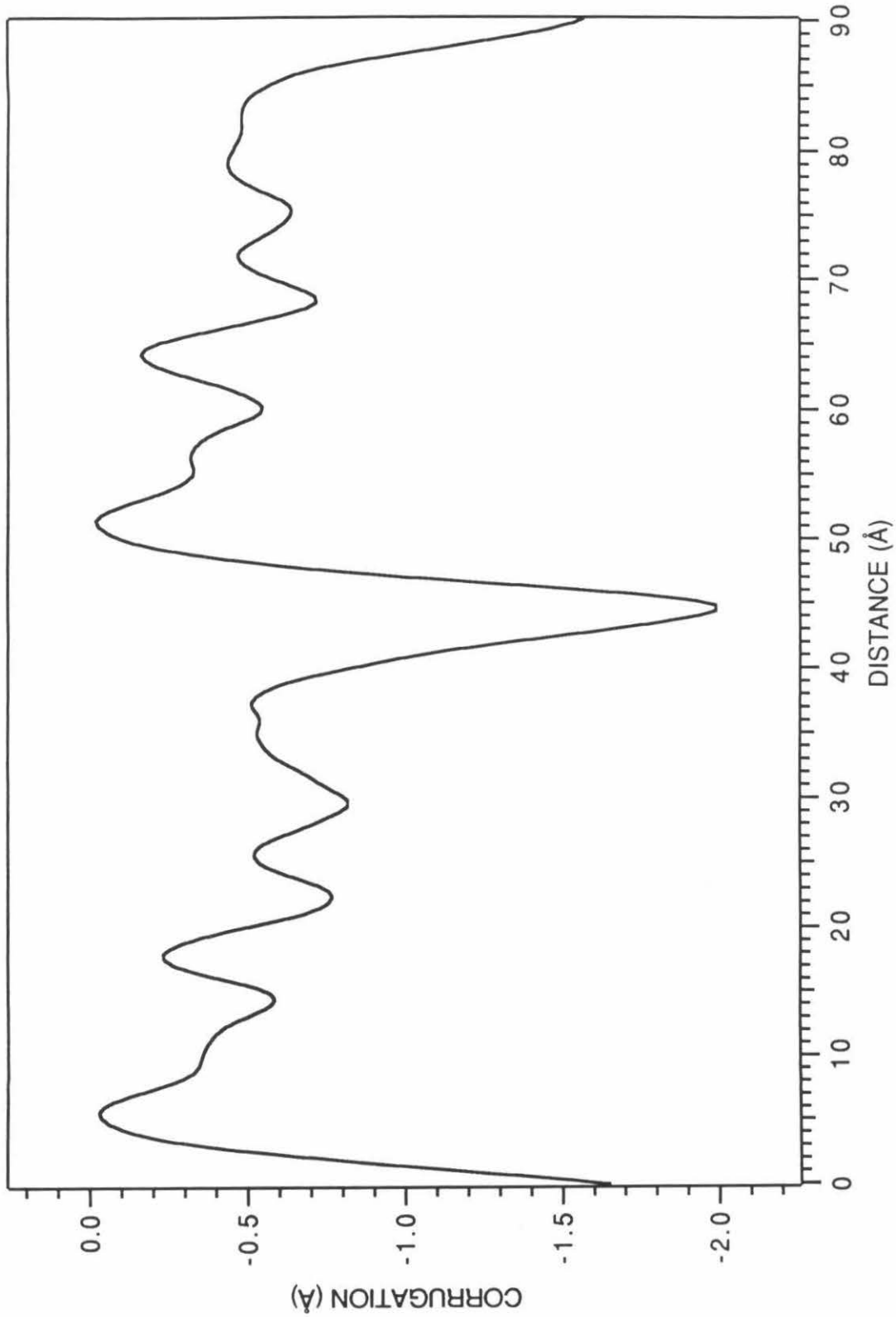
CORRUGATION (Å)
0.0
-0.5
-1.0
-1.5
-2.0
0
10
20
30
40
50
60
70
80
90
DISTANCE (Å)

**Figure 20**

An example comparing a constant current image to a barrier height image of the (7x7) surface is provided here. The images are each ~ (60 Å)$^2$ in size; the constant current image is shown at left, the barrier height image is at right. In both cases, raw data are shown. Greater image contrast is observed in the barrier height data. Some of the apparent "vacancies" in the constant current image appear only as peaks of diminished size, relative to the surrounding adatom lattice. These features are probably not true vacancies, but rather are reacted adatoms (reacted with either hydrogen or oxygen). The barrier heights over the adatoms are maxima, and are minima over the corner holes; therefore, the two imaging modes exhibit the same contrast polarity over surface features. The barrier height maxima are typically about 2.8-3.0 eV, compared with the bulk electron work function of about 4.6 eV. The sample bias was positive.

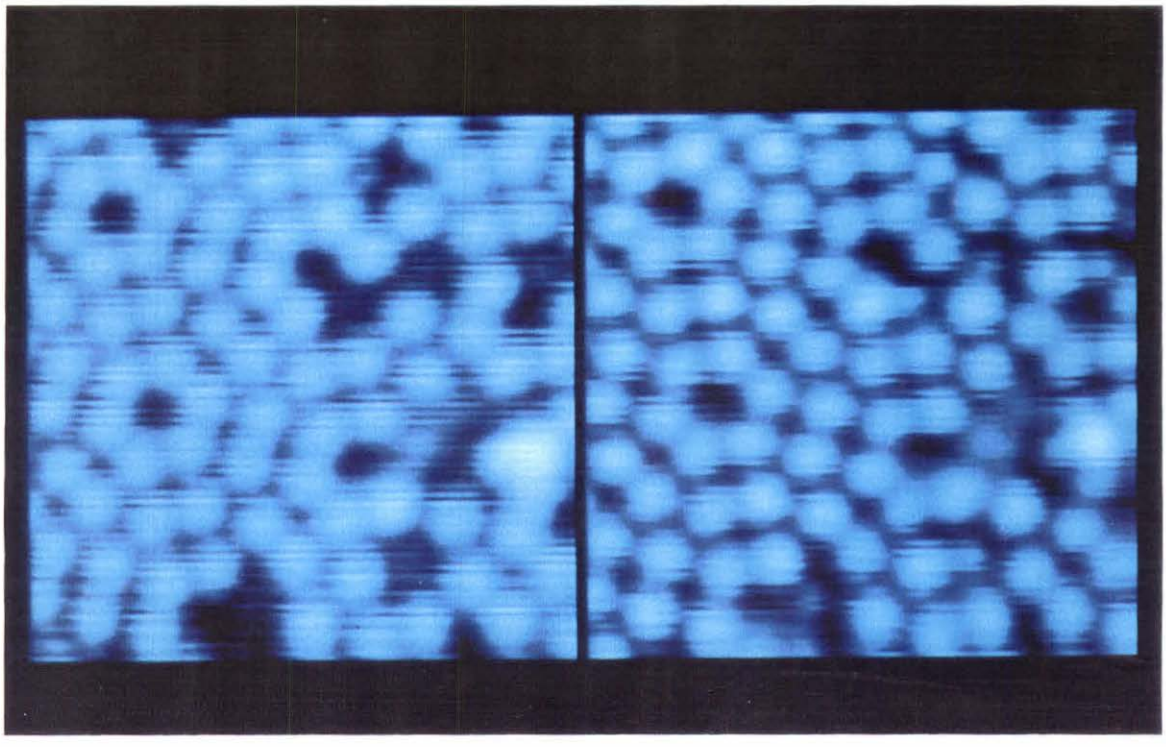

**Figure 21**

A cross-sectional linecut through a long diagonal of Figure 20 is shown here. The barrier height reaches 2.8 eV over adatoms and decreases to 2.0 eV over the corner holes. The overall geometry and contrast polarity are in agreement with those of the constant current image. The sample bias for these data was positive.

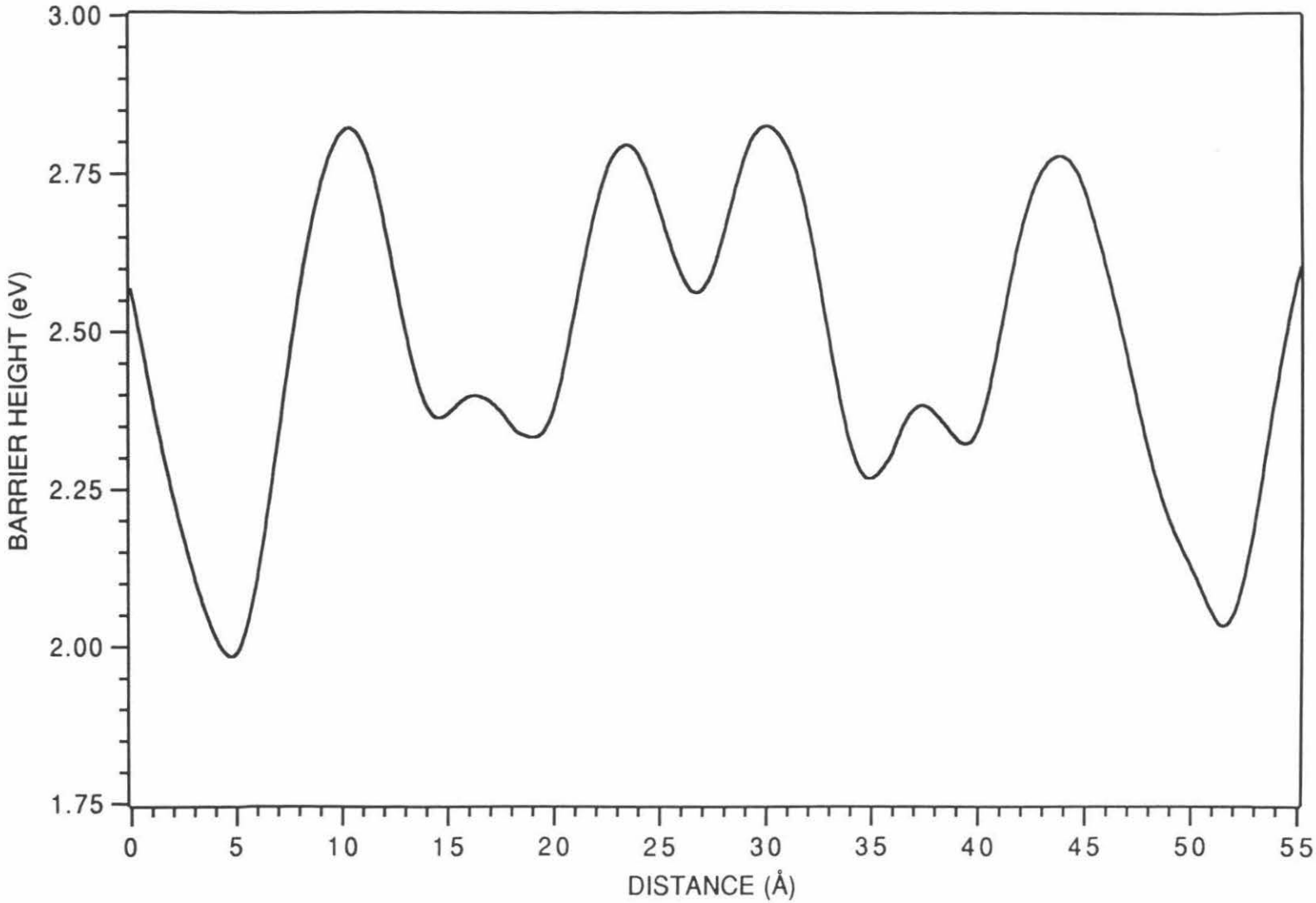
3.00
2.75
2.50
2.25
2.00
1.75
BARRIER HEIGHT (eV)
0
5
10
15
20
25
30
35
40
45
50
55
DISTANCE (Å)

**Figure 22**

The two-dimensional Fourier transform power spectrum of the Si(111)-(7x7) reconstructed surface provides information about the periodic nature of the surface. The 2-D power spectrum can be directly compared to diffraction patterns, such as those from LEED. The outermost 7th order Fourier components (faint dots in a hexagonal pattern) indicate the periodicity of the underlying bulk Si(111)-(1x1) surface. The 3rd and 4th order components are strongest, as in transmission electron diffraction (TED) and LEED experiments. These components correspond to the presence of double-spaced atoms within the unit cell, i.e., the adatoms.

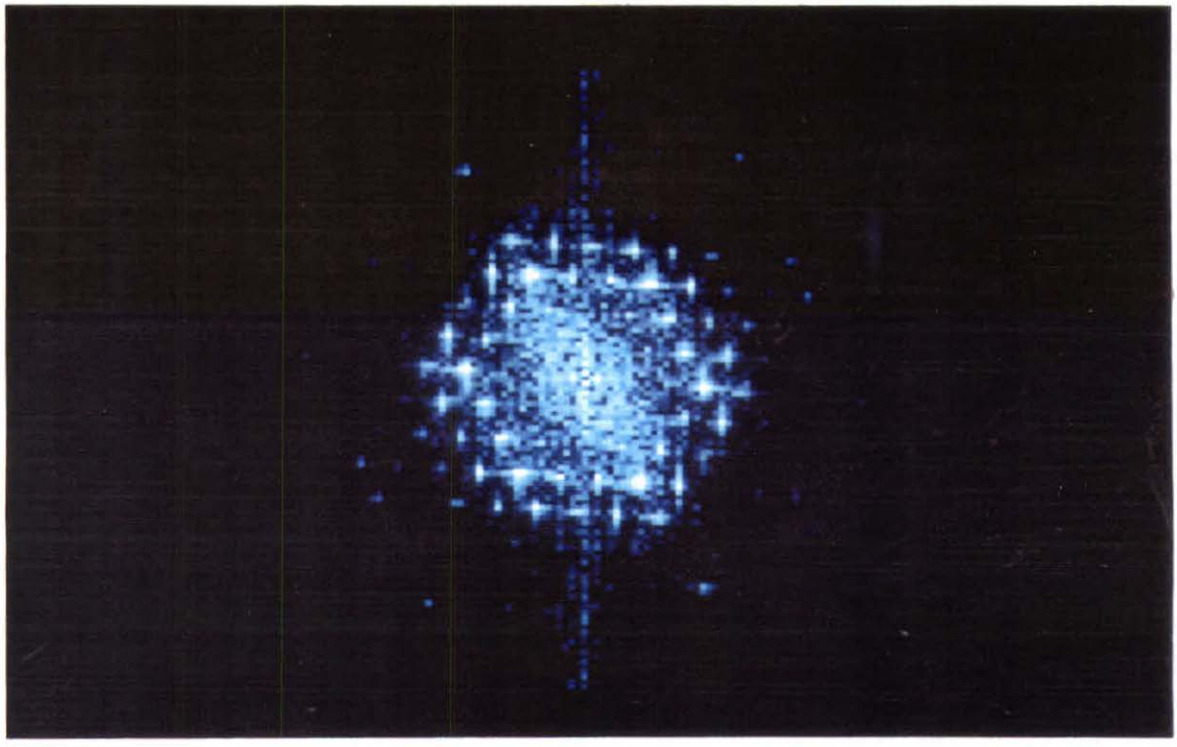

**Figure 23**

This (1000 Å)$^2$ constant current STM image of the Si(111)-(7x7) reconstructed surface is slope-keyed to accentuate step structure. Raw data are shown. Two large step bunches running vertically in the image are shown at the center and the right. The (7x7) unit cell mesh is visible on the flat terraces. The "ribbed" appearance of the central step bunch is indicative of multiple-tipping, probably a double-tip which comes into play at large step edges. There is an interesting double step structure, with several kinks, located at the upper left of the image. The very top left of the image is magnified at higher pixel resolution in Figure 24.

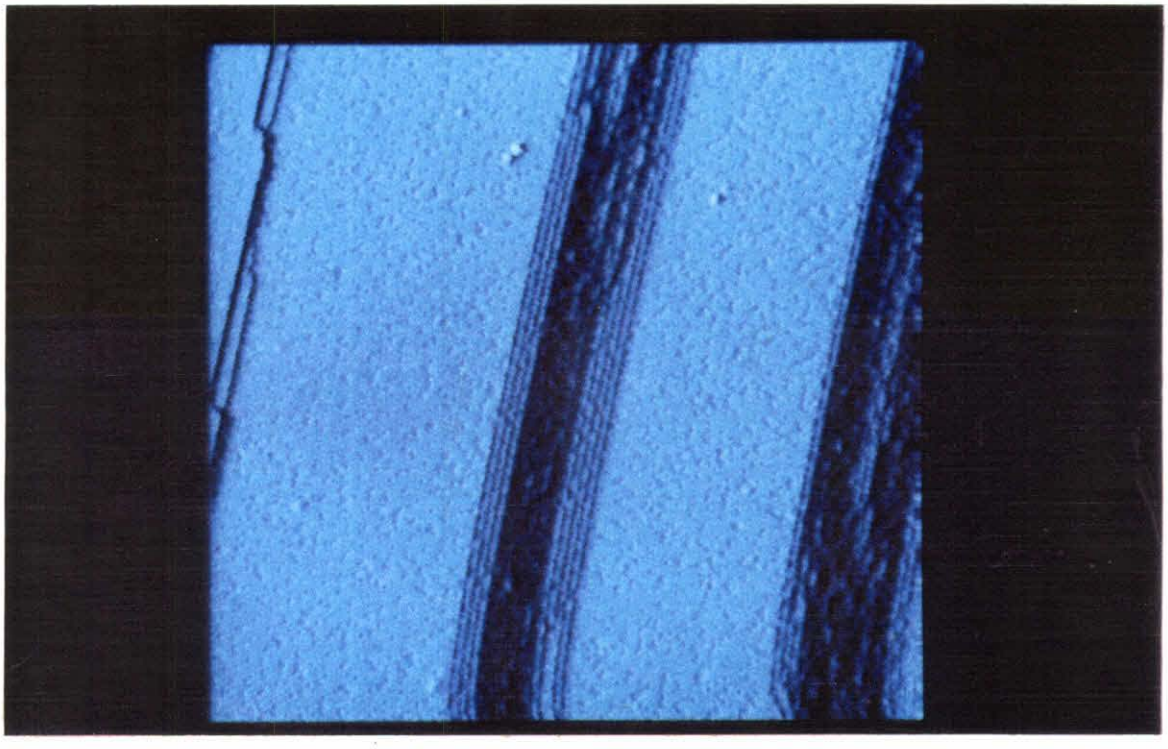

**Figure 24**

The top left of the image in Figure 23 is reimaged with higher pixel density in this ~ (200 Å)$^2$ top-view, slope-keyed constant current STM image. Raw data are shown. The double-height step experiences an one unit cell kink, which causes the step to split into two single-height steps. Each of these steps is 3.13 Å in height. Associated with the step kink is a line fault defect in which an extra row of adatoms is inserted into the (7x7) adatom structure (see white arrow). The upper step edge passes through the corner holes of the (7x7) reconstruction. A cross-sectional linecut through the step edge is provided in Figure 25.

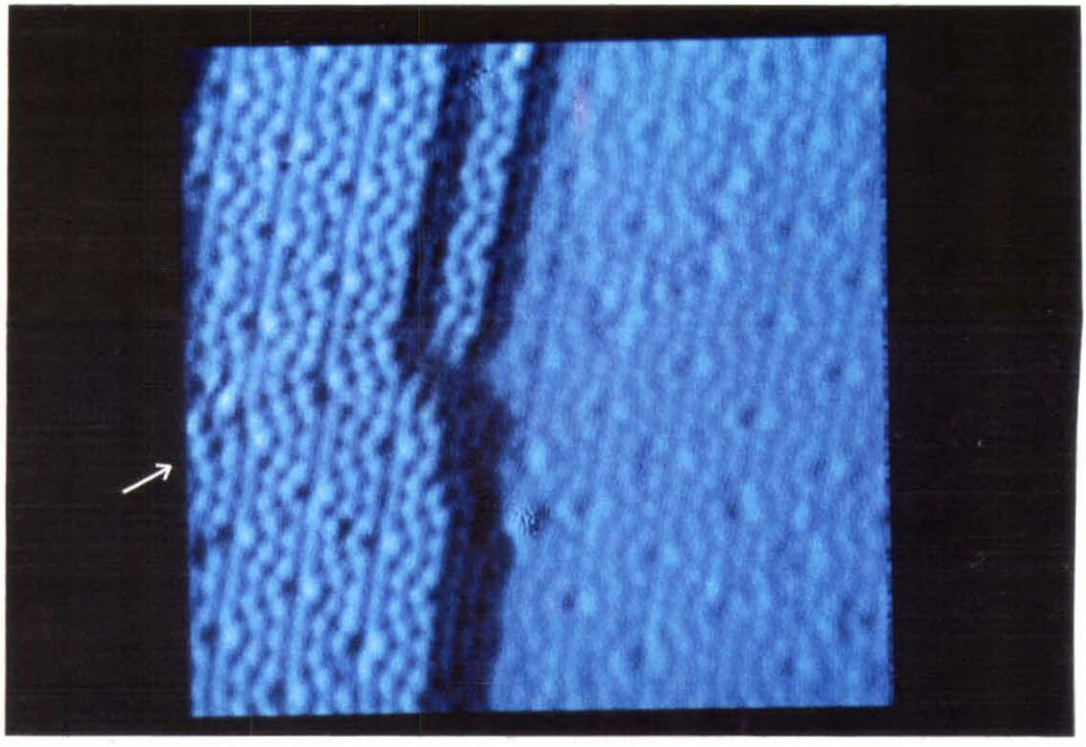

**Figure 25**

The "doublet" step structure above the step kink in Figure 24 is analyzed by a cross-sectional linecut. The linecut reveals that each of the steps is monatomic (consisting of a silicon double-layer), 3.13 Å high. The (7x7) reconstruction is seen to continue to the step edge and exists even on the intermediate step terrace, which is only ~ 20 Å wide.

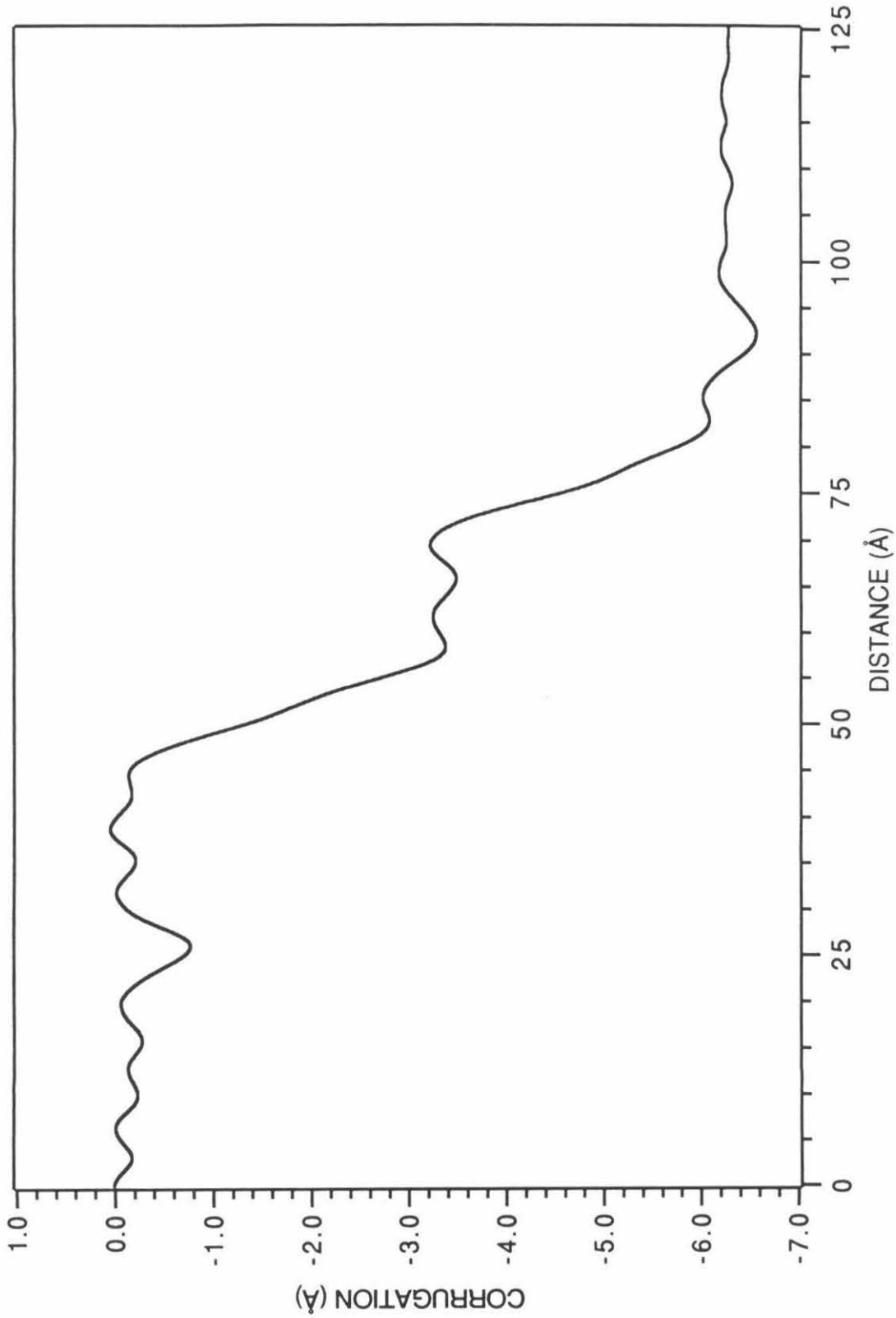
CORRUGATION (Å)
1.0
0.0
-1.0
-2.0
-3.0
-4.0
-5.0
-6.0
-7.0
0
25
50
75
100
125
DISTANCE (Å)

**Figure 26**

The slope-keyed ("lit" from the right) solid-modeled presentation of Figure 24 highlights the step structure. The double-height step and the step kink, leading into the splitting of the two individual monatomic steps, are visible. Also visible are the individual silicon(111) atomic layers which compose the steps. Consequently, four silicon atomic layers are discernible for the double-step and two silicon layers are seen for each of the single-height steps. Although this may be the effect of a multiple tip, this would represent the first report of the imaging of the individual silicon layers which make up the steps on Si(111) surfaces. See Figure 1 for reference.

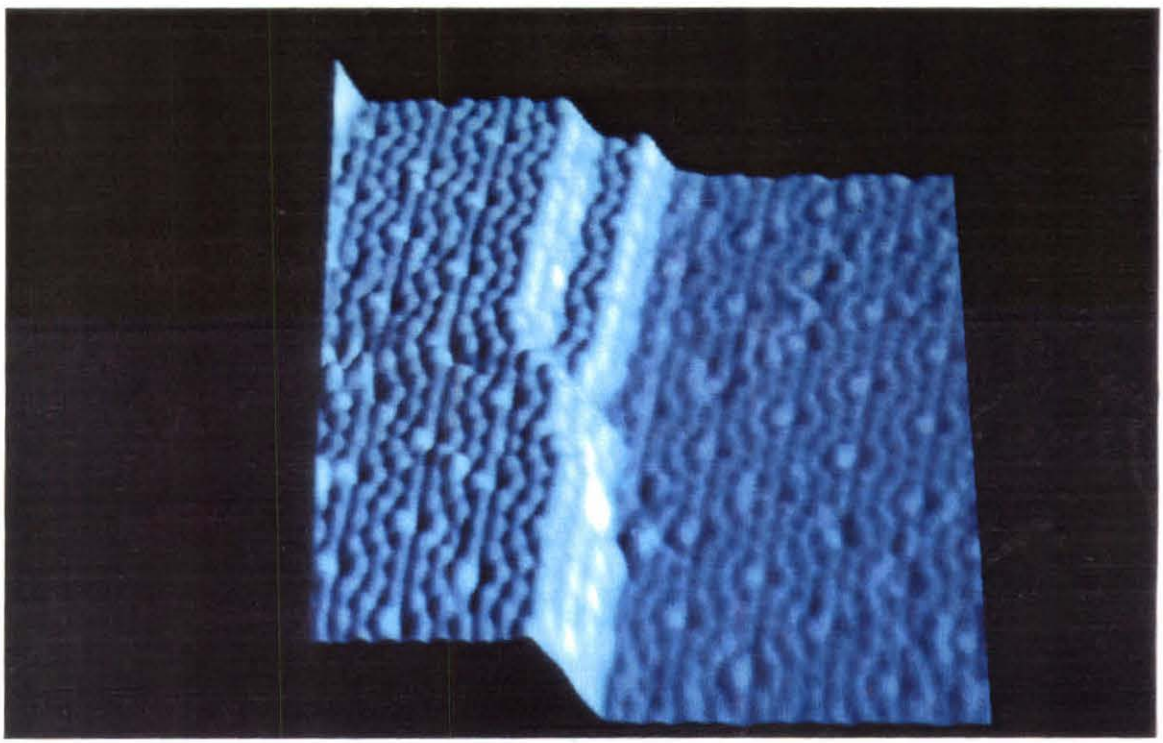

**Figure 27**

The line fault defect contained within Figures 24 and 26 is accounted for by the model developed by Hadley and Tear.[59] In this model, the unfaulted half of the unit cell is extended by one bulk unit cell (6.65 Å) to include the extra row of adatoms. The extra row of adatoms is terminated at the extended corner hole by the formation of a dimer in the third atomic layer and by an extra dangling bond on one of the dimerized atoms. The model is discussed in detail in the text of this chapter.

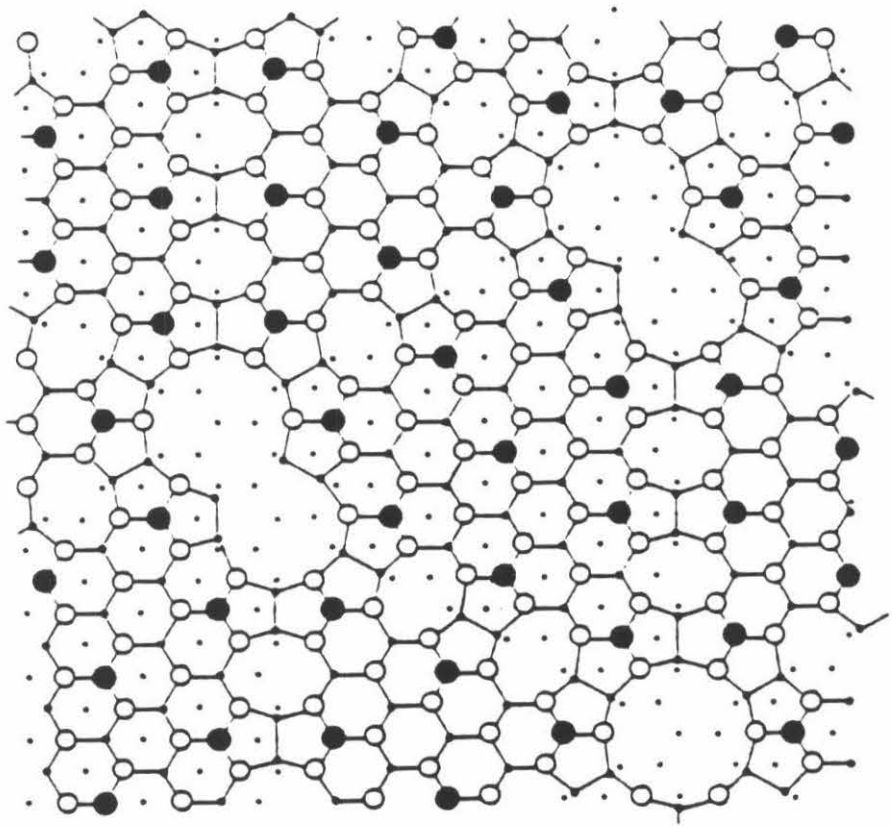

(●) adatoms, (○) 2nd layer atoms, (•) 3rd layer atoms, (·) 4th and 5th layer atoms. No bonds are shown between 4th and 5th, and 4th and 3rd layer atoms for clarity.

**Figure 28**

The double-height step edge in Figures 24 and 26 is studied by using current imaging tunneling spectroscopy (CITS). The technique involves obtaining current-voltage (*I-V*) spectra at selected points during the acquisition of a constant current topograph. In this way, one can build up a current image (analogous to a constant height image) at any bias voltage within the voltage scan range of the *I-V* spectra. This CITS series shows the following data: at upper left, the constant current image at +2.0 V sample bias; at upper right, the current image at +2.0 V; at bottom left, the current image at +1.0 V; and at bottom right, the current image at -2.0 V. All of the images except that at the bottom right reveal the unfilled states of the surface. In this manner, the unfilled and filled surface states of the sample, anywhere within the voltage scan range, can be analyzed. The energy dependence of surface states is evident; there are several reacted adatoms, which are more visible at one energy (bias voltage) than at others. The unfaulted halves of the unit cell are the left-pointing triangular subunits, as seen in the image taken at negative sample bias.

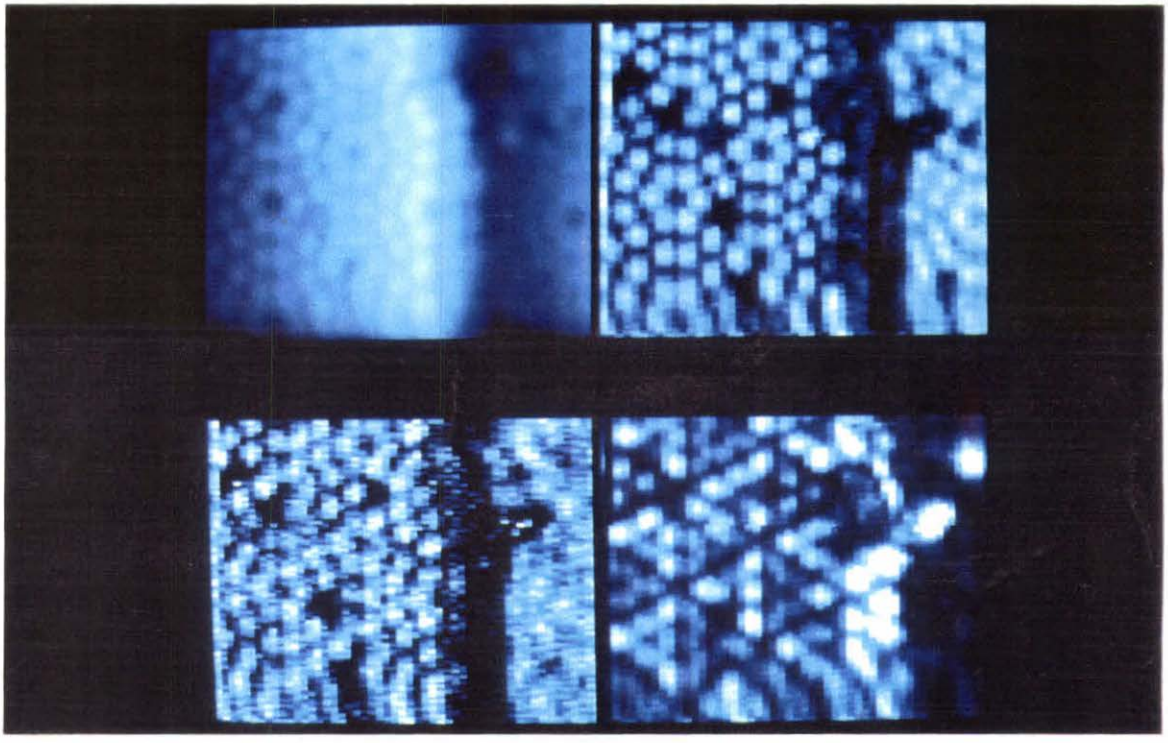

**Figure 29**

The two examples contained within this figure show the effect of multiple tipping on the appearance of the Si(111)-(7x7) surface. The images are each ~ (130 Å)$^2$ and were obtained in the barrier height imaging mode. The images show a couple of different patterns which can result from the contribution of multiple tunneling points to a STM image. The patterns bear little resemblance to the familiar (7x7) reconstruction. The problem of multiple tipping is especially important to consider when the structure of the sample is not known with certainty.

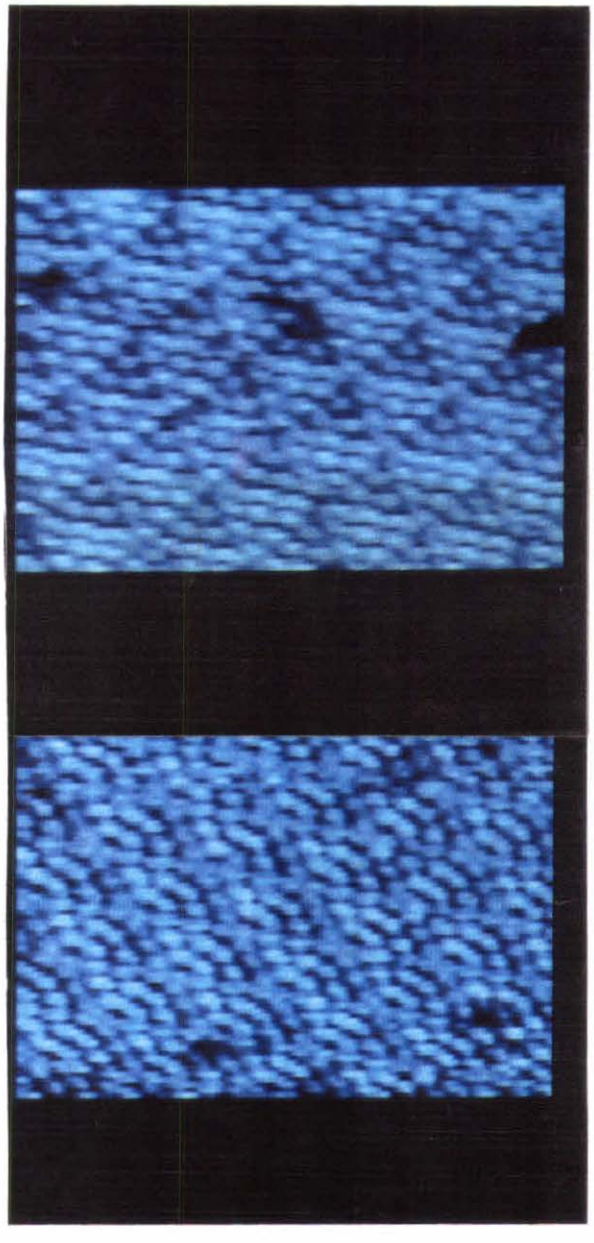

**Figure 30**

Multiple tipping is evident in this large-scale image of the (7x7) surface. The contribution of multiple tunneling points, probably separated by appreciable distances, is seen in this (500 Å)$^2$ slope-keyed constant current image. Although the (7x7) unit cell mesh is visible on the large terraces, it is only "clear" and well-resolved (with good corrugation) at the three small terraces adjacent to step bunches. It is only at these points that it is probable that the tunneling tip is a single point. The large step bunches cause other regions of the tip to contribute to tunneling, thereby blurring the atomic pattern on the large terraces. A surface with large-height surface features provides a good test of the sharpness and quality of a STM tip.

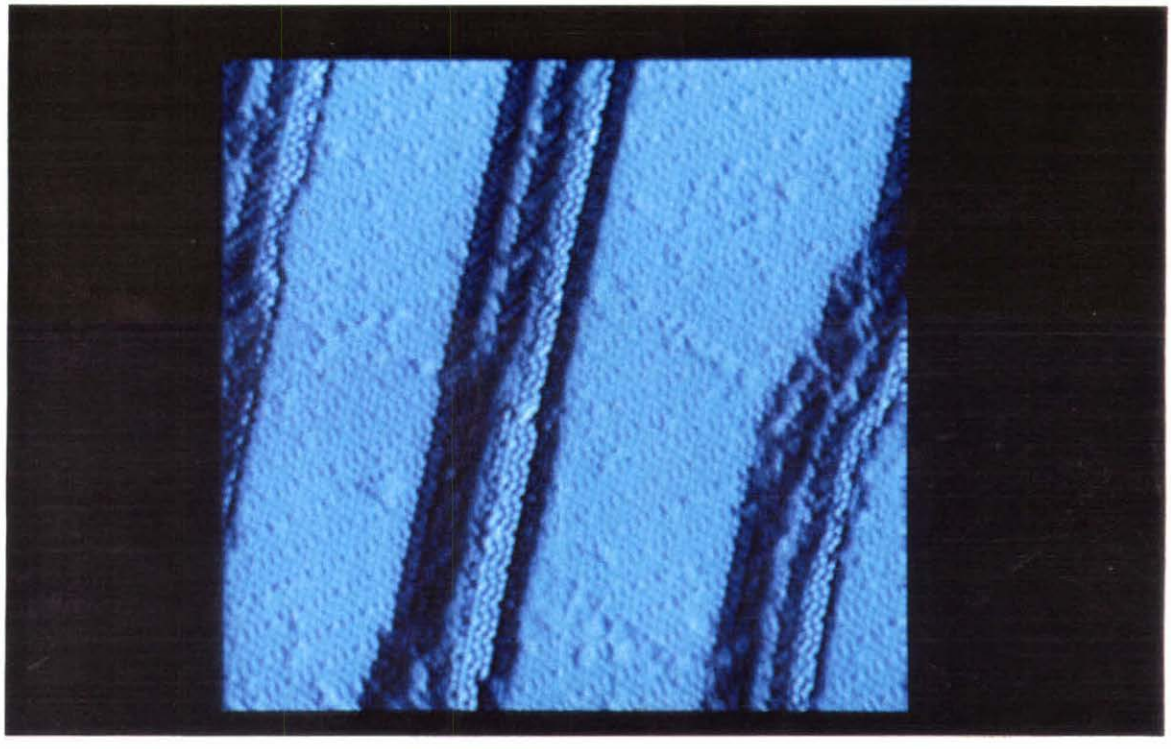

**Figure 31**

The cross-sectional linecuts for the long diagonals of the (7x7) unit cells acquired with qualitatively "sharp" and "dull" tips are shown here. The sharper tip (solid line) provides a larger measured atomic corrugation than the dull tip (dashed line). The corrugation for the sharp tip is 1.3-1.5 Å peak-to-valley while that for the dull tip is less than 1.0 Å.

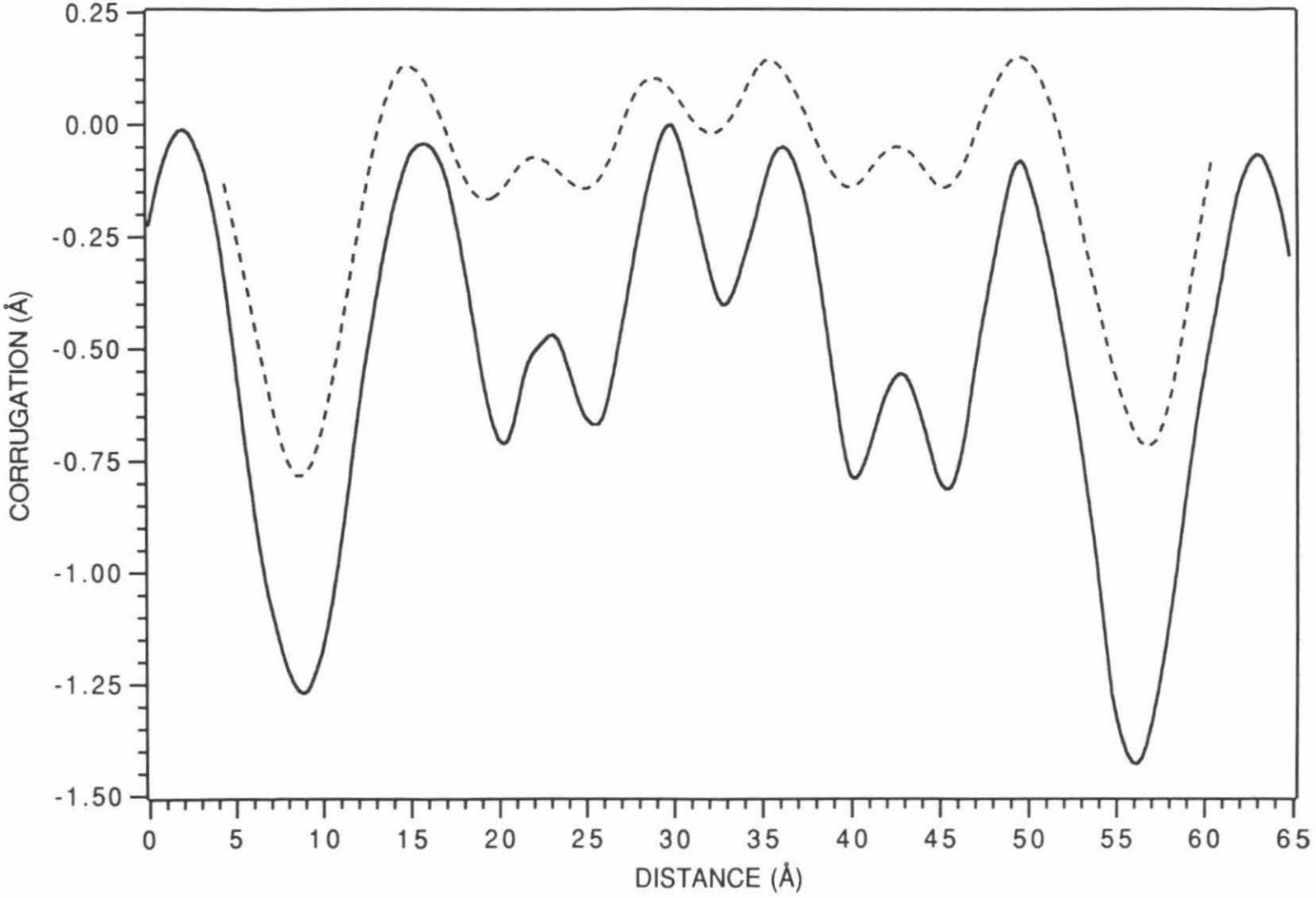
0.25
0.00
-0.25
-0.50
-0.75
-1.00
-1.25
-1.50
CORRUGATION (Å)
0
5
10
15
20
25
30
35
40
45
50
55
60
65
DISTANCE (Å)

**Figure 32**

Tip changes for two slope-keyed constant current STM images of Si(111)-(7x7) are shown here. The top image is taken with a positive sample bias, the bottom image with a negative sample bias. In each case, a tip change in the middle of the image causes a dramatic decrease in image contrast (atomic corrugation). Even small tip changes can result in dramatically different image appearances. In fact, the corrugation and atomic resolution almost completely disappear as a result of the tip changes. These images show the importance of a sharp tip in obtaining atom-resolved images.

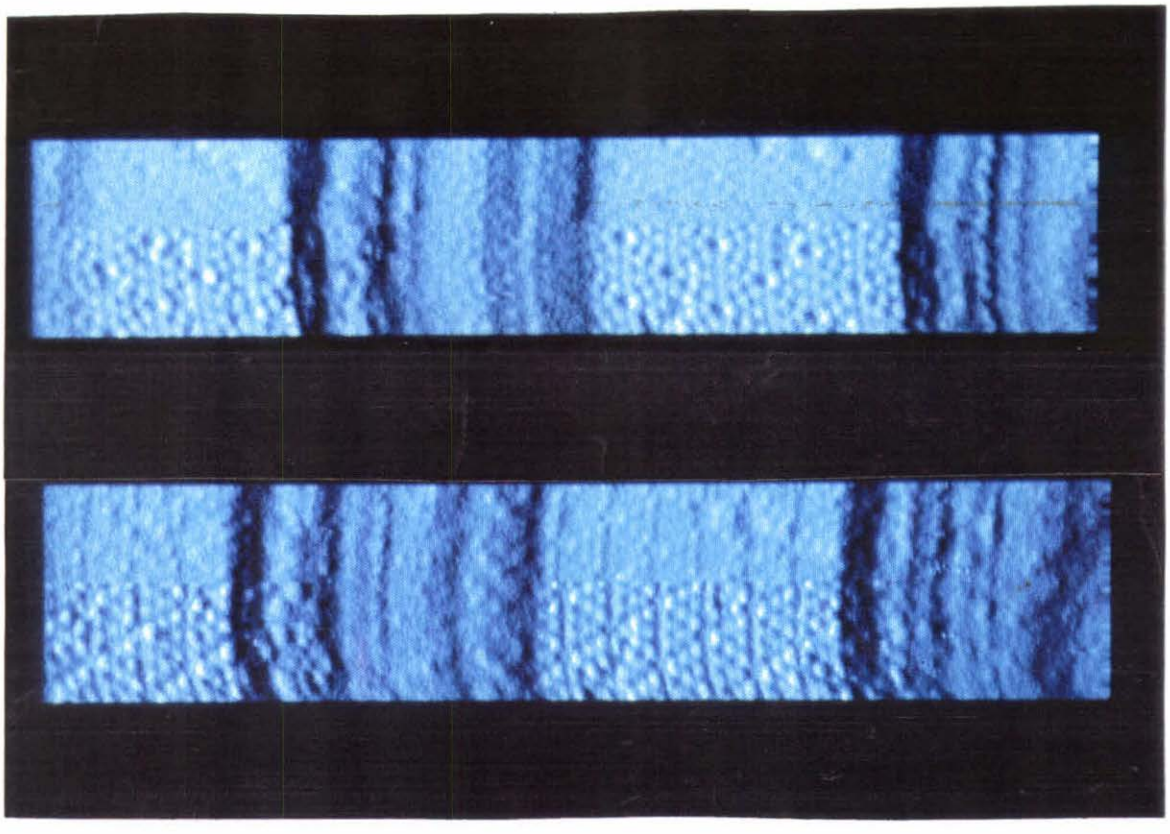

## *REFERENCES*


1. H.E. Farnsworth, R.E. Schlier, and J.A. Dillon, *J. Phys. Chem. Solids* **8**, 116 (1959).

2. K. Takayanagi, S. Tanishiro, and M. Takahashi, *Surf. Sci.* **164**, 367 (1985).

3. K. Takayanagi, Y. Tanishiro, M. Takahashi, and S. Takahashi, *J. Vac. Sci. Technol. A* **3**, 1502 (1985).

4. G. Binnig, H. Rohrer, Ch. Gerber, and E. Weibel, *Phys. Rev. Lett.* **50**, 120 (1983).

5. W. Mönch and P.P. Auer, *J. Vac Sci. Technol.* **15**, 1230 (1978).

6. F. Florio and W.D. Robertson, *Surf. Sci.* **24**, 173 (1971).

7. H.D. Hagstrum and G.E. Becker, *Phys. Rev. B* **8**, 1580 (1973); *J. Vac. Sci. Technol. B* **14**, 369 (1977).

8. P.A. Bennet and M.W. Webb, *Surf. Sci.* **104**, 74 (1981).

9. S. Ino, *Jap. J. Appl. Phys.* **16**, 891 (1977).

10. N. Osakabe, K. Yagi, and G. Honjo, *Jap. J. Appl. Phys.* **19**, L309 (1980).

11. K. Takayanagi, *Proc. XI Congress Electron Microsc. J. Electron Microsc. Suppl.* **35**, 133 (1986).

12. W. Telieps and E. Bauer, *Surf. Sci.* **162**, 163 (1985).

13. D. Haneman and R. Haydock, *J. Vac. Sci. Technol.* **21**, 330 (1982).

14. D.J. Chadi, *Phys. Rev. B* **30**, 4470 (1984).

15. D. Haneman, *Rep. Prog. Phys.* **50**, 1045 (1987).

16. K. Takayanagi, Y. Tanishiro, M. Takahashi, H. Motoyoshi, and K. Yagi, *Electron Microscopy* **2**, 285 (1984).

17. J.J. Boland, *Surf. Sci.* **244**, 1 (1991); *J. Phys. Chem.* **95**, 1521 (1991).

18. J.E. Demuth, U. Koehler, and R.J. Hamers, *J. Microsc.* **152**, 299 (1988).

19. R.S. Becker, J.A. Golovchenko, E.G. McRae, and B.S. Swartzentruber, *Phys. Rev. Lett.* **55**, 2028 (1985).

20. B.S. Swartzentruber, Y.-W. Mo, M.B. Webb, and M.G. Lagally, *J. Vac. Sci. Technol. A* **7**, 2901 (1989).

21. S.-I. Kitamura, T. Sato, and M. Iwatsuki, *Nature* **351**, 215 (1991).

22. G. Binnig and H. Rohrer, *IBM J. Res. Develop.* **30**, 355 (1986).

23. R.M. Tromp, R.J. Hamers, and J.E. Demuth, *Science* **234**, 304 (1986); *Phys. Rev. B* **34**, 1388 (1986).

24. R.J. Hamers, R.M. Tromp, and J.E. Demuth, *Phys. Rev. Lett.* **56**, 1972 (1986).

25. R.M. Tromp, *J. Phys.: Condens. Matter* **1**, 10211 (1989).

26. R.S. Becker, B.S. Swartzentruber, and J.S. Vickers, *J. Vac. Sci. Technol. A* **6**, 472 (1988).

27. St. Tosch and H. Neddermeyer, *J. Microsc.* **152**, 415 (1988).

28. Y. Hasegawa, I. Kamiya, T. Hashizume, T. Sakurai, H. Tochihara, M. Kubota, and Y. Murata, *J. Vac. Sci. Technol. A* **8**, 238 (1990).

29. U. Köhler, J.E. Demuth, and R.J. Hamers, *J. Vac. Sci. Technol. A* **7**, 2860 (1989).

30. Ph. Avouris and R. Wolkow, *Phys. Rev. B* **39**, 5091 (1989).

31. J.J. Boland, *Surf. Sci.* **244**, 1 (1991).

32. J.S. Villarrubia and J.J. Boland, *Phys. Rev. Lett.* **63**, 306 (1989).

33. B.S. Swartzentruber, Y.W. Mo, M.B. Webb, and M.G. Lagally, *J. Vac. Sci. Technol. A* **8**, 210 (1990).

34. W.E. Packard, N. Dai, J.D. Dow, R.C. Jaklevic, and W.J. Kaiser, *J. Vac. Sci. Technol. A* **8**, 3512 (1990).

35. F.K. Men, W.E. Packard, and M.B. Webb, *Phys. Rev. Lett.* **61**, 2469 (1988).

36. The wafers were obtained from International Wafer Service (Palo Alto, CA). The wafers were cut 4° ± 1° off the (111) orientation. The local vicinality however may be affected by wafer polishing. Another wafer sample from the same lot was confirmed to be 4° off (111) by Laue X-ray diffraction (M.G. Youngquist, personal communication).

37. described in S.M. Baker, Ph.D. Thesis, "Scanning Tunneling Microscopy and Spectroscopy of Silicon and Carbon Surfaces," California Institute of Technology, 1992.

38. R.J. Driscoll and M.B. Weimer, unpublished results.

39. Y. Borensztein, T. Lopez-Rios, and G. Vuye, *Appl. Surf. Sci.* **41/42**, 439 (1989).

40. Y. Ishikawa, N. Ikeda, M. Kenmochi, and T. Ichinokawa, *Surf. Sci.* **159**, 256 (1985).

41. taken from the newsletter, "Burleigh STM Tips," December 1990, Burleigh Instruments, Fishers, NY.

42. B.A. Joyce, *Surf. Sci.* **35**, 1 (1973).

43. J.M. Lenssinck, A.J. Hoeven, E.J. van Loenen, and D. Dijkkamp, *J. Vac. Sci. Technol. B* **9**, 1963 (1991).

44. M.D. Pashley, K.W. Haberern, and W. Friday, *J. Vac. Sci. Technol. A* **6**, 488 (1988).

45. R. Phaneuf and E.D. Williams, *Phys. Rev. Lett.* **58**, 2563 (1987).

46. Y.-W. Mo, B.S. Swartzentruber, M.B. Webb, and M.G. Lagally, *Bull. Am. Phys. Soc.* **34**, 466 (1989).

47. O.L. Alerhand, D. Vanderbilt, R.D. Meade, and J.D. Joannopoulos, *Phys. Rev. Lett.* **61**, 1973 (1988).

48. A.V. Latyshev, A.L. Aseev, A.B. Krasilnikov, and S.I. Stenin, *Surf. Sci.* **213**, 157 (1989).

49. Y. Homma, R.J. McClelland, and H. Hibino, *Jap. J. Appl. Phys.* **29**, L2254 (1990).

50. R.T. Tung, F. Schrey, and D.J. Eaglesham, *J. Vac. Sci. Technol. B* **8**, 237 (1990).

51. H. Hibino,Y. Shinoda, Y. Kobayashi, and K. Sugii, *Extended Abstracts, 22nd Conf. Solid State Devices and Materials* (Business Center for Academic Societies Japan, Tokyo, 1990), p. 1135.

52. R.J. Phaneuf, E.D. Williams, and N.C. Bartelt, *Phys. Rev. B* **38**, 1984 (1988).

53. E.D. Williams and N.C. Bartelt, *Ultramicroscopy* **31**, 36 (1989).

54. R. Wiesendanger, G. Tarrach, D. Buergler, L. Scandella, and H.-J. Guentherodt, *Mat. Res. Soc. Symp. Proc.* **183**, 237 (1990).

55. J.L. Goldberg, X.-S. Wang, N.C. Bartelt, and E.D. Williams, *Surf. Sci. Lett.* **249**, L285 (1991).

56. X.-S. Wang, J.L. Goldberg, N.C. Bartelt, T.L. Einstein, and E.D. Williams, *Phys. Rev. Lett.* **65**, 2430 (1990).

57. R.J. Phaneuf and E.D. Williams, *Phys. Rev. B* **41**, 2991 (1990).

58. F.G. Allen and G.W. Gobeli, *J. Appl. Phys.* **35**, 597 (1964).

59. M.J. Hadley and S.P. Tear, *Surf. Sci. Lett.* **247**, L221 (1991).

60. R. Wiesendanger, G. Tarrach, D. Bürgler, and H.-J. Güntherodt, *Europhys. Lett.* **12**, 57 (1990).

61. O. Nishikawa, M. Tomitori, and F. Iwawaki, *Mat. Sci. and Eng. B* **8**, 81 (1991).

# *Chapter 5*

# *ATOM-RESOLVED IMAGING OF DNA*

## *INTRODUCTION*

### *Motivation for Studying DNA with STM*

Deoxyribonucleic acid, or DNA, is the single most important material in biology; the DNA molecule in fact is often referred to as the "molecule of life." Contained within the double helix of DNA is the genetic code which directs life processes and the development of the living organism. Although the Watson and Crick model for the double helix is well established and is supported by numerous volumes of x-ray crystallographic data, it still remains the goal of many biologists to directly visualize the detailed structure of a DNA molecule.

The three-dimensional structures of molecules contained within DNA crystals have been successfully determined by x-ray crystallography over the past forty years. Since the first structure determination by Watson and Crick, with Wilkins and Franklin providing the main x-ray diffraction data, numerous DNA and DNA-derived crystals with various preparations and different environments have been analyzed. However, x-ray diffraction yields structural information averaged over millions of molecules contained within a crystal. As a result, such methods are insensitive to the slight variations which can exist between different DNA molecules. In addition, the sample must be crystallized in sufficient quantities, which frequently is problematic. The crystallization process also eliminates critical parameters such as electrolyte concentration and composition from the experiment. The crystal packing forces may also be large enough to significantly affect the DNA molecular structure.[1] While electron microscopy (EM) has had some success in imaging single DNA molecules, the samples often must be coated or stained with heavy metal atoms in order to increase electron density, and

consequently, improve image contrast. Unfortunately, this practice also results in a loss of resolution and disruption of the molecular structure. In addition, the samples must be studied in vacuum, far removed from the native environment of biological molecules. Some uncoated or "naked" DNA molecules have been studied by EM to provide molecular resolution (about 10 Å resolution, barely sufficient to distinguish single-stranded from double-stranded DNA); however, attempts at increasing the resolution (magnification) by increasing the electron beam energy have resulted in unacceptable specimen damage. Scanning tunneling microscopy (STM) has been shown to provide real-space atom-resolved images of conducting or semi-conducting surfaces, using low-energy probe electrons. With STM, there is the potential for **non-destructive, real-space** imaging of **individual** biological molecules, like DNA, with **atomic resolution**. In addition, STM studies on biological molecules may be carried out either in vacuum or under conditions approximating those of the natural environment, i.e., in solution. The ability to study single molecules in a heterogeneous population and detect local intramolecular structural variations would make STM the ideal technique for studying DNA.

Although STM studies must be performed with molecules deposited on substrates, this configuration is not as biologically "unnatural" as it first sounds. The majority of the processes that occur in living systems actually take place at surfaces or interfaces.[2] Biomolecules are usually considered to exist in a homogeneous solution phase where diffusion limitations and the particular influences of surfaces are not taken into account. However, the interface between the solid and the aqueous phase is an important consideration in biological systems. Therefore, although surface adsorption

may cause significant distortion of biomolecular structure, STM can still be a very useful and informative tool for the investigation of DNA structure.

Of course, one of the most interesting and important possibilities for biological STM is DNA sequencing. It may or may not be necessary to tag the four bases with specific labels in order to distinguish them. Identification of the $3.2 \times 10^9$ base pairs contained within the human genome would assist in understanding hereditary diseases. STM may in fact provide an increase of $10^3$-$10^4$ in sequencing rate over present-day conventional techniques. The subject of DNA sequencing using scanned probe microscopy is discussed briefly later in this chapter.

***Physical Properties of DNA***

The basic subunit of DNA is the nucleotide, which is composed of a phosphate group, a sugar (deoxyribose), and any one of four different bases. It is the sequence of these nitrogen-containing nucleic acid bases which determines the genetic code. Two of the bases, thymine (T) and cytosine (C), are each composed of a single six-membered ring, and are called pyrimidines. The other two bases, adenine (A) and guanine (G), each consist of a five- and a six-membered ring, and are called purines. The primary structure of the DNA strand then consists of a backbone of alternating phosphates and sugars, off of which hang the nucleotide bases. DNA is usually found as a double strand (duplex), in which the two strands are wrapped around each other, held together by numerous weak hydrogen bonds. In this configuration, the double helix, the sugar-phosphate backbones curl around each other so that the nucleotide bases point inward. The bases pair up in a specific manner, adenines with thymines, and guanines with cytosines, such that the two DNA strands are complementary.

The most common form of double-helical DNA, that found naturally occurring in biological environments, is known as B-DNA. This right-handed helical structure is 22 Å in diameter and contains bases separated by 3.4 Å (also known as the nucleotide rise), each turned 36° from the previous one, so that a complete helix turn comprises 10 base pairs and is 34 Å long (helical period). The rotation of the double helix around its axis also generates one "major" (wide) and one "minor" (narrow) groove in each complete turn. There are other forms or configurations of DNA (called A, C, D, and so on) which differ in respect to the spacing and tilting of the base pairs, and arises from differences in the preparation technique of the DNA molecule and its humidity content. There also exists a left-handed double helix (Z-form)[3] which may exist in some DNA locations in which gene function is being regulated.

The low humidity form of DNA is A-DNA, in which the helical pitch is ~ 29 Å and the axial nucleotide rise is 2.6 Å. The helical symmetry of A-DNA is 11 base pairs/turn and the turn angle between nucleotides is ~33°. The relative widths of the minor and major groove for A-DNA are reversed compared to B-DNA. Subtracting the van der Waals radii of the backbone phosphate groups, the minor and major groove widths are 11.0 Å and 2.7 Å, respectively. The depths of the grooves, unlike those of B-DNA which are almost equal, are quite different; the minor groove is only 2.8 Å deep while the major groove is 13.5 Å deep. The overall diameter of the A-DNA molecule is 23 Å and the base pairs are tilted at a +19° angle to the helix axis. The helix axis is in fact pushed out considerably (nearly 5 Å) from the base pairs into the major groove.

An excellent comprehensive review on the subject of DNA structure is provided by Saenger.[4]

*STM Studies of DNA*

Atomic resolution STM imaging of individual large biomolecules has been of great interest since its invention;[5] however, it has remained largely an elusive goal. The first STM image of DNA[6] was obtained by Binnig and Rohrer in 1984; in fact, DNA was the first biomolecule to be studied by STM. The DNA sample in this study was deposited unmodified onto a standard EM amorphous carbon support film and examined in ultra-high vacuum (UHV). The authors observed a trough-shaped depression, about 40 Å wide, with an approximately 35 Å structural periodicity along its length. When its inverted topography was presented, the snake-like feature had the appearance of a DNA strand, much like that seen in previous EM experiments. However, no further detail could be discerned from the image. Since that initial experiment, there have been literally dozens of published reports, presenting results from STM investigations of DNA. Unfortunately, many of these results have met with considerable criticism, much of it justified. In this review of STM studies on DNA, we will focus on those reports which were particularly well-received or marked important progress in the field.

Other early studies of DNA by Amrein *et al.*[7] used heavy metal shadowing. In those studies, the authors observed with STM freeze-dried recA-DNA complexes coated with a Pt-Ir-C conducting film. The STM topographs, acquired in air, revealed the expected right-handed single helix of ~ 100 Å diameter, composed of about six recA monomers per helical turn. These studies demonstrated that STM, even involving metal coating, could be superior to transmission electron microscopy (TEM) in evaluating

biomolecular structure. Similar studies by the same authors on uncoated recA-DNA in high humidity provided images of comparable quality to those on metal-coated samples.[8] Lindsay and coworkers[9,10,11] have pioneered the study of DNA by STM in aqueous and electrochemically-controlled environments. These investigators successfully imaged uncoated DNA submerged in aqueous solutions. These results showed the ability of STM to study biological materials like DNA under conditions similar to their native environments. Faradaic deposition of the DNA molecules on gold surfaces provided fairly uniform coverage of the interface. However, in these experiments, the resolution was only sufficient enough to discern the overall periodicity or pitch of the double helix. This limitation may have been due to increased molecular "flexibility" (blurring by molecular movement) in solution.

Over the past few years, there have been several reports of DNA imaging by STM which have received considerable attention. Keller *et al.*[12] used three methods of DNA deposition: (1) drying a drop of highly concentrated (10 mg/mL) DNA solution, in 10 mM potassium chloride, that had been sonicated, (2) drying and then peeling a drop of DNA solution, using ammonium acetate instead of potassium chloride as the solute, and (3) contact-spreading a droplet containing lysed T7 bacteriophage particles. Similar results were obtained for the three different spreads, although the first method was reported to promote liquid-crystalline packing. The second method apparently left little DNA behind, and the third method provided a good spread of the DNA molecules. Only general structural dimensions could be determined from the images: molecular width and helix periodicity. Beebe *et al.*[13] obtained STM images in air of uncoated double-stranded DNA

deposited on highly oriented pyrolitic graphite (HOPG) from a salt solution. They reported for the first time resolution sufficiently good to distinguish major and minor grooves. The helix pitch was seen to vary between 27 Å and 63 Å. Lee *et al.*[14] also reported being able to measure the major and minor grooves on RNA and DNA fibers dried on HOPG. As in the previous Beebe study, the resolution was barely sufficient to interpret image features as major and minor grooves; no further structural detail could be discerned from the data. More recently, higher resolution STM images of uncoated DNA have been published. Arscott *et al.*[15,16] used STM to image the left-handed helical twist of Z-DNA. The DNA sample, deposited on HOPG, was covered with mineral oil during scanning, in order to reduce drying effects. Their images clearly resolved the left-handedness of the helix and the minor groove of the molecule. The helix pitch was measured to be 42 Å, in good agreement with the x-ray crystallographic value of 45 Å.[17] The lateral resolution of the image was about 3 Å, nearly good enough to resolve individual atomic details. This experiment was the first time that the unusual Z-form of DNA had been observed by real-space imaging. Cricenti and coworkers[18,19,20] deposited a drop of DNA solution onto a gold-plated aluminum substrate. The molecules were "activated" by the addition of tris (1-aziridinyl) phosphine oxide (TAPO). Their gap-modulated barrier height, $d(\ln I)/ds$, images (see chapter 1 for a detailed description of this imaging technique) revealed submolecular structure on a single turn of the helix. Although somewhat confusing, the results suggested that submolecular resolution was possible and that barrier height imaging could be a valuable technique for accomplishing this. Dunlap and Bustamante[21] successfully imaged with STM single-stranded DNA, polydispersed poly-deoxyadenylate (dA) molecules,

deposited on HOPG. The images revealed the poly(dA) molecules aligned parallel to each other, in small "islands." The data, although difficult to interpret, suggested that atomic resolution imaging of biological molecules with STM was possible. The authors also claimed to be able to discern the individual adenine aromatic rings; hence, the possibility of DNA sequencing by STM was presented.

Atom-resolved imaging of uncoated double-helical DNA using STM has recently been demonstrated.[22,23] These studies, performed in UHV, revealed double-helical structure, base pairs, and atomic-scale substructure. These experiments are described in detail in the remainder of this thesis chapter.

*EXPERIMENTAL*

The DNA sample used for the initial STM experiments was an approximately 550 base pair (bp) *AvaII* fragment of mouse B-cell V-region DNA,[24] derived from pBV13L. A micropipette was used to deposit a 2 μl drop of 10 mM aqueous ammonium acetate solution, containing 10 ng DNA/μl, onto a piece of freshly cleaved ZYA-grade HOPG[25] in air. The HOPG sample had been repeatedly cleaved in order to produce a "clean" and shiny surface, that to the naked eye and under low-power magnification was free of obvious defects, steps, and flakes. The wet sample was immediately placed into the load lock and dried in vacuum using a mechanical rotary pump and a turbomolecular pump, and eventually an ion pump. After the pressure decreased below ~ $10^{-6}$ torr (approximately 30 minutes), the sample was transferred via the translator to the STM chamber with a base pressure of ~ 3 x $10^{-11}$ torr. No visible residue was present on the HOPG surface. In some later

experiments, we used other sample preparation methods, alternate substrates, such as gold and boronated pyrolitic graphite (BPG), and various DNA samples from different sources. The specific details of these cases are included at the points in this chapter where these experiments are discussed.

Imaging was performed on the Caltech UHV-STM system described in chapter 1. We often concurrently obtained topographical (constant current) and gap-modulated barrier height images in these studies. Probe tips were ac-etched tungsten without further treatment. The sample bias for the atom-resolved data in this report was +100 mV with a feedback tunneling current of 1 nA. Little or no change in the appearance of the DNA images was observed within the bias range ± 1 V. The z modulation in barrier height measurements was 0.6 Å p-p at 1 kHz. The specific tunneling parameters, acquisition conditions, and image processing descriptions are included within the text and figure captions.

## *RESULTS AND DISCUSSION*

### *General Observations*

The sample preparation technique described above was chosen for specific reasons. The dried-drop deposition method was chosen because it was simple and quick, and HOPG was used as the substrate for similar characteristics. In addition, HOPG is atomically flat with few defects, if carefully cleaved. However, the basal plane of graphite is also chemically inert. The concentration of the DNA solution (10 ng/μL) was chosen to provide approximately monolayer DNA coverage, if the DNA was unaggregated and evenly distributed on the surface. The salt solute used to provide the DNA counterion, ammonium acetate, was chosen because it is

volatile. Therefore, in vacuum, it should sublime away, leaving only DNA on the substrate. The technique at first sounds like it would be quite good, leaving only "clean" DNA on the surface. This sample preparation technique however turned out to be, in practice, far from ideal for typical STM experiments. The dried-drop deposition method, although simple, provided samples with poor DNA coverage. As a result, large areas of the HOPG surface were devoid of any visible DNA features. It was common to find no evidence of DNA in the maximum scan range (approximately a third of a micron on a side) images of our STM. Consequently, it required many repeated iterations of louse walking (sometimes over macroscopic distances) and tip reapproaching to find an area with any DNA. This process was quite tedious and very time-consuming. It is obvious from this description that the DNA deposition method was far from ideal and was particularly unsuited to the limited scan range of our STM design. Large areas of atomically flat graphite with occasional mono- and bi-atomic steps were observed. These steps can however be mistaken for biological structure, i.e., DNA, in topographical scans, especially if an insufficient data-pixel density is used.[26] Steps on high-quality HOPG are usually linear over hundreds of ångströms and accompanied by similar steps oriented at 60° or 120° to one another, due to the symmetry of the surface. Substrate features can often be distinguished from DNA structures by using barrier height information.[27] The barrier height changes appear to be much greater over DNA than steps. The barrier height behavior of the DNA samples is discussed in detail later in this chapter.

When DNA was found to be present, it was usually aggregated into large clumps, often measuring as large as hundreds or thousands of Å in size

laterally and a few hundred Å high. An example of a DNA cluster is shown in Figure 1, a "zoom" series of three successive STM topographical images, focussing on a single "toroid"-shaped aggregate of DNA molecules, at progressively higher magnification (and pixel density), moving clockwise from upper left. Although the rear half of the aggregate appears to "collapse," the barrier height response is almost constant around the entire structure. This phenomenon may be attributed to variations in the extent of interaction between the DNA and the substrate around the aggregate. The bottom right portion of the DNA feature in the highest magnification image in Figure 1 is provided "blown-up" and smoothed in Figure 2. Several parallel strand-like features closely packed side-by-side, resembling DNA, are discernible in Figure 2, each with a repeat periodicity of ~ 30 Å. However, the resolution is insufficient to definitively identify these features as DNA strands, much less discriminate submolecular features. The aggregation, as seen in Figure 1, may result from drying effects, especially surface tension forces which are exerted by the evaporating and receding solvent droplet. Some of these negative effects can be minimized or eliminated by rapid freeze-drying (lyophilization) of the DNA samples. It would seem from the observed clumping behavior that the DNA molecules have a greater affinity for each other than for the underlying HOPG substrate. Although "naked" DNA molecules are polyanionic, DNA in salt solutions tends to crystallize with its counterion.[4] Therefore, although the DNA molecules by themselves repel each other strongly, the inert character of the HOPG basal plane surface offers less attraction for the DNA molecules than their natural tendency to crystallize out of solution.

It was rare (only on about 10 or 20 occasions) to find a scan window which contained an isolated, unclumped DNA molecule. Unfortunately, the tip in these cases was almost always insufficiently "sharp" and/or "clean" to provide more than molecular resolution; occasionally, however, strand periodicity of ~ 30 Å was also occasionally observed. With one particular DNA molecule/tip combination, atomic-scale resolution was achieved. The details of this case are discussed in the following section.

We implemented a variety of scan rates and bias voltages in these experiments. Although our highest resolution images were obtained using a sample bias of +100 mV and a very slow scan rate of 100 Å/s, these parameters are probably not critical. The only requirement concerning scan rate is that it be sufficiently slow for the feedback to respond to ~ 20 Å topographic changes before the tip has moved more than approximately an ångström laterally. Topographic images obtained with an opposite bias polarity are generally indistinguishable and appear qualitatively the same over the bias range from 50 mV up to 1 V.

***Atom-Resolved Imaging***

Although UHV conditions provide an extremely clean experimental environment, it may also lead to DNA denaturation.[4] However, no obvious denaturation was observed in images of individual DNA molecules in our STM studies. However, any intact DNA in vacuum would probably exist in the A-form, which is the most prevalent form in low humidity conditions.[28] The structural characteristics of A-DNA were provided in an earlier section of this chapter. The most obvious features however of A-DNA are its tilted base pairs, and especially, its narrow and deep major groove and its wide and shallow minor groove. Therefore, it can be expected that if an isolated DNA

molecule could be imaged at high resolution, that features within the minor groove could be resolved; no features, however, within the major groove would be expected to be imaged, even with an atomically sharp tip. A model of the van der Waals surface structure of A-DNA derived from x-ray crystallographic data is shown in Figure 3. The sugar-phosphate backbone is shown in red and the base pairs in yellow.

We successfully imaged one region of an isolated DNA molecule with atomic-scale resolution. Figure 4, a (200 Å)$^2$ image, shows this region of a single, isolated DNA molecule. The image is neither filtered nor smoothed and shows slightly more than seven full turns of the double helix. The helix pitch varies somewhat over this length, however, averages about 30 Å. The measured molecular width is ~ 25 Å. Recall that the actual molecular width is probably slightly smaller, due to the convolution of the tip shape and size with large surface features which are comparable in size with the imaging portion of the tip. The most striking feature of the image is at the center of the molecule, in which there is a distinct bend in the molecule. This probable kink site causes the single helical turn to lie at a 30° angle to the helix axis. The resolution of this image however is limited by the data-pixel density; the image is composed of only 100 data lines in $y$ (there are 500 data pixels in $x$ per line). Therefore, the data pixels are separated by ~ 2 Å along the molecule, spaced too far apart to observe atomic-scale details. However, the middle portion of Figure 4 was consequently rescanned several times with a higher pixel density. Figure 5 provides one of these images, which reveals atomic-scale detail.

The image shown in Figure 5 is approximately 80 Å in $x$ by 120 Å in $y$ and was acquired using a scan rate of 100 Å/s. As with the image in the

previous figure, no filtering or smoothing has been applied to the data; only plane-subtraction was performed. The twist of the double-helix and the major-minor groove alternation are evident, as are parallel features spanning the minor grooves at a +18° ± 3° angle to the helix axis. These features are probably the bases of the nucleotide pairs; their spacing and tilt angle are consistent with this interpretation. The base pairs appear to bridge the thick phosphate-sugar backbones, which each measure ~ 10 Å wide. Several of the base pairs crossing one of the minor grooves are indicated by red arrows. The helix symmetry, estimated from the spacing of these visible bases, is approximately 11 base pairs per helical turn, again consistent with A-DNA. The measured average helix pitch is 29 Å and the axial nucleotide rise (base pair spacing) is 2.6 Å. Again, these values are in good agreement with the structure of conventional A-form DNA. These STM-derived dimensions and those obtained from x-ray crystallography are compared in Table 1. Any discrepancies may be explained by the variability in the structure of A-family polynucleotides, substrate-tip thermal drift, or piezo creep. It should be noted that the STM data reflect measurements made from a single molecule out of a heterogeneous population, while the x-ray information averages dimensions over millions of molecules. In addition, it is not expected that DNA dried on a substrate in UHV would have a structure fully consistent with x-ray crystallographic data. The kink site from Figure 4 is also quite pronounced in this image; the affected helix turn is marked by the lines labeled A and B. Although the bending of the helix is probably due to a kink site, it may also be a result of the tip instability which occurred in the immediately preceding helical turn.

Approximately four full turns of the double helix are contained in Figure 5. Starting from the bottom of the image (the scan lines are built up from bottom to top, each moving right to left in this image), we observe a wide (~ 10 Å) minor groove with considerable substructure leading into a narrow (~ 3 Å), less well-resolved major groove, consistent with the structure of A-DNA. As noted earlier, the major groove is too narrow for the STM tip to enter. During a scan line in the second minor groove, a tip instability, indicated by the yellow arrow, occurred. Following this event, the appearance of the DNA molecule is slightly changed; the major groove appears as a small notch on the right side of the molecule in the transition region between adjacent minor grooves. This may be explained by the tip having moved the upper half of the DNA slightly (relative to the bottom half). A tilting of a few degrees can result in this orientation and appearance change, as is demonstrated with the model shown in Figure 3. In Figure 3, the transition point between the two different rotational orientations is indicated by the arrow at mid-point, approximating the point at which the tip instability in Figure 5 occurred. However, the same change in orientation is observed in previous images and more likely represents a true kink site. Kink sites, in which the helix bends by 26°, are known[29] to exist at junctions of A- (11-fold) and B-form (10-fold) helices. The kink site in our images may actually represent such an A-B transition.

Our results were quite surprising; we did not expect the STM to faithfully reproduce the van der Waals topography of a DNA molecule. It was also not expected that DNA dried in vacuum on a substrate would have a structure fully consistent with x-ray crystallographic data. The average width of the molecule was measured to be ~ 23 Å, and the average "apparent

height" to be ~ 12 Å. The image acquired scanning in the opposite direction in $x$ shows qualitatively similar structure, but the molecule appears slightly narrower (~ 21 Å). This may indicate some elastic interaction between the tip and the molecule. This effect would be magnified if the DNA molecule were adsorbed at a step edge. The DNA molecule is expected in fact to appear broadened in STM images due to the size and curvature of the tip on the scale of DNA. A shortened "height" of the molecule may be due to dependence of the tunneling probability on both the tip-sample separation and the tunneling barrier. In the topographic imaging mode used in these experiments, the STM maintains a constant electron tunneling current and therefore a constant tip-sample separation if the local effective barrier height is constant. In response to an increased potential barrier over the molecule, however, the feedback system must reduce tip-sample separation to maintain constant current. The influence of tip structure on DNA images have also been experienced in which the edge of the tip "senses" the DNA molecule tens of ångströms from the position of the lowest point on the tip. The comparable sizes of the tip and the DNA molecule can lead to an image which is a noticeable convolution of the two structures.

Figure 6 is a solid-modeled perspective representation of the bottom three-fourths of Figure 5. The data have been smoothed using a binomially weighted sliding window average corresponding to a Gaussian of ~ 0.60 Å FWHM (which is quite small compared to the typical van der Waals atomic diameter of 3 Å). This presentation provides visual evidence of atomic-scale resolution. The "bumpy" texture of the molecular surface indeed results from atomic structure on the DNA molecule. Additional evidence is provided by directly comparing the STM image to the A-DNA model. The

bottom third of Figure 5 is compared to a corresponding section of a van der Waals model in Figure 7. The $y$ axis has been skewed to facilitate direct comparison with the model. The STM image is ~ 35 x 55 Å and contrast has been enhanced by histogram equalization; however, no smoothing has been effected. Starting at the bottom, the alternating minor-major-minor groove sequence is readily apparent. The varying thicknesses of the backbones on the surface of the DNA molecule are visible, as are two well-resolved base pairs in the bottom minor groove. There is excellent agreement in the general features between the STM image and the model, and the image suggests true atomic-scale resolution; even down to the Å scale, the STM image appears remarkably similar to the x-ray model. The most convincing evidence however is provided by comparing cross-sectional linecuts through the STM experimental data to corresponding cross-sections of the van der Waals model.

In Figure 8, interpolated cross-sections of the STM tip trajectories over the DNA molecule along the lines A and B shown in Figure 5 are compared to the atomic contours of A-DNA approximating the cross-sectional regions. These line cuts were chosen to span the minor groove showing the best base pair resolution. In each case, the experimental cross-section is placed above the corresponding region of the model. The sugar-phosphate backbone is again red and the base pairs yellow. The data used for the cuts were also smoothed 0.60 Å FWHM. In the top half of Figure 8, the cut was taken across the base pair planes, approximating the minor groove axis. Starting at the left, line A cuts through the phosphate-sugar backbone on the leading edge and shows the base pair periodicity across the groove. The cross-section in the bottom half of Figure 8 shows a similar comparison for line B taken across the

minor groove through the two high backbones and an intermediate base pair. The nearly atom-for-atom agreement of the experimental cross-sections to the contours of the model indicates atomic resolution in this region of the image.

A STM topographic image, 50 x 100 Å, in a solid-modeled presentation similar to Figure 6, but acquired about 15 minutes earlier, is shown in Figure 9. The regions of the molecule which are scanned in the two figures are nearly the same, but the image in Figure 9 is not "straightened out" by the image rotator (see description in chapter 1). There is a "tip instability" at nearly the same location along the molecule as seen in Figure 5. The origin of this instability however is unknown, but the molecular orientation is the same. The appearance of the molecule is also very similar to that of Figure 6, even down to the atomic scale. This is in fact borne out in Figure 10. The STM image of Figure 7 (left) is compared to the identical corresponding bottom portion of Figure 9 (right) in Figure 10. The image at right was obtained 15 minutes earlier. The two successive images are essentially identical, providing evidence of the nondestructive imaging capabilities of STM. The STM is shown here to be able to image repeatedly even a "fragile" biomolecule without any noticeable structural modification. The images are each 35 x 55 Å and are not histogram equalized.

Six complete topographical, as well as six complete simultaneous barrier height, images, including both forward and reverse traces, were obtained with atomic resolution. Following these images, however, nearly two hours were needed to make "back-up" copies of the data and free-up space on the computer's hard disk. Following this procedure, the molecule was again located with comparable resolution. However, during this next image, there was an irreversible tip change which reduced the image

resolution dramatically. As a result, it appeared that only the very top of the molecule was imaged. The tip structure that afforded the atomic resolution images is unknown.

***Barrier Height Measurements***

Interpolated cross-sections from the topographical and barrier height data, along the lines marked A (top) and B (bottom) in Figure 5, are compared in Figure 11. The solid lines are tip trajectories as shown in Figure 8; the dashed lines are corresponding data from a simultaneously acquired gap-modulated barrier height image. The effective local barrier height was measured using the standard technique of modulating sinusoidally the tip-sample separation (0.67 Å p-p at 1 kHz) and then detecting $d(\ln I)/ds$, the derivative of the natural logarithm of the tunneling current with respect to the tip-sample gap, with a lock-in amplifier. Although the barrier height axes are shown here in arbitrary units, we typically measured effective local barrier heights over DNA ranging 0.2-1.5 eV. The barrier height image is not shown here but has a generally similar appearance to the topographical image. The topographical and barrier height features show general correlation in structure over the backbone atoms. However, the barrier height reveals considerable anti-correlation (complementarity) within the minor groove where atoms of the base pairs are resolved. In other words, the barrier height shows a peak where there is a valley in the topographical cross-section and vice versa. This complementarity is quite pronounced over the base pair atoms in the topmost graph. The topography in the bottom plot shows two high backbones with a concave minor groove of depth 2-3 Å and width 10 Å, again consistent with the van der Waals surface model. The agreement of features over the backbone and complementarity over the bases is also

evident in this cross-section. The complementarity may be due to the stronger influence of chemical identity in barrier height imaging. The anti-correlation may in fact arise from the aromatic nature of the base pairs, in which electron density is concentrated "vertically" within the π-bonding located between the base pairs. Current imaging tunneling spectroscopy (CITS) may be able to reveal additional chemical information, but casual attempts at these measurements showed little consistent difference in current-voltage character between the bare substrate and the adsorbed molecule.

*Electron Microscopy*

DNA samples prepared by drying drops of DNA-containing solutions on HOPG were found to be aggregated or clumped in STM images. These results were substantiated by scanning electron microscopy (SEM). SEM has been used for a number of years to image DNA; two excellent reviews on biological sample preparation methods for EM are given by Coggins[30] and Robinson *et al.*[31]. These reviews address in detail the problems and difficulties associated with preparing nucleic acid samples for EM investigation.

On samples prepared similarly to those used in the STM experiments, using a variety of DNA samples (including single-stranded DNA and synthetic short oligomers of duplex DNA) and deposition techniques (including preliminary attempts at electrospray ionization, which is described later in this chapter), SEM showed that the DNA was aggregated into clumps. These clumps were "bushy" in appearance, on the order of 1000 Å in size. The SEM results were consistent with prior STM observations, as discussed earlier in this chapter.

An example typical of a DNA aggregate as imaged by SEM is shown in Figure 12. The SEM image reveals a clump of DNA caused by the drying of a droplet of DNA on HOPG in air, followed by a moderate vacuum (~ $10^{-2}$ torr, using a rotary mechanical pump). The DNA appears relatively thick, and is approximately 0.1 x 1 μm in size. We showed with similar studies, using electron diffraction analysis of x-rays (EDAX) in combination with SEM, that these aggregates were almost definitely DNA, with a high phosphorus signal. SEM confirmed that such preparation methods are far from ideal.

*POSSIBLE IMAGING MECHANISM*

The contrast mechanism which permits STM imaging of relatively thick, presumably insulating, biomolecules like DNA remains poorly understood in the literature. An early theory on the contrast mechanism responsible for DNA imaging was proposed by Lindsay *et al.*,[32] who suggested that adsorbate deformation can contribute to STM imaging of biopolymers in aqueous environments. The authors used barrier height imaging to illustrate how local fluctuations in the deformability of the molecule (adsorbate) could lead to contrast in STM images. Numerous other theories for STM imaging have been proposed in recent years. Keller *et al.*[12] proposed that there exist conductance pathways through the DNA molecule itself. Although the bulk conductivity of dry DNA at room temperature is small enough for DNA to be considered insulating, about $10^{-16}$ S/cm, they suggested that the bulk conductivity is dominated by intermolecular contacts and is therefore a poor estimate of a single molecule's conductivity. Keller proposed that the conjugated π systems of the bases may be conductive; there exist considerable potential barriers only at the two phosphate backbones, and not at the

conductive core. This theory however is quite simple and cannot account for the variety of observations with STM. Salmeron and coworkers[26] postulated that resonance tunneling effects could contribute to the observations in such a way that the thickness of the DNA molecule would not affect the one-dimensional tunneling barrier width. They suggested that for most electron energies, the effect of the DNA's thickness is to affect only the phase, not the amplitude, of the tunneling electron wave function. This mechanism, considered by itself, is again quite unlikely. Garcia and Garcia[33] explored the issue of electron conductance through organic chains. These authors presented a mechanism based on both inter- and intra-molecular energy relaxations and chain disorder to explain the support of nanoamp currents and DNA imaging by STM. Zhdanov *et al.*[34] calculated the tunneling current in the vacuum region between two metallic electrodes with a bias voltage between them, in the instance where there is an adsorbed molecule on one of the electrodes. They found that if the molecule is small, the electronic eigenfunctions of the substrate/adsorbate system are delocalized, and subsequently, the influence of the adsorbate on the tunneling current is nearly negligible. However, the most probable theory postulated in the literature to date to explain DNA imaging by STM has been proposed recently by Lindsay and coworkers.[35] The authors investigated an empirical tight-bonding model of a tunnel junction which contains a molecule in the gap, and addressed pressure and resonance effects in STM of molecular adsorbates. If the gap contains an insulator in which a molecule, with a resonant molecular orbital, is located equidistant from the metal electrodes, the transmission through the resulting double-barrier can approach unity, independent of the thickness of the gap. However, they concluded that

resonant tunneling alone could not account for the STM images. Instead, they invoked the fact that the pressure in the STM tunnel gap may approach a few gigapascals. The ultraviolet absorption of DNA at these pressures is red-shifted by ~ 0.5 eV, suggesting that the molecular orbitals are shifted and broadened by comparable amounts, making it possible to access molecular energy levels for STM imaging. We have developed our own theories on this subject.

The ability to resolve surface atoms on a 20 Å diameter "insulating" biomolecule is an extremely interesting result which places a new constraint on proposed imaging mechanisms. While it is recognized that intramolecular conduction pathways may exist in DNA, none are consistent with the transport of $10^{10}$ electrons per second, the tunneling current in our experiments. Furthermore, as Tersoff and Hamann[36] and others have shown, the STM current arises from states near the Fermi level of the sample. In particular, the current accepting states in our experiment must be within 100 meV of the Fermi level. States generated by the strong covalent bonds of a biomolecule composed primarily of second row atoms would be well below (or above) these levels. This suggests the mechanism for tunneling current modulation is only indirectly related to the physisorbed molecule's states.

We propose[23,37] that the current contrast mechanism arises from an interaction between the adsorbate and graphite substrate which serves only to modulate the underlying bulk states. There are two parts to this interaction, both of which can affect the tunneling current and lead to contrast changes near an adsorbate. The first part of the modulation effect arises from the Pauli principle which effectively requires the orbitals for different bond pairs to be orthogonal. Whereas graphite band states would normally decay

exponentially into the vacuum, the presence of the adsorbate interferes with this decay. Orthogonalization of the graphite band states to the orbitals of the adsorbate causes the tail of the band orbitals to rapidly oscillate in the region of the adsorbate and then resume exponential fall-off above the adsorbed molecule. This leads to an extension of the band orbitals to larger distances with the total extent depending on the orientation and character of the molecular orbitals of the interfering molecule. Thus it is plausible that some adsorbate features will be imageable with atomic resolution. However, even without a quantitative understanding of the imaging mechanism, it is clear from the images we and others have obtained that a worthwhile contribution can indeed be made using STM to investigate biological molecules.

*ALTERNATE DEPOSITION METHODS*

The simple DNA deposition method employed in these studies (dried drop) unfortunately does not yield an even distribution of unaggregated DNA on a HOPG surface. Considerable additional development is required to make such high-resolution imaging of DNA and similar biomolecular adsorbates reliable and reproducible. We have explored preliminarily other deposition techniques with the intention of minimizing aggregation and providing a more even DNA distribution. Electrospray ionization (ESI)[38] is considered to be one of the more promising methods, relatively simple to use, with the potential to provide highly uniform molecular distributions. ESI has been in use for decades, originally for industrial applications such as electrostatic spray painting. Electrostatic spraying of a liquid sample occurs between two electrodes, one the surface onto which the spray is to be deposited and the other the liquid to be sprayed. ESI involves the flow of a

sample solution through a fine capillary or hypodermic needle maintained at a high potential (several kV) with respect to the substrate located in close proximity (on the order of cm) to the needle. The high electric field promotes the charging of the surface of the sample solution droplet located at the needle tip. The competing forces of electrostatic repulsion and surface tension cause the liquid to become atomized. When the charge accumulates, the drop explodes into a fine spray of charged droplets, which evaporate as the droplets move toward the substrate. As they evaporate, the charge density on each drop's surface increases (the individual free charges repel each other) until the droplets explode into even smaller droplets, producing a cascading effect of progressively smaller droplets. This process continues until the droplets are small enough for the surface charge density to be no longer sufficient to overcome surface tension forces, and causes ions to be removed from the droplets. These charged (positively or negatively, depending on the geometry of the set-up) ions in turn carry with them molecules from the sample solution. The droplets may be as small as approximately 0.1 to 1 μm in diameter, small enough so that only one to several molecules of DNA can be contained within the volume of a single droplet. This procedure presumably minimizes the chances of aggregation since the droplets would contain so few molecules and because the molecules would be highly charged and therefore would repel each other strongly. The ESI method has been shown to be applicable to thermally labile biomolecules like DNA.[39] Unfortunately, preliminary attempts at using ESI for DNA deposition onto HOPG have yielded inconsistent and poor results, using both SEM and STM for sample evaluation. The results show little improvement in reducing molecular clumping and in promoting even substrate distribution. However,

little effort has been made to optimize the spraying conditions and geometry; no definitive conclusions can yet be made about the future usefulness of this technique to general sample deposition applications.

Another option that was briefly explored was the Kleinschmidt-type "spreading" deposition[40] of histone-depleted chromosomes, as previously used in several electron microscopy (EM) studies.[41] By depleting a chromosome of its DNA-binding histones, it has been shown by TEM that one can obtain an even "halo" spread of DNA (diameter roughly 20 μm) still bound to its central protein scaffold. A modification of these EM methods should yield an even and broad distribution of "clean" DNA which would be in a convenient form for routine imaging by STM. Although considerable effort toward this end was invested, it was not possible to reproduce the EM results, much less develop this method of preparation into a generally applicable technique for molecular spreading.

The most commonly used sample preparation technique in modern EM experiments involving "fragile" biomolecules is freeze-drying. This technique shows considerable promise for STM applications as well. However, this method has not been used for similar DNA preparations to date. The freeze-drying process has in fact reached an extremely high level of understanding. Biological samples in fact have been found to show little physical damage, even on the level of tens of nanometers, due to either the freezing or drying processes.[42,43] Such freeze-drying would probably minimize the influence of surface tension (caused by the slowly receding droplet surface) on the sample structure. No efforts have been made by our research group to use freeze-drying or lyophilization to prepare DNA samples for STM imaging.

*EVALUATION OF SUBSTRATES FOR DNA*

As mentioned earlier, graphite, i.e., HOPG, has been the most popular substrate for the deposition of DNA and other biological materials in STM experiments. The primary reasons for its popularity are its atomic flatness and ease of preparation. Although ZYA-grade HOPG, when well-cleaved, contains very few surface defects, it is these defects, especially steps, that have made graphite a controversial substrate choice for STM studies of biomolecules. These criticisms of HOPG are especially strong when the samples are poorly cleaved and when the biomolecule is linear like DNA. Clemmer and Beebe[44] showed that HOPG surface features, especially steps, could give rise to image misinterpretation when biomolecules are being studied. They observed large-scale regular periodicity at step edges, which could be interpreted as the DNA helix repeat, as well as contamination collected near steps, sometimes appearing as "molecules" meandering across steps. Their results have brought into question previous reports of DNA imaging where only helix periodicity was resolved. Many of these previous images of DNA on HOPG indeed appear similar to Clemmer and Beebe's images of HOPG substrates without DNA deposited on them. Their results however do not necessitate reevaluation of results which show unambiguous atomic-scale periodicity, like ours.[45] However, they do necessitate careful scrutiny and cautious interpretation of DNA images that are ambiguous. It is possible to use other modes of imaging, such as barrier height imaging, or tunneling spectroscopy to distinguish between true DNA features and merely surface defects. On the other hand, tunneling spectroscopy cannot necessarily be interpreted without ambiguity.[46] With high-quality HOPG and good cleaves, coupled to an awareness of graphite's idiosyncrasies, there are no

severe disadvantages imposed by its use. In fact, since we have already established that atom-resolved imaging of DNA is possible on HOPG, while no other substrate has been used with similar success, there exists no reason why HOPG should be abandoned as a possible substrate.

In response to these reservations about using HOPG as a biomolecular substrate, as well as the fact that molecules do not adhere well to the inert hydrophobic basal plane surface of graphite, other substrates have been tested. Unfortunately, it is difficult to find an appropriate substitute for HOPG that would meet the requirements of atomic flatness and ease of preparation. Additionally, other substrates may be just as prone to surface features which could be misinterpreted as biomolecules. The only other substrate that has been used with any frequency is gold, either in the form of molten spheres[47,48] or epitaxial films (typically grown on mica).[49] The former consists of melting gold wire in air using a torch flame. The resulting ball, when cooled, contains many atomically flat facets with (111) orientation. The latter requires careful evaporation of gold onto suitably flat substrates at elevated temperatures in moderate to high vacuums in order to produce clean and flat surfaces. The gold substrates permit a broader range of surface chemistry options for the attachment of biomolecules than do the HOPG substrates. However, features on the gold surface can also often appear as "strands" or biomolecules, and contamination in air is much more likely to occur on gold than on graphite. The search for the ideal substrate for biomolecular STM investigations continues. However, even if a perfect substrate does exist, there are numerous other preparation problems, especially involving molecular deposition and/or spreading, that need to be addressed before one can expect reliable and reproducible STM imaging of DNA.

*DNA SEQUENCING?*

DNA sequence information provides a considerable contribution to our understanding and control of the role of genes in human health and regulation. The STM imaging of DNA has received special attention because of the obvious potential of using this technique for DNA base sequencing. The notion of sequencing with STM has been suggested since the first images of DNA were reported, and has become a topic of great discussion after atomic resolution was shown to be possible. In addition to STM, atomic force microscopy (AFM) has been used[50] in attempts to image DNA and reveal its base sequence. AFM of course offers an advantage over STM in that its data are more straightforward to interpret; unlike STM information, AFM images reveal "pure" topography without contributions from electronic structure. Unfortunately, AFM to date has not shown resolution comparable to STM. This is probably due to image blurring caused by movement of the DNA molecules under the substantial forces imposed by the scanning tip. Consequently, the majority of discussions on DNA sequencing has focussed on STM. The use of STM for sequencing is attractive because of its potential speed and its low cost.

There exist presently well-developed biochemical techniques for sequencing DNA, but they are generally acknowledged at this time to be too slow and too costly to sequence the entire human genome of ~ $3 \times 10^9$ base pairs. Even at the sequencing rate of 1 base pair per second, the human genome would take 100 years to identify. The STM holds promise for a substantial increase in this rate, to such an extent to perhaps make it feasible. STM may also be able to sequence longer fragments of DNA than existing techniques.

Recently, two papers have directly addressed the issue of DNA sequencing by STM-related technology. Heckl and Holzrichter[51] proposed using STM and AFM as an alternate technique to conventional biochemical methods for elucidation of the human genome. They addressed the specific obstacles to making this practical; it is necessary to select and prepare a specific desired DNA segment, anchor it with the bases exposed to the STM/AFM probe, follow its length with the tip, and identify its sequence unambiguously. In addition, they showed that the bases when deposited as two-dimensional arrays can be distinguished from one another using STM. The authors were able to image the four bases on graphite individually and show them to be unique in appearance. A number of techniques to aid in DNA sequencing, including base labeling, both biochemical and optical, are suggested in this paper. Lindsay and Philipp[52] present an excellent review of the present state of STM technology, and the probable limitations that would face STM as a practical tool for sequencing DNA. Although the sequencing rate could potentially be as high as kilobases per minute, there is no assurance of this rate, especially in light of the difficulties in sample preparation and image interpretation.

Although base labeling may aid dramatically to the success of DNA sequencing by STM, it is not necessarily required. In fact, the potential sequencing rate would probably be greatest if such labeling techniques are unnecessary and the DNA is directly imaged. Positioning of the DNA molecular segment under the STM tip may be facilitated by "optical tweezers," by using lasers to drag the DNA molecule across the substrate.[53] The theoretical throughput of automated sequencing using conventional radiolabeling and fluorescence techniques is about 15,000 bases/day for a

single device. This rate has not been practically demonstrated, but even this rate would require exorbitant time and costs. If atom-resolved imaging of single-stranded DNA is routinely possible, and bases could be identified by direct observation, it is not unreasonable then to expect a potential STM sequencing rate $10^3$ to $10^4$ times faster than the aforementioned theoretical throughput of conventional automated chemical sequencers.

## *CONCLUSION*

Ever since the first STM image of DNA was presented, the STM has shown great potential for the investigation of biological structures. However, until the studies described here, atom resolved imaging of large biomolecules like duplex DNA had been an elusive goal. Topographic STM images of uncoated duplex DNA on a graphite substrate obtained in ultra-high vacuum (UHV) were presented which showed double-helical structure, base pairs, and atomic-scale substructure. Comparisons of experimental STM profiles to atomic contours of the van der Waals surface of an A-DNA model derived from x-ray crystallography showed excellent correlation. Cross-sections of gap-modulated barrier height images obtained simultaneously with topographs showed general correlation with the atomic-scale topography over the phosphate-sugar backbone but showed marked anticorrelation over base pairs. This relationship may have been due to the different chemical characteristics of different parts of the molecule. The improved resolution compared to previously published STM images of DNA may have been due to the UHV conditions, the relatively high data-pixel density, the slow scan rate, a fortuitously clean (dirty?) and/or sharp tip and/or a relatively dilute and extremely clean sample solution. This work demonstrated the potential

of the STM for characterization of large biomolecular structures, but additional development is still required in order to make such high resolution imaging of DNA and other large molecules routine. Attempts at improving the sample deposition and spreading techniques were not generally successful.

The conditions necessary for reliable and reproducible imaging of DNA with atomic resolution remain a mystery. Although these experiments, which yielded atom-resolved imaging, were performed in UHV, these conditions may be unnecessary (see next paragraph) for successful results. The "clean" environment provided by UHV can be afforded more easily by using a drop of mineral oil or water on the sample. The latter approach would maintain some degree of molecular hydration (and presumably a more natural structure as a consequence), and has been shown in previous studies to provide nearly the same high resolution on DNA. Freeze-drying, or lyophilization, may provide another way of preparing samples with a significant reduction in structural damage. However, sample preparation, as aforementioned, needs considerable additional research. The tip structure (shape, sharpness, and cleanliness) which gave rise to our best results is also unknown. The tip may have been fortuitously clean or "dirty." The attachment of a dangling and soft material to the tip may have been responsible for the imaging. This in fact may account for the lack of damage to the molecule and the instability of the tip upon repeated scanning.

Although the UHV conditions presumably "dehydrated" the sample, it may also have contributed to the success of the experiments. In nearly all the previous STM experiments performed on DNA, the samples were not substantially dehydrated. In fact, in many of these experiments, attempts

were made to maintain hydration by using high humidity environments. It is known[4] that B-DNA in solution is highly and inhomogeneously hydrated; the hydration exists as two discrete layers, primary and secondary hydration shells. The primary hydration layer consists of at least 11-12 water molecules per nucleotide, reaching a complete 20/nucleotide at 80% relative humidity. The 8 or 9 water molecules in direct contact with DNA is impermeable to cations and is not ice-like. The secondary hydration shell however is indistinguishable from bulk water. The hydration of A-DNA is considerably different from that of B-DNA. As opposed to B-DNA, phosphate groups are hydrated and there is no obvious primary hydration shell. In A-DNA, water molecules span the major groove and stitch phosphate groups together. It is probable that these water molecules remained attached even in UHV; however, all other water molecules are probably removed in vacuum. Therefore, the major groove remained hydrated; in fact, this arrangement is necessary to stabilize the A-DNA molecule. Consequently, the wide minor groove was likely stripped of all water, while waters filled the deep major groove. The STM then presumably was able to easily probe the wide minor groove, without interference from water molecules. This fact probably contributed to the better resolution of the minor groove, compared to the major groove.

The limitations of HOPG as a substrate for the deposition of biological materials were discussed. We concluded that there are no significant inherent advantages to using other substrates for these purposes. The potential use of STM for DNA sequencing was briefly discussed. If practical, at the present state-of-the-art, the STM could potentially provide a three or four order of magnitude increase over the theoretical throughput of conventional

chemical techniques. Most importantly, these experiments, regardless of the fact that methods have not been successful in making them more reproducible, were successful in demonstrating the ability of STM to image relatively large biomolecules with atomic resolution.

**Table 1**

The dimensions of general features in the STM image are compared here with dimensions derived from x-ray crystallography for "random-sequence" A-DNA. The STM values listed here are average approximate values based on the image in Figure 5. STM differs from x-ray crystallography in its ability to study local dimension and orientation variations on an individual molecule. Crystallographic data reflect the average dimensions of many molecules in a crystal and therefore cannot be used to study local structural variations.

## COMPARISON OF DIMENSIONS: STM vs. X-RAY

| | STM* | X-RAY** |
|---|---|---|
| Helix Pitch | 29 Å | 28.5 Å |
| Minor Groove Width | 10 Å | 11.0 Å |
| Major Groove Width | 3 Å | 2.7 Å |
| Molecular Width | 23 Å | 23 Å |
| Phosphate Backbone Width | 10 Å | 11.6 Å |
| Axial Nucleotide Rise | 2.6 Å | 2.59 Å |
| Base Pair Angle | + 18° | + 19° |
| Helix Symmetry | 11 | 11.0 |

* STM measurements are approximate average values, as determined from the image

** Derived from X-ray crystallographic data for "random sequence " A-DNA

**Figure 1**

A typical DNA aggregate is shown here in this series of three successive topographical images acquired at higher magnification and pixel density, moving clockwise from upper left. The images "zoom in," focussing on a single toroidally shaped aggregate. Raw data are shown; white corresponds to topographic maxima. The image areas are approximately (3000 Å)$^2$, (1500 Å)$^2$, and (750 Å)$^2$, respectively. The upper left image shows two atomically flat terraces, including an exfoliated region. The surface is scattered with DNA structures. The lower right region of the highest magnification image shows several parallel closely-packed side-by-side DNA strands with pitch repeats of ~ 30 Å. This region is shown in Figure 2. The tunneling current was 1 nA and the sample bias was +200 mV.

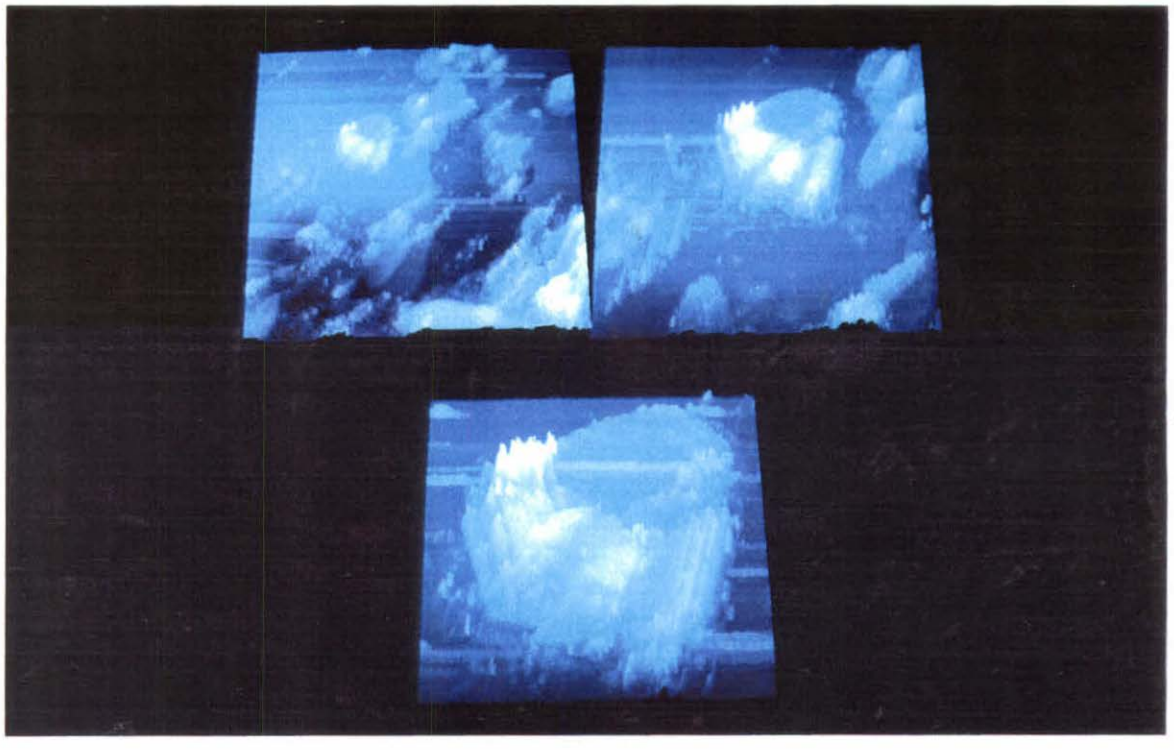

**Figure 2**

A section of Figure 1, ~ 200 Å x 500 Å in size, located at the bottom right of the aggregate in the highest magnification image, is "blown-up" here to show the side-by-side DNA-like features, with a periodicity of ~ 30 Å. The data are slightly smoothed (Gaussian of ~ 3 Å FWHM).

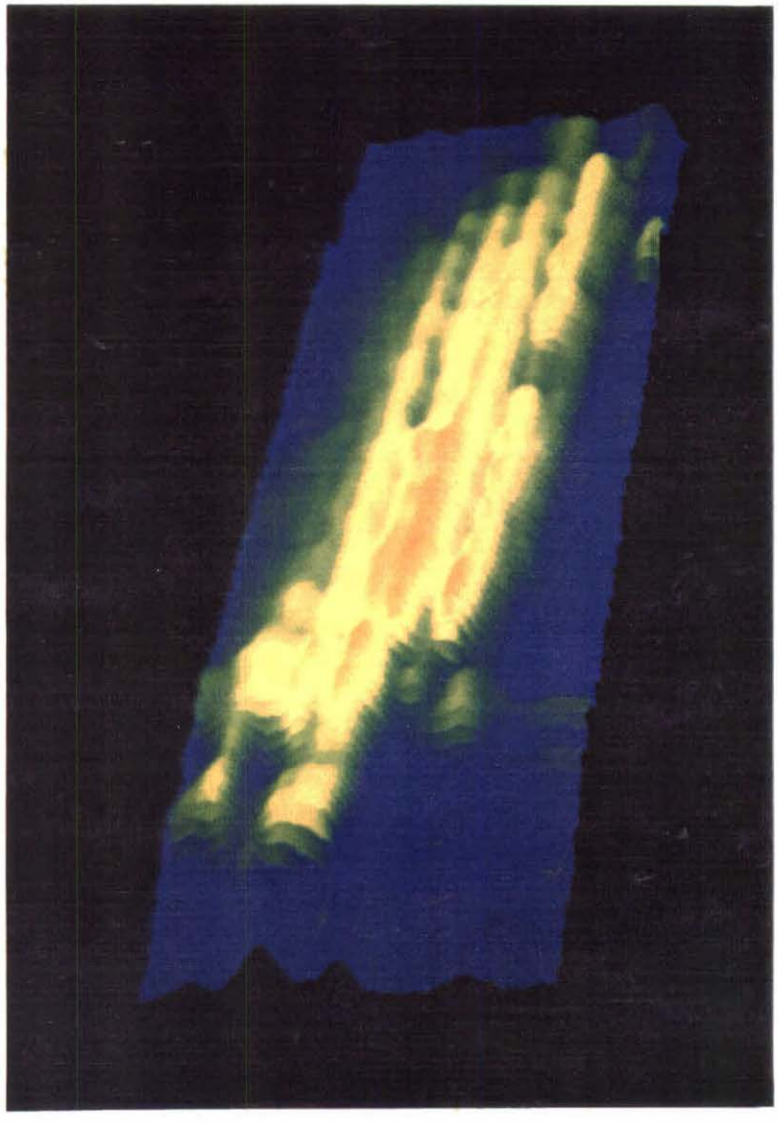

**Figure 3**

The van der Waals surface of an A-DNA molecule is provided here in a model based on x-ray crystallographic data. The phosphate-sugar backbone is shown in red and the base pairs in yellow. Hydrogen atoms are omitted for clarity. Two distinct rotational orientations of the A-DNA model, differing by only a few degrees, are shown. The white arrow indicates this transition point. The significance of this transition is discussed in the text.

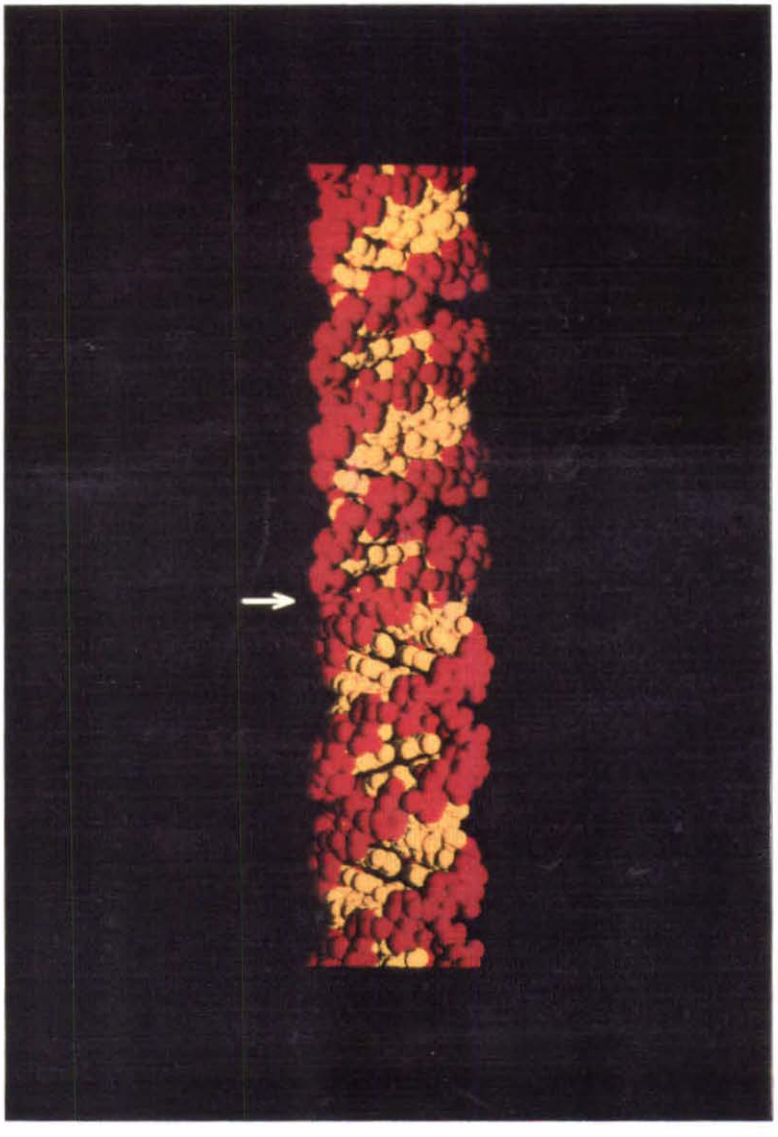

**Figure 4**

An isolated DNA molecule is imaged at high resolution in this unsmoothed, unfiltered, plane-subtracted constant current STM topograph. The image is (200 Å)$^2$ and is composed of 500 x 100 data pixels; the resolution is limited by the density of data pixels, which are spaced 2 Å apart in $y$. Just over seven full turns of the helix are shown here. The helix pitch varies but averages ~ 30 Å, and the molecular width is measured at 25 Å. A kink site with a relative angle of 30° to the helix axis is located at the center of the image. The tunneling current was 1 nA and the sample bias was +100 mV.

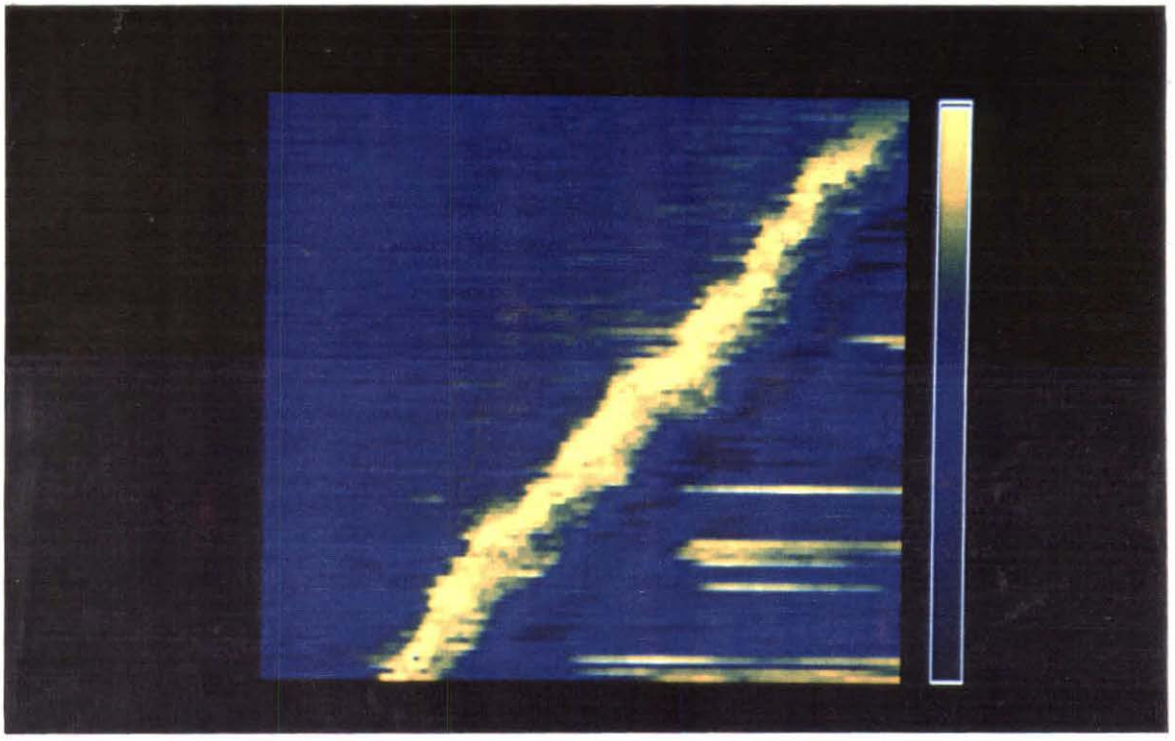

**Figure 5**

A plane-subtracted atom-resolved STM constant current topograph of DNA deposited on HOPG is shown here in an image roughly 80 x 120 Å in size. The image comprises 400 x 250 data pixels, and is not filtered or smoothed. Yellow represents topographic maxima. The parallel bands at +18° ± 3° to the helix axis are base pairs spanning the wide minor grooves. Several of the base pairs crossing one of the minor grooves are indicated by red arrows. During a brief instability (yellow arrow) the probe tip may have tilted the molecule. See the text for additional details regarding this image.

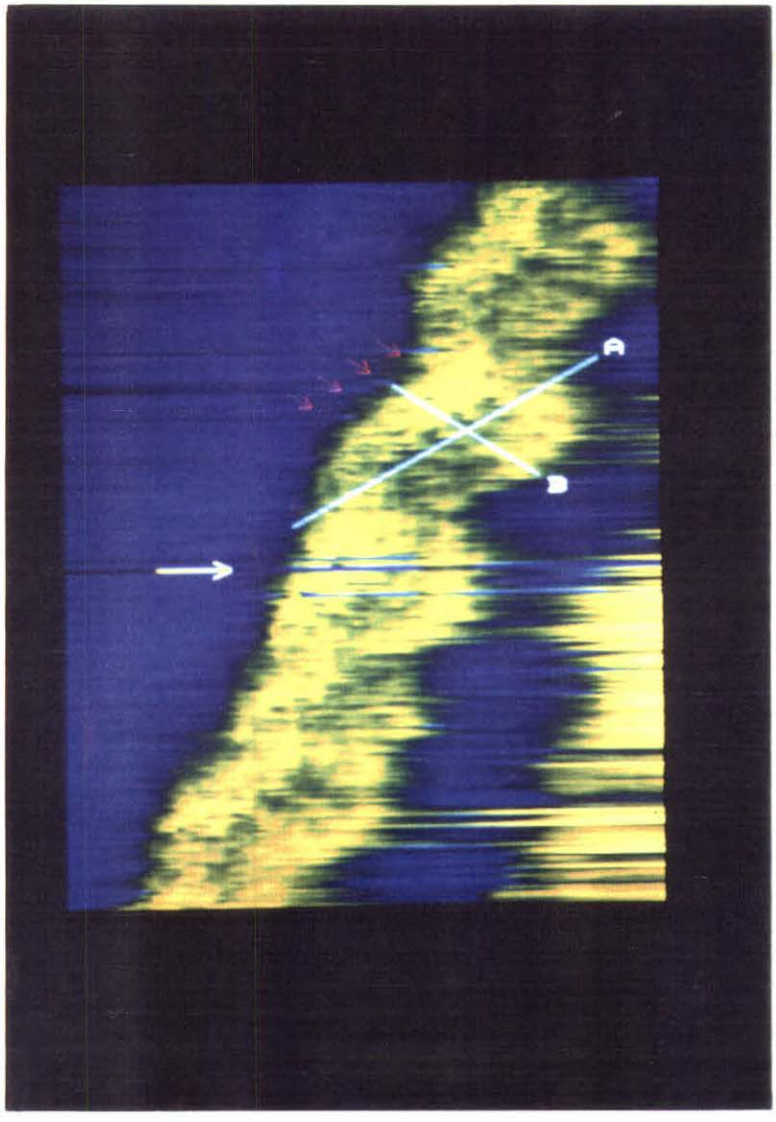
A
B

**Figure 6**

Shown here is a solid-modeled perspective presentation of the bottom three-fourths of the DNA strand shown in Figure 5. The same data are provided, except that the image has been smoothed ~ 0.60 Å. The image is 50 x 100 Å in size. The atomic-scale surface structure becomes evident in this type of presentation. Each of the round "bumps" on the molecule probably represents an individual atom. Further evidence of this atomic resolution is provided in Figures 7 and 8.

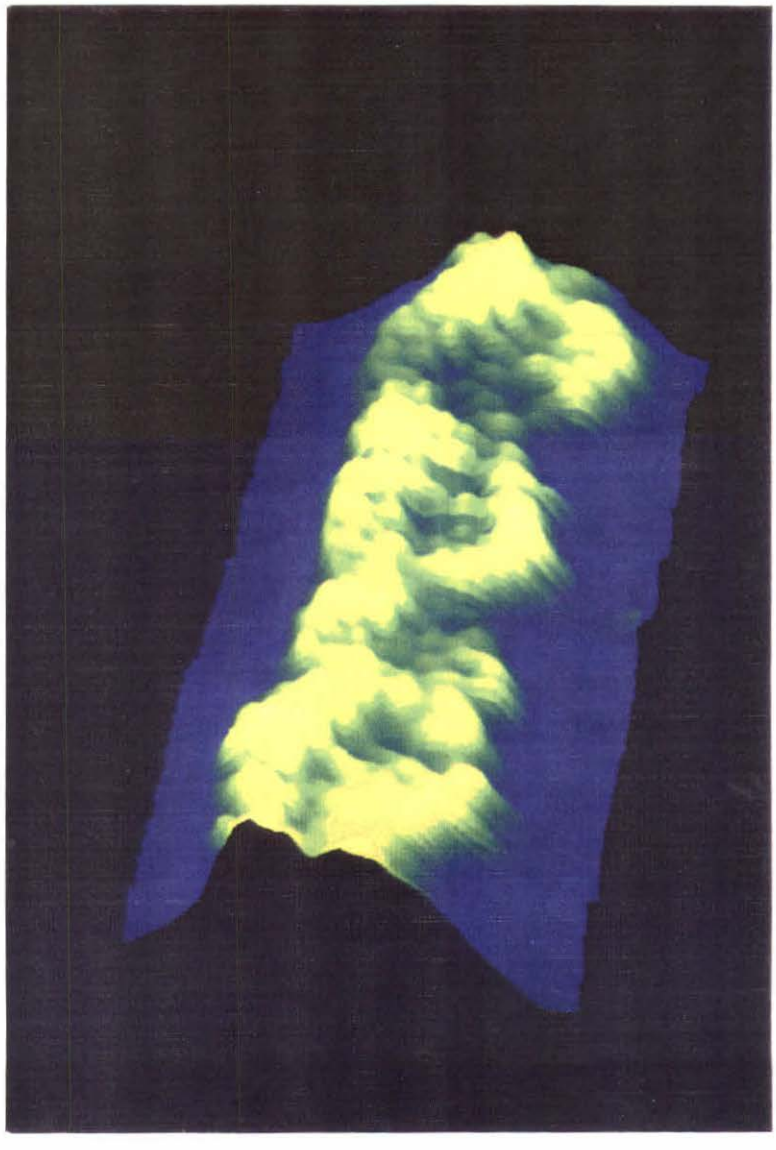

**Figure 7**

The bottom portion of Figure 5 is compared with a corresponding section of a van der Waals model of A-DNA (right). The STM data (left) are raw; the image has been plane-subtracted and unsmoothed, but contrast has been enhanced by histogram equalization. Hydrogen atoms are omitted from the model for clarity. The model was based on x-ray crystallographic data and was constructed using Biodesign Biograf™ software. The STM image is ~ 35 x 55 Å, and the *y* axis is skewed by several degrees to facilitate direct comparison with the model.

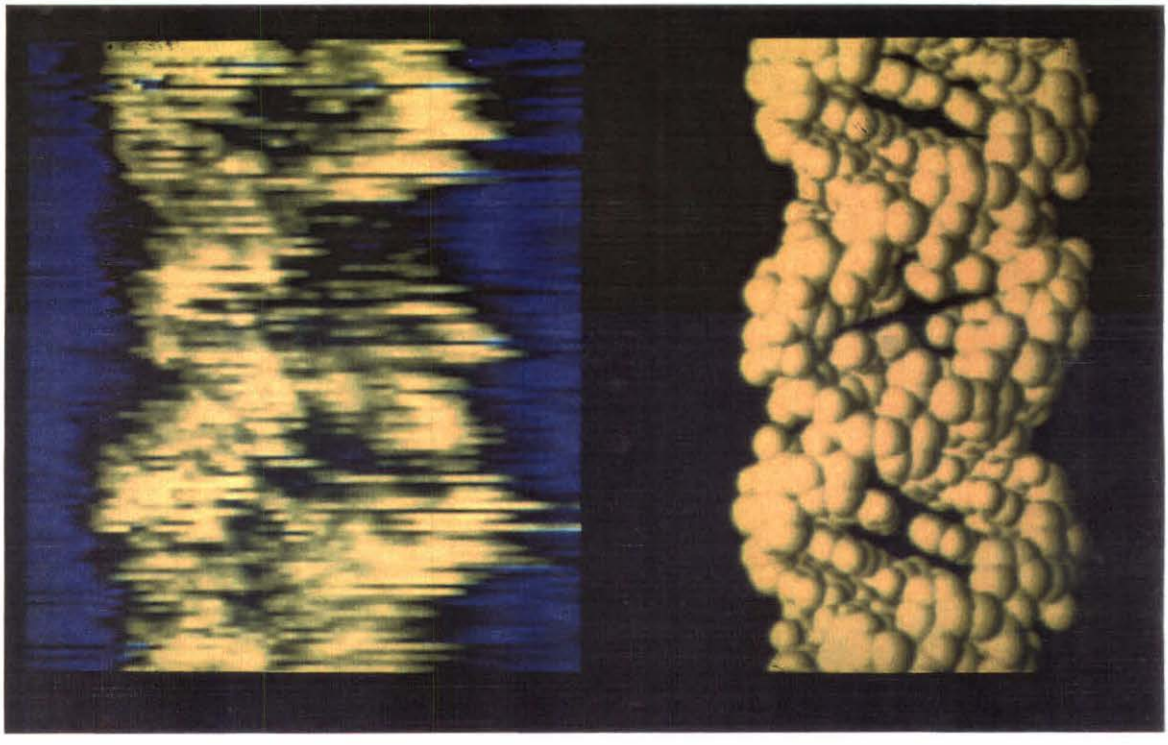

**Figure 8**

Interpolated experimental STM tip trajectories following lines marked A and B in Figure 5 are compared with corresponding atomic contours of an A-DNA van der Waals model. In each case, the experimental cross-section is placed above the corresponding region of the model. The data for line A are shown on top and that for line B are shown on the bottom. Line A cuts across the base pair planes approximating the minor groove axis. Starting at the left, the line cuts through the phosphate-sugar backbone and reveals the base pair periodicity across the groove. Line B shows a similar comparison across the minor groove through the two backbones and a single intermediate base pair. Height and length for the experimental and model data are on the same scale for direct comparison. The STM cross-sectional linecuts have been smoothed ~ 0.60 Å FWHM. Again, hydrogen atoms are omitted for clarity, even though STM may be influenced by their presence.

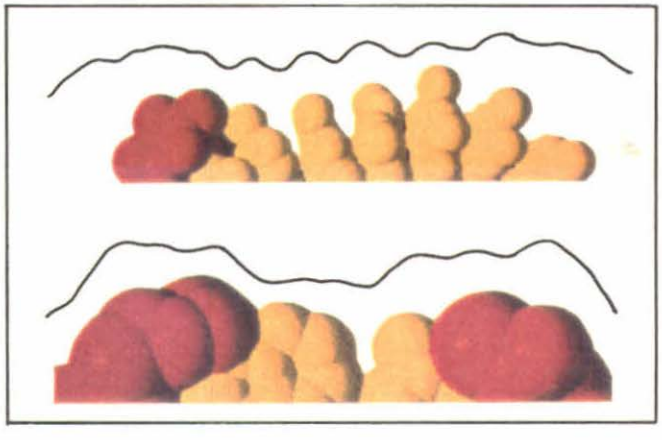

**Figure 9**

A STM image ~ 50 x 100 Å, similar to Figure 6, but acquired about 15 minutes earlier. The region of the molecule which is scanned is almost the same as that shown in Figure 6 but is not "straightened out" by the image rotator (see description in chapter 1). There is a "tip instability" at nearly the same location along the molecule as seen in Figure 5. The origin of this instability is unknown. The appearance of the molecule is very similar to that of Figure 6, even down to the atomic scale. This is in fact borne out in the next figure.

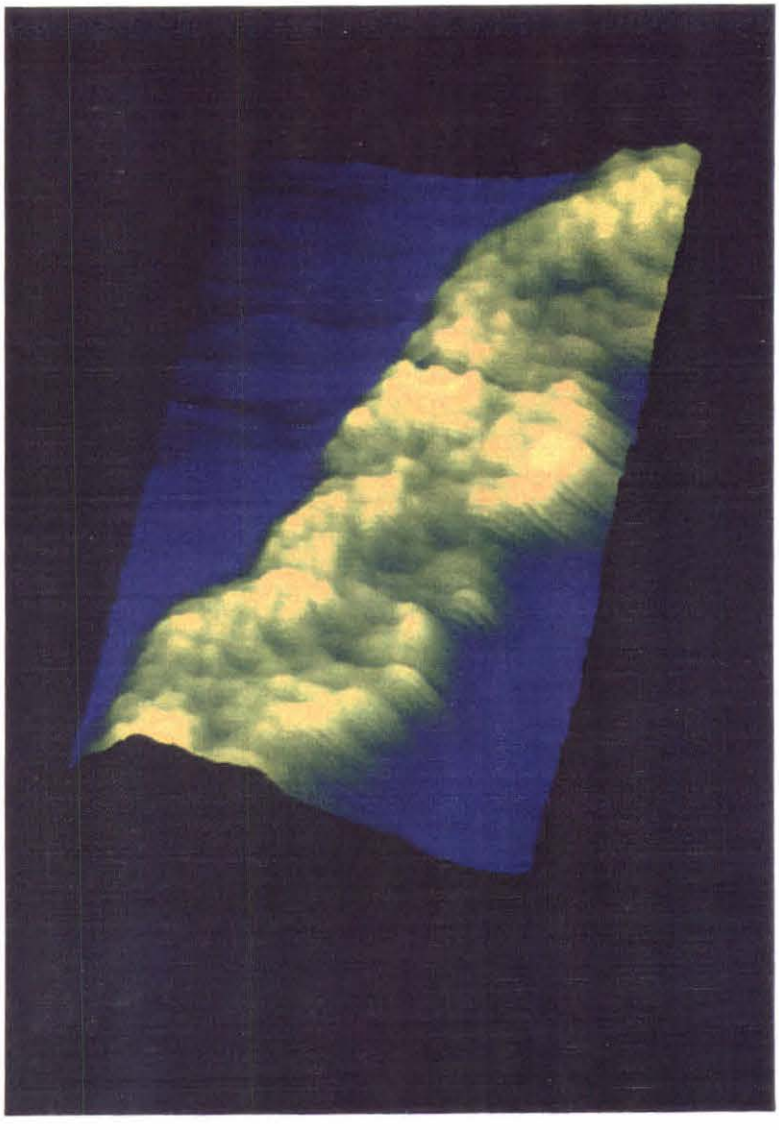

**Figure 10**

The STM image of Figure 7 (left) is compared to the identical corresponding bottom portion of Figure 9 (right). The image at right was obtained 15 minutes earlier. The two images are essentially identical, providing evidence of the nondestructive imaging capabilities of STM. The STM is shown here to be able to image repeatedly even a "fragile" biomolecule without any noticeable structural modification. The images are each 35 x 55 Å and are not histogram equalized.

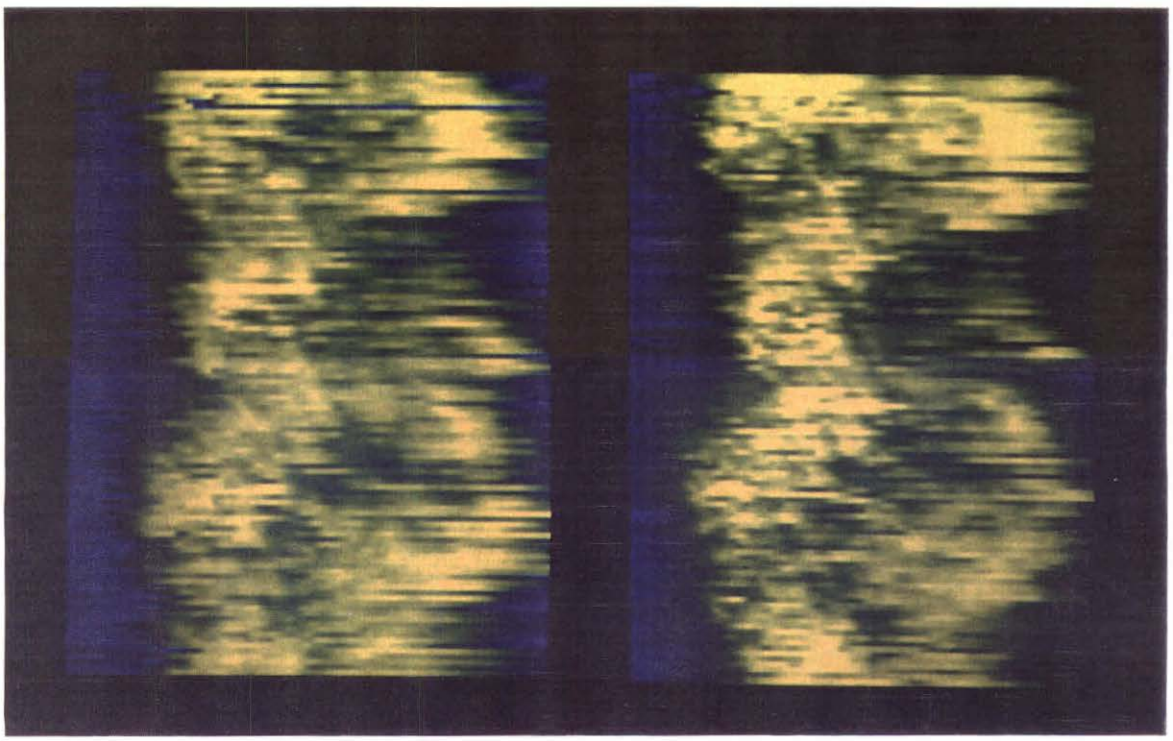

**Figure 11**

Interpolated cross-sections from the topographical and barrier height data, along the lines marked A (top) and B (bottom) in Figure 5. The solid lines are tip trajectories as shown in Figure 8; the dashed lines are corresponding data from a simultaneously acquired gap-modulated barrier height image. The barrier height axes are in arbitrary units. The local effective barrier height was measured using the standard technique of modulating the tip-sample separation sinusoidally (0.67 Å p-p at 1 kHz) and detecting $d(\ln I)/ds$, the derivative of the natural logarithm of the tunneling current with respect to the tip-sample gap, with a lock-in amplifier.

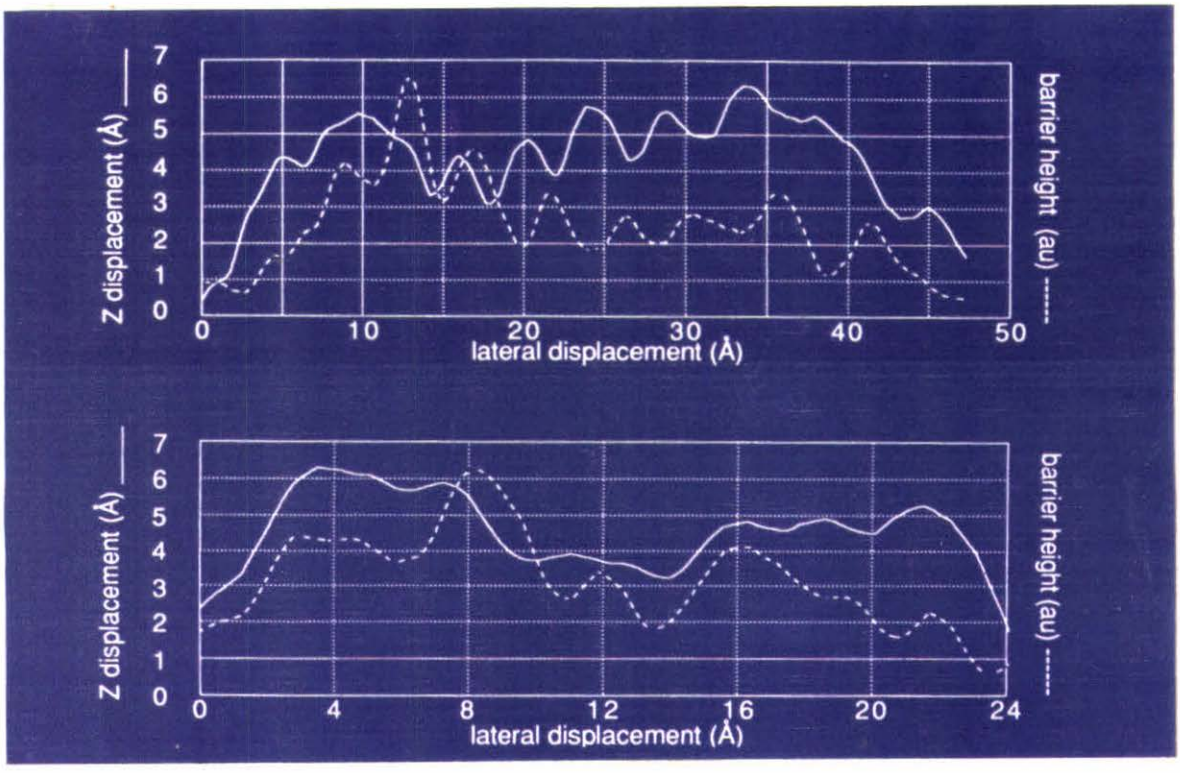
Z displacement (Å) ——
barrier height (au) ------
lateral displacement (Å)
0
10
20
30
40
50
4
8
12
16
24

**Figure 12**

A scanning electron microscope (SEM) image of a typical aggregate of DNA caused by the drying of a droplet of DNA-containing solution on HOPG. The "bushy" clump of DNA is ~ 0.1 x 1 μm in size (see scale marker at bottom) and appears relatively thick. These SEM images confirm previous STM experimental observations of DNA aggregation.

## *REFERENCES*


1. S.M. Lindsay, L.A. Nagahara, T. Thundat, and P. Oden, *J. Biomolec. Struc. Dynam.* **7**, 289 (1989).

2. B.D. Ratner, D.G. Castner, T.A. Horbett, T.J. Lenk, K.B. Lewis, and R.J. Rapoza, *J. Vac. Sci. Technol. A* **8**, 2306 (1990).

3. A.H.-J. Wang, G.J. Quigley, F.J. Kolpak, J.L. Crawford, J.H. Van Boom, G. Van der Marel, and A. Rich, *Nature* **282**, 680 (1979).

4. W. Saenger, *Principles of Nucleic Acid Structure* (Springer-Verlag, New York, 1988).

5. G. Binnig, H. Rohrer, Ch. Gerber, and E. Weibel, *Phys. Rev. Lett.* **50**, 120 (1983).

6. G. Binnig and H. Rohrer, in *Trends in Physics*, J. Janta and J. Pantoflicek, Eds. (European Physical Society, The Hague, 1984), pp. 38-46.

7. M. Amrein, A. Stasiak, H. Gross, E. Stoll, and G. Travaglini, *Science* **240**, 514 (1988).

8. M. Amrein, R. Dürr, A. Stasiak, H. Gross, and G. Travaglini, *Science* **243**, 1708 (1989).

9. S.M. Lindsay and B. Barris, *J. Vac. Sci. Technol. A* **6**, 544 (1988).

10. B. Barris, U. Knipping, S.M. Lindsay, L. Nagahara, and T. Thundat, *Biopolymers* **27**, 1691 (1988).

11. S.M. Lindsay, T. Thundat, L. Nagahara, U. Knipping, and R.L. Rill, *Science* **244**, 1063 (1989).

12. D. Keller, C. Bustamante, and R.W. Keller, *Proc. Natl. Acad. Sci.* **86**, 5356 (1989).

13. T.P. Beebe, Jr., T.E. Wilson, D.F. Ogletree, J.E. Katz, R. Balhorn, M.B. Salmeron, and W.J. Siekhaus, *Science* **243**, 370 (1989).

14. G. Lee, P.G. Arscott, V.A. Bloomfield, D.F. Evans, *Science* **244**, 475 (1989).

15. P.G. Arscott, G. Lee, V.A. Bloomfield, and D.F. Evans, *Nature* **339**, 484 (1989).

16. P.G. Arscott and V.A. Bloomfield, *Ultramicrosc.* **33**, 127 (1990).

17. S. Fujii, A.H.-J. Wang, G. van der Marel, J.H. van Boom, and A. Rich, *Nucl. Acids Res.* **10**, 7879 (1982).

18. A. Cricenti, S. Selci, A.C. Felici, R. Generosi, E. Gori, W. Djaczenko, and G. Chiarotti, *Science* **245**, 1226 (1989).

19. S. Selci, A. Cricenti, A.C. Felici, R. Generosi, E. Gori, W. Djaczenko, and G. Chiarotti, *J. Vac. Sci. Technol. A* **8**, 642 (1990).

20. S. Selci and A. Cricenti, *Phys. Scripta* **T35**, 107 (1991).

21. D.D. Dunlap and C. Bustamante, *Nature* **342**, 204 (1989).

22. R.J. Driscoll, M.G. Youngquist, and J.D. Baldeschwieler, *Nature* **346**, 294 (1990).

23. M.G. Youngquist, R.J. Driscoll, T.R. Coley, W.A. Goddard, and J.D. Baldeschwieler, *J. Vac. Sci. Technol. B* **9**, 1304 (1991).

24. originally prepared by Jerry Siu, California Institute of Technology. The sample was further purified and put into solution by Joseph Meier and Charles Spence of Dr. Leroy Hood's group in the Caltech biology department.

25. ZYA monochromator-grade HOPG (Union Carbide, Advanced Ceramics Division, Cleveland, OH) was used throughout these studies, unless otherwise noted.

26. M. Salmeron, T. Beebe, J. Odriozola, T. Wilson, D.F. Ogletree, and W. Siekhaus, *J. Vac. Sci. Technol. A* **8**, 635 (1990).

27. S.M. Lindsay, *EMSA Bull.* **19**, 60 (1989).

28. there exists, however, limited evidence that "dry" DNA exists in the B-form rather than in the A-form: see S.M. Lindsay, S.A. Lee, J.W. Powell, T. Weidlich, C. Demarco, G.D. Lewen, N.J. Tao, and A. Rupprecht, *Biopolymers* **27**, 1015 (1988), or Y. Fujiyoshi and Y. Uyeda, *Ultramicroscopy* **7**, 189 (1981).

29. E. Selsing, R.D. Wells, C.J. Alden, and S. Arnott, *J. Biol. Chem.* **254**, 5417 (1979).

30. L.W. Coggins, in *Electron Microscopy in Molecular Biology: A Practical Approach*, ed. J. Sommerville and U. Scheer (IRL Press, Oxford, 1987), pp. 1-29.

31. D.G. Robinson, U. Ehlers, R. Herken, B. Herrmann, F. Mayer, and F.-W. Schürmann, *Methods of Preparation for Electron Microscopy: An Introduction for the Biomedical Sciences* (Springer-Verlag, Berlin, 1987).

32. S.M. Lindsay, T. Thundat, and L. Nagahara, *J. Microsc.* **152**, 213 (1988).

33. R. Garcia and N. Garcia, *Chem. Phys. Lett.* **173**, 44 (1990).

34. V.P. Zhdanov, O.V. Gritsenko, and G.M. Zhidomirov, *Phys. Lett. A* **153**, 40 (1991).

35. S.M. Lindsay, O.F. Sankey, Y. Li, and C. Herbst, *J. Phys. Chem.* **94**, 4655 (1990).

36. J. Tersoff and D.R. Hamann, *Phys. Rev. Lett.* **50**, 1998 (1983).

37. T.R. Coley, personal communication.

38. R.L. Hines, *J. Appl. Phys.* **37**, 2730 (1966).

39. C.J. McNeal, R.D. Macfarlane, and E.L. Thurston, *Anal. Chem.* **51**, 2036 (1979).

40. A.K. Kleinschmidt and R.K. Zahn, *Zeit. Naturforsch.* **14B**, 730 (1959).

41. J.R. Paulson and U.K. Laemmli, *Cell* **12**, 817 (1977).

42. B. Wolfgang and A.M. Hermansson, *J. Microsc.* **123**, 115 (1981).

43. J.G. Linner, S.A. Livesey, D.S. Harrison, and A.L. Steiner, *Chem. Cytochem.* **34**, 1123 (1986).

44. C.R. Clemmer and T.P. Beebe, Jr., *Science* **251**, 640 (1991).

45. T.P. Beebe, Jr., personal communication and United Press International press release.

46. M.L. Myrick, N.V. Hud, S.M. Angel, and D.G. Garvis, *Chem. Phys. Lett.* **180**, 156 (1991).

47. T. Hsu, *Ultramicrosc.* **11**, 167 (1983).

48. J. Schneir, R. Sonnenfeld, O. Marti, P.K. Hansma, J.E. Demuth, and R.J. Hamers, *J. Appl. Phys.* **63**, 717 (1988).

49. L.A. Nagahara, T. Thundat, P.I. Oden, S.M. Lindsay, and R.L. Rill, *Ultramicrosc.* **33**, 107 (1990).

50. A.L. Weisenhorn, M. Egger, F. Ohnesorge, S.A.C. Gould, S.-P. Heyn, H.G. Hansma, R.L. Sinsheimer, H.E. Gaub, and P.K. Hansma, *Langmuir* **7**, 8 (1991).

51. W.M. Heckl and J.F. Holzrichter, *Nonlinear Optics* **1**, 53 (1992).

52. S.M. Lindsay and M. Philipp, *GATA* **8**, 8 (1991).

53. optical tweezers developed by S. Chu, Stanford University.